Computational strategies for multi-scale analysis of solids: Small and large strain formulations.

Somer, D. Deniz

CIVIL AND COMPUTATIONAL ENGINEERING CENTRE
PRIFYSGOL ABERTAWE
SWANSEA UNIVERSITY

Computational Strategies For Multi-Scale Analysis of Solids: Small and Large Strain Formulations

D. DENIZ SOMER

Submitted to Swansea University in partial fulfillment of the requirements for the degree of PhD.

January 2010

ProQuest LLC.
789 East Eisenhower Parkway
P.O. Box 1346
Ann Arbor, MI 48106 – 1346

Acknowledgements

I would like to thank my supervisors Prof. D. Perić and. Dr. E. A de Souza Neto, for their guidance and help throughout this work.

I am clearly indebted to Dr. W. Dettmer for sharing his code, also for his friendship and support through hard times.

Thanks Derek and Maziar, for discussing your experiences openly, and providing insights when necessary.

This work was funded by EPSRC of UK under grant No. EP/D500281/1. This support is gratefully acknowledged.

Summary

This work is concerned with simultaneous multi-scale modelling of heterogeneous solids, whereby phenomena associated with the micro-structure have significant influence on the macroscopic behaviour. A compact and efficient computational framework that links the micro and macro scales in small and large strain regimes is presented, which is derived from the variational treatment of the homogenization problem.

Multi-scale analysis is infamous for its enormous memory and processing power requirements. Two methods are proposed to address the issue: Interface discretizion, where an independently discretized interface replaces the discrete Representative Volume Element (RVE) boundary; and a Sub-Stepping procedure that obtains better initial guesses for failed iteration steps of the micro-scale equilibrium Newton-Raphson scheme. The success of both approaches is supported with numerical examples.

The use of the resulting robust and efficient framework is demonstrated by a number of 2D and 3D applications. In addition to reference problems from literature, a study on long fibre composites, from determination of mechanical properties to fully coupled large strain analysis of a two ply laminate is presented.

Finally, composites with weak interfaces are considered, where local degradation associated with inter phase cracking, debonding and sliding within the RVE is investigated using Coulomb frictional contact and cohesive zone models.

Contents

Chapter 1

Introduction

Almost any material has a heterogeneous micro-structure, even if the observed, or macroscopic properties appear to be homogeneous. Metals have polycrystalline structure characterized by grains that vary in their size and orientation. In a metal alloy which is produced by solidification of a homogeneous mix, a second phase exists in precipitate form, while composites consist of two or more distinct phases with significantly different physical or chemical properties, separated by a distinct interface which remains separate and distinct on the macroscopic level. Most biological materials exhibit heterogeneity, eg. wood consists of cellulose fibres embedded in a matrix of lignin, whereas bone or teeth are composed of hard inorganic crystals in a collagen dominated matrix. Heterogeneity could be manifested by existence of voids as well: osteoporosis refers to excessive porosity of the bone.

As Willis [127] points out, because of the micro-heterogeneity, a description of any material in terms of continuum mechanics is an approximation, while any experimental determination of constitutive behaviour is in fact a measurement of *effective* properties. Continuum approach is indifferent to local constitutive relations occurring at microscopic level, thus has limited validity. Furthermore, many macroscopical phenomena (eg. plasticity, creep) have their roots in the micro-structure.

Micro-mechanical material models take into account the shape, size, distribution and mechanical properties of micro-structural constituents, as well as their interactions between them. The procedure which relates the macroscopic stress and strain and of the micro constitutive laws is termed *homogenization* [110], while the inverse procedure, termed *localization* amounts to a micro-mechanics problem which permits to determine microscopic quantities from macroscopic ones.

Prediction of material properties of heterogeneous media has been the focus of analytical, experimental and numerical research in the last 40 years, resulting in an impressive collection of literature.

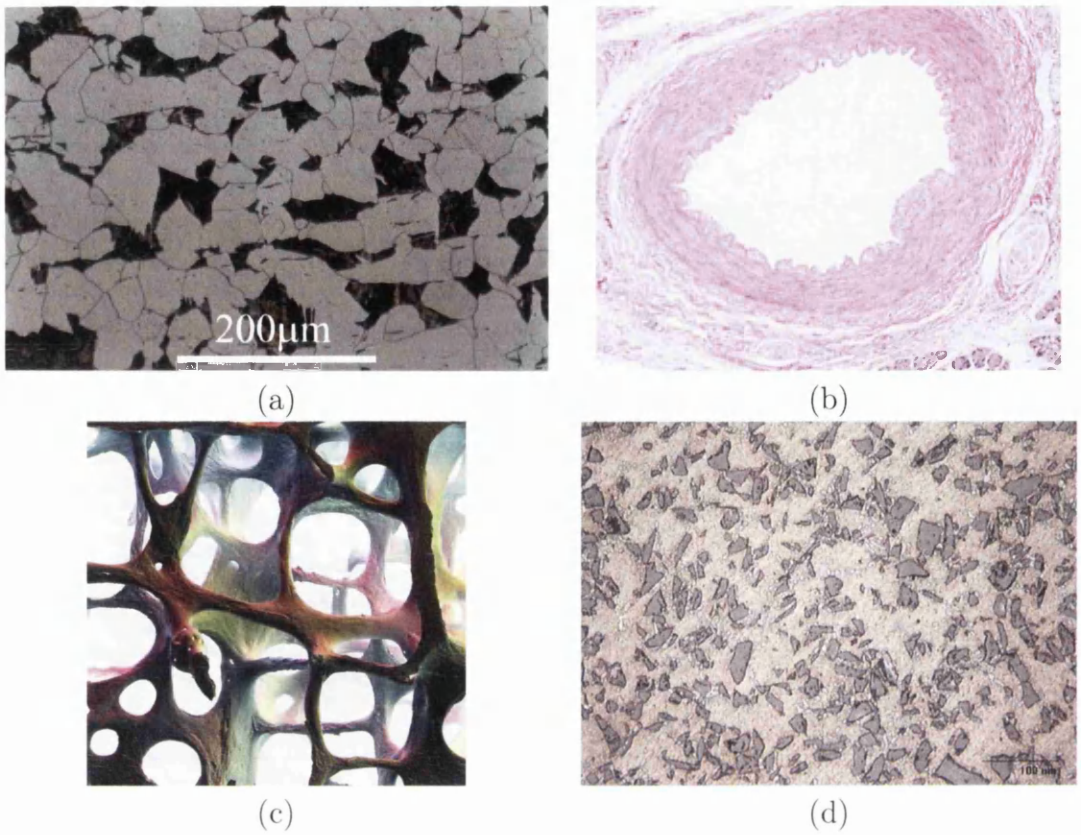

Figure 1.1: Heterogeneous media: (a) Low carbon steel, from Cochrane [20] (b) Artery, from Ross *et al.* [96] (c) Trabecular bone, from Timothy [119] (d) Al-SiC composite, from Hecht *et al.* [44].

Analytical or direct approaches could be dated back to a 1906 paper by Einstein [17], where he computed the effective viscosity of a fluid containing a small amount of rigid spherical particles. Eshelby developed the *equivalent inclusion* method [27], where he studied a misfitting inclusion, caused by eg. thermal expansion, martensitic transformation etc., embedded within an infinite isotropic solid. First, the inclusion is removed and a stress free strain is prescribed. Next, the now misfitting inclusion is made to fit back by applying surface tractions, and finally allowed to relax by deforming the solid. Eshelby also retrieved effective properties of a very dilute composite ($f << 1$) consisting of spherical particles embedded in infinite medium. Eshelby's method was generalized and extended to cover a broad range of application, from electrodynamics to plasticity to interface effects see, eg. Mura [83] or Taya [114]. Mori and Tanaka [81] extended Eshelby's model to cover an inclusion within a finite matrix, as well as multiple inclusions, while taking into account in-

teraction among them. Mori-Tanaka scheme was further developed by eg. Luo and Weng [68] and Benveniste [4].

Hashin [40] used the *composite spheres model*, where the volume is assumed to be filled by varying sizes of composite spheres having the same outside radius to inside radius ratios, as in Figure 1.2 (a), to calculate only the effective bulk modulus of a composite. Hashin and Rosen [42] extended this model to cover composite cylinders and calculated some properties for transverse isotropy associated with random and hexagonal distribution of fibres. They have not supplied closed form expressions for elasticity material properties G_{23}, ν_{23} or E_2, but provided bounds for them. Christensen and Lo [18] derived G_{23} later, using a composite model employed by the generalized self-consistent scheme.

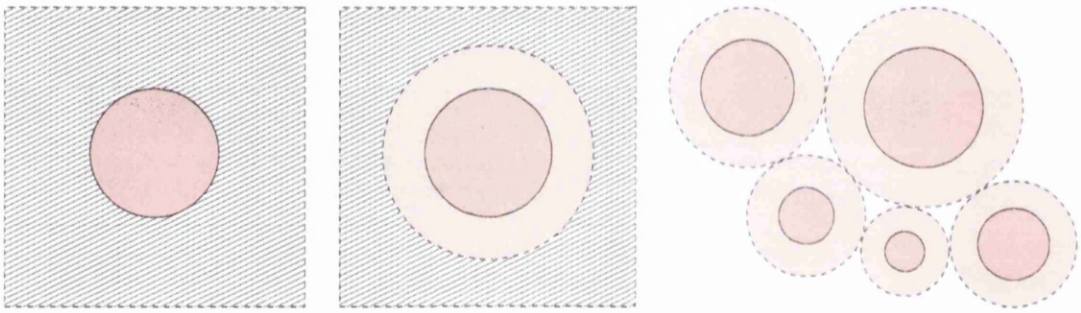

Figure 1.2: RVEs used by analytical approaches: (a) composite spheres/cylinders (b) self-consistent (c) generalized self consistent

The *self-consistent micro-mechanics method* was developed by Hill [48], who introduced incremental solutions for a composite defined by a particle embedded within an infinite homogeneous medium whose unknown properties are the same as the composite, as in Figure 1.2 (b). Hill obtained closed form expressions of bulk K and shear moduli G for a spherical inclusion.

The generalized self-consistent scheme (see eg. [54, 55, 18]) assumes the particle is encased in a matrix shell which is embedded within an infinite homogeneous medium whose unknown properties are the same as the composite, as in Figure 1.2 (c). Because of the non-linear nature of the problem, no closed form solution is available and simplifying assumptions should be made. See Benveniste [5] for a present day perspective for the generalized self-consistent scheme. Halpin and Tsai simplified Hermans' [45] generalized self-consistent model analysis of a composite with aligned continuous fibres [39] , where a closed form applicable to an extended range of reinforcement geometries is provided. Halpin and Tsai approach will be

discussed in detail later for fibre reinforced composites.

Bounds on Properties had been another front of research since Hill [46] had shown that Voigt [123] and Reuss [95] assumptions of uniform strain and stress are the *upper* and *lower bounds* for the elastic moduli. Voigt and Reuss assumptions coincide with a simple volume weighing of phase stiffnesses, called *the rule of mixtures* and volume weighing of compliances, respectively. Hashin and Shtrikman [41] computed narrower bounds using variational principles, for a reference cube of a composite with n phases, by prescribing displacements at the boundary of the composite. Higher order bounds were developed by other workers [7, 126, 12, 112, 33] and extended to cover non-linearity and phase interactions [11, 111, 113, 61].

Unit Cell approaches use axisymmetric unit cells to model hexagonal packing arrangement of the second phase, and compute effective properties of a periodic media, as well as its microscopic stress state by solving the equilibrium problem by the finite element method. Unit cell method was applied for a number of applications, e.g. particle reinforced composites [19, 3, 66], or influence of fibre packing and shape on the overall properties of composites with continuous fibres [10]. In spite of their relatively low computational cost, unit cell models require strict periodicity, which is not commonly found in existing materials. Furthermore, they are not well suited for the non-linear regime.

Classical homogenization procedure requires solving the equilibrium problem of a *representative volume element* (RVE) subject to either uniform tractions or uniform displacements at its boundary. The term RVE was introduced by Hill [47] to refer to a sample that,

1. is structurally entirely typical of the whole mixture on average, and

2. contains a sufficient number of inclusions for the apparent overall moduli to be effectively independent of the surface values of traction and displacement, so long as these values are "macroscopically uniform." That is, they fluctuate about a mean with a wavelength small compared with the dimensions of the sample, and the effects of such fluctuations become insignificant within a few wavelengths from the surface.

Hashin [41] considered a *reference cube* in the composite material that is large compared to the size of non-homogeneities, yet small compared to the whole body, and identified *statistical homogeneity* as a necessary characteristic of the composite material, which implies that body averages and RVE averages are the same. It results

from classical arguments on oscillation functions that the macroscopic stress and strain tensors must be averages of the microscopic quantities [110]:

$$\bar{\varepsilon} = \frac{1}{V}\int_{\Omega} \varepsilon dV \quad , \quad \bar{\sigma} = \frac{1}{V}\int_{\Omega} \sigma dV \tag{1.1}$$

The classical homogenization problem, given by (1.1) together with the microscopic equilibrium should be complemented by a proper selection of boundary conditions. Since the in-situ boundary conditions are unknown, either uniform tractions or uniform displacements are assumed. Hollister and Kikuchi [49] note the lack of uniqueness in (1.1), as the same homogenized state can be obtained by averaging microscopic fields obtained from imposition of different boundary conditions. For a periodic media, the fluctuations of traction and displacement about their mean is large compared to their average [110], so assumptions of uniform traction or displacement fields at the boundary are not applicable. Furthermore, effective stiffness predictions will change as the number of repeating units contained in the RVE changes [49].

Asymptotic homogenization theory was developed by Bensoussan *et al.* [6] and Sanchez-Palencia [97] for spatially periodic media, and originates from studies of partial differential equations with rapidly varying coefficients. Since it assumes that fields vary on multiple spatial scales due to the existence of a micro-structure, asymptotic homogenization is well suited to problems where such separation of scales exist naturally. Such a field is approximated by the asymptotic expansion:

$$u^{\eta}(\boldsymbol{x}, \boldsymbol{y}) = u_0(\boldsymbol{x}, \boldsymbol{y}) + \eta u_1(\boldsymbol{x}, \boldsymbol{y}) + \eta^2 u_2(\boldsymbol{x}, \boldsymbol{y}) + ... \tag{1.2}$$

where, u^{η} is the exact value of the field variable, u_0 is the macroscopic or average value of the field variable, and u_1, u_2 are perturbations in the field variables due to micro-structure [49]. Macro coordinates $\boldsymbol{x}$ and micro coordinates $\boldsymbol{y}$ are related by the size ratio, η:

$$\boldsymbol{y} = \frac{\boldsymbol{x}}{\eta} \tag{1.3}$$

by replacing u^{η} with the microscopic displacement field $\boldsymbol{u}$, the microscopic strain field is found as:

$$\begin{aligned} \varepsilon(\boldsymbol{u}) &= \frac{1}{2}(\nabla \boldsymbol{u} + \nabla^T \boldsymbol{u}) \\ &= \frac{1}{2}(\nabla_{\boldsymbol{x}} \boldsymbol{u}_0 + \nabla_{\boldsymbol{x}}^T \boldsymbol{u}_0) + \frac{1}{2}(\nabla_{\boldsymbol{y}} \boldsymbol{u}_1 + \nabla_{\boldsymbol{y}}^T \boldsymbol{u}_1) + \frac{\eta}{2}(\nabla_{\boldsymbol{x}} \boldsymbol{u}_1 + \nabla_{\boldsymbol{x}}^T \boldsymbol{u}_1) + ... \\ &\approx \bar{\varepsilon} + \tilde{\varepsilon} \end{aligned} \tag{1.4}$$

Terms $\bar{\varepsilon}$ and $\tilde{\varepsilon}$ refer to average and fluctuating components of the strain field respectively, approximated by dropping terms of order η and higher. These methods

try to solve the differential equations with varying coefficients and the homogenized equations emerge naturally, associated with the low order terms in η.

The effective stiffness calculated by homogenization theory is not dependent on the RVE size due to periodicity assumption; see Hollister and Kikuchi [49] for comparison of asymptotical and classical homogenization approaches. Toledano and Murakami [120], as well as Guedes and Kikuchi [37] used homogenization theory to obtain effective average elastic constants of linear elasticity. In the latter [37], the authors solved a macroscopical equilibrium problem with the average properties. They also used the resulting macroscopic stresses to investigate the microscopic stress field.

Multi-scale methods[1], also called global-local or micro-macro methods, solve equilibrium problems simultaneously on different scales, and retrieve the stress fields associated with these scales. In fact, as Matsui and Terada [71] note, this approach seems to be the only way to evaluate the non-linear macroscopic response of a heterogeneous medium when the analytical expression of the macro scale constitutive relation is not available. See e.g. Suquet [110] or Terada and Kikuchi [117] for the initial ideas. Moulinec *et al.* [82] and Michel *et al.* [75] decomposed boundary displacements and solved for fluctuations of displacement in response to the prescribed strain, using Fast Fourier Transforms (FFT) instead of Finite Element Method (FEM). Miehe and co-workers drew a clear framework for micro to macro transitions of non-linear elastoplasticity of polycrystals for large [76] and small strains [77], and joined periodicity requirement of asymptotic homogenization with the classical uniform boundary conditions.

Ghosh and co-workers [35, 36] coupled the macroscopical scale with polygons containing a single second phase inclusion, called *Voronoi* cells. Smit *et al.* [102] and Feyel *et al.* [28] were able to perform simultaneous multilevel finite element simulations for periodic media, while the latter used a perturbation approach to calculate the tangent stiffness. Geers and Kouznetsova [32, 58, 57] developed a second order scheme based on a higher order mapping between current and reference configurations. Miehe [78] used Lagrangian multipliers to enforce a family of boundary constraints. For heterogeneous materials where the scale separation is not of orders of magnitude, multi-grid methods provide a numerical multi-scale modelling of different grids [80], eg. Fish and Belsky [29, 30] used global-local techniques with a multi-grid method for a periodic heterogeneous medium based on homogenization theory.

[1]Previously mentioned methods has been described as multi-scale as well, in the present work we refer to a narrower class of methods that solve homogenization/localization problems simultaneously

Fully coupled simultaneous multi-scale analysis is associated with enormous computational costs. Selective use of multi-scale analysis for critical regions was suggested [57], where non-critical regions would either be modelled by continuum-form homogenized constitutive relations, or by constitutive tangents obtained from the micro-structural analysis. Parallel computation [28, 71] is more than a necessity for three-dimensional problems, and any method to decrease computational costs is quite welcome.

1.1 Aim of the Thesis

In this work, we aim to develop a robust and efficient computational framework for the multi-scale analysis of solids for small and large strain problems, and use this framework in conjunction with non-continuous contact and cohesive zone concepts to investigate behaviour of heterogeneous materials with strong and weak interfaces. This methodology would act as a black box and simply replace local constitutive models in the conventional sense. To this aim, an axiomatic framework based on equilibrium of the RVE, Hill-Mandel Principle of Macro-homogeneity and volume averaging of stress and strain tensors is adopted, based on the assumption that the space of kinematically admissible RVE displacement fluctuation fields is a subspace of the space of minimally constrained displacement fluctuations compatible with the strain averaging hypothesis. This assumption allows implementation of some commonly referred boundary conditions such as uniform displacements, uniform tractions and periodic displacements with anti-periodic tractions into a unified master-slave type dependency structure. The master-slave type dependencies are incorporated into a direct method to solve the micro equilibrium problem efficiently, where the number of unknowns is minimalized, avoiding problems associated with the Lagrangian approach related to distinct wavelengths of the unknowns.

The two-scale problem can be viewed as interaction of distinct domains that are linked by kinematical constraints on the displacement field of the boundary of the homogenized domain. The discrete interaction surface of the homogenized domain can be economized by introducing an independently discretized interface that is linked to the discrete RVE boundary by a finite element type interpolation. This interface would not only liberate the RVE discretization, eg. from periodicity requirement, but would also reduce the time cost substantially, as, at the RVE boundary, only fluctuating degrees of freedom need to be solved for.

Another aspect that needs attention is the gross memory and floating-point calculation requirements associated with fully coupled multi-scale simulations. The (possibly non-linear) incremental microscopic boundary value problem for the associated RVE is solved by a Newton-Raphson scheme. If a solution for the RVE

equilibrium problem cannot be found for the given incremental macroscopic strain, then the updated stress cannot be computed and the macroscopic iterative solution algorithm has to be stopped. The usual course of action in such cases is to cut the macroscopic load increment and try to solve a new incremental problem with reduced load increment, which usually incurs a dramatic increase in overall computational costs. We will propose a sub-stepping procedure [103] that obtains better initial guesses for failed iteration steps of the Newton-Raphson scheme, which allows larger time/load steps to be prescribed at the macroscopic scale, leading to substantial savings in computing time.

1.2 Layout of the Thesis

Chapter 2 covers the aspects of continuum mechanics: Kinematical concepts, definitions of strain and time rates of kinematic quantities are developed. Stress is defined and alternative stress measures introduced as well as equilibrium equations and the virtual work expression, with a brief view of Finite Element method and the Newton-Raphson scheme.

Chapter 3: Thermodynamic laws are used to derive the essential dissipation inequality which the constitutive relations for small and large strains are based on. Constitutive relations are developed for isotropic and transversely isotropic elasticity, as well as elastoplasticity for small and large strain regimes.

Chapter 4: Homogenization based multi-scale theory is developed in this chapter. The macroscopic boundary value problem, as well as homogenized stress and strain concepts are defined, and kinematical constraints essential for the macro-micro transition are introduced. In the second part, the general computational implementation of the multi-scale constitutive theory is developed within a finite element framework. Here, we present the discretized model and develop a direct solution procedure. Numerical examples are provided for verification of the framework.

Chapter 5: Large strain multi-scale theory is developed, followed by general computational implementation within a finite element framework. The layout intimately follows the previous chapter

Chapter 6: Techniques for efficient computational implementation of the family of multi-scale models are developed, namely interface discretization and sub-stepping. Numerical examples are presented in order to illustrate the scope and benefits of developed strategies.

Chapter 7: The use of the multi-scale framework is demonstrated by deriving predictions of elastic behaviour of long fibre composites. Single and multi-scale ex-

amples are provided covering small and large strains.

Chapter 8: Assumption of perfect bonding between composite phases is relaxed. By embedding contact and cohesive laws at weak interfaces within the RVE, we explore the impact of imperfect interfaces on overall material behaviour.

Chapter 9: Conclusions, achievements and suggestions for future work.

Chapter 2

Elements of Continuum Mechanics

A continuum is a body that can be continually sub-divided into infinitesimal elements with properties being those of the bulk material. Continuum mechanics deals with mechanical behaviour of materials that can be considered a continuum and is essentially an approximation as all matter is heterogeneous, whether the heterogeneity is manifested at the microscopic level, or at a smaller scale. The accuracy of this approximation depends on the relative size of the heterogeneities with respect to the body under consideration. Even multi-scale models that consider heterogeneities at different scales assume a continuum at the lower scale. Note, however, that non-continuum models employing molecular dynamics or quantum mechanics also exist.

This chapter is concerned with the basic aspects of continuum mechanics. Concepts related to *kinematics*, which is the study of motion without reference to the cause, are developed first. Next, *stress* is defined in conjunction with *conservation and balance* principles, from which the *virtual work* equation is derived. A number of *alternative stress definitions* are developed in the large deformation context using *work conjugacy*. Finally, the finite element approximation is introduced, as well as the Newton-Raphson method that is used to solve systems of non-linear equations.

The material presented in this chapter is standard and is explained in great detail elsewhere. We refer to Bonet and Wood [8] for kinematics, as well as continuum and discrete treatment of large deformations, Zienkiewicz [129] for the finite element method and de Souza Neto *et al.* [13] for its application to solid mechanics problems.

2.1 Kinematics

In the following, the basic concepts of kinematics will be briefly introduced. In the first part, the concept of displacement will be used to develop a key quantity in finite deformation analysis, the *deformation gradient*, which leads to the definition

of strain. It will be shown that the small strain concept is an approximation of the finite strain terms for infinitesimal displacements and rotations. Material and spatial descriptions will be defined with push forward and pull back concepts that are used to switch between these two configurations.
In the second part the velocity concept will be introduced, and time rates of quantities derived in the first part will be established.

2.1.1 Deformation and Displacement

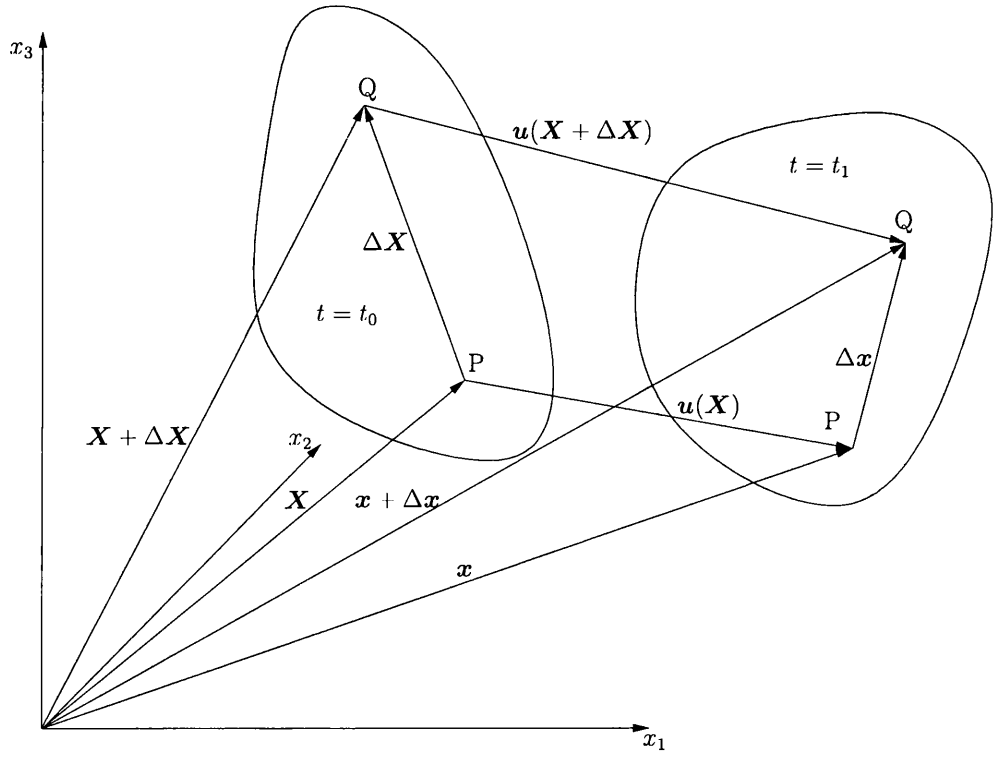

Figure 2.1: Displacement

Consider the motion of the body Ω from $t = t_0$ to $t = t_1$ in Figure 2.1. Let the coordinates of particle P be denoted by $\boldsymbol{X}$ at $t = t_0$, $\boldsymbol{x}$ at $t = t_1$ and the displacement of the particle by $\boldsymbol{u}(\boldsymbol{X})$. Now consider particle Q in neighbourhood of P. Denote $\overline{PQ}$ by $\Delta\boldsymbol{X}$, coordinates of particle Q at $t = t_0$ by $\boldsymbol{X} + \Delta\boldsymbol{X}$, at $t = t_1$ by $\boldsymbol{x} + \Delta\boldsymbol{x}$ and the displacement of the particle Q by $\boldsymbol{u}(\boldsymbol{X} + \Delta\boldsymbol{X})$.

It is apparent from Figure 2.1 that:

$$\boldsymbol{u}(\boldsymbol{X}) + \Delta\boldsymbol{x} = \boldsymbol{u}(\boldsymbol{X} + \Delta\boldsymbol{X}) + \Delta\boldsymbol{X} \quad \Rightarrow \quad \Delta\boldsymbol{x} = \boldsymbol{u}(\boldsymbol{X} + \Delta\boldsymbol{X}) - \boldsymbol{u}(\boldsymbol{X}) + \Delta\boldsymbol{X}$$

The Taylor series expansion for $\boldsymbol{u}(\boldsymbol{X} + \Delta\boldsymbol{X})$ reads:

$$\boldsymbol{u}(\boldsymbol{X} + \Delta\boldsymbol{X}) = \boldsymbol{u}(\boldsymbol{X}) + \frac{\partial \boldsymbol{u}(\boldsymbol{X})}{\partial \boldsymbol{X}} \Delta\boldsymbol{X} + O(\Delta\boldsymbol{X}^2)$$

by taking the limit as $\Delta\boldsymbol{X} \to 0$, the higher order terms disappear and $(\Delta\boldsymbol{X}, \Delta\boldsymbol{x})$ become $(d\boldsymbol{X}, d\boldsymbol{x})$. Combining the two expressions above, and noting that $\frac{\partial \boldsymbol{u}(\boldsymbol{X})}{\partial \boldsymbol{X}} = \nabla_0 \boldsymbol{u}$,

$$d\boldsymbol{x} = (\boldsymbol{I} + \nabla_0 \boldsymbol{u}) d\boldsymbol{X} \tag{2.1}$$

2.1.2 Deformation Gradient

The motion can be mathematically described by a mapping φ between initial and current particle positions as:

$$\boldsymbol{x} = \varphi(\boldsymbol{X}, t) \tag{2.2}$$

The *deformation gradient* $\boldsymbol{F}$ is defined as:

$$\boldsymbol{F} = \frac{\partial \varphi}{\partial \boldsymbol{X}} = \nabla_0 \varphi \tag{2.3}$$

then it follows from (2.1) that

$$\boldsymbol{F} = \boldsymbol{I} + \nabla_0 \boldsymbol{u} \tag{2.4}$$

or,

$$d\boldsymbol{x} = \boldsymbol{F} d\boldsymbol{X} \quad ; \quad \boldsymbol{F} = \frac{\partial \boldsymbol{x}}{\partial \boldsymbol{X}} \tag{2.5}$$

2.1.3 Material and Spatial Descriptions

It is important to make a clear distinction between the coordinate systems used in finite deformation analysis. The *material (Lagrangian)* description refers to the behaviour of a material particle with respect to its original (*reference*) configuration, whereas the *spatial (Eulerian)* description refers to the behaviour (not necessarily the particle) at the current configuration.

Note that the deformation gradient $\boldsymbol{F}$ as defined in (2.5) is a *two point tensor*, as it transforms vectors in the initial configuration into vectors in the current configuration.

2.1.4 Push Forward and Pull Back

It is possible to relate vectors and tensors between material and spatial configurations in terms of the general concepts of *push forward* and *pull back*. (2.5) can be considered to be a push forward of $d\boldsymbol{X}$ to obtain $d\boldsymbol{x}$ or,

$$d\boldsymbol{x} = \boldsymbol{F}d\boldsymbol{X} = \phi_*[d\boldsymbol{X}]$$

Likewise, $d\boldsymbol{x}$ can be pulled back to obtain $d\boldsymbol{X}$ as:

$$d\boldsymbol{X} = \boldsymbol{F}^{-1}d\boldsymbol{x} = \phi_*^{-1}[d\boldsymbol{x}]$$

Note that ϕ_* implies an operation that will be performed in different ways for different operands.

2.1.5 Strain

A measure of strain can be determined by observing the change in scalar product of $d\boldsymbol{x}$ or $d\boldsymbol{X}$ by itself. First, consider the scalar product $d\boldsymbol{x} \cdot d\boldsymbol{x}$, which involves both the change in length and change in angle:

$$d\boldsymbol{x} \cdot d\boldsymbol{x} = \boldsymbol{F}d\boldsymbol{X} \cdot \boldsymbol{F}d\boldsymbol{X} = d\boldsymbol{X} \cdot \boldsymbol{F}^T\boldsymbol{F}d\boldsymbol{X} = d\boldsymbol{X} \cdot \boldsymbol{C}d\boldsymbol{X} \tag{2.6}$$

$\boldsymbol{C}$ is the *right Cauchy Green* tensor, and is defined in the initial configuration. Similarly, $\boldsymbol{b}$, the *left Cauchy Green* or *Finger* tensor is obtained by considering the scalar product $d\boldsymbol{X} \cdot d\boldsymbol{X}$ as:

$$d\boldsymbol{X} \cdot d\boldsymbol{X} = \boldsymbol{F}^{-1}d\boldsymbol{x} \cdot \boldsymbol{F}^{-1}d\boldsymbol{x} = d\boldsymbol{x} \cdot \boldsymbol{F}^{-T}\boldsymbol{F}^{-1}d\boldsymbol{x} = d\boldsymbol{x} \cdot (\boldsymbol{F}\boldsymbol{F}^T)^{-1}d\boldsymbol{x} = d\boldsymbol{x} \cdot \boldsymbol{b}^{-1}d\boldsymbol{x} \tag{2.7}$$

The change in the scalar product is expressed as:

$$\frac{1}{2}(d\boldsymbol{x} \cdot d\boldsymbol{x} - d\boldsymbol{X} \cdot d\boldsymbol{X}) = \frac{1}{2}(d\boldsymbol{X} \cdot \boldsymbol{C}d\boldsymbol{X} - d\boldsymbol{X} \cdot d\boldsymbol{X}) = d\boldsymbol{X} \cdot \frac{1}{2}(\boldsymbol{C} - \boldsymbol{I})d\boldsymbol{X} = d\boldsymbol{X} \cdot \boldsymbol{E}d\boldsymbol{X} \tag{2.8}$$

$\boldsymbol{E}$ is the *Lagrangian* or *Green* strain tensor and is defined in the initial configuration.

Alternatively, the change in the scalar product can be expressed in the current configuration to give the *Eulerian* or *Almansi* strain tensor $\boldsymbol{e}$, which operates in the current configuration:

$$\frac{1}{2}(d\boldsymbol{x} \cdot d\boldsymbol{x} - d\boldsymbol{X} \cdot d\boldsymbol{X}) = \frac{1}{2}(d\boldsymbol{x} \cdot d\boldsymbol{x} - d\boldsymbol{x} \cdot \boldsymbol{b}^{-1}d\boldsymbol{x}) = d\boldsymbol{x} \cdot \frac{1}{2}(\boldsymbol{I} - \boldsymbol{b}^{-1})d\boldsymbol{x} = d\boldsymbol{x} \cdot \boldsymbol{e}d\boldsymbol{x}$$

Note that $\boldsymbol{E}$ and $\boldsymbol{e}$ can be related in terms of push forward and pull back as:

$$\begin{aligned} \boldsymbol{e} &= \phi_*[\boldsymbol{E}] = \boldsymbol{F}^{-T}\boldsymbol{E}\boldsymbol{F}^{-1} \\ \boldsymbol{E} &= \phi_*^{-1}[d\boldsymbol{e}] = \boldsymbol{F}^T\boldsymbol{e}\boldsymbol{F} \end{aligned}$$

By decomposing the displacement gradient tensor $\nabla_0 \boldsymbol{u}$, we can obtain the symmetric $\boldsymbol{\varepsilon}$ and skew $\boldsymbol{\omega}$ as:

$$\boldsymbol{\varepsilon} = \frac{1}{2}(\nabla_0 \boldsymbol{u} + \nabla_0 \boldsymbol{u}^T) \quad ; \quad \boldsymbol{\omega} = \frac{1}{2}(\nabla_0 \boldsymbol{u} - \nabla_0 \boldsymbol{u}^T)$$

so that

$$\nabla_0 \boldsymbol{u} = \boldsymbol{\varepsilon} + \boldsymbol{\omega} \quad ; \quad \nabla_0 \boldsymbol{u}^T = \boldsymbol{\varepsilon} - \boldsymbol{\omega}$$

Now $\boldsymbol{E}$ can be rewritten as:

$$\begin{aligned} \boldsymbol{E} &= \frac{1}{2}(\boldsymbol{C} - \boldsymbol{I}) \\ &= \frac{1}{2}((\boldsymbol{I} + \nabla_0 \boldsymbol{u})^T(\boldsymbol{I} + \nabla_0 \boldsymbol{u}) - \boldsymbol{I}) \\ &= \boldsymbol{\varepsilon} + \frac{1}{2}(\boldsymbol{\varepsilon}\boldsymbol{\varepsilon} - \boldsymbol{\varepsilon}\boldsymbol{\omega} + \boldsymbol{\omega}\boldsymbol{\varepsilon} + \boldsymbol{\omega}\boldsymbol{\omega}) \end{aligned}$$

If $\|\boldsymbol{\varepsilon}\|$ and $\|\boldsymbol{\omega}\| \ll 1$, then $\boldsymbol{\varepsilon}$ is an approximation for $\boldsymbol{E}$ and is known as the *infinitesimal strain tensor.* $\boldsymbol{\omega}$ is called the *infinitesimal rotation tensor.* This approximation can be shown to hold for $\boldsymbol{e}$ as well. Note that both deformation and rotation must be infinitesimal for this approximation to be true.

2.1.6 Volume Change

Consider a volume element in the current configuration whose sides are given by $d\boldsymbol{x}_1$, $d\boldsymbol{x}_2$ and $d\boldsymbol{x}_3$. The volume of the element is expressed as:

$$\begin{aligned} dv &= d\boldsymbol{x}_1(d\boldsymbol{x}_2 \times d\boldsymbol{x}_3) \\ &= \boldsymbol{F}d\boldsymbol{X}_1(\boldsymbol{F}d\boldsymbol{X}_2 \times \boldsymbol{F}d\boldsymbol{X}_3) \\ &= \frac{\partial \varphi}{\partial \boldsymbol{X}_1}dX_1(\frac{\partial \varphi}{\partial \boldsymbol{X}_2}dX_2 \times \frac{\partial \varphi}{\partial \boldsymbol{X}_3}dX_3) \\ &= \frac{\partial \varphi}{\partial \boldsymbol{X}_1}(\frac{\partial \varphi}{\partial \boldsymbol{X}_2} \times \frac{\partial \varphi}{\partial \boldsymbol{X}_3})dX_1 dX_2 dX_3 \\ &= det[\boldsymbol{F}])dV \\ &= J\,dV \end{aligned}$$

where the *Jacobian* J is defined as $J = det[\boldsymbol{F}]$. The rate change of volume is given as:

$$\frac{d}{dt}(dv) = \dot{J}\,dV = \frac{\dot{J}}{J}dv$$

2.1.7 Isochoric/Volumetric Split

Any deformation can be split into an isochoric (volume preserving) and a purely volumetric component. In case of large (finite) deformations, this is accomplished by the multiplicative split of the deformation gradient as:

$$\boldsymbol{F} = \boldsymbol{F}_{\text{iso}}\boldsymbol{F}_{\text{vol}}$$

where

$$\boldsymbol{F}_{\text{iso}} = J^{-\frac{1}{3}}\boldsymbol{F} \quad ; \quad \boldsymbol{F}_{\text{vol}} = J^{\frac{1}{3}}\boldsymbol{I}$$

Note that $det[\boldsymbol{F}_{\text{iso}}] = (J^{-\frac{1}{3}})^3 det[\boldsymbol{F}] = J^{-1}J = 1$.
A similar split is possible for small strains in an additive manner, so that:

$$\boldsymbol{\varepsilon} = \boldsymbol{\varepsilon}^{\text{dev}} + \boldsymbol{\varepsilon}^{\text{vol}}$$

where, $\boldsymbol{\varepsilon}^{\text{vol}} = \frac{1}{3}tr[\boldsymbol{\varepsilon}]\boldsymbol{I}$ is the purely volumetric component and $\boldsymbol{\varepsilon}^{\text{dev}} = \boldsymbol{\varepsilon} - \boldsymbol{\varepsilon}^{\text{vol}} = \boldsymbol{\varepsilon} - \frac{1}{3}tr[\boldsymbol{\varepsilon}]\boldsymbol{I}$ is the *deviatoric* or isochoric component of the infinitesimal strain tensor. It can be shown that $\boldsymbol{E}_{\text{iso}}$ and $\boldsymbol{E}_{\text{vol}}$, as well as $\boldsymbol{e}_{\text{iso}}$ and $\boldsymbol{e}_{\text{vol}}$ reduce to $\boldsymbol{\varepsilon}^{\text{dev}}$ and $\boldsymbol{\varepsilon}^{\text{vol}}$ as $\boldsymbol{F}$ approaches $\boldsymbol{I}$.

2.1.8 Velocity

Consider the mapping $\boldsymbol{x} = \varphi(\boldsymbol{X}, t)$. The velocity of a particle is defined as:

$$\boldsymbol{v}(\boldsymbol{X}, t) = \frac{\partial\varphi(\boldsymbol{X}, t)}{\partial t}$$

As velocity is naturally a spatial quantity, it is more convenient to define it as:

$$\boldsymbol{v}(\boldsymbol{X}, t) = \boldsymbol{v}(\varphi^{-1}(\boldsymbol{x}, t), t)$$

The derivative of the velocity (as a function of spatial coordinates as $\boldsymbol{v}(\boldsymbol{x}, t)$) with respect to the spatial coordinates define the *velocity gradient* $\boldsymbol{l}$ as

$$\boldsymbol{l} = \frac{\partial\boldsymbol{v}}{\partial\boldsymbol{x}} = \nabla\boldsymbol{v}$$

$\boldsymbol{l}$ relates to the time derivative of the deformation gradient, which is defined as $\dot{\boldsymbol{F}} = \nabla_0\boldsymbol{v}$ as:

$$\dot{\boldsymbol{F}} = \boldsymbol{l}\boldsymbol{F} \quad ; \quad \boldsymbol{l} = \dot{\boldsymbol{F}}\boldsymbol{F}^{-1}$$

2.1.9 Rate of Deformation

The rate of deformation can be obtained by differentiation with respect to time the scalar product of two vectors. In terms of the current configuration, this can simply be achieved by taking the time derivative of $\boldsymbol{E}$ to give

$$\dot{\boldsymbol{E}} = \frac{1}{2}\dot{\boldsymbol{C}} = \frac{1}{2}(\dot{\boldsymbol{F}}^T\boldsymbol{F} + \boldsymbol{F}^T\dot{\boldsymbol{F}})$$

so that the change in the rate of deformation can be expressed as:

$$\frac{d}{dt}(d\boldsymbol{x}\cdot d\boldsymbol{x}) = 2d\boldsymbol{X}\cdot\dot{\boldsymbol{E}}d\boldsymbol{X}$$

or in spatial terms as:

$$\begin{aligned}\frac{d}{dt}(d\boldsymbol{x}\cdot d\boldsymbol{x}) &= \boldsymbol{F}^{-1}d\boldsymbol{x}\cdot\dot{\boldsymbol{E}}\boldsymbol{F}^{-1}d\boldsymbol{x}\\ &= d\boldsymbol{x}\cdot\boldsymbol{F}^{-T}\dot{\boldsymbol{E}}\boldsymbol{F}^{-1}d\boldsymbol{x}\\ &= d\boldsymbol{x}\cdot\boldsymbol{d}\,d\boldsymbol{x}\end{aligned}$$

The *rate of deformation tensor* $\boldsymbol{d} = \boldsymbol{F}^{-T}\dot{\boldsymbol{E}}\boldsymbol{F}^{-1}$ is the push forward of $\dot{\boldsymbol{E}}$, and is identified as the symmetrical part of the velocity gradient $\boldsymbol{l}$ as:

$$\boldsymbol{d} = \frac{1}{2}(\boldsymbol{l} + \boldsymbol{l}^T)$$

2.2 Stress and Equilibrium

The problem of solid mechanics is to determine the response of a body under external loads. The response is the consequence of a set of differential equations, known as the equations of motion. The weak form of these equations is the starting point for the finite element analysis, known as the virtual work.

Stress is simply defined as the force per unit area. In small strain analysis there is a unique concept of stress as the change in area can be ignored. In finite deformation analysis however, change in kinematic quantities can no longer be ignored, so that one has to identify the stress with respect to the deformed area or the initial area.

In this section, after recalling the global equations of motion, the true (*Cauchy*) stress will be introduced, which is defined as the force per unit deformed area. Then the spatial virtual work equation will be developed, followed by the introduction of *work conjugate* concept, which will enable definition of alternative stress measures, namely, the Kirchoff, first Piola-Kirchoff and second Piola-Kirchoff stress tensors.

2.2.1 Equations of Motion

Consider a body occupying the region Ω with boundary $\partial\Omega$. The motion of the body will be caused by body forces which act on Ω and by boundary forces which act on $\partial\Omega$. Any oriented surface element $d\boldsymbol{a} = \boldsymbol{n}da$ experiences a contact force $\boldsymbol{t}(\boldsymbol{n})\,da$, where $\boldsymbol{t}(\boldsymbol{n})$ is called the *surface traction.* Linear and angular momentum balance equations that express the acceleration field on a body are:

$$\int_\Omega \rho\boldsymbol{b}\,dv + \int_{\partial\Omega} \boldsymbol{t}(\boldsymbol{n})\,da = \int_\Omega \rho\ddot{\boldsymbol{x}}\,dv \tag{2.9}$$

$$\int_\Omega \rho\boldsymbol{x}\times\boldsymbol{b}\,dv + \int_{\partial\Omega} \boldsymbol{x}\times\boldsymbol{t}(\boldsymbol{n})\,da = \int_\Omega \rho\boldsymbol{x}\times\ddot{\boldsymbol{x}}\,dv \tag{2.10}$$

2.2.2 Stress

Consider the *Cauchy tetrahedron* shown in Figure 2.2. If the tetrahedron is sufficiently small, (2.9) can be approximated as:

$$\rho(\boldsymbol{b}-\ddot{\boldsymbol{x}})\frac{\Delta v}{\Delta a} + \boldsymbol{t}(\boldsymbol{n}) - \boldsymbol{t}_j n_j = \boldsymbol{0}$$

where Δv and Δa denote the approximate volume and area of the tetrahedron respectively. The approximation becomes exact as the tetrahedron shrinks to zero (i.e. $\frac{\Delta v}{\Delta a} \to 0$), so that $\boldsymbol{t}(\boldsymbol{n}) = \boldsymbol{t}_j n_j$. If $\boldsymbol{\sigma}$ is defined as $\sigma_{ij} = \boldsymbol{e}_i \cdot \boldsymbol{t}_j$, then

$$\boldsymbol{t}(\boldsymbol{n}) = \boldsymbol{\sigma}\boldsymbol{n} \tag{2.11}$$

defines the current or true or *Cauchy stress tensor* $\boldsymbol{\sigma}$. It can be shown that $\boldsymbol{\sigma}$ is symmetric, using (2.10). By applying Gauss theorem on integral form of (2.11),

$$\int_{\partial\Omega} \boldsymbol{t}\,da = \int_{\partial\Omega} \boldsymbol{\sigma}\boldsymbol{n}\,da = \int_\Omega \mathrm{div}[\boldsymbol{\sigma}]\,dv$$

and defining $\boldsymbol{f} = \rho\,\boldsymbol{b}$ as the body force per unit volume, and admitting no accelerations, the global equilibrium equations become:

$$\int_\Omega \boldsymbol{f}\,dv + \int_\Omega \mathrm{div}[\boldsymbol{\sigma}]\,dv = \int_\Omega (\mathrm{div}[\boldsymbol{\sigma}] + \boldsymbol{f})\,dv = \boldsymbol{0} \tag{2.12}$$

The *local force equations of motion* are obtained using the standard argument that the above equation can be equally applied to any region of integration, so that the integrand vanishes:

$$\mathrm{div}[\boldsymbol{\sigma}] + \boldsymbol{f} = \boldsymbol{0} \tag{2.13}$$

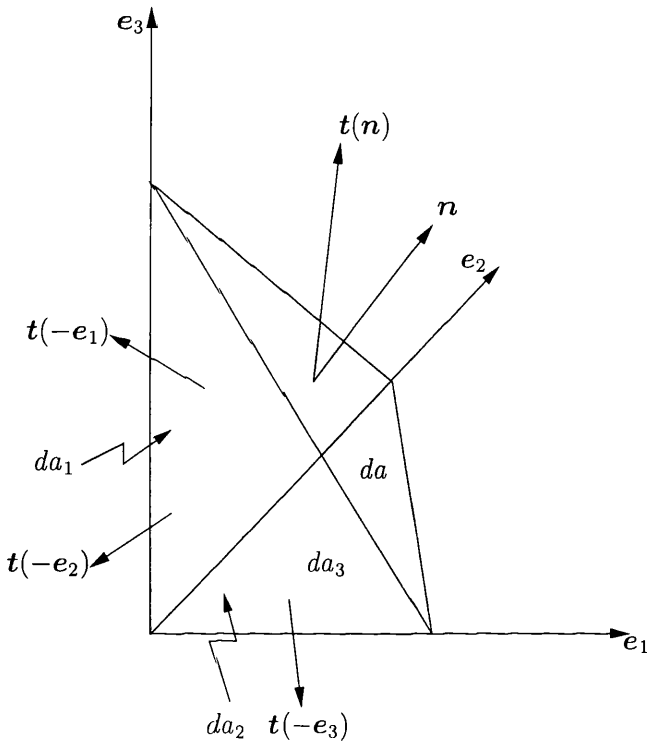

Figure 2.2: The Cauchy tetrahedron

2.2.3 Virtual Work

The weak counterpart of (2.13) is the basis for the finite element formulation which is employed throughout this work to obtain approximations to the boundary value problem at hand. Formulated in terms of a virtual displacement η, the virtual work expression states that "the body $\mathscr{B}$, which is subject to the body force and surface traction fields $\boldsymbol{f}$ and $\boldsymbol{t}$ respectively, is in equilibrium if and only if the Cauchy stress field satisfies the variational equation:

$$\delta W = \int_{\Omega} \boldsymbol{\sigma} : \nabla \boldsymbol{\eta} dv - \int_{\Omega} \boldsymbol{f} \cdot \boldsymbol{\eta} dv - \int_{\partial\Omega} \boldsymbol{t} \cdot \boldsymbol{\eta} da = 0 \ ; \ \forall \boldsymbol{\eta} \in \mathscr{V} \tag{2.14}$$

where $\mathscr{V}$ is the space of virtual displacements of $\mathscr{B}$." Small strain version is essentially the same, except that the volume and area changes are ignored.

2.2.4 Linearized Virtual Work

The weak equilibrium represented by (2.14) is generally non-linear (with the common exception of linear elasticity within the small strain framework); and a solution state can only be reached by using an iterative procedure, such as the Newton-Raphson scheme, which requires linearization of the virtual work equation in the direction of an increment $\Delta \boldsymbol{u}$ about a configuration ϕ_k as:

$$\delta W(\phi_k, \boldsymbol{\eta}) + D\delta W(\phi_k, \boldsymbol{\eta})[\Delta \boldsymbol{u}] = 0 \tag{2.15}$$

The body force term does not depend on the current geometry, and we limit our interest to tractions that do not depend on the current geometry, so, only the internal virtual work is linearized as:

$$D\delta W_{int}(\phi, \boldsymbol{\eta})[\Delta \boldsymbol{u}] = \int_\Omega \nabla^s \boldsymbol{\eta} : \boldsymbol{c} : (\nabla^s \Delta \boldsymbol{u}) dv + \int_\Omega (\nabla \Delta \boldsymbol{u}) \boldsymbol{\sigma} : \nabla \boldsymbol{\eta} \, dv \tag{2.16}$$

These two terms will become the constitutive and initial stress components of the tangent stiffness matrix after discretization. Note that the last term disappears under the small strain assumption.

2.2.5 Work Conjugacy and Alternative Stress Definitions

Let $\delta \boldsymbol{v}$ denote an arbitrary virtual velocity from the current position of the body. Equilibrium requires the virtual work per unit time done on the body by the virtual velocity be zero, thus, analogous to (2.14), we can write the virtual power expression:

$$\delta P = \int_\Omega \boldsymbol{\sigma} : \delta \boldsymbol{d} dv - \int_\Omega \boldsymbol{f} \cdot \delta \boldsymbol{v} dv - \int_{\partial\Omega} \boldsymbol{t} \cdot \delta \boldsymbol{v} da = 0 \tag{2.17}$$

The first term gives the internal virtual power, δP_{int}. As their product gives work per unit volume (per time), $\boldsymbol{\sigma}$ and $\boldsymbol{d}$ are called *work conjugate* with respect to current deformed volume. Work conjugacy will be used to develop alternative stress definitions in the following:

Kirchoff Stress Tensor.

Using $dv = J dV$, the internal power term is expressed as:

$$\delta P_{\text{int}} = \int_{\Omega_0} J\boldsymbol{\sigma} : \delta \boldsymbol{d} dV \tag{2.18}$$

the term $\boldsymbol{\tau} = J\boldsymbol{\sigma}$ is called the *Kirchoff stress tensor* and is work conjugate with $\boldsymbol{d}$ with respect to the initial volume.

First Piola-Kirchoff Stress Tensor.

Noting that $\boldsymbol{\sigma} : \delta\boldsymbol{d} = \boldsymbol{\sigma} : \delta\boldsymbol{l} = \boldsymbol{\sigma} : \delta\dot{\boldsymbol{F}}\boldsymbol{F}^{-1} = \boldsymbol{\sigma}\boldsymbol{F}^{-T} : \delta\dot{\boldsymbol{F}}$ because of the symmetry of $\boldsymbol{\sigma}$, (2.18) becomes:

$$\begin{aligned} \delta P_{\text{int}} &= \int_{\Omega_0} J\boldsymbol{\sigma}\boldsymbol{F}^{-T} : \delta\dot{\boldsymbol{F}} dV \\ &= \int_{\Omega_0} \boldsymbol{P} : \delta\dot{\boldsymbol{F}} dV \end{aligned} \tag{2.19}$$

where, the term $\boldsymbol{P} = J\boldsymbol{\sigma}\boldsymbol{F}^{-T}$ is called the *First Piola-Kirchoff stress tensor* and is work conjugate with $\dot{\boldsymbol{F}}$ with respect to the initial volume. Note that $\dot{\boldsymbol{F}}$, like $\boldsymbol{F}$ is a two point tensor.

Second Piola-Kirchoff Stress Tensor.

Recalling that $\boldsymbol{d}$ is the push forward of $\dot{\boldsymbol{E}}$ as $\boldsymbol{d} = \boldsymbol{F}^{-T}\dot{\boldsymbol{E}}\boldsymbol{F}^{-1}$, (2.18) can be re-written as:

$$\begin{aligned} \delta P_{\text{int}} &= \int_{\Omega_0} J\boldsymbol{\sigma} : \boldsymbol{F}^{-T}\delta\dot{\boldsymbol{E}}\boldsymbol{F}^{-1} dV \\ &= \int_{\Omega_0} \boldsymbol{F}^{-1}J\boldsymbol{\sigma}\boldsymbol{F}^{-T} : \delta\dot{\boldsymbol{E}} dV \\ &= \int_{\Omega_0} \boldsymbol{S} : \delta\dot{\boldsymbol{E}} dV \end{aligned} \tag{2.20}$$

where, the term $\boldsymbol{S} = \boldsymbol{F}^{-1}\boldsymbol{\tau}\boldsymbol{F}^{-T}$ is called the *Second Piola-Kirchoff stress tensor* and is work conjugate with $\dot{\boldsymbol{E}}$ with respect to the initial volume. Note that all terms in (2.20) are defined in the material configuration.

2.3 Boundary Value Problem

For elastic/hyperelastic bodies where the stress field exclusively depends on the current value of the deformation gradient (or the small strain tensor), a constitutive functional $\hat{\boldsymbol{\sigma}}$ can be introduced as:

$$\boldsymbol{\sigma} = \hat{\boldsymbol{\sigma}}(\boldsymbol{F}(or\ \boldsymbol{\varepsilon})) \tag{2.21}$$

which is implanted into the weak equilibrium (2.14) to establish the *boundary value problem* as: "Given the body force and surface traction fields on the body $\mathscr{B}$, find a kinematically admissible deformation $\varphi \in \mathscr{K}$ such that

$$\int_{\Omega} \hat{\boldsymbol{\sigma}} : \nabla\boldsymbol{\eta} dv - \int_{\Omega} \boldsymbol{f} \cdot \boldsymbol{\eta} dv - \int_{\partial\Omega} \boldsymbol{t} \cdot \boldsymbol{\eta} da = 0 \ \forall\boldsymbol{\eta} \in \mathscr{V} \tag{2.22}$$

where $\mathscr{K}$ and $\mathscr{V}$ denote, respectively, the functional set of kinematically admissible displacements and the corresponding space of virtual displacements of the body in question."

Incremental Boundary Value Problem. In cases where the stress field is path-dependent as well as the current value of the deformation gradient (or the small strain tensor), the dependence is approximated by discretization of time, so that the constitutive relation is replaced by an incremental counterpart, which is path-independent within a typical time increment $[t^n \rightarrow t^{n+1}]$. Path-dependence is commonly represented by a set of internal variables $\boldsymbol{\xi}$, whose value at time step t^n is known. Now, the algorithmic constitutive functional $\boldsymbol{\sigma}^{n+1}$ can be defined as:

$$\boldsymbol{\sigma}^{n+1} = \hat{\boldsymbol{\sigma}}(\boldsymbol{\xi}^n, \boldsymbol{F}^{n+1}(or\ \boldsymbol{\varepsilon}^{n+1})) \tag{2.23}$$

so that the *incremental boundary value problem* is established as: "Given the internal variables at time t^n, and given body force and surface traction fields at time t^{n+1}, find a kinematically admissible deformation $\varphi \in \mathscr{K}$ such that

$$\int_\Omega \hat{\boldsymbol{\sigma}} : \nabla\boldsymbol{\eta} dv - \int_\Omega \boldsymbol{f}^{n+1} \cdot \boldsymbol{\eta} dv - \int_{\partial\Omega} \boldsymbol{t}^{n+1} \cdot \boldsymbol{\eta} da = 0 \ \ \forall \boldsymbol{\eta} \in \mathscr{V} \tag{2.24}$$

2.4 Finite Element Approximation

The functional sets $\mathscr{K}$ and $\mathscr{V}$ of the boundary value problem given by (2.22) or (2.24) are replaced with discrete subsets within a finite element discretization, to obtain an approximation to the boundary value problem. A wide range of references (eg [129]) are available for a detailed account of the finite element method. The discrete form of the boundary value problem is formulated in terms of internal and external global force vectors $\mathbb{T}$ and $\mathbb{F}$ as:

$$\mathbb{R} = \mathbb{T} - \mathbb{F} = 0 \tag{2.25}$$

which are formed by assembling contributions from discrete subsets called finite elements. It is convenient to express the virtual work contribution of element e to node a in terms of internal and external nodal forces $\mathbb{T}_a^e$ and $\mathbb{F}_a^e$ as:

$$\begin{aligned} \mathbb{T}_a^e &= \int_{v^e} \boldsymbol{\sigma} \nabla N_a \, dv \\ \mathbb{F}_a^e &= \int_{v^e} \boldsymbol{f} N_a \, dv + \int_{\partial v} \boldsymbol{t} N_a \, da \end{aligned} \tag{2.26}$$

where N_a is the shape function associated with node a. The next step is summing contribution of nodal forces from all elements $e_{1,..M}$ containing node a to the virtual

work done at node a, and then assembling forces on all nodes $(1, ...N)$ to give the global virtual work equation as:

$$\mathbb{T} = \bigcup_{a=1}^{N} \sum_{e=1}^{M} \mathbb{T}_a^e \quad , \quad \mathbb{F} = \bigcup_{a=1}^{N} \sum_{e=1}^{M} \mathbb{F}_a^e \tag{2.27}$$

2.4.1 Solution: Newton-Raphson Method

Newton-Raphson method is used commonly for solution of systems of non-linear equations, and provides quadratic convergence. Note that, in presence of geometrical or material non-linearities, (2.25) is likely to produce a set of residuals. The k^{th} iteration of a typical Newton-Raphson procedure, characterized by an arbitrary configuration φ_k, is formulated as:

$$\mathbb{R}(\varphi_{k+1}) \approx \mathbb{R}(\varphi_k) + \mathbb{K}(\varphi_k)[\delta \boldsymbol{u}] = \mathbf{0}$$

so that a solution $\boldsymbol{u}_{k+1} = \boldsymbol{u}_k + \delta \boldsymbol{u}$ can be obtained by solving the set of linear equations

$$\mathbb{K}(\varphi_k) \cdot \delta \boldsymbol{u} = -\mathbb{R}(\varphi_k)$$

where $\mathbb{K}$ is the global tangent stiffness matrix. Let $\mathbb{K}_{ab}^e$ express the change in the nodal equivalent forces $\mathbb{T}_a^e$ and $\mathbb{F}_a^e$ at node a, due to a change in the current position of node b. $\mathbb{K}_{ab}^e$ is the discretized version of (2.16), and consists of constitutive $\mathbb{K}_{c_{ab}}^e$ and initial stress $\mathbb{K}_{\sigma_{ab}}^e$ components, which are given as:

$$\begin{aligned} \mathbb{K}_{ab}^e &= \mathbb{K}_{c_{ab}}^e + \mathbb{K}_{\sigma_{ab}}^e \\ \mathbb{K}_{c_{ab}}^e &= \int_{v^e} \nabla N_a \, \mathbb{D} \, \nabla N_b \, dv \\ \mathbb{K}_{\sigma_{ab}}^e &= \int_{v^e} (\nabla N_a \cdot \boldsymbol{\sigma} \nabla N_b) \boldsymbol{I} \, dv \end{aligned} \tag{2.28}$$

where $\mathbb{D}$ is the matrix form of the fourth order constitutive tensor. Next step is the assembly of the tangent matrix, which will be carried out in a similar way to the assembly of nodal forces. First, the contributions to node a from node b associated with all elements $e(1, ..M)$ containing nodes a and b is summed to form $\mathbb{K}_{ab}$:

$$\mathbb{K}_{ab} = \sum_{e=1}^{M} \mathbb{K}_{ab}^e \tag{2.29}$$

and finally contributions from all connected nodes $ab(1, ..N)$ are assembled to form the global tangent stiffness matrix:

$$\mathbb{K} = \bigcup_{ab=1}^{N} \mathbb{K}_{ab} \tag{2.30}$$

Chapter 3

Constitutive Relations

This chapter reviews continuum material models for small and large strains, including isotropic and transversely isotropic elasticity and elastoplasticity. A process is physically admissible if it satisfies the energy conservation laws as well as the conservation of mass and the dissipation inequality. First, the mechanical dissipation inequality will be derived from the consistency requirement of the solid mechanics problem with the first and second laws of thermodynamics, forming the basis for all continuum models developed next. Small and large strain elasticity relations for isotropic and transversely isotropic materials are well established, see eg. Daniel [22], Lemaitre [60] or Bonet and Wood [8]. The transversely isotropic hyperelastic model is due to Spencer [108] and Bonet et al [9]. Finally, continuum and algorithmic treatment of elastoplasticity is developed for small and large strains, based on Somer [104] and Dettmer [24]. For more information on elastoplasticity, we refer to Lubliner [67], Perić [92] and de Souza Neto *et al.* [13].

3.1 Energy and Thermodynamic Relations

The kinetic energy of a body occupying a region Ω is defined as:

$$K = \frac{1}{2}\int_{\Omega} \rho \dot{\boldsymbol{x}} \cdot \dot{\boldsymbol{x}}\, dv$$

so that,

$$\dot{K} = \frac{d}{dt}K = \int_{\Omega} \rho \dot{\boldsymbol{x}} \cdot \ddot{\boldsymbol{x}}\, dv$$

The external power acting on the body is

$$P = \int_{\Omega} \rho \boldsymbol{b} \cdot \dot{\boldsymbol{x}}\, dv + \int_{\partial\Omega} \boldsymbol{t}(\boldsymbol{n}) \cdot \dot{\boldsymbol{x}}\, da$$

Noting that $\boldsymbol{t}(\boldsymbol{n}) = \boldsymbol{\sigma}\boldsymbol{n}$, and recalling the divergence theorem,

$$P = \int_\Omega [(\text{div}(\boldsymbol{\sigma}) + \rho\boldsymbol{b}) \cdot \dot{\boldsymbol{x}} + \boldsymbol{\sigma} : \nabla\dot{\boldsymbol{x}}]\, dv$$

Note that, $\text{div}(\boldsymbol{\sigma}) + \rho\boldsymbol{b} = \rho\ddot{\boldsymbol{x}}$ and recall $\nabla\dot{\boldsymbol{x}} = \boldsymbol{l}$, so that $\boldsymbol{\sigma} : \nabla\dot{\boldsymbol{x}} = \boldsymbol{\sigma} : \boldsymbol{l} = \boldsymbol{\sigma} : \boldsymbol{d}$ as $\boldsymbol{\sigma}$ is symmetric. Now the external power takes the form:

$$P = \int_\Omega [\rho\dot{\boldsymbol{x}} \cdot \ddot{\boldsymbol{x}} + \boldsymbol{\sigma} : \boldsymbol{d}]\, dv$$

The deformation power can be introduced as the difference between external power and kinetic energy as:

$$P_d = P - \dot{K} = \int_\Omega \boldsymbol{\sigma} : \boldsymbol{d}\, dv$$

The heat flow into the body is given as:

$$Q = \int_\Omega \rho r\, dv - \int_{\partial\Omega} h(\boldsymbol{n})\, da$$

Similar to the relationship $\boldsymbol{t}(\boldsymbol{n}) = \boldsymbol{\sigma}\boldsymbol{n}$, a heat flux vector $\boldsymbol{h}$ can be defined to give $h(\boldsymbol{n}) = \boldsymbol{h} \cdot \boldsymbol{n}$. Thus,

$$Q = \int_\Omega \rho r\, dv - \int_{\partial\Omega} \boldsymbol{h} \cdot \boldsymbol{n} da = \int_\Omega \Big[\rho r - \text{div}(\boldsymbol{h})\Big]\, dv$$

by Gauss's theorem. The *first law of thermodynamics* states that there exists a state variable u such that

$$\frac{d}{dt}\int_\Omega \rho u\, dv = Q + P_d$$

which yields the *local energy balance equation* as

$$\rho\dot{u} = \boldsymbol{\sigma} : \boldsymbol{d} + \rho r - \text{div}(\boldsymbol{h}) \tag{3.1}$$

The stress-strain relation is not arbitrary, and must be consistent with the *second law of thermodynamics*, which states that, there exists a state function $\eta = \overline{\eta}(u, \boldsymbol{d})$ (entropy density) such that $\dot{\eta} = 0$ for an adiabatic process. (3.1) can now be rewritten as:

$$T\rho\dot{\eta} = \rho\dot{u} - \boldsymbol{\sigma} : \boldsymbol{d} = \rho r - \text{div}(\boldsymbol{h})$$

by defining the absolute temperature T by

$$T^{-1} = \frac{\partial\overline{\eta}}{\partial u}$$

If the total entropy of the body is defined as $S = \int_R \rho\eta \, dv$, then

$$\begin{aligned}
\dot{S} &= \int_\Omega \rho\dot{\eta} \, dv \\
&= \int_\Omega T^{-1}\Big[\rho r - \mathrm{div}(\boldsymbol{h})\Big] \, dv \\
&= \int_\Omega \Big[\rho\frac{r}{T} - \mathrm{div}(\frac{\boldsymbol{h}}{\mathrm{T}}) + \boldsymbol{h}\cdot\nabla\mathrm{T}^{-1}\Big] \, dv \\
&= \int_\Omega \rho\frac{r}{T} \, dv - \int_{\partial R} \frac{h(\boldsymbol{n})}{T} dS + \int_\Omega \boldsymbol{h}\cdot\nabla T^{-1} \, dv
\end{aligned}$$

Note that the last term in the above equation is always equal to or greater than zero, as heat flows from hotter to the colder part of a body. Now the *global Clasius-Duhem inequality* can be stated as:

$$\dot{S} - \left[\int_\Omega \rho\frac{r}{T} \, dv - \int_\Omega \frac{h(\boldsymbol{n})}{T} \, da\right] \geq 0 \tag{3.2}$$

The divergence theorem may be employed to express (3.2) as:

$$\int_\Omega \left[\rho\dot{\eta} - \rho\frac{r}{T} + \nabla\cdot\left(\frac{\boldsymbol{h}}{T}\right)\right] dv \geq 0$$

And following the standard assumption that the equation must apply to any region of integration, the *local Clasius-Duhem inequality* is expressed as

$$\rho\dot{\eta} - \rho\frac{r}{T} + \nabla\cdot\left(\frac{\boldsymbol{h}}{T}\right) \geq 0 \tag{3.3}$$

Combining equations (3.1) and (3.3), and employing the divergence theorem,

$$-\rho(\dot{u} - T\dot{\eta}) + \boldsymbol{\sigma} : \boldsymbol{d} - \boldsymbol{h}\cdot\left(\frac{\nabla T}{T}\right) \geq 0 \tag{3.4}$$

If the Helmholtz free energy per unit mass is defined as: $\psi = u - T\eta$, then $\dot{u} - T\dot{\eta} = \dot{\psi} + \dot{T}\eta$, so that (3.4) becomes

$$-\rho(\dot{\psi} + \dot{T}\eta) + \boldsymbol{\sigma} : \boldsymbol{d} - \boldsymbol{h}\cdot\left(\frac{\nabla T}{T}\right) \geq 0 \tag{3.5}$$

or, formulated in the initial configuration (using standard kinematic conversions and work conjugacy):

$$-\rho_0(\dot{\psi} + \dot{T}\eta) + \frac{1}{2}\boldsymbol{S} : \dot{\boldsymbol{C}} - \boldsymbol{h}_0\cdot\left(\frac{\nabla T}{T}\right) \geq 0 \tag{3.6}$$

(3.5) can be expressed for small strains as:

$$-\rho(\dot{\psi}+\dot{T}\eta)+\boldsymbol{\sigma}:\dot{\boldsymbol{\varepsilon}}-\boldsymbol{h}\cdot\left(\frac{\nabla T}{T}\right)\geq 0 \tag{3.7}$$

Two sets of assumptions are introduced at this stage. Elastic deformations are assumed to take place place at constant ($\dot{T}=0$) and uniformly distributed ($\nabla T=0$) temperature and at any elastic strain rate. Also, thermal deformations are assumed to be independent of all state variables except temperature, and taking place at any temperature rate. These assumptions yield the *dissipation inequality* for small strains :

$$\dot{\mathfrak{D}}=\boldsymbol{\sigma}:\dot{\boldsymbol{\varepsilon}}-\dot{\Psi}\geq 0 \tag{3.8}$$

Note that the free energy density ψ has been replaced by the *strain energy function* Ψ (per unit volume). $\dot{\mathfrak{D}}$ is called the *dissipation function.* The dissipation inequality is formulated for large strains in initial configuration as:

$$\dot{\mathfrak{D}}=\frac{1}{2}\boldsymbol{S}:\dot{\boldsymbol{C}}-\dot{\Psi}\geq 0 \tag{3.9}$$

3.2 Small Strain Elasticity

An elastic body is defined as one in which the strain at any point of the body is completely determined by the current stress and temperature. The Helmhotz free-energy is a function of state variables only, so that $\psi=\psi(\boldsymbol{\varepsilon},T)$ and the time derivative appearing in (3.8) is expressed as:

$$\dot{\psi}=\frac{\partial\psi}{\partial\boldsymbol{\varepsilon}}\dot{\boldsymbol{\varepsilon}}+\frac{\partial\psi}{\partial T}\dot{T}$$

Second term disappears due to the set of assumptions yielding (3.8). Now, (3.8) becomes,

$$\left(\boldsymbol{\sigma}-\frac{\partial\Psi}{\partial\boldsymbol{\varepsilon}}\right):\dot{\boldsymbol{\varepsilon}}=0$$

or,

$$\boldsymbol{\sigma}=\frac{\partial\Psi}{\partial\boldsymbol{\varepsilon}}, \tag{3.10}$$

which is the hyperelastic relation in small strains. When Ψ is quadratic in $\boldsymbol{\varepsilon}$, then the *generalized Hooke's law* relates the second order stress and small strain tensors linearly by means of the fourth order *elasticity tensor* $\mathcal{C}$ as

$$\sigma_{ij}=\mathcal{C}_{ijkl}\varepsilon_{kl}\quad;\quad\boldsymbol{\mathcal{C}}=\frac{\partial^2\Psi}{\partial\boldsymbol{\varepsilon}^2} \tag{3.11}$$

The elasticity tensor $\boldsymbol{C}$ has 81 components that relate the 9 components of stress to the 9 components of strain. The symmetry of stress and strain tensors reduces the number of these components to 36. The indifference of the order of differentiation in (3.11) brings up more symmetries which reduce the number of independent constants of the elasticity tensor to 21 for a general anisotropic material.

Contracted notation It is convenient to represent the stress, strain and elasticity tensors in the contracted notation, such that:

$$\begin{Bmatrix} \sigma_{11} \\ \sigma_{22} \\ \sigma_{33} \\ \sigma_{12} \\ \sigma_{23} \\ \sigma_{31} \end{Bmatrix} = \begin{Bmatrix} \sigma_1 \\ \sigma_2 \\ \sigma_3 \\ \sigma_4 \\ \sigma_5 \\ \sigma_6 \end{Bmatrix} \; ; \; \begin{Bmatrix} \epsilon_{11} \\ \epsilon_{22} \\ \epsilon_{33} \\ 2\epsilon_{12} \\ 2\epsilon_{23} \\ 2\epsilon_{31} \end{Bmatrix} = \begin{Bmatrix} \epsilon_1 \\ \epsilon_2 \\ \epsilon_3 \\ \epsilon_4 \\ \epsilon_5 \\ \epsilon_6 \end{Bmatrix} \; ; \; \begin{Bmatrix} C_{1111} \\ C_{2222} \\ C_{3333} \\ C_{1212} \\ C_{2323} \\ C_{3131} \\ C_{1122} \\ C_{1133} \\ C_{2233} \end{Bmatrix} = \begin{Bmatrix} C_{11} \\ C_{22} \\ C_{33} \\ 2C_{44} \\ 2C_{55} \\ 2C_{66} \\ C_{12} \\ C_{13} \\ C_{23} \end{Bmatrix}$$

Orthotropy An *orthotropic* material has three mutually perpendicular planes of material symmetry, which further reduce the number of independent components of the elasticity tensor to 9. A simplified representation is possible where the reference system of coordinates are chosen to coincide with the principal planes of material symmetry:

$$\begin{Bmatrix} \sigma_1 \\ \sigma_2 \\ \sigma_3 \\ \sigma_4 \\ \sigma_5 \\ \sigma_6 \end{Bmatrix} = \begin{bmatrix} C_{11} & C_{12} & C_{13} & 0 & 0 & 0 \\ & C_{22} & C_{23} & 0 & 0 & 0 \\ & & C_{33} & 0 & 0 & 0 \\ & & & C_{44} & 0 & 0 \\ & sym. & & & C_{55} & 0 \\ & & & & & C_{66} \end{bmatrix} \begin{Bmatrix} \epsilon_1 \\ \epsilon_2 \\ \epsilon_3 \\ \epsilon_4 \\ \epsilon_5 \\ \epsilon_6 \end{Bmatrix}$$

3.2.1 Transversely Isotropic Elasticity

Isotropy is defined by requiring the constitutive behaviour to be identical in any material direction. An orthotropic material is called *transversely isotropic* when one of its principal planes is a plane of isotropy, which yet reduces the number of independent components of the elasticity tensor to 5. For example, if the 2-3 plane is the plane of isotropy, then $C_{12} = C_{13}$, $C_{22} = C_{33}$, $C_{44} = C_{66}$ and, $C_{55} = (C_{22} - C_{23})/2$,

so the constitutive relation takes the form:

$$\begin{Bmatrix} \sigma_1 \\ \sigma_2 \\ \sigma_3 \\ \sigma_4 \\ \sigma_5 \\ \sigma_6 \end{Bmatrix} = \begin{bmatrix} C_{11} & C_{12} & C_{12} & 0 & 0 & 0 \\ & C_{22} & C_{23} & 0 & 0 & 0 \\ & & C_{22} & 0 & 0 & 0 \\ & & & C_{44} & 0 & 0 \\ & sym. & & & \frac{C_{22}-C_{23}}{2} & 0 \\ & & & & & C_{44} \end{bmatrix} \begin{Bmatrix} \epsilon_1 \\ \epsilon_2 \\ \epsilon_3 \\ \epsilon_4 \\ \epsilon_5 \\ \epsilon_6 \end{Bmatrix} \tag{3.12}$$

3.2.2 Isotropic Elasticity

For an isotropic material $C_{13} = C_{23} = C_{12}$, $C_{22} = C_{33} = C_{11}$, and $C_{44} = C_{55} = C_{66} = (C_{11} - C_{12})/2$, so only two independent components are required to define the relationship:

$$\begin{Bmatrix} \sigma_1 \\ \sigma_2 \\ \sigma_3 \\ \sigma_4 \\ \sigma_5 \\ \sigma_6 \end{Bmatrix} = \begin{bmatrix} C_{11} & C_{12} & C_{12} & 0 & 0 & 0 \\ & C_{11} & C_{12} & 0 & 0 & 0 \\ & & C_{11} & 0 & 0 & 0 \\ & & & \frac{C_{11}-C_{12}}{2} & 0 & 0 \\ & sym. & & & \frac{C_{11}-C_{12}}{2} & 0 \\ & & & & & \frac{C_{11}-C_{12}}{2} \end{bmatrix} \begin{Bmatrix} \epsilon_1 \\ \epsilon_2 \\ \epsilon_3 \\ \epsilon_4 \\ \epsilon_5 \\ \epsilon_6 \end{Bmatrix} \tag{3.13}$$

3.2.3 Link to Engineering Constants

The components of the elasticity tensor are expressed in terms of the *Young's modulus* E and *Poisson's ratio* ν as:

$$\begin{aligned} C_{11} &= \frac{1 - \nu_{23}\nu_{32}}{E_2 E_3 \Delta} \\ C_{22} &= \frac{1 - \nu_{13}\nu_{31}}{E_1 E_3 \Delta} \\ C_{33} &= \frac{1 - \nu_{12}\nu_{21}}{E_1 E_2 \Delta} \\ C_{12} &= \frac{\nu_{21} + \nu_{31}\nu_{23}}{E_2 E_3 \Delta} \\ C_{23} &= \frac{\nu_{32} + \nu_{12}\nu_{31}}{E_1 E_3 \Delta} \\ C_{13} &= \frac{\nu_{13} + \nu_{12}\nu_{23}}{E_1 E_2 \Delta} \\ C_{44} &= G_{12} \; ; \; C_{55} = G_{23} \; ; \; C_{66} = G_{31} \end{aligned} \tag{3.14}$$

where,

$$\Delta = \frac{1}{E_1 E_2 E_3}\begin{bmatrix} 1 & -\nu_{21} & -\nu_{31} \\ -\nu_{12} & 1 & -\nu_{32} \\ -\nu_{13} & -\nu_{23} & 1 \end{bmatrix}$$

and $\nu_{ji} = E_j * \nu_{ij}/E_i$. Note that, for an isotropic material

$$\begin{aligned} E_1 = E_2 = E_3 &= E \\ \nu_{12} = \nu_{23} = \nu_{31} &= \nu \\ G_{12} = G_{23} = G_{31} &= \frac{E}{2(1+\nu)} \end{aligned}$$

so that (3.13) becomes:

$$\begin{Bmatrix} \sigma_1 \\ \sigma_2 \\ \sigma_3 \\ \sigma_4 \\ \sigma_5 \\ \sigma_6 \end{Bmatrix} = \begin{bmatrix} \frac{E(1-\nu)}{(1+\nu)(1-2\nu)} & \frac{E\nu}{(1+\nu)(1-2\nu)} & \frac{E\nu}{(1+\nu)(1-2\nu)} & 0 & 0 & 0 \\ & \frac{E(1-\nu)}{(1+\nu)(1-2\nu)} & \frac{E\nu}{(1+\nu)(1-2\nu)} & 0 & 0 & 0 \\ & & \frac{E(1-\nu)}{(1+\nu)(1-2\nu)} & 0 & 0 & 0 \\ & sym & & \frac{E}{2(1+\nu)} & 0 & 0 \\ & & & & \frac{E}{2(1+\nu)} & 0 \\ & & & & & \frac{E}{2(1+\nu)} \end{bmatrix} \begin{Bmatrix} \epsilon_1 \\ \epsilon_2 \\ \epsilon_3 \\ \epsilon_4 \\ \epsilon_5 \\ \epsilon_6 \end{Bmatrix} \tag{3.15}$$

whereas for a transversely isotropic material with the 2-3 plane as the plane of isotropy,

$$\begin{aligned} E = E_2 = E_3 = &\neq E_A = E_1 \\ \nu = \nu_{23} &\neq \nu_A = \nu_{13} = \nu_{12} \\ G = G_{23} = \frac{E}{2(1+\nu)} &\neq G_A = G_{13} = G_{12} \end{aligned}$$

so that (3.12) becomes:

$$\begin{Bmatrix} \sigma_1 \\ \sigma_2 \\ \sigma_3 \\ \sigma_4 \\ \sigma_5 \\ \sigma_6 \end{Bmatrix} = \begin{bmatrix} \frac{E_A^2(\nu-1)}{k} & -\frac{E_A E\nu_A}{k} & -\frac{E_A E\nu_A}{k} & 0 & 0 & 0 \\ & \frac{E(E\nu_A^2 - E_A)}{k(1+\nu)} & -\frac{E(E\nu_A^2 + E_A\nu)}{k(1+\nu)} & 0 & 0 & 0 \\ & & \frac{E(E\nu_A^2 - E_A)}{k(1+\nu)} & 0 & 0 & 0 \\ & sym & & G_A & 0 & 0 \\ & & & & \frac{E}{2(1+\nu)} & 0 \\ & & & & & G_A \end{bmatrix} \begin{Bmatrix} \epsilon_1 \\ \epsilon_2 \\ \epsilon_3 \\ \epsilon_4 \\ \epsilon_5 \\ \epsilon_6 \end{Bmatrix} \tag{3.16}$$

where $k = E_A(\nu - 1) + 2E\nu_A^2$.

3.3 Large Strain Hyperelasticity

For large strains in the initial configuration $\psi = \psi(\boldsymbol{C}, T)$, and

$$\dot{\psi} = \frac{\partial \psi}{\partial \boldsymbol{C}} \dot{\boldsymbol{C}} + \frac{\partial \psi}{\partial T} \dot{T}$$

Inserting this into (3.9),

$$\left(\frac{1}{2} \boldsymbol{S} - \frac{\partial \Psi}{\partial \boldsymbol{C}} \right) : \dot{\boldsymbol{C}} = 0$$

or,

$$\boldsymbol{S} = 2 \frac{\partial \Psi}{\partial \boldsymbol{C}} \tag{3.17}$$

Note that since the relationship between $\boldsymbol{S}$ and $\boldsymbol{C}$ is non-linear, it needs to be linearized in the direction of an increment $\boldsymbol{u}$ for use within the framework of the Newton-Raphson procedure. The elasticity tensor now relates the linearized tensors:

$$D\boldsymbol{S}[\boldsymbol{u}] = \frac{1}{2} \boldsymbol{\mathcal{C}} : D\boldsymbol{C}[\boldsymbol{u}] \quad ; \quad \boldsymbol{\mathcal{C}} = 2 \frac{\partial \boldsymbol{S}}{\partial \boldsymbol{C}} = \frac{4 \partial^2 \Psi}{\partial \boldsymbol{C}^2} \tag{3.18}$$

3.3.1 Isotropic Hyperelasticity

To satisfy isotropy, the relationship between Ψ and $\boldsymbol{C}$ must be independent of the material axes, thus Ψ must only be a function of the invariants of $\boldsymbol{C}$, i.e. $\Psi = \Psi(I_1, I_2, I_3)$, so that (3.17) becomes:

$$\boldsymbol{S} = 2 \frac{\partial \Psi}{\partial I_1} \frac{\partial I_1}{\partial \boldsymbol{C}} + 2 \frac{\partial \Psi}{\partial I_2} \frac{\partial I_2}{\partial \boldsymbol{C}} + 2 \frac{\partial \Psi}{\partial I_3} \frac{\partial I_3}{\partial \boldsymbol{C}} \tag{3.19}$$

Invariants of $\boldsymbol{C}$ with their derivatives with respect to $\boldsymbol{C}$ are given as:

$$\begin{aligned} I_1 &= tr[\boldsymbol{C}] = \boldsymbol{C} : \boldsymbol{I} \; ; \; \frac{\partial I_1}{\partial \boldsymbol{C}} = \boldsymbol{I} \\ I_2 &= \boldsymbol{C} : \boldsymbol{C} \; ; \; \frac{\partial I_2}{\partial \boldsymbol{C}} = 2\boldsymbol{C} \qquad (3.20) \\ I_3 &= det(\boldsymbol{C}) = J^2 \; ; \; \frac{\partial I_3}{\partial \boldsymbol{C}} = J^2 \boldsymbol{C}^{-1} \end{aligned}$$

(3.21)

so that the Second Piola-Kirchoff stress is now found as:

$$\boldsymbol{S} = 2 \frac{\partial \Psi}{\partial I_1} \boldsymbol{I} + 4 \frac{\partial \Psi}{\partial I_2} \boldsymbol{C} + 2 J^2 \frac{\partial \Psi}{\partial I_3} \boldsymbol{C}^{-1} \tag{3.22}$$

Note that in the current configuration Ψ is a function of the invariants of $\boldsymbol{b}$, and relates $\boldsymbol{\sigma}$ and $\boldsymbol{b}$ as:

$$\boldsymbol{\sigma} = 2 J^{-1} \frac{\partial \Psi}{\partial I_1^b} + 4 J^{-1} \frac{\partial \Psi}{\partial I_2^b} \boldsymbol{b}^2 + 2 J \frac{\partial \Psi}{\partial I_3^b} \boldsymbol{I} \tag{3.23}$$

Compressible Neo-Hookean Material Model Several material models defining the relationship between Ψ and invariants of $\boldsymbol{C}$ are available, however, attention will be focused on the Compressible Neo-Hookean type throughout this work, for which the strain energy is given as:

$$\Psi = \frac{\mu}{2}(I_1 - 3) - \mu \ln J + \frac{\lambda}{2}(J-1)^2 \tag{3.24}$$

where $J^2 = I_3$. The derivatives with respect to the invariants of $\boldsymbol{C}$ are given as:

$$\begin{aligned} \frac{\partial \Psi}{\partial I_1} &= \frac{\mu}{2} \\ \frac{\partial \Psi}{\partial I_2} &= 0 \\ \frac{\partial \Psi}{\partial I_3} &= \frac{\partial \Psi}{\partial J}\frac{\partial J}{\partial I_3} \\ &= (\lambda(J-1) - \frac{\mu}{J})\frac{1}{2J} \end{aligned} \tag{3.25}$$

where μ and λ are the material constants. The second Piola-Kirchoff stress for this material model is found by inserting the above equations into (3.22):

$$\boldsymbol{S} = \mu(\boldsymbol{I} - \boldsymbol{C}^{-1}) + \lambda J(J-1)\boldsymbol{C}^{-1} \tag{3.26}$$

The Lagrangian elasticity tensor $\boldsymbol{\mathcal{C}}$ is found by taking the derivative of the above equation with respect to $\boldsymbol{C}$ as:

$$\boldsymbol{\mathcal{C}} = \lambda J(2J-1)\boldsymbol{C}^{-1} \otimes \boldsymbol{C}^{-1} - 2[\mu - \lambda J(J-1)]\frac{\partial \boldsymbol{C}^{-1}}{\partial \boldsymbol{C}} \tag{3.27}$$

To complete the material model in the current configuration as well, the Cauchy stress and the Eulerian elasticity tensor are found to be:

$$\boldsymbol{\sigma} = \frac{\mu}{J}(\boldsymbol{b} - \boldsymbol{I}) + \lambda(J-1)\boldsymbol{I} \tag{3.28}$$

and

$$\boldsymbol{c} = \lambda J(2J-1)(\boldsymbol{I} \otimes \boldsymbol{I}) + \frac{2}{J}(\mu - \lambda J(2J-1))\mathbf{i} \tag{3.29}$$

where $\mathbf{i} = \delta_{ik}\delta_{jl}$ in indicial notation.

3.3.2 Transversely Isotropic Hyperelasticity

A matrix material reinforced by a single family of fibres can be considered transversely isotropic on the macroscopic scale as long as the fibres are aligned and nearly

homogeneous in their distribution. In addition to the three invariants of $\boldsymbol{C}$, two additional *pseudo* invariants I_4 and I_5 are required to define the strain energy function $\Psi = \Psi(I_1, I_2, I_3, I_4, I_5)$. Let $\boldsymbol{A}$ and $\boldsymbol{a}$ denote vector fields which define the fibre direction in the initial and current configurations respectively. The deformation gradient relates these vector fields as:

$$\boldsymbol{a} = \boldsymbol{F}\boldsymbol{A} \tag{3.30}$$

λ_a is the stretch of the fibres, and defines the first pseudo invariant as:

$$I_4 = \lambda_a = \boldsymbol{a} \cdot \boldsymbol{a} = \boldsymbol{A} \cdot \boldsymbol{C}\boldsymbol{A} \tag{3.31}$$

The other required invariant is defined as

$$\boldsymbol{I}_5 = \boldsymbol{A} \cdot \boldsymbol{C}^2\boldsymbol{A} \tag{3.32}$$

We refer to Spencer [108] for further details. Note that the derivatives of the invariants with respect to $\boldsymbol{C}$ are given as:

$$\begin{aligned} \frac{\partial I_4}{\partial \boldsymbol{C}} &= \boldsymbol{A} \otimes \boldsymbol{A} \\ \frac{\partial I_5}{\partial \boldsymbol{C}} &= \boldsymbol{A} \otimes \boldsymbol{C}\boldsymbol{A} + \boldsymbol{C}\boldsymbol{A} \otimes \boldsymbol{A} \end{aligned}$$

Due to Bonet *et al.*[9], it could be assumed that the strain energy function could be decomposed into fully isotropic and orthotropic transversely isotropic components, i.e $\Psi = \Psi_{iso}(I_1, I_2, I_3) + \Psi_{trn}(I_1, I_2, I_3, I_4, I_5)$. It follows that the Second Piola-Kirchoff stress tensor could also be decomposed similarly as $\boldsymbol{S} = \boldsymbol{S}_{iso} + \boldsymbol{S}_{trn}$ where,

$$\begin{aligned} \boldsymbol{S}_{iso} &= 2\frac{\partial \Psi_{iso}}{\partial \boldsymbol{C}} \\ \boldsymbol{S}_{trn} &= 2\frac{\partial \Psi_{trn}}{\partial \boldsymbol{C}} \end{aligned}$$

Similarly, the elasticity tensor becomes $\boldsymbol{\mathcal{C}} = \boldsymbol{\mathcal{C}}_{iso} + \boldsymbol{\mathcal{C}}_{trn}$. Note that the compressible neo-Hookean material potential defined in (3.24) can be employed for the isotropic part. For the transversely isotropic part, we adopt the potential proposed in [9]:

$$\Psi_{trn} = [\alpha + \beta \ln J + \gamma(I_4 - 1)](I_4 - 1) - \frac{\alpha}{2}(I_5 - 1) \tag{3.33}$$

from which we derive the transversely isotropic component of the second Piola-Kirchoff stress as:

$$\boldsymbol{S}_{trn} = 2\beta(I_4 - 1)\boldsymbol{C}^{-1} + 2[\alpha + 2\beta \ln J + 2\gamma(I_4 - 1)]\boldsymbol{A} \otimes \boldsymbol{A} - \alpha(\boldsymbol{A} \otimes \boldsymbol{C}\boldsymbol{A} + \boldsymbol{C}\boldsymbol{A} \otimes \boldsymbol{A}) \tag{3.34}$$

The corresponding elasticity tensor follows as:

$$\begin{aligned}\boldsymbol{C}_{trn} &= 8\gamma \boldsymbol{A}\otimes\boldsymbol{A}\otimes\boldsymbol{A}\otimes\boldsymbol{A} + 4\beta(\boldsymbol{A}\otimes\boldsymbol{A}\otimes\boldsymbol{C}^{-1} + \boldsymbol{C}^{-1}\otimes\boldsymbol{A}\otimes\boldsymbol{A}) \\ &\quad -\alpha\boldsymbol{\mathcal{A}} - 4\beta(I_4-1)\frac{\partial \boldsymbol{C}^{-1}}{\partial \boldsymbol{C}}\end{aligned} \tag{3.35}$$

where $\mathcal{A}_{ijkl} = A_iA_l\delta_{jk} + \delta_{ik}A_jA_l$. For completeness, the spatial counterparts are given as:

$$J\boldsymbol{\sigma}_{trn} = 2\beta(I_4-1)\boldsymbol{I} + 2[\alpha + 2\beta\ln J + 2\gamma(I_4-1)]\boldsymbol{a}\otimes\boldsymbol{a} - \alpha(\boldsymbol{a}\otimes\boldsymbol{ba} + \boldsymbol{ba}\otimes\boldsymbol{a}) \tag{3.36}$$

and

$$\begin{aligned}J\boldsymbol{c}_{trn} &= 8\gamma \boldsymbol{a}\otimes\boldsymbol{a}\otimes\boldsymbol{a}\otimes\boldsymbol{a} + 4\beta(\boldsymbol{a}\otimes\boldsymbol{a}\otimes\boldsymbol{I} + \boldsymbol{I}\otimes\boldsymbol{a}\otimes\boldsymbol{a}) \\ &\quad -\alpha\mathfrak{a} - 4\beta(I_4-1)\mathbf{i}\end{aligned} \tag{3.37}$$

where $\mathfrak{a}_{ijkl} = a_ia_lb_{jk} + b_{ik}a_ja_l$

3.3.3 Parameter identification

It is tempting to express the isotropic and transversely isotropic material models in terms of familiar engineering constants. This can be achieved by linearizing $\boldsymbol{S}_{iso}$ and $\boldsymbol{S}_{trn}$ to yield the linear elastic matrices $\boldsymbol{D}_{iso}$, $\boldsymbol{D}_{trn}$ and comparing the elasticity matrices with their small strain counterparts (3.16) and (3.15). We refer to Latif *et al.*[59] for details of linearization. Expression (3.26) is linearized to give the stress term for small strain isotropy as:

$$\boldsymbol{\sigma}^{ss}_{iso} = 2\mu\boldsymbol{\varepsilon} + \lambda tr\boldsymbol{\varepsilon}\boldsymbol{I} \tag{3.38}$$

which reveals the linearized elastic matrix $\boldsymbol{D}_{iso}$ as:

$$\boldsymbol{D}_{iso} = \begin{bmatrix} \lambda+2\mu & \lambda & \lambda & 0 & 0 & 0 \\ & \lambda+2\mu & \lambda & 0 & 0 & 0 \\ & & \lambda+2\mu & 0 & 0 & 0 \\ & & & \mu & 0 & 0 \\ & sym. & & & \mu & 0 \\ & & & & & \mu \end{bmatrix} \tag{3.39}$$

(3.34) is linearized to give the stress term for small strain transverse isotropy as:

$$\boldsymbol{\sigma}^{ss}_{trn} = 2\beta(\boldsymbol{\varepsilon} : \boldsymbol{M})\boldsymbol{I} + [2\beta tr\boldsymbol{\varepsilon} + 8\gamma(\boldsymbol{\varepsilon} : \boldsymbol{M}) - 4\alpha\boldsymbol{\varepsilon}]\boldsymbol{M}$$

Following the convention of (3.16), we assume the 2-3 plane as the plane of isotropy, where $\boldsymbol{A}$ is given by $[1,0,0]^T$, so that the combined linearized elastic matrix $\boldsymbol{D}_{iso+trn}$ takes the form:

$$\boldsymbol{D}_{iso+trn} = \begin{bmatrix} \lambda+2\mu+8\beta+8\gamma-4\alpha & \lambda+4\beta & \lambda+4\beta & 0 & 0 & 0 \\ & \lambda+2\mu & \lambda & 0 & 0 & 0 \\ & & \lambda+2\mu & 0 & 0 & 0 \\ & & & \mu-\alpha & 0 & 0 \\ & sym. & & & \mu & 0 \\ & & & & & \mu-\alpha \end{bmatrix} \tag{3.40}$$

Comparison of $\boldsymbol{D}_{iso+trn}$ with (3.16) reveals the material parameters as follows:

$$\begin{aligned} \mu &= \frac{E}{2(1+\nu)} \\ \lambda &= -\frac{E(E\nu_A^2+E_A\nu)}{k(1+\nu)} \\ \beta &= \frac{E(E\nu_A^2-E_A(\nu_A-\nu+\nu_A\nu))}{4k(1+\nu)} \\ \alpha &= \frac{E}{2(1+\nu)} - G_A \\ \gamma &= \frac{1}{8}\left(\frac{E_A^2(\nu-1)}{k} - [\lambda+2\mu+8\beta-4\alpha]\right) \end{aligned} \tag{3.41}$$

where $k = E_A(\nu-1)+2E\nu_A^2$. Note that in case of isotropy, α, β and γ vanish, and λ becomes:

$$\lambda = \frac{E\nu}{(1+\nu)(1-2\nu)} \tag{3.42}$$

which could also be confirmed by comparing $\boldsymbol{D}_{iso}$ with (3.15).

3.4 Small Strain Elasto-Plasticity

The current strain state at any point of the body undergoing inelastic deformations is not completely determined by the current stress and temperature. The behaviour of most engineering materials is nearly elastic within a certain range of stresses, but history dependent outside that range. A similar range for temperature exists as well, outside of which the behaviour becomes highly non-linear and rate-dependent. Here, attention will be focused on rate-independent plasticity only.

In rate-independent plasticity, the stress strain relation is assumed to be independent of the rate of straining. Furthermore, in addition to the current state variables, the past history of loading affects the current equilibrium, which can be

represented by a set of *internal variables*. In modelling rate independent plasticity, internal variables are often assumed to consist of the plastic strain tensor and an additional variable κ, called the hardening variable. Moreover, rate equations of κ and the plastic strain are interrelated.

It is commonly assumed that the small strain tensor can be decomposed into elastic and plastic components:

$$\boldsymbol{\varepsilon} = \boldsymbol{\varepsilon}^e + \boldsymbol{\varepsilon}^p; \qquad \boldsymbol{\varepsilon}^e = \boldsymbol{\varepsilon} - \boldsymbol{\varepsilon}^p$$

Note that relation above is also valid in rate form as:

$$\dot{\boldsymbol{\varepsilon}}^e = \dot{\boldsymbol{\varepsilon}} - \dot{\boldsymbol{\varepsilon}}^p$$

The time derivative appearing in (3.8) is expressed as:

$$\begin{aligned} \dot{\Psi} &= \frac{\partial \Psi}{\partial \boldsymbol{\varepsilon}^e} \dot{\boldsymbol{\varepsilon}}^e + \frac{\partial \Psi}{\partial T} \dot{T} + \sum \frac{\partial \Psi}{\partial \xi_k} \dot{\xi}_k \\ &= \frac{\partial \Psi}{\partial \boldsymbol{\varepsilon}^e} \dot{\boldsymbol{\varepsilon}} - \frac{\partial \Psi}{\partial \boldsymbol{\varepsilon}^e} \dot{\boldsymbol{\varepsilon}}^p + \frac{\partial \Psi}{\partial T} \dot{T} + \sum \frac{\partial \Psi}{\partial \xi_k} \dot{\xi}_k \end{aligned} \tag{3.43}$$

Admitting no change in temperature for elastic deformations $\dot{T} = 0$ and inserting this expression into (3.8):

$$\dot{\mathfrak{D}} = \left(\boldsymbol{\sigma} - \frac{\partial \Psi}{\partial \boldsymbol{\varepsilon}^e} \right) : \dot{\boldsymbol{\varepsilon}} + \left(\frac{\partial \Psi}{\partial \boldsymbol{\varepsilon}^e} : \dot{\boldsymbol{\varepsilon}}^p - \sum \frac{\partial \psi}{\partial \xi_k} \dot{\xi}_k \right) \geq 0 \tag{3.44}$$

3.4.1 Elastic Constitutive Equation

Inequality (3.44) must be valid in case when no plastic deformation is present, so that the elastic part of the constitutive relation reads:

$$\boldsymbol{\sigma} = \frac{\partial \Psi}{\partial \boldsymbol{\varepsilon}^e} \tag{3.45}$$

The dissipation inequality then reduces to:

$$\dot{\mathfrak{D}} = \boldsymbol{\sigma} : \dot{\boldsymbol{\varepsilon}}^p - \sum \frac{\partial \psi}{\partial \xi_k} \dot{\xi}_k \geq 0 \tag{3.46}$$

3.4.2 Generalized Flow Potential

Define $q_k = \rho \frac{\partial \psi}{\partial \dot{\xi}_k}$ as the thermodynamic force conjugate to ξ_k. A convex *dissipation potential* $\Omega = \Omega(\boldsymbol{\sigma}, T, \xi)$ is assumed to depend on stress only through the thermodynamic forces conjugate to ξ_k. It is further assumed that

$$\dot{\xi}_k = \frac{\partial \Omega}{\partial q_k}$$

which represents the hypothesis of *generalized normality*. It can be shown that

$$\dot{\boldsymbol{\varepsilon}}^p = \frac{\partial \Omega}{\partial \boldsymbol{\sigma}} \tag{3.47}$$

Now the dissipation inequality becomes

$$\dot{\mathfrak{D}} = \boldsymbol{\sigma} : \frac{\partial \Omega}{\partial \boldsymbol{\sigma}} - \sum q_k \frac{\partial \Omega}{\partial p_k} \geq 0$$

3.4.3 Maximum Dissipation

The associative evolution equations in plasticity arise as a result of the *postulate of maximum dissipation* which characterizes the actual state $(\boldsymbol{\sigma}, q)$ as the one among all possible admissible states $(\boldsymbol{\sigma}^*, q^*)$ leading to maximum dissipation for prescribed rates of deformation:

$$(\boldsymbol{\sigma} - \boldsymbol{\sigma}^*) : \dot{\boldsymbol{\varepsilon}}^p + (q - q^*)\dot{\xi}_k \geq 0$$

3.4.4 Associative Flow Rule

The *normality rule*, which is a consequence of the postulate of maximum dissipation, states that if the above inequality is to be valid for all $\boldsymbol{\sigma}^*$, then $\dot{\boldsymbol{\varepsilon}}^p$ must be directed along the outward normal to the yield surface, which is defined by $\frac{\partial \Phi}{\partial \boldsymbol{\sigma}}$. Thus, recalling (3.47), the yield criterion Φ itself can be employed as the flow potential, and the normality rule is also called a flow rule that is associated with the yield criterion, or briefly, associative flow rule.

3.4.5 Derivation of the Flow Rule

The problem is to find the thermodynamical forces that render a maximum rate of dissipation for any material state, and at the same time satisfy the yield criterion. The only internal variable is κ. The dissipation is expressed as:

$$\dot{\mathfrak{D}} = \boldsymbol{\sigma} : \dot{\boldsymbol{\varepsilon}}^p - q\dot{\kappa} \tag{3.48}$$

and will be solved by augmenting the dissipation function with a Lagrange multiplier term $\dot{\lambda}$ such that:

$$\hat{\dot{\mathfrak{D}}}_L(\boldsymbol{\sigma}, q, \dot{\lambda}) = -\hat{\dot{\mathfrak{D}}}(\boldsymbol{\sigma}, q) + \dot{\lambda}\hat{\Phi}(\boldsymbol{\sigma}, q) \tag{3.49}$$

which gives the stationary condition for $\dot{\mathfrak{D}}_L$ as:

$$\delta\dot{\mathfrak{D}}_L = (-\dot{\boldsymbol{\varepsilon}}^p + \dot{\lambda}\frac{\partial \Phi}{\partial \boldsymbol{\sigma}}) : \delta\boldsymbol{\sigma} + (\dot{\kappa} + \dot{\lambda}\frac{\partial \Phi}{\partial q}) : \delta q + \Phi\delta\dot{\lambda}$$

so that the flow equations emerge as the solution to the maximization problem:

$$\dot{\boldsymbol{\varepsilon}}^p = \dot{\lambda}\frac{\partial \Phi}{\partial \boldsymbol{\sigma}} \tag{3.50}$$

$$\dot{\kappa} = -\dot{\lambda}\frac{\partial \Phi}{\partial q} \tag{3.51}$$

subject to the *Kuhn-Tucker*, or the loading/unloading conditions:

$$\dot{\lambda} \geq 0 \quad ; \quad \Phi \leq 0 \tag{3.52}$$

Also,

$$\begin{aligned} \Phi < 0 \quad &\Rightarrow \quad \dot{\lambda} = 0 \\ \dot{\lambda} > 0 \quad &\Rightarrow \quad \Phi = 0 \end{aligned}$$

which implies:

$$\dot{\lambda}\Phi = 0 \tag{3.53}$$

The *consistency condition* also follows as:

$$\dot{\lambda}\dot{\Phi} = 0 \tag{3.54}$$

It is apparent in the above formulation that $\frac{\partial \Phi}{\partial \boldsymbol{\sigma}}$ defines the direction of plastic straining, whereas $\dot{\lambda}$ defines the size.

3.4.6 The von Mises Yield Criterion

The von Mises yield criterion for isotropic yielding states that plastic deformation occurs when the *maximum octahedral shear stress* reaches its critical value given by the yield stress in shear (or $\frac{\sigma_Y}{\sqrt{3}}$). As the distortional energy is directly related to the maximum octahedral shear stress, this yield criterion is also known as the *distortional energy* criterion. The von Mises yield criterion is shown graphically in Figure 3.1 in the principal stress space. The yield surface is the surface of the cylinder defined by the axis $\sigma_1 = \sigma_2 = \sigma_3$ and radius $\sqrt{\frac{2}{3}}\sigma_Y$. Note that the pressure component of the stress does not influence yielding. The von Mises yield criterion can be mathematically expressed as:

$$\Phi = \sqrt{\boldsymbol{\sigma}^{\text{dev}} : \boldsymbol{\sigma}^{\text{dev}}} - \sqrt{\frac{2}{3}}\sigma_Y \tag{3.55}$$

Note that the admissible stress has to be on or within the elastic domain defined by the yield surface ($\Phi \leq 0$).

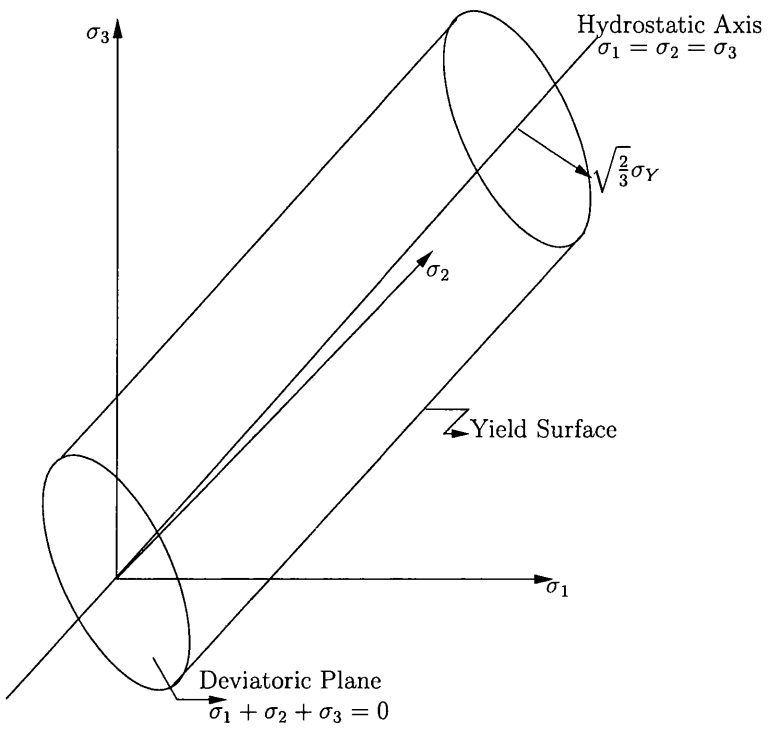

Figure 3.1: Representation of the von Mises yield criterion in principal stress space

3.4.7 Hardening Rule

Due to its simplicity, isotropic linear hardening will be employed in this work where applicable. In linear hardening, the hardening function q is assumed to be a linear function of the hardening variable κ as

$$q = H\kappa \tag{3.56}$$

where H is called the *hardening modulus*. Evolution of the elastic domain is given as

$$\sigma_Y = \sigma_0 + q \tag{3.57}$$

where σ_0 denotes the yield stress of the virgin specimen.

3.4.8 Flow Equations for von Mises Yield Criterion

The elastoplastic model given by equations (3.45), (3.50), (3.51), (3.52) and (3.53) is now complete. To finalize, the flow rule (3.50) is subjected to von Mises yield

function (3.55) to give :

$$\dot{\boldsymbol{\varepsilon}}^p = \dot{\lambda}\frac{\partial \Phi}{\partial \boldsymbol{\sigma}} = \dot{\lambda}\frac{\boldsymbol{\sigma}^{\text{dev}}}{\sqrt{\boldsymbol{\sigma}^{\text{dev}} : \boldsymbol{\sigma}^{\text{dev}}}} = \dot{\lambda}\boldsymbol{n} \tag{3.58}$$

Note that $\boldsymbol{n}$ is the unit normal to the yield surface.

$$\dot{\kappa} = -\dot{\lambda}\frac{\partial \Phi}{\partial q} = \sqrt{\frac{2}{3}}\dot{\lambda} \tag{3.59}$$

Two more important relationships are derived from (3.58) and (3.59). Note that $\dot{\lambda}$ defines the magnitude of plastic strain as $\boldsymbol{n}$ is the unit normal, so that:

$$\dot{\lambda} = \|\dot{\boldsymbol{\varepsilon}}^p\| \tag{3.60}$$

Also, the relation between rates of plastic strain and hardening variable is revealed, so that the hardening variable can be named the *equivalent plastic strain* as:

$$\kappa = \int \sqrt{\frac{2}{3}}\|\dot{\boldsymbol{\varepsilon}}^p\|\, dt \tag{3.61}$$

3.4.9 Time Integration: Simple Backward Euler Scheme.

Consider the first order differential equation $\dot{x} = f(x)$. with the initial value $x(0) = x_0$. Time integration of this equation with a numerical scheme provides approximate solutions $x^n \approx x(t^n)$ at discrete points of the interval.
The class of algorithms known as *generalized midpoint algorithms* are commonly employed for time integration of elastoplasticity problems. The generalized midpoint algorithm, applied to the above defined differential equation gives:

$$\begin{aligned} x^{n+1} &= x^n + \Delta t f(x^{n+\theta}) \\ x^{n+\theta} &= \theta x^{n+1} + (1-\theta)x^n \end{aligned}$$

The choice of θ yields some well known time integration schemes as:

$$\begin{aligned} \theta &= 0 \quad \Rightarrow \quad \text{Forward Euler Rule (Explicit)} \\ \theta &= \frac{1}{2} \quad \Rightarrow \quad \text{Midpoint Rule (Implicit)} \\ \theta &= 1 \quad \Rightarrow \quad \text{Backward Euler Rule (Implicit)} \end{aligned}$$

Note that implicit algorithms are unconditionally stable even for large time steps. In this thesis, attention will be focused on the *backward Euler scheme* which becomes:

$$x^{n+1} = x^n + \Delta t f(x^{n+1})$$

For a differential equation of the form $\dot{x} = \dot{\lambda} f(x)$, the approximation $\Delta\lambda = \Delta t\dot{\lambda}$ is adopted, and the backward Euler scheme now reads:

$$x^{n+1} = x^n + \Delta\lambda f(x^{n+1}) \tag{3.62}$$

which is used to numerically integrate (3.58) and (3.59) to give the incremental version as:

$$\boldsymbol{\varepsilon}^p = \boldsymbol{\varepsilon}^{pn} + \Delta\lambda \frac{\boldsymbol{s}}{\sqrt{\boldsymbol{s} : \boldsymbol{s}}} \tag{3.63}$$

$$\kappa = \kappa^n + \sqrt{\frac{2}{3}}\Delta\lambda \tag{3.64}$$

For simplicity, all expressions without subscript will refer to $n+1$ in the remaining part of this section. Note that $(.)^{pn}$ refers to the plastic component of (.) at time t^n.

3.4.10 Stress Update

The aim is to update the current stress in the frame given by the above equations. The total strain $\boldsymbol{\varepsilon}$ is provided by the global Newton-Raphson procedure. Also the plastic strain $\boldsymbol{\varepsilon}^{pn}$ and the equivalent plastic strain κ^n from the previous step t^n are known.

The solution will be carried out in two distinct steps, known as *Elastic Predictor-Plastic Corrector.*

Elastic Predictor. Plastic flow is frozen at t^n to yield a trial elastic state given by:

$$\boldsymbol{s}^{\text{trial}} = 2\mu(\boldsymbol{e} - \boldsymbol{e}^{pn}) \tag{3.65}$$

$$\Phi^{\text{trial}} = \sqrt{\boldsymbol{s}^{\text{trial}} : \boldsymbol{s}^{\text{trial}}} - \sqrt{\frac{2}{3}}\sigma_Y^{\text{trial}} \tag{3.66}$$

$$\sigma_Y^{\text{trial}} = \sigma_0 + H\kappa^n \tag{3.67}$$

Note that, if the step is purely elastic $\Phi^{\text{trial}} \leq 0$, above equations completely define the stress state and no further action is necessary. However, if $\Phi^{\text{trial}} > 0$, this state is physically inadmissible and requires further correction.

Plastic Corrector. The plastic corrector phase, is given by equations:

$$\boldsymbol{s} = \boldsymbol{s}^{\text{trial}} - 2\mu\Delta\lambda\frac{\boldsymbol{s}^{\text{trial}}}{\sqrt{\boldsymbol{s}^{\text{trial}} : \boldsymbol{s}^{\text{trial}}}} \tag{3.68}$$

$$\Delta\lambda = \frac{\Phi^{\text{trial}}}{2\mu(1+\frac{H}{3\mu})} \tag{3.69}$$

Note that the explicit expression of $\Delta\lambda$ is only possible in case of linear hardening. Otherwise, a Newton-Raphson procedure should be employed to solve for $\Delta\lambda$.

3.4.11 Consistent Tangent Modulus

The *consistent tangent modulus* $\boldsymbol{\mathcal{C}}_{ep}$ is obtained by linearizing the stress given by (3.68):

$$\boldsymbol{\mathcal{C}}_{ep} = K\boldsymbol{I}\otimes\boldsymbol{I} + 2\mu\beta(\boldsymbol{\mathcal{I}} - \frac{1}{3}\boldsymbol{I}\otimes\boldsymbol{I}) - 2\mu\gamma(\boldsymbol{n}^{\text{trial}}\otimes\boldsymbol{n}^{\text{trial}}) \tag{3.70}$$

$$\beta = 1 - \frac{2\mu\Delta\lambda}{\sqrt{\boldsymbol{s}^{\text{trial}} : \boldsymbol{s}^{\text{trial}}}}$$

$$\gamma = \frac{1}{1+\frac{H}{3\mu}} - (1-\beta)$$

Note that if the stress state is elastic, the consistent tangent modulus reduces to the elasticity tensor $\boldsymbol{\mathcal{C}}$. See Appendix A.2 for derivation of the modulus.

3.5 Large Strain Elasto-Plasticity

The *multiplicative decomposition* of the deformation gradient $\boldsymbol{F}$ into elastic $\boldsymbol{F}^e$ and plastic $\boldsymbol{F}^p$ components is commonly accepted as:

$$\boldsymbol{F} = \boldsymbol{F}^e\boldsymbol{F}^p$$

As shown in figure (3.5), $\boldsymbol{F}^p$ maps the particle in the initial configuration on to a stress free *intermediate configuration*, which is then mapped on to the current configuration by $\boldsymbol{F}^e$.

Elastic and plastic components of right Cauchy tensor emerge as $\boldsymbol{C}^e = \boldsymbol{F}^{e^T}\boldsymbol{F}^e$ and $\boldsymbol{C}^p = \boldsymbol{F}^{p^T}\boldsymbol{F}^p$. Also, the *plastic velocity gradient* is defined as $\boldsymbol{l}^p = \dot{\boldsymbol{F}}^p\boldsymbol{F}^{p^{-1}}$. Following kinematic relations will be used:

$$\boldsymbol{C}^e = \boldsymbol{F}^{p^{-T}}\boldsymbol{C}\boldsymbol{F}^{p^{-1}} \quad ; \quad \boldsymbol{C} = \boldsymbol{F}^{p^T}\boldsymbol{C}^e\boldsymbol{F}^p$$

$$\dot{\boldsymbol{C}}^e = \boldsymbol{F}^{p^{-T}}\dot{\boldsymbol{C}}\boldsymbol{F}^{p^{-1}} - \left(\boldsymbol{l}^{p^T}\boldsymbol{C}^e + \boldsymbol{C}^e\boldsymbol{l}^p\right)$$

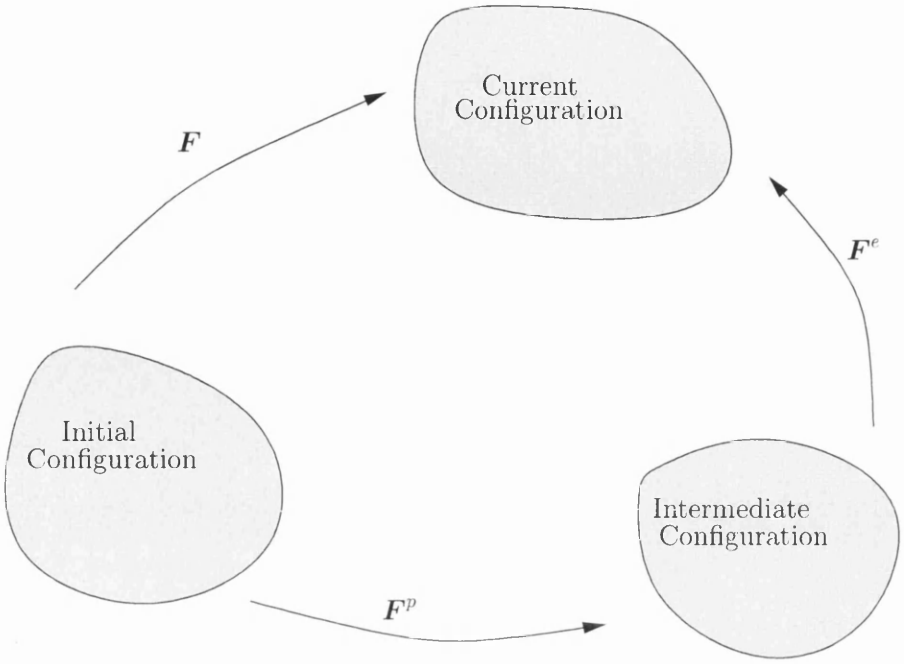

Figure 3.2: Multiplicative Decomposition

The Helmhotz free energy is now a function of elastic strain, temperature and internal variables as ($\psi = \psi(\boldsymbol{C}^e, T, \xi_k)$), and the time derivative appearing in (3.9) is expressed as:

$$\begin{aligned}
\dot{\Psi} &= \frac{\partial \Psi}{\partial \boldsymbol{C}^e} : \dot{\boldsymbol{C}}^e + \frac{\partial \psi}{\partial T}\dot{T} + \sum \frac{\partial \psi}{\partial \xi_k}\dot{\xi}_k \\
&= \frac{\partial \Psi}{\partial \boldsymbol{C}^e} : \boldsymbol{F}^{p^{-T}} \dot{\boldsymbol{C}} \boldsymbol{F}^{p^{-1}} - \frac{\partial \Psi}{\partial \boldsymbol{C}^e} : \left(\boldsymbol{l}^{p^T} \boldsymbol{C}^e + \boldsymbol{C}^e \boldsymbol{l}^p \right) \\
&\quad + \frac{\partial \psi}{\partial T}\dot{T} + \sum \frac{\partial \psi}{\partial \xi_k}\dot{\xi}_k \\
&= \boldsymbol{F}^{p^{-1}} \frac{\partial \Psi}{\partial \boldsymbol{C}^e} \boldsymbol{F}^{p^{-T}} : \dot{\boldsymbol{C}} - 2\frac{\partial \Psi}{\partial \boldsymbol{C}^e} \boldsymbol{C}^e : \frac{1}{2}\left(\boldsymbol{l}^{p^T} + \boldsymbol{l}^p \right) \\
&\quad + \frac{\partial \psi}{\partial T}\dot{T} + \sum \frac{\partial \psi}{\partial \xi_k}\dot{\xi}_k
\end{aligned} \tag{3.71}$$

Two terms will be defined at this stage. The *plastic deformation rate* $\boldsymbol{d}^p = \frac{1}{2}(\boldsymbol{l}^{p^T} + \boldsymbol{l}^p)$ is the symmetric part of $\boldsymbol{l}^p$. Note that definition of $\boldsymbol{d}^p$ is not unique, see Lubliner

[67] for further information. The *Mandel stress*, $\boldsymbol{M}$, is defined in Dettmer [24] as:

$$\boldsymbol{M} = 2\frac{\partial \Psi}{\partial \boldsymbol{C}^e}\boldsymbol{C}^e \tag{3.72}$$

Mandel stress is associated with the intermediate configuration, and its relation with $\frac{\partial \Psi}{\partial \boldsymbol{C}}$ is given below:

$$\boldsymbol{M} = \boldsymbol{F}^p 2\frac{\partial \Psi}{\partial \boldsymbol{C}}\boldsymbol{C}\boldsymbol{F}^{p^{-1}}$$

the first term in the time derivative $\dot{\Psi}$ is:

$$\boldsymbol{F}^{p^{-1}}\frac{\partial \Psi}{\partial \boldsymbol{C}^e}\boldsymbol{F}^{p^{-T}} : \dot{\boldsymbol{C}} = \frac{\partial \Psi}{\partial \boldsymbol{C}} : \dot{\boldsymbol{C}}$$

so that $\dot{\Psi}$ now becomes:

$$\dot{\Psi} = \frac{\partial \Psi}{\partial \boldsymbol{C}} : \dot{\boldsymbol{C}} - \boldsymbol{M} : \boldsymbol{d}^p + \frac{\partial \psi}{\partial T}\dot{T} + \sum \frac{\partial \psi}{\partial \xi_k}\dot{\xi}_k$$

Admitting no change in temperature for elastic deformations $\dot{T} = 0$ and inserting this expression into (3.9):

$$\dot{\mathfrak{D}} = \frac{1}{2}\boldsymbol{S} : \dot{\boldsymbol{C}} - \frac{\partial \Psi}{\partial \boldsymbol{C}} : \dot{\boldsymbol{C}} + \boldsymbol{M} : \boldsymbol{d}^p + \sum \frac{\partial \psi}{\partial \xi_k}\dot{\xi}_k \geq 0$$

or,

$$\dot{\mathfrak{D}} = \left(\frac{1}{2}\boldsymbol{S} - \frac{\partial \Psi}{\partial \boldsymbol{C}}\right) : \dot{\boldsymbol{C}} + \boldsymbol{M} : \boldsymbol{d}^p + \sum \frac{\partial \psi}{\partial \xi_k}\dot{\xi}_k \geq 0 \tag{3.73}$$

3.5.1 Elastic Constitutive Equation

Expression (3.73) must be valid in case when no plastic deformation is present, so that the elastic part of the constitutive relation reads:

$$\boldsymbol{S} = 2\frac{\partial \Psi}{\partial \boldsymbol{C}} \tag{3.74}$$

3.5.2 Isotropic Elasticity

In case of isotropy, $\Psi(\boldsymbol{C}^e)$ is a function of invariants of $\boldsymbol{C}^e$, which are expressed as $I_{1^e} = tr[\boldsymbol{C}\boldsymbol{C}^{p^{-1}}]$, $I_2^e = tr[\boldsymbol{C}\boldsymbol{C}^{p^{-1}}\boldsymbol{C}\boldsymbol{C}^{p^{-1}}]$ and $I_3^e = det(\boldsymbol{C})$. Now (3.74) becomes:

$$\boldsymbol{S} = 2\frac{\partial \Psi}{\partial I_{1^e}}\frac{\partial I_1^e}{\partial \boldsymbol{C}} + 2\frac{\partial \Psi}{\partial I_2^e}\frac{\partial I_2^e}{\partial \boldsymbol{C}} + 2\frac{\partial \Psi}{\partial I_3^e}\frac{\partial I_3^e}{\partial \boldsymbol{C}} \tag{3.75}$$

where

$$\begin{aligned}\frac{\partial I_1^e}{\partial \boldsymbol{C}} &= \boldsymbol{C}^{p^{-1}} \\ \frac{\partial I_2^e}{\partial \boldsymbol{C}} &= \boldsymbol{C}^{p^{-1}}\boldsymbol{C}\boldsymbol{C}^{p^{-1}} + \boldsymbol{C} : \frac{\partial \boldsymbol{C}^{p^{-1}}\bar{\boldsymbol{C}}\boldsymbol{C}^{p^{-1}}}{\partial \bar{\boldsymbol{C}}} \\ \frac{\partial I_3^e}{\partial \boldsymbol{C}} &= J^2\boldsymbol{C}^{-1}\end{aligned}$$

so that

$$\boldsymbol{S} = 2\frac{\partial \Psi}{\partial I_1^e}\boldsymbol{C}^{p^{-1}} + 4\frac{\partial \Psi}{\partial I_2^e}\boldsymbol{C}^{p^{-1}}\boldsymbol{C}\boldsymbol{C}^{p^{-1}} + 2\frac{\partial \Psi}{\partial I_3^e}J^2\boldsymbol{C}^{-1} \tag{3.76}$$

a Neo-Hookean type compressible material model will be adopted, which is defined as:

$$\Psi = \frac{\mu}{2}(I_1^e - 3) - \mu \ln J + \frac{\lambda}{2}(\ln J)^2$$

so that the derivatives with respect to the invariants of $\boldsymbol{C}^e$ are given as:

$$\frac{\partial \Psi}{\partial I_1^e} = \frac{\mu}{2}\ , \quad \frac{\partial \Psi}{\partial I_2^e} = 0 \tag{3.77}$$

$$\begin{aligned}\frac{\partial \Psi}{\partial I_3^e} &= \frac{\partial \Psi}{\partial J}\frac{\partial J}{\partial I_3^e} \\ &= \left(\frac{\lambda \ln J}{J} - \frac{\mu}{J}\right)\frac{1}{2J} \\ &= (\lambda \ln J - \mu)\frac{1}{2J^2}\end{aligned} \tag{3.78}$$

Finally, the expression for the second Piola-Kirchoff stress emerges by inserting (3.78) into (3.76) as:

$$\boldsymbol{S} = \mu\boldsymbol{C}^{p^{-1}} + (\lambda \ln J - \mu)\boldsymbol{C}^{-1} \tag{3.79}$$

3.5.3 Yield Criterion

von Mises yield criterion in the large strain regime is expressed as:

$$\Phi = \sqrt{\boldsymbol{\tau}^{\text{dev}} : \boldsymbol{\tau}^{\text{dev}}} - \sqrt{\frac{2}{3}}\sigma_Y$$

Note that (See Appendix A.1 for a proof)

$$\sqrt{\boldsymbol{M}^{\text{dev}} : \boldsymbol{M}^{\text{dev}}} = \sqrt{\boldsymbol{\tau}^{\text{dev}} : \boldsymbol{\tau}^{\text{dev}}}$$

such that the yield criterion can be expressed as:

$$\Phi = \sqrt{\boldsymbol{M}^{\text{dev}} : \boldsymbol{M}^{\text{dev}}} - \sqrt{\frac{2}{3}}\sigma_Y \tag{3.80}$$

3.5.4 Derivation of the Flow Rule

Inequality (3.73) now reduces to:

$$\dot{\mathfrak{D}} = \boldsymbol{M} : \boldsymbol{d}^p + \sum \frac{\partial \Psi}{\partial \xi_k} \dot{\xi}_k \geq 0 \tag{3.81}$$

Following the small strain argument for the postulate of maximum dissipation, an associative flow rule can be developed using the yield function as the flow potential, which states that plastic strain must be directed along the outward normal to the yield surface, which is defined by $\frac{\partial \Phi}{\partial \boldsymbol{\tau}}$ or $\frac{\partial \Phi}{\partial \boldsymbol{M}}$. The problem is to find the thermodynamical forces that render a maximum rate of dissipation for any material state, and at the same time satisfy the yield criterion. The only internal variable is κ. Noting that $\boldsymbol{d}^p = \frac{1}{2}\boldsymbol{F}^{p^{-T}} \dot{\boldsymbol{C}}^p \boldsymbol{F}^{p^{-1}}$, the dissipation is expressed as:

$$\dot{\mathfrak{D}} = \boldsymbol{M} : \frac{1}{2}\boldsymbol{F}^{p^{-T}} \dot{\boldsymbol{C}}^p \boldsymbol{F}^{p^{-1}} - q\dot{\kappa} \tag{3.82}$$

and will be solved by augmenting the dissipation function with a Lagrange multiplier term $\dot{\lambda}$ such that:

$$\hat{\dot{\mathfrak{D}}}_L(\boldsymbol{M}, q, \dot{\lambda}) = -\hat{\dot{\mathfrak{D}}}(\boldsymbol{M}, q) + \dot{\lambda}\hat{\Phi}(\boldsymbol{M}, q) \tag{3.83}$$

which gives the stationary condition for $\dot{\mathfrak{D}}_L$ as:

$$\delta\dot{\mathfrak{D}}_L = (-\frac{1}{2}\boldsymbol{F}^{p^{-T}} \dot{\boldsymbol{C}}^p \boldsymbol{F}^{p^{-1}} + \dot{\lambda}\frac{\partial \Phi}{\partial \boldsymbol{M}}) : \delta\boldsymbol{M} + (\dot{\kappa} + \dot{\lambda}\frac{\partial \Phi}{\partial q}) : \delta q + \Phi\delta\dot{\lambda}$$

so that the flow equations emerge as the solution to the maximization problem:

$$\frac{1}{2}\boldsymbol{F}^{p^{-T}} \dot{\boldsymbol{C}}^p \boldsymbol{F}^{p^{-1}} = \dot{\lambda}\frac{\partial \Phi}{\partial \boldsymbol{M}} \quad \Rightarrow \quad \dot{\boldsymbol{C}}^p = 2\dot{\lambda}\boldsymbol{F}^{p^T}\frac{\partial \Phi}{\partial \boldsymbol{M}}\boldsymbol{F}^p \tag{3.84}$$

$$\dot{\kappa} = -\dot{\lambda}\frac{\partial \Phi}{\partial q} \tag{3.85}$$

$$\Phi = 0 \tag{3.86}$$

subject to loading/unloading Conditions outlined in (3.52) and (3.53)

3.5.5 Flow Equations for von Mises Yield Criterion

The large strain elastoplastic model in initial configuration given by equations (3.74), (3.84), (3.85), (3.52) and (3.53) is now complete, only the flow equations need to be applied to the von Mises yield criterion. The flow rule (3.84) is subjected to von Mises yield function (3.80) to give :

$$\dot{\boldsymbol{C}}^p = 2\dot{\lambda}\boldsymbol{F}^{p^T}\frac{\partial \Phi}{\partial \boldsymbol{M}}\boldsymbol{F}^p = 2\dot{\lambda}\frac{[\boldsymbol{CS}]^{\text{dev}}}{\sqrt{tr[\boldsymbol{CSCS}] - \frac{1}{3}tr^2\boldsymbol{CS}]}}\boldsymbol{C}^p \tag{3.87}$$

Note that (3.59) is valid in the large strain regime as well.

3.5.6 Time Integration: Backward Euler Exponential Map.

Consider the first order scalar differential equation $\dot{x} = f(x)x.$ with the initial value $x(0) = x_0$, for which the exact solution is given as:

$$x(t) = exp\left(\int_{t_0}^{t} f(x(t))dt\right)x_0$$

The integral in the exponent can be approximated by the backward Euler scheme for any $t^n < t$ to give:

$$x(t) = exp\Big(\Delta t f(x(t))\Big)x^n$$

if the solution at x^n is known. The scalar differential equation is now transformed into tensor valued case as $\dot{\boldsymbol{A}} = \boldsymbol{f}(\boldsymbol{A})\boldsymbol{A}$, which yields:

$$\boldsymbol{A}(t) = exp\Big(\Delta t \boldsymbol{f}(\boldsymbol{A})\Big)\boldsymbol{A}^n$$

In a similar fashion to the previous paragraph, the approximate solution of the differential equation of the form $\dot{\boldsymbol{A}} = \dot{\lambda}\boldsymbol{f}(\boldsymbol{A})\boldsymbol{A}^{-1}\boldsymbol{A}$, with the approximation $\Delta\lambda = \Delta t\dot{\lambda}$ reads:

$$\boldsymbol{A} = exp\Big(\Delta\lambda \boldsymbol{f}(\boldsymbol{A})\boldsymbol{A}^{-1}\Big)\boldsymbol{A}^n$$

The exponential term can be expanded in a series to give:

$$exp\Big(\Delta\lambda \boldsymbol{f}(\boldsymbol{A})\boldsymbol{A}^{-1}\Big) = \boldsymbol{I} + \Delta\lambda \boldsymbol{f}\boldsymbol{A}^{-1} + \frac{\Delta\lambda^2}{2!}\boldsymbol{f}\boldsymbol{A}^{-1}\boldsymbol{f}\boldsymbol{A}^{-1} + \frac{\Delta\lambda^3}{3!}\boldsymbol{f}\boldsymbol{A}^{-1}\boldsymbol{f}\boldsymbol{A}^{-1}\boldsymbol{f}\boldsymbol{A}^{-1} + ...$$

so that the approximate solution to the differential equation $\dot{\boldsymbol{A}} = \dot{\lambda}\boldsymbol{f}(\boldsymbol{A})\boldsymbol{A}^{-1}\boldsymbol{A}$ becomes:

$$\boldsymbol{A} = \left(\boldsymbol{I} + \Delta\lambda \boldsymbol{f}\boldsymbol{A}^{-1} + \frac{\Delta\lambda^2}{2!}\boldsymbol{f}\boldsymbol{A}^{-1}\boldsymbol{f}\boldsymbol{A}^{-1} + \frac{\Delta\lambda^3}{3!}\boldsymbol{f}\boldsymbol{A}^{-1}\boldsymbol{f}\boldsymbol{A}^{-1}\boldsymbol{f}\boldsymbol{A}^{-1} + ...\right)\boldsymbol{A}^n$$

or, after some manipulation:

$$\boldsymbol{A} = \boldsymbol{A}(\boldsymbol{A}^n)^{-1}\boldsymbol{A} - \Delta\lambda \boldsymbol{f} - \frac{\Delta\lambda^2}{2!}\boldsymbol{f}\boldsymbol{A}^{-1}\boldsymbol{f} - \frac{\Delta\lambda^3}{3!}\boldsymbol{f}\boldsymbol{A}^{-1}\boldsymbol{f}\boldsymbol{A}^{-1}\boldsymbol{f} - ... \tag{3.88}$$

this integration scheme can be shown to preserve the plastic volume within time steps. As for small strains, for simplicity, all expressions without time superscript will refer to $n+1$ in the remaining part of this section. Also, note that $(.)^{p\,n}$ refers to the plastic component of (.) at time t^n. The incremental version of evolution equation for $\boldsymbol{C}^p$ can now be derived from the constitutive evolution equation and

the backward Euler exponential map (3.88)as follows:
Let,

$$\boldsymbol{f}[\boldsymbol{C}, \boldsymbol{S}(\boldsymbol{C}, \boldsymbol{C}^p)] = 2\frac{[\boldsymbol{CS}]^{\text{dev}}}{\sqrt{tr[\boldsymbol{CSCS}] - \frac{1}{3}tr^2[\boldsymbol{CS}]}}\boldsymbol{C}^p$$

Then the evolution equation for $\boldsymbol{C}^p$ reads:

$$\dot{\boldsymbol{C}}^p = \dot{\lambda}\boldsymbol{f} \quad \Rightarrow \quad \dot{\boldsymbol{C}}^p = \dot{\lambda}\boldsymbol{f}(\boldsymbol{C}^p)^{-1}\boldsymbol{C}^p$$

and the incremental backward Euler exponential map becomes:

$$\boldsymbol{C}^p = exp\Big(\Delta\lambda\boldsymbol{f}(\boldsymbol{C}^p)^{-1}\Big)\boldsymbol{C}^{p\,n} \tag{3.89}$$

and after expanding in a series:

$$\boldsymbol{C}^p = \boldsymbol{C}^p(\boldsymbol{C}^{p\,n})^{-1}\boldsymbol{C}^p - \Delta\lambda\boldsymbol{f} - \frac{\Delta\lambda^2}{2!}\boldsymbol{f}(\boldsymbol{C}^p)^{-1}\boldsymbol{f} - \frac{\Delta\lambda^3}{3!}\boldsymbol{f}(\boldsymbol{C}^p)^{-1}\boldsymbol{f}(\boldsymbol{C}^p)^{-1}\boldsymbol{f} - ... \tag{3.90}$$

or,

$$\boldsymbol{R}^p = \boldsymbol{C}^p - \boldsymbol{C}^p(\boldsymbol{C}^{p\,n})^{-1}\boldsymbol{C}^p + \Delta\lambda\boldsymbol{f} - \frac{\Delta\lambda^2}{2!}\boldsymbol{f}(\boldsymbol{C}^p)^{-1}\boldsymbol{f} + \frac{\Delta\lambda^3}{3!}\boldsymbol{f}(\boldsymbol{C}^p)^{-1}\boldsymbol{f}\boldsymbol{C}^{p-1}\boldsymbol{f} + ... = 0 \tag{3.91}$$

Incremental version of the evolution equation for κ is derived using (3.62) as:

$$\kappa = \kappa^n + \sqrt{\frac{2}{3}}\Delta\lambda \tag{3.92}$$

and,

$$\boldsymbol{S} = \mu\boldsymbol{C}^{p^{-1}} + (\lambda \ln J - \mu)\boldsymbol{C}^{-1} \tag{3.93}$$

$$\Delta\lambda \geq 0 \quad ; \quad \Phi \leq 0 \quad ; \quad \Delta\lambda\Phi = 0 \tag{3.94}$$

3.5.7 Stress Update

The aim is to update the current stress in the frame given by the above equations. The total strain $\boldsymbol{C}$ is provided by the global Newton-Raphson procedure. Also the plastic strain $\boldsymbol{C}^{p\,n}$ and the equivalent plastic strain κ^n from the previous step t^n are known.
The solution will be carried out in two distinct steps as before.

Elastic Predictor. Plastic flow is frozen at t^n to yield a trial elastic state given by:

$$\boldsymbol{S}^{\text{trial}} = \mu(\boldsymbol{C}^{p\,n})^{-1} + (\lambda \ln J - \mu)\boldsymbol{C}^{-1} \tag{3.95}$$

$$\Phi^{\text{trial}} = \sqrt{tr[\boldsymbol{C}\boldsymbol{S}^{\text{trial}}\boldsymbol{C}\boldsymbol{S}^{\text{trial}}] - \frac{1}{3}tr^2[\boldsymbol{C}\boldsymbol{S}^{\text{trial}}]} - \sqrt{\frac{2}{3}}\sigma_Y^{\text{trial}} \tag{3.96}$$

$$\sigma_Y^{\text{trial}} = \sigma_0 + q(\kappa^n) \tag{3.97}$$

Note that, if the step is purely elastic $\Phi^{\text{trial}} \leq 0$, above equations completely define the stress state and no further action is necessary. However, if $\Phi^{\text{trial}} > 0$, this state is physically inadmissible and requires further correction.

Plastic Corrector. Because of the high non-linearity involved, it is not possible to derive an explicit expression like (3.69). However there are six equations given by (3.91), and the additional condition that $\Phi = 0$, i.e.,

$$\Phi = \sqrt{tr[\boldsymbol{C}\boldsymbol{S}\boldsymbol{C}\boldsymbol{S}] - \frac{1}{3}tr^2[\boldsymbol{C}\boldsymbol{S}]} - \sqrt{\frac{2}{3}}\sigma_Y = 0 \tag{3.98}$$

$$\sigma_Y = \sigma_0 + q(\kappa) \tag{3.99}$$

so that there are seven equations to solve the seven unknowns $\boldsymbol{C}^p$ and $\Delta\lambda$. Note that $\Delta\lambda$ will be found instead of κ as it appears in all equations and κ can be directly evaluated from (3.92) once $\Delta\lambda$ is known. Standard Newton-Raphson procedure for this system of equations reads:

$$\left[\begin{array}{c|c} \frac{\partial \boldsymbol{R}^p}{\partial \boldsymbol{C}^p} & \frac{\partial \boldsymbol{R}^p}{\partial \Delta\lambda} \\ \hline \frac{\partial \Phi}{\partial \boldsymbol{C}^p} & \frac{\partial \Phi}{\partial \Delta\lambda} \end{array}\right] \cdot \left\{\begin{array}{c} \delta\boldsymbol{C}_{p11} \\ \delta\boldsymbol{C}_{p22} \\ \delta\boldsymbol{C}_{p33} \\ 2\delta\boldsymbol{C}_{p12} \\ 2\delta\boldsymbol{C}_{p23} \\ 2\delta\boldsymbol{C}_{p31} \\ \hline \delta\Delta\lambda \end{array}\right\} = \left\{\begin{array}{c} -\boldsymbol{R}^p \\ \\ \\ \\ \\ \\ \hline -\Phi \end{array}\right\} \tag{3.100}$$

or,

$$\{R\}_{7\times1} + [dR]_{7\times7} \cdot \{\delta u\}_{7\times1} = 0 \tag{3.101}$$

The iteration process starts with initial values $\boldsymbol{C}^p = \boldsymbol{C}^{p\,n}$ and $\Delta\lambda = 0$. The matrix equation (3.100) is then solved for the unknowns $\delta\boldsymbol{C}^p$ and $\delta\Delta\lambda$. At the end of each k^{th} iteration, $\boldsymbol{C}^p$ and $\Delta\lambda$ are updated as:

$$\boldsymbol{C}^p_{k+1} = \boldsymbol{C}^p_k + \delta\boldsymbol{C}^p \quad , \quad \Delta\lambda_{k+1} = \Delta\lambda_k + \delta\Delta\lambda$$

until the norm of the 7×1 residual vector is below a specified tolerance value. The terms appearing in (3.100) are given as:

$$\frac{\partial \boldsymbol{R}^p}{\partial \Delta\lambda} = \boldsymbol{f} - \Delta\lambda \boldsymbol{f}\boldsymbol{C}^{p^{-1}}\boldsymbol{f} + \frac{\Delta\lambda^2}{2}\boldsymbol{f}\boldsymbol{C}^{p^{-1}}\boldsymbol{f}\boldsymbol{C}^{p^{-1}}\boldsymbol{f} + \frac{\Delta\lambda^3}{6}\boldsymbol{f}\boldsymbol{C}^{p^{-1}}\boldsymbol{f}\boldsymbol{C}^{p^{-1}}\boldsymbol{f}\boldsymbol{C}^{p^{-1}}\boldsymbol{f} \quad (3.102)$$

$$\frac{\partial \Phi}{\partial \Delta\lambda} = -\sqrt{\frac{2}{3}}\frac{\partial q}{\partial \kappa}\frac{\partial \kappa}{\partial \Delta\lambda} = -\frac{2}{3}H$$

$$\frac{\partial \Phi}{\partial \boldsymbol{C}^p} = \frac{\partial \|[\boldsymbol{C}\boldsymbol{S}]^{\mathrm{dev}}\|}{\partial \boldsymbol{C}^p} \quad (3.103)$$

$$\frac{\partial \boldsymbol{R}^p}{\partial \boldsymbol{C}^p} = \boldsymbol{\mathcal{I}} - \boldsymbol{\mathcal{B}} + \Delta\lambda \boldsymbol{f} - \frac{\Delta\lambda^2}{2}\boldsymbol{\mathcal{A}}_I + \frac{\Delta\lambda^3}{6}\boldsymbol{\mathcal{A}}_{II} + \frac{\Delta\lambda^4}{24}\boldsymbol{\mathcal{A}}_{III}\cdots \quad (3.104)$$

where,

$$\boldsymbol{\mathcal{B}} = \frac{\partial \boldsymbol{C}^p(\boldsymbol{C}^{p\,n})^{-1}\boldsymbol{C}^p}{\partial \boldsymbol{C}^p}\ ,\ \boldsymbol{\mathcal{A}}_I = \frac{\partial \boldsymbol{f}\boldsymbol{C}^{p^{-1}}\boldsymbol{f}}{\partial \boldsymbol{C}^p}$$

$$\boldsymbol{\mathcal{A}}_{II} = \frac{\partial \boldsymbol{f}\boldsymbol{C}^{p^{-1}}\boldsymbol{f}\boldsymbol{C}^{p^{-1}}\boldsymbol{f}}{\partial \boldsymbol{C}^p}\ ,\ \boldsymbol{\mathcal{A}}_{III} = \frac{\partial \boldsymbol{f}\boldsymbol{C}^{p^{-1}}\boldsymbol{f}\boldsymbol{C}^{p^{-1}}\boldsymbol{f}\boldsymbol{C}^{p^{-1}}\boldsymbol{f}}{\partial \boldsymbol{C}^p}$$

and so on... Derivatives of $\boldsymbol{S}$ with respect to $\boldsymbol{C}$ and $\boldsymbol{C}^p$ emerge from (3.93) as:

$$\frac{\partial \boldsymbol{S}}{\partial \boldsymbol{C}^p} = \mu \frac{\partial \boldsymbol{C}^{p^{-1}}}{\partial \boldsymbol{C}^p} \quad (3.105)$$

$$\frac{\partial \boldsymbol{S}}{\partial \boldsymbol{C}} = \frac{\lambda}{2}\boldsymbol{C}^{-2} - (\lambda \ln J - \mu)\frac{\partial \boldsymbol{C}^{-1}}{\partial \boldsymbol{C}} \quad (3.106)$$

3.5.8 Consistent Tangent Modulus

The consistent tangent modulus $\boldsymbol{\mathcal{C}}_{ep}$ for large strains, given as:

$$\boldsymbol{\mathcal{C}}_{ep} = \frac{\partial \boldsymbol{S}(\boldsymbol{C}, \boldsymbol{C}^p, \Delta\lambda)}{\partial \boldsymbol{C}} \quad (3.107)$$

needs to be computed for the global Newton-Raphson procedure. See Appendix A.3 for the derivation of the modulus.

Chapter 4

Small Strain Computational Homogenization

The class of *multi-scale* solid mechanics problems with which this work is concerned is characterized by a conventional equilibrium boundary value problem at the so-called *macroscopic scale*, where the constitutive response at each point of the macroscopic continuum is defined in a non-conventional way by homogenizing the response of a *Representative Volume Element* (RVE) that models the material micro-structure at that point (see Figure 4.1).

The RVE itself is modelled as a conventional (generally dissipative) continuum and

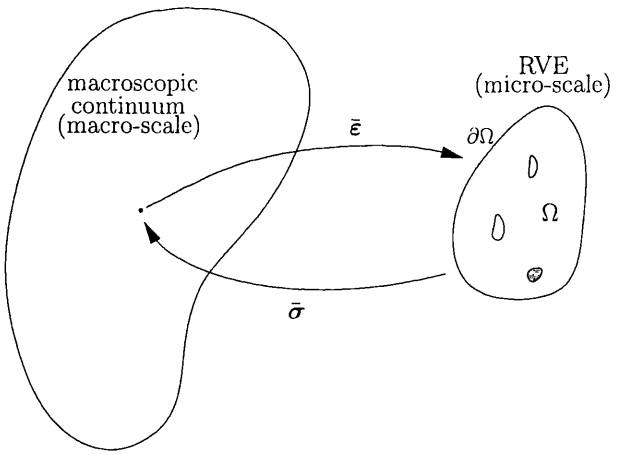

Figure 4.1: Macro-micro transition

the macroscopic stress and strain tensor are volume averages of their so-called *mi-*

croscopic counterparts over the RVE.

The kinematical variational foundation formulated by de Souza Neto and Feijóo [16] proposes a clearly structured axiomatic framework based on the following principles:

- equilibrium of the RVE,
- Hill-Mandel principle of macro-homogeneity [48, 69],
- volume averaging of stress and strain tensors, and,
- assumption that the space of kinematically admissible RVE displacement fluctuation fields is a subspace of the space of minimally constrained displacement fluctuations compatible with the strain averaging hypothesis.

One outcome of [16] is that, some commonly used classes of boundary conditions of the RVE, namely uniform displacements, uniform tractions and periodic displacements with anti-periodic tractions, are merely defined by the choice of the functional space of virtual displacements. The variational statement of Hill-Mandel principle of macro-homogeneity [48, 69] causes the body forces and surface tractions to be merely reactive to the prescribed RVE kinematical constraints (implicit in the choice of the functional space of virtual displacements). As a consequence, eg. the uniform boundary tractions are not prescribed (as in [76]), but are the natural response of a *minimally constrained* RVE.

In this Chapter, we will develop a theoretical and practical framework for the *multi-scale* or *micro-macro* analysis of solids for small strain problems. We will start by defining the boundary value problem at the macro scale. Then, we will develop the homogenization theory based on averaging of stress and strain tensors at micro scale –from which a family of kinematical constraints are derived–, complemented by the Hill-Mandel principle. Next, the time and space discrete models will be developed, where the kinematical constraint is imposed on the RVE boundary by a unified master-slave type approach, through displacement fluctuations. The most limiting boundary constraint is set by imposing zero fluctuations, resulting in linear deformations at the RVE boundary. The minimal constraint is set by the volume averaging, and yields uniform tractions at the RVE boundary. Periodic deformations at the RVE boundary are obtained by declaring equal fluctuations on mirror image pairs, where the boundary tractions are anti-periodic. The master-slave type dependencies are incorporated into a direct method (as by Michel *et al.* [75]) to solve the micro equilibrium problem efficiently, where the number of unknowns is minimalized. Alternatively, use of Lagrangian multipliers have been suggested by Miehe [77, 79]. The equilibrium state is used to compute the homogenized response of the RVE, which is then fully linearized and formulated in terms of these dependencies,

so that asymptotically quadratic convergence of the macro equilibrium problem is achieved.

Finally, two numerical examples are provided for verification of the framework for the areas of prospective application: single RVE homogenization and fully coupled two-scale analysis.

4.1 Macroscopic Boundary Value Problem

The macroscopic equilibrium problem consists in finding a kinematically admissible displacement field $\bar{\boldsymbol{u}} \in \bar{\mathscr{K}}$[1] such that

$$\int_{\bar{\Omega}} \bar{\boldsymbol{\sigma}} : \nabla \boldsymbol{\eta} \, d\bar{V} - \int_{\bar{\Omega}} \bar{\boldsymbol{b}} \cdot \boldsymbol{\eta} \, d\bar{V} - \int_{\partial\bar{\Omega}} \bar{\boldsymbol{t}} \cdot \boldsymbol{\eta} \, d\bar{A} = 0 \qquad \forall \boldsymbol{\eta} \in \bar{\mathscr{V}}, \tag{4.1}$$

where $\bar{\boldsymbol{\sigma}}$ is the macroscopic stress tensor, $\bar{\boldsymbol{b}}$ and $\bar{\boldsymbol{t}}$ are, respectively, the prescribed body force per unit volume, and the boundary tractions per unit area. The domain of the macroscopic continuum is denoted $\bar{\Omega}$ and $\bar{\mathscr{K}}$ and $\bar{\mathscr{V}}$ denote, respectively, the functional set of kinematically admissible displacements and the corresponding space of virtual displacements of the body in question. At any time t, the stress at each point $\bar{\boldsymbol{x}}$ of the macro-continuum is assumed to be delivered by a constitutive functional $\bar{\mathscr{G}}$ of the strain history $\bar{\boldsymbol{\varepsilon}}^t(\bar{\boldsymbol{x}})$ at that point up to time t:

$$\bar{\boldsymbol{\sigma}}(\bar{\boldsymbol{x}}, t) = \bar{\mathscr{G}}(\bar{\boldsymbol{\varepsilon}}^t(\bar{\boldsymbol{x}})) = \bar{\mathscr{G}}([\nabla_s \bar{\boldsymbol{u}}(\bar{\boldsymbol{x}})]^t), \tag{4.2}$$

so that the first term in (4.1) is a functional of the solution $\bar{\boldsymbol{u}}$:

$$\int_{\bar{\Omega}} \bar{\mathscr{G}}([\nabla_s \bar{\boldsymbol{u}}(\bar{\boldsymbol{x}})]^t) : \nabla \boldsymbol{\eta} \, dV. \tag{4.3}$$

In a conventional (single-scale) analysis, the constitutive response represented by (4.2) is typically described by internal variable-based dissipative theories, such as the elasto-plastic models outlined in Chapter 3, where the stress was obtained by integrating a set of ordinary differential equations in time for the given history of the strain tensor. Numerical approximations in time to problem (4.1) were obtained by using Euler-type difference schemes to integrate the constitutive equations of the model. Numerical schemes of this type result in an *incremental constitutive relation* such that, for a typical time interval $[t^n, t^{n+1}]$, with known set $\bar{\boldsymbol{\xi}}^n$ of internal variables at t^n, the stress $\bar{\boldsymbol{\sigma}}^{n+1}$ at t^{n+1} is a function of the strain tensor $\bar{\boldsymbol{\varepsilon}}^{n+1}$:

$$\bar{\boldsymbol{\sigma}}^{n+1} = \hat{\boldsymbol{\sigma}}(\bar{\boldsymbol{\varepsilon}}^{n+1}, \bar{\boldsymbol{\xi}}^n). \tag{4.4}$$

[1] The superimposed bar is used in this work to emphasize that the corresponding mathematical entities are associated with the macroscopic continuum.

The introduction of the incremental constitutive function (4.4) in (4.1) results in the incremental version of (4.1) which consists in finding an admissible displacement field $\bar{\boldsymbol{u}}^{n+1}$ such that

$$\int_{\bar{\Omega}} \hat{\boldsymbol{\sigma}}(\bar{\boldsymbol{\varepsilon}}^{n+1}, \boldsymbol{\xi}^n) : \nabla \boldsymbol{\eta} \, d\bar{V} - \int_{\bar{\Omega}} \bar{\boldsymbol{b}}^{n+1} \cdot \boldsymbol{\eta} \, d\bar{V} - \int_{\partial\bar{\Omega}} \bar{\boldsymbol{t}}^{n+1} \cdot \boldsymbol{\eta} \, d\bar{A} = 0 \qquad \forall \, \boldsymbol{\eta} \in \bar{\mathscr{V}}^{n+1}. \tag{4.5}$$

4.2 Coupling of Scales: Homogenization

Homogenization is defined as the mapping of a distribution of a microscopic quantity over the RVE into a macroscopic quantity. The relationship between microscopic and macroscopic domains is assumed to be based on homogenization of strain and stress tensors of the RVE, giving the *homogenized strain* and *homogenized stress.*

4.2.1 Homogenized Strain

The first basic assumption underlying the present multi-scale model states that the macroscopic strain tensor $\bar{\boldsymbol{\varepsilon}}$ at a point $\bar{\boldsymbol{x}}$ of the macro continuum is the *volume average* of the micro strain field $\boldsymbol{\varepsilon}$ of the RVE associated with $\bar{\boldsymbol{x}}$.

$$\bar{\boldsymbol{\varepsilon}} = \frac{1}{V} \int_{\Omega} \boldsymbol{\varepsilon} \, dV = \frac{1}{V} \int_{\Omega} \nabla_s \boldsymbol{u} dV. \tag{4.6}$$

The volume averaging of the micro strain, as given by (4.6) sets a constraint to the possible deformation fields of the RVE. This constraint can be expressed as $\boldsymbol{u} \in \mathscr{K}^*$, the *minimally constrained set of kinematically admissible microscopic displacements*:

$$\mathscr{K}^* \equiv \left\{ \boldsymbol{v}, \text{ sufficiently regular } \mid \int_{\Omega} \nabla_s \boldsymbol{v} dV = \bar{\boldsymbol{\varepsilon}} \, V \right\}. \tag{4.7}$$

The micro displacement field $\boldsymbol{u}$ can be assumed to be additively decomposed into a component that is prescribed by the homogenized strain $\bar{\boldsymbol{\varepsilon}}$ and varies linearly with $\boldsymbol{x}$, and a displacement fluctuation as:

$$\boldsymbol{u} = \boldsymbol{u}^* + \tilde{\boldsymbol{u}} = \bar{\boldsymbol{\varepsilon}} \boldsymbol{x} + \tilde{\boldsymbol{u}} \tag{4.8}$$

so that

$$\int_{\Omega} \nabla_s \boldsymbol{u}^* \, dV = \bar{\boldsymbol{\varepsilon}} \, V \tag{4.9}$$

Note that (4.7) can be equivalently expressed in terms of the unit normal $\boldsymbol{n}$ to the RVE boundary $\partial\Omega$ as:

$$\mathscr{K}^* \equiv \left\{ \boldsymbol{v}, \text{ sufficiently regular } \mid \int_{\partial\Omega} \boldsymbol{v} \otimes_s \boldsymbol{n} \, dA = \bar{\boldsymbol{\varepsilon}} \, V \right\} \tag{4.10}$$

where $\otimes_s$ denotes the symmetric tensor product. By combining (4.10) and (4.9), the constraint set is finalized as $\tilde{\boldsymbol{u}} \in \tilde{\mathscr{K}}^*$, where:

$$\tilde{\mathscr{K}}^* \equiv \left\{ \boldsymbol{v}, \text{ sufficiently regular } \mid \int_{\partial\Omega} \boldsymbol{v} \otimes_s \boldsymbol{n}\, dA = \boldsymbol{0} \right\} \tag{4.11}$$

Let the *actual* set of kinematically admissible RVE displacement fields be denoted by $\mathscr{K} \subset \mathscr{K}^*$. The space of *virtual* kinematically admissible displacements of the RVE are given as:

$$\mathscr{V} = \tilde{\mathscr{K}} \subset \tilde{\mathscr{K}}^* \tag{4.12}$$

The choice for the appropriate space of kinematically admissible displacements $\mathscr{V}$, which satisfies (4.11), defines the actual constraints imposed on the RVE. A family of such constraints is discussed below:

The minimum kinematical constraint is set by the most generic space that satisfies (4.11), such that

$$\mathscr{V}^{min} \equiv \tilde{\mathscr{K}}^*. \tag{4.13}$$

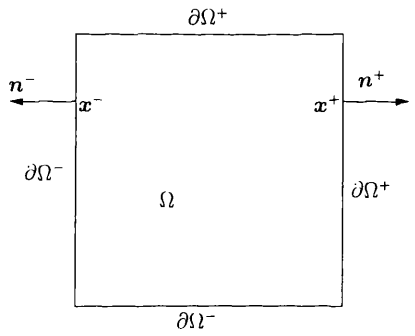

Figure 4.2: RVE with Periodic b.c.

Periodic deformations over the RVE boundary , referred to as the *periodic b.c.*, can be prescribed for materials with periodic micro-structure. The RVE needs to have certain symmetries, such that, repetition of the RVE generates the macro-structure. A two dimensional square RVE is depicted in Figure 4.2. For such RVE, the boundary is the sum of equally sized mirror image sets $\partial\Omega^+$ and $\partial\Omega^-$, with respective unit normals $\boldsymbol{n}^+$ and $\boldsymbol{n}^-$, such that $\{\boldsymbol{n}^+ = -\boldsymbol{n}^- \mid \forall \boldsymbol{x} \in \partial\Omega\}$. The periodic constraint space $\mathscr{V}^{per}$ can be defined as:

$$\mathscr{V}^{per} \equiv \left\{ \tilde{\boldsymbol{u}} \in \tilde{\mathscr{K}}^* \;\middle|\; \tilde{\boldsymbol{u}}(\boldsymbol{x}^+) = \tilde{\boldsymbol{u}}(\boldsymbol{x}^-) \quad \forall \text{ pairs} \{\boldsymbol{x}^+, \boldsymbol{x}^-\} \in \partial\Omega \right\} \tag{4.14}$$

It is important to note that, as pointed by Guedes and Kikuchi [37], the periodicity requirement is not necessarily global. That is, the whole macroscopic continuum does not consist of repetition of a single RVE. Instead, local periodicity is assumed, so that the RVE lies within an array of identical RVEs at its vicinity, where elsewhere on the macro continuum, there exist other RVEs which lie in arrays of identical RVEs. This allows better representation for variation of micro-structure over the macro continuum.

Linear deformations over the RVE boundary , referred to as the *linear b.c.*, assumes no fluctuations over the RVE boundary :

$$\mathcal{Y}^{lin} \equiv \left\{ \tilde{\boldsymbol{u}} \in \tilde{\mathscr{K}}^* \;\middle|\; \tilde{\boldsymbol{u}} = \boldsymbol{0} \quad \forall \boldsymbol{x} \in \partial\Omega \right\} \tag{4.15}$$

Prescribed deformations over the RVE assumes no fluctuations over the RVE. As all deformations over the RVE are prescribed, with no fluctuations, there is no micro boundary value problem to solve:

$$\mathcal{Y}^{pre} \equiv \left\{ \tilde{\boldsymbol{u}} \in \tilde{\mathscr{K}}^* \;\middle|\; \tilde{\boldsymbol{u}} = \boldsymbol{0} \quad \forall \boldsymbol{x} \in \Omega \right\} \tag{4.16}$$

Prescribed deformations over the RVE coincides with the so-called rule of mixtures, where the contribution of RVE constituents are multiplied with their volume ratios enter the response. As it fails to capture interactions between different phases or voids within the RVE, it is not going to be considered any further.

Note that the response of the constraint spaces defined above follow an order of increasing stiffness, as each set is the subset of the previous set:

$$\mathcal{Y}^{pre} \subset \mathcal{Y}^{lin} \subset \mathcal{Y}^{per} \subset \mathcal{Y}^{min} \tag{4.17}$$

4.2.2 Homogenized Stress

Analogous to the homogenized strain, the macro-stress tensor $\bar{\boldsymbol{\sigma}}$ at a point $\bar{\boldsymbol{x}}$ of the macro continuum is defined as the homogenization of the micro stress field $\boldsymbol{\sigma}$ of the RVE associated with $\bar{\boldsymbol{x}}$:

$$\bar{\boldsymbol{\sigma}} = \frac{1}{V} \int_{\Omega} \boldsymbol{\sigma} \, dV \tag{4.18}$$

The homogenized stress can be expressed in terms of the boundary traction $\boldsymbol{t}$

and body force $\boldsymbol{b}$, by use of the tensor relation:

$$\begin{aligned}\frac{1}{V}\int_\Omega \boldsymbol{\sigma} dV &= \frac{1}{V}\int_\Omega \boldsymbol{\sigma}\boldsymbol{I} dV \\ &= \frac{1}{V}\int_\Omega \boldsymbol{\sigma}(\nabla \boldsymbol{x})^T dV \\ &= \frac{1}{V}\Big(\int_{\partial\Omega}(\boldsymbol{\sigma}\boldsymbol{n})\otimes \boldsymbol{x}\, dA - \int_\Omega (\mathrm{div}\boldsymbol{\sigma})\otimes \boldsymbol{x} dV\Big) \end{aligned} \tag{4.19}$$

which, together with the strong form of equilibrium and the symmetry of the stress tensor, becomes:

$$\bar{\boldsymbol{\sigma}} = \frac{1}{V}\Big(\int_{\partial\Omega} \boldsymbol{t}\otimes_s \boldsymbol{x}\, dA - \int_\Omega \boldsymbol{b}\otimes_s \boldsymbol{x} dV\Big) \tag{4.20}$$

4.2.3 Hill-Mandel Principle

Another important aspect of homogenization is the Hill-Mandel principle of macro-homogeneity [48, 69], which states the macroscopic stress power to be equal to the volume average of the microscopic stress power for any kinematically admissible motion of the RVE, and is expressed as:

$$\bar{\boldsymbol{\sigma}} : \dot{\bar{\boldsymbol{\varepsilon}}} = \frac{1}{V}\int_\Omega \boldsymbol{\sigma} : \dot{\boldsymbol{\varepsilon}} dV \tag{4.21}$$

which leads to both the boundary traction $\boldsymbol{t}$ and the body force $\boldsymbol{b}$ being purely reactive to the chosen constraint. Note that, from (4.8),

$$\begin{aligned}\dot{\boldsymbol{\varepsilon}} &= \nabla_s \dot{\boldsymbol{u}} \\ &= \dot{\bar{\boldsymbol{\varepsilon}}} + \nabla_s \dot{\tilde{\boldsymbol{u}}} \quad \dot{\tilde{\boldsymbol{u}}} \in \mathscr{V} \end{aligned} \tag{4.22}$$

so that the right side of (4.21) becomes:

$$\begin{aligned}\frac{1}{V}\int_\Omega \boldsymbol{\sigma} : \dot{\boldsymbol{\varepsilon}} dV &= \frac{1}{V}\int_\Omega \boldsymbol{\sigma} : (\dot{\bar{\boldsymbol{\varepsilon}}} + \nabla_s \dot{\tilde{\boldsymbol{u}}}) dV \\ &= \bar{\boldsymbol{\sigma}} : \dot{\bar{\boldsymbol{\varepsilon}}} + \frac{1}{V}\int_\Omega \boldsymbol{\sigma} : \nabla_s \dot{\tilde{\boldsymbol{u}}} dV \end{aligned} \tag{4.23}$$

(4.21) is valid if and only if:

$$\frac{1}{V}\int_\Omega \boldsymbol{\sigma} : \nabla_s \dot{\tilde{\boldsymbol{u}}} dV = 0 \quad \forall \dot{\tilde{\boldsymbol{u}}} \in \mathscr{V} \tag{4.24}$$

which can be expressed in terms of strong equilibrium as:

$$\int_\Omega \boldsymbol{b}\cdot\dot{\tilde{\boldsymbol{u}}}\, dV + \int_{\partial\Omega} \boldsymbol{t}\cdot\dot{\tilde{\boldsymbol{u}}}\, dA = 0 \quad \forall \dot{\tilde{\boldsymbol{u}}} \in \mathscr{V}. \tag{4.25}$$

Since $\mathscr{V}$ is a vector space, (4.25) holds if and only if each of the integrals vanish,

$$\int_{\Omega} \boldsymbol{b} \cdot \boldsymbol{\eta} \, dV = 0 \quad \forall \boldsymbol{\eta} \in \mathscr{V} \tag{4.26}$$

$$\int_{\partial\Omega} \boldsymbol{t} \cdot \boldsymbol{\eta} \, dA = 0 \quad \forall \boldsymbol{\eta} \in \mathscr{V}, \tag{4.27}$$

so both the boundary traction $\boldsymbol{t}$ and the body force $\boldsymbol{b}$ are purely reactive to the chosen constraint, thus they can not be prescribed independently. Furthermore, they belong to the functional space orthogonal to $\mathscr{V}$, the *space of kinematically admissible displacements*, the choice of which imposes the constraint on the RVE. The implication of this on the family of chosen spaces is considered next:

The minimum kinematical constraint is given by $\mathscr{V}^{min}$ in (4.13), which is defined on the boundary of the RVE. Body forces can only be reactive to the constraint, thus have to be zero over the domain:

$$\boldsymbol{b}(\boldsymbol{x}) = \boldsymbol{0} \quad \forall \boldsymbol{x} \in \Omega \tag{4.28}$$

The boundary traction $\boldsymbol{t}$, also reactive to the constraint (4.13), can be shown to satisfy

$$\boldsymbol{t}(\boldsymbol{x}) = \boldsymbol{\sigma}(\boldsymbol{x})\boldsymbol{n}(\boldsymbol{x}) = \bar{\boldsymbol{\sigma}}\boldsymbol{n}(\boldsymbol{x}) \quad \forall \boldsymbol{x} \in \partial\Omega \tag{4.29}$$

We refer to de Souza Neto and Feijóo [16] for proof. The minimum kinematical constraint is also referred to as the *uniform traction b.c.*, only because of (4.29), as a consequence of the Hill-Mandel principle.

Periodic b.c. is given by $\mathscr{V}^{per}$ in (4.14), which is also defined on the boundary of the RVE. Thus, body forces should be zero over the domain:

$$\boldsymbol{b}(\boldsymbol{x}) = \boldsymbol{0} \quad \forall \boldsymbol{x} \in \Omega \tag{4.30}$$

(4.27) implies that $\boldsymbol{t}$ is *anti-periodic* on $\partial\Omega$, i.e.,

$$\boldsymbol{t}(\boldsymbol{x}^+) = -\boldsymbol{t}(\boldsymbol{x}^-) \quad \forall \,\text{pairs}\, \{\boldsymbol{x}^+, \boldsymbol{x}^-\} \in \partial\Omega \tag{4.31}$$

Linear b.c. is given by $\mathscr{V}^{lin}$ in (4.15), which is defined on the boundary of the RVE as well, so the body forces has to be zero over the domain:

$$\boldsymbol{b}(\boldsymbol{x}) = \boldsymbol{0} \quad \forall \boldsymbol{x} \in \Omega. \tag{4.32}$$

Boundary tractions are purely reactive to the constraint set by (4.15).

Remark 4.1 The body force orthogonal to the space defined by all three constraints considered is zero, so the homogenized stress (4.20) now becomes:

$$\bar{\boldsymbol{\sigma}} = \frac{1}{V} \int_{\partial\Omega} \boldsymbol{t} \otimes_s \boldsymbol{x} \, dA. \tag{4.33}$$

4.3 Microscopic Boundary Value Problem

The small strain boundary value problem for the micro-continuum consists in finding a kinematically admissible deformation $\boldsymbol{u} \in \mathscr{K}$ such that:

$$\int_\Omega \boldsymbol{\sigma} : \nabla_s \boldsymbol{\eta}\, dV - \int_\Omega \boldsymbol{b} \cdot \boldsymbol{\eta}\, dV - \int_{\partial\Omega} \boldsymbol{t} \cdot \boldsymbol{\eta}\, dA = 0 \;\; \forall \boldsymbol{\eta} \in \mathscr{V} \tag{4.34}$$

which is different from a conventional boundary value problem because of the constraint set on $\mathscr{K}$ and $\mathscr{V}$ by the homogenization process. The Hill-Mandel principle implies (from (4.26) and (4.27)) that (4.34) reduces to:

$$\int_\Omega \boldsymbol{\sigma} : \nabla_s \boldsymbol{\eta}\, dV = 0 \;\; \forall \boldsymbol{\eta} \in \mathscr{V}. \tag{4.35}$$

We also assume that at any time t, the stress at each point $\boldsymbol{x}$ of the RVE is delivered by a generic constitutive functional $\mathscr{G}$ of the strain history $\boldsymbol{\varepsilon}^t(\boldsymbol{x})$ at that point up to time t:

$$\boldsymbol{\sigma}(\boldsymbol{x}, t) = \mathscr{G}(\boldsymbol{\varepsilon}^t(\boldsymbol{x})). \tag{4.36}$$

This assumption, along with the equilibrium equation (4.35) defines the *RVE equilibrium problem* which consists in finding, for a given macroscopic strain $\bar{\boldsymbol{\varepsilon}}(t)$, a displacement fluctuation function $\tilde{\boldsymbol{u}} \in \mathscr{V}$ such that

$$\int_\Omega \mathscr{G}(\bar{\boldsymbol{\varepsilon}}(t) + \nabla_s \tilde{\boldsymbol{u}}(\boldsymbol{x}, t))|_t : \nabla_s \boldsymbol{\eta}\, dV = 0 \;\; \forall \boldsymbol{\eta} \in \mathscr{V}. \tag{4.37}$$

We assume that the constitutive behaviour at the micro level can be described by conventional internal variable-based dissipative constitutive theories, e.g. elasto-plasticity, whereby the stress tensor is obtained by integrating a set of ordinary differential equations in time for the given history of the strain tensor. Numerical approximations to the initial value problem defined by the constitutive equations of the model are typically obtained by Euler type difference schemes. For a typical time interval $[t^n, t^{n+1}]$, with known set $\boldsymbol{\xi}^n$ of internal variables, the stress $\boldsymbol{\sigma}^{n+1}$ is a function of the strain $\boldsymbol{\varepsilon}^{n+1}$. The incremental version of RVE equilibrium problem (4.35),

$$\int_\Omega \boldsymbol{\sigma}^{n+1}(\bar{\boldsymbol{\varepsilon}}^{n+1} + \nabla_s \tilde{\boldsymbol{u}}^{n+1}, \boldsymbol{\xi}^n) : \nabla_s \boldsymbol{\eta}\, dV = 0 \;\; \forall \boldsymbol{\eta} \in \mathscr{V}, \tag{4.38}$$

together with the incremental version of stress homogenization (4.18):

$$\bar{\boldsymbol{\sigma}}^{n+1} = \frac{1}{V_0} \int_\Omega \boldsymbol{\sigma}^{n+1}(\bar{\boldsymbol{\varepsilon}}^{n+1} + \nabla_s \tilde{\boldsymbol{u}}^{n+1}, \boldsymbol{\xi}^n)\, dV \tag{4.39}$$

complete the time-discrete model.

4.4 Finite Element Approximation

In this section, the small strain non-linear finite element approximation to the microscopic boundary value problem will be developed. The treatment of the macroscopic boundary value problem does not differ from a standard solid mechanics problem, so it is omitted here.

The fully (time- and space-) discrete multi-scale constitutive model is obtained by introducing a conventional finite element approximation to (4.38,4.39). That is, the infinite-dimensional functional space $\mathscr{V}$ is replaced with a finite-dimensional counterpart, ${}^{h}\mathscr{V}$, spanned by the finite element shape functions of a mesh h, and the domain Ω is replaced with an approximated counterpart ${}^{h}\Omega$ comprising an assembly of finite element domains. The corresponding fully discrete version of (4.38) consists in finding a vector $\tilde{\mathbf{u}}^{n+1} \in {}^{h}\mathscr{V}$ of global nodal displacements fluctuations such that

$$\int_{{}^{h}\Omega} \boldsymbol{\eta}^T \left[\mathbf{G}^T \boldsymbol{\sigma}^{n+1}(\bar{\boldsymbol{\varepsilon}}^{n+1} + \mathbf{G}\,\tilde{\mathbf{u}}^{n+1}, \boldsymbol{\xi}^n) \right] dV = 0 \ , \ \forall\, \boldsymbol{\eta} \in {}^{h}\mathscr{V}, \tag{4.40}$$

where $\mathbf{G}$ denotes the global discrete gradient matrix containing the appropriate shape function derivatives, $\boldsymbol{\sigma}^{n+1}$ is the incremental constitutive functional at the RVE level that delivers the array of stress components, $\bar{\boldsymbol{\varepsilon}}^{n+1}$ is the array of macroscopic strain components and $\boldsymbol{\eta}$ is the vector of global nodal virtual displacements.

Problem (4.40) together with the finite element-discrete version of (4.39) define the fully discretized small strain multi-scale constitutive model.

4.4.1 Boundary Condition

Problem (4.40) may differ from finite element versions of conventional solid mechanics problems of the type (4.5) only in the construction of the relevant finite-dimensional space ${}^{h}\mathscr{V}$. Note that the constraints embedded in space definitions (4.11) and (4.14) – and also (4.15) – involve only the boundary of the RVE. The constraints themselves are *linear dependencies* among the RVE boundary degrees of freedom. Hence, an arbitrary vector $\tilde{\mathbf{v}} \in {}^{h}\mathscr{V}$ can be conveniently arranged as

$$\tilde{\mathbf{v}} = \begin{Bmatrix} \tilde{\boldsymbol{u}}_f \\ \tilde{\boldsymbol{u}}_d \end{Bmatrix} \tag{4.41}$$

The linear dependence constraint requires that

$$\tilde{\boldsymbol{u}}_d = \boldsymbol{\alpha}\, \tilde{\boldsymbol{u}}_f, \tag{4.42}$$

where $\tilde{\boldsymbol{u}}_f$ and $\tilde{\boldsymbol{u}}_d$ contain the fluctuating part of the *free* and *dependent* degrees of freedom of the boundary respectively, and $\boldsymbol{\alpha}$ is a matrix of constraint coefficients expressing the linear dependencies that characterize the model in question.

Remark 4.2 The linear dependency given by (4.42) can be expressed in terms of displacements (instead of displacement fluctuations) with the help of (4.8):

$$\begin{aligned} \boldsymbol{u}_f &= \boldsymbol{u}_f^* + \tilde{\boldsymbol{u}}_f \\ \boldsymbol{u}_d &= \boldsymbol{u}_d^* + \tilde{\boldsymbol{u}}_d \\ &= \boldsymbol{u}_d^* + \boldsymbol{\alpha}(\boldsymbol{u}_f - \boldsymbol{u}_f^*) \\ &= (\boldsymbol{u}_d^* - \boldsymbol{\alpha}\boldsymbol{u}_f^*) + \boldsymbol{\alpha}\boldsymbol{u}_f \end{aligned} \tag{4.43}$$

Uniform Traction b.c. For the minimally constrained case, $\boldsymbol{\alpha}$ is obtained from:

$$\mathbb{C}\begin{Bmatrix} \tilde{\boldsymbol{u}}_f \\ \tilde{\boldsymbol{u}}_d \end{Bmatrix} = \mathbf{0}, \tag{4.44}$$

where $\mathbb{C}$ is the global matrix obtained from the discrete version of the integral constraint of definition (4.11). Note that this choice of constraint means there will be a maximum number of *free* degrees of freedom of the boundary corresponding to a minimum number of *dependent* ones.

In 2D, the minimum number of dependent boundary degrees of freedom is 3, one that corresponds to each component of the stress tensor. To eliminate rigid body motion, 3 degrees of freedom are prescribed by the macro strain. All remaining boundary degrees of freedom are treated as free and are masters of these 3 dependants, as shown in Figure 4.3(c). To obtain the dependency coefficient vectors $\boldsymbol{\alpha}$, (4.11) is expressed in the discrete sense as the sum of integrals evaluated at the boundary of each boundary element e^b:

$$\sum^{b} \int_{e^b} \tilde{\boldsymbol{u}} \otimes_s \boldsymbol{n}\, dS = \mathbf{0} \tag{4.45}$$

Note that $\tilde{\boldsymbol{u}}$ can be expressed in terms of interpolation functions N as:

$$\tilde{\boldsymbol{u}}(l) = \sum \tilde{\boldsymbol{u}}^q N^q(l), \tag{4.46}$$

where $\tilde{\boldsymbol{u}}^q = [\tilde{u}_1^q \quad \tilde{u}_2^q]^T$, so that the integral at the element boundary becomes:

$$\int_{e^b} \tilde{\boldsymbol{u}} \otimes_s \boldsymbol{n}\, dS = \begin{bmatrix} \int_{e^b} \sum \tilde{u}_1^q N^q n_1\, dS & 0 \\ 0 & \int_{e^b} \sum \tilde{u}_2^q N^q n_2\, dS \\ \frac{1}{2}\int_{e^b} \sum \tilde{u}_1^q N^q n_2\, dS & \frac{1}{2}\int_{e^b} \sum \tilde{u}_2^i N^q n_1\, dS \end{bmatrix}.$$

The integral above has contributions from each boundary node within the element. The contribution of node q takes the form of a coefficient matrix $\mathbb{C}^q$, which multiplies

the nodal displacement fluctuation vector $\tilde{\boldsymbol{u}}^q$. For the present case, $\mathbb{C}^q$ takes the form:

$$\mathbb{C}^q = \begin{bmatrix} a^q & 0 \\ 0 & b^q \\ \frac{b^q}{2} & \frac{a^q}{2} \end{bmatrix}, \tag{4.47}$$

where,

$$a^q = \int_{e^b} N^q n_1 \, dS \quad , \quad b^q = \int_{e^b} N^q n_2 \, dS.$$

Note that this integration can be performed numerically at a high accuracy by choosing appropriate number of Gauss points on the element boundary. After adding contributions to $\mathbb{C}^q$ from all elements that share node q, the sum given in (4.45) is expressed as the product of the global coefficient matrix $\mathbb{C}^b$ and the vector of fluctuating displacements as:

$$\begin{aligned} \mathbb{C}^b_{(3\times bdof)} . \tilde{u}^b_{(bdof)} &= \mathbf{0}_{(3)} \\ \mathbb{C}^f_{(3\times mdof)} . \tilde{u}^f_{(mdof)} + \mathbb{C}^d_{(3\times 3)} . \tilde{u}^d_{(3)} &= \mathbf{0}_{(3)} \\ \tilde{u}^d_{(3)} = \mathbb{R}_{(3\times mdof)} \tilde{u}^f_{(mdof)}, \qquad \mathbb{R} &= -(\mathbb{C}^d)^{-1}\mathbb{C}^f, \end{aligned} \tag{4.48}$$

where *bdof* and *mdof* denote the number of boundary and master degrees of freedom respectively. Note that each one of the three rows of $\mathbb{R}$ is a vector of dependency coefficients $\boldsymbol{\alpha}$, so that the dependency can be expressed as in (4.43). The prescribed degrees of freedom do not appear in the formulation above, as they do not have fluctuating components. The selection of dependent degrees of freedom is not trivial, distinct nodes should be assigned to guarantee that $\mathbb{C}^d$ is invertible. There is no shape limitation for the RVE for the uniform traction b.c.

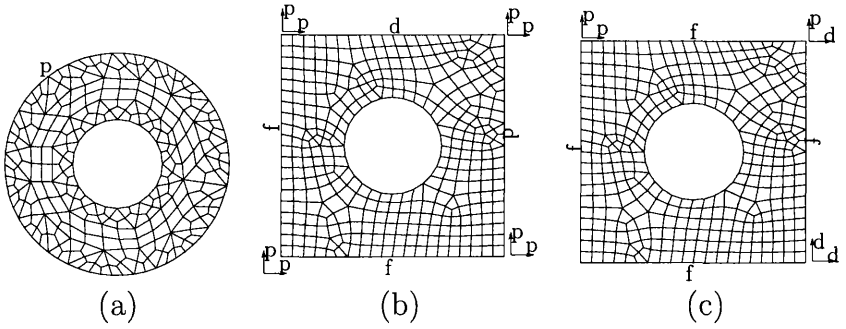

Figure 4.3: The choice of boundary condition specifies whether a boundary degree of freedom is free (*f*), prescribed (*p*) or dependent (*d*) on other degree(s) of freedom. Arrangement of nodes for 2-D RVE for small strains: (a) Linear b.c., (b) Periodic b.c., and (c) Uniform Traction b.c.

Periodic b.c. For a periodic fluctuations model with pairing boundary nodes located at pairing points $\boldsymbol{x}^+$ and $\boldsymbol{x}^-$ lying on opposite sides of $\partial^h\Omega$, $\boldsymbol{\alpha}$ is an identity matrix, so that there is a one-to-one correspondence between master and dependent degrees of freedom. As a result of periodicity, all degrees of freedom at corner nodes are prescribed by the macro strain, as shown on the 2-D square RVE of Figure 4.3 (b).

We treat the case of non-paired boundary nodes as a geometrical dependency, which is imposed by a finite element type interpolation of master degrees of freedom. We will exploit this approach further in Chapter 6 to improve the computational efficiency.

Linear b.c. For the linear boundary displacements constraint, the solution of the finite element RVE problem follows the same route as conventional solid mechanics problems, as the construction of space ${}^h\mathscr{V}$ is trivial and, according to (4.15), requires only that all fluctuating nodal degrees of freedom of the RVE boundary be fixed as zero, which follows from (4.8), that all RVE boundary degrees of freedom are solely prescribed by the macroscopic strain:

$$\boldsymbol{u}_b = \boldsymbol{u}_p \tag{4.49}$$

Note that, as depicted in Figure 4.3(a), there is no shape limitation for the RVE for the linear boundary displacements constraint.

4.4.2 Prescribed Displacements

The prescription of the macro strain $\bar{\boldsymbol{\varepsilon}}$ is performed in discrete terms as:

$$\boldsymbol{u}_q^* = \boldsymbol{x}_q\bar{\boldsymbol{\varepsilon}} \equiv^h \mathbb{D}_q^T\bar{\boldsymbol{\varepsilon}} \tag{4.50}$$

at each node q. For 2D:

$$\begin{aligned} \bar{\boldsymbol{\varepsilon}} &= \{\bar{\varepsilon}_{11}\ \bar{\varepsilon}_{22}\ 2\bar{\varepsilon}_{12}\}^T \\ \boldsymbol{u}_q &= \{u_1\ u_2\}^T \\ \mathbb{D}_q &= \begin{bmatrix} x_1 & 0 \\ 0 & x_2 \\ \frac{x_2}{2} & \frac{x_1}{2} \end{bmatrix} \end{aligned} \tag{4.51}$$

and for 3D:

$$\begin{aligned} \bar{\boldsymbol{\varepsilon}} &= \{\bar{\varepsilon}_{11}\ \bar{\varepsilon}_{22}\ \bar{\varepsilon}_{33}\ 2\bar{\varepsilon}_{12}\ 2\bar{\varepsilon}_{23}\ 2\bar{\varepsilon}_{31}\}^T \\ \boldsymbol{u}_q &= \{u_1\ u_2\ u_3\}^T \\ \mathbb{D}_q &= \begin{bmatrix} x_1 & 0 & 0 \\ 0 & x_2 & 0 \\ 0 & 0 & x_3 \\ \frac{x_2}{2} & \frac{x_1}{2} & 0 \\ 0 & \frac{x_3}{2} & \frac{x_2}{2} \\ \frac{x_3}{2} & 0 & \frac{x_1}{2} \end{bmatrix} \end{aligned} \tag{4.52}$$

the matrix notations of Miehe [79] are adopted. $\mathbb{D}_q$ is defined as the nodal coordinate matrix.

4.4.3 Problem Statement

We aim to find the unknown set of inner ($\boldsymbol{u}_i$) and free boundary displacements ($\boldsymbol{u}_f$), as a response to the set of prescribed displacements ($\boldsymbol{u}^*$), that satisfy the equilibrium and the kinematical constraint The final reduced set of non-linear algebraic finite element equations to be solved is obtained by introducing representation (4.41,4.42) for $\boldsymbol{\eta}$ and $\tilde{\mathbf{u}}^{n+1}$ in (4.40). After straightforward matrix manipulations, this gives

$$\begin{Bmatrix} \mathbf{g}_i \\ \mathbf{g}_f + \boldsymbol{\alpha}^T \mathbf{g}_d \end{Bmatrix} = \begin{Bmatrix} \mathbf{0} \\ \mathbf{0} \end{Bmatrix}, \tag{4.53}$$

where $\mathbf{g}_i$, $\mathbf{g}_f$ and $\mathbf{g}_d$ are the components of the global vector

$$\mathbf{g} \equiv \int_{h\Omega} \mathbf{G}^T \boldsymbol{\sigma}^{n+1}(\bar{\boldsymbol{\varepsilon}}^{n+1} + \mathbf{G}\,\tilde{\mathbf{u}}^{n+1}, \boldsymbol{\xi}^n) dV \tag{4.54}$$

associated, respectively, with the internal, master and dependent degrees of freedom of the RVE.

4.4.4 Solution Procedure

The Newton-Raphson iterative scheme is used to solve the system $\mathbf{g} = \mathbf{0}$, whereby, given a solution estimate, the k^{th} guess $\tilde{\mathbf{u}}^{(k)}$ for $\tilde{\mathbf{u}}^{n+1}$ is found by establishing the linear approximation:

$$\mathbf{g}(\boldsymbol{u}^{(k)}) \approx \mathbf{g}(\boldsymbol{u}^{(k-1)}) + D\mathbf{g}(\boldsymbol{u}^{(k-1)})[\delta\boldsymbol{u}] = \mathbf{0} \tag{4.55}$$

where the directional derivative is evaluated as

$$D\mathbf{g}(\boldsymbol{u}^{(k-1)})[\delta\boldsymbol{u}] = \left.\frac{\partial \mathbf{g}}{\partial \boldsymbol{u}}\right|^{(k-1)} \delta\boldsymbol{u} \tag{4.56}$$

so that at each iteration the system

$$\left.\frac{\partial \mathbf{g}}{\partial \boldsymbol{u}}\right|^{(k-1)} \delta \boldsymbol{u} = -\mathbf{g}(\boldsymbol{u}^{(k-1)}) \tag{4.57}$$

or,

$$\begin{bmatrix} \mathbf{k}_{ii} & \mathbf{k}_{if} + \mathbf{k}_{id}\boldsymbol{\alpha} \\ \mathbf{k}_{fi} + \boldsymbol{\alpha}^T\mathbf{k}_{di} & \mathbf{k}_{mm} + \mathbf{k}_{fd}\boldsymbol{\alpha} + \boldsymbol{\alpha}^T\mathbf{k}_{df} + \boldsymbol{\alpha}^T\mathbf{k}_{dd}\boldsymbol{\alpha} \end{bmatrix}^{(k-1)} \begin{Bmatrix} \delta\mathbf{u}_i \\ \delta\mathbf{u}_f \end{Bmatrix} = - \begin{Bmatrix} \mathbf{g}_i \\ \mathbf{g}_f + \boldsymbol{\alpha}^T\mathbf{g}_d \end{Bmatrix}^{(k-1)} \tag{4.58}$$

is solved for the iterative corrections $\delta\mathbf{u}_i$ and $\delta\mathbf{u}_f$, and then

$$\begin{Bmatrix} \mathbf{u}_i \\ \mathbf{u}_f \end{Bmatrix}^{(k)} = \begin{Bmatrix} \mathbf{u}_i \\ \mathbf{u}_f \end{Bmatrix}^{(k-1)} + \begin{Bmatrix} \delta\mathbf{u}_i \\ \delta\mathbf{u}_f \end{Bmatrix} \tag{4.59}$$

where $\mathbf{k}_{ii}^{(k-1)}, \mathbf{k}_{if}^{(k-1)}, \cdots, \mathbf{k}_{dd}^{(k-1)}$ etc. are corresponding sub-matrices of the tangent stiffness matrix, e.g.

$$\mathbf{k}_{im} \equiv \frac{\partial \mathbf{g}_i}{\partial \mathbf{u}_f} \tag{4.60}$$

The process is repeated until for some k, the convergence criterion:

$$\|\mathbf{g}\| \leq \epsilon \tag{4.61}$$

is satisfied for a given convergence tolerance ϵ.

4.4.5 Homogenized Stress

The homogenized stress (4.33) can be expressed in the discrete setting as an assembly of integrals performed at element level:

$$\bar{\boldsymbol{\sigma}}^h = \frac{1}{V} \sum \int_e \boldsymbol{\sigma} dV \tag{4.62}$$

where the integration is performed numerically in a standard manner. An alternative expression in terms of nodal forces $\mathbb{F}_b$ at the boundary has been pointed by Miehe *et al.*[77], by considering the limit $\boldsymbol{t}\, dA \rightarrow \mathbb{F}_b$ as:

$$\bar{\boldsymbol{\sigma}}^h = \frac{1}{V} \mathbb{D}_b \mathbb{F}_b \tag{4.63}$$

where the boundary coordinate matrix, $\mathbb{D}_b$ is defined as the collection of all nodal coordinate matrices $\mathbb{D}_q$, such that, for M nodes on the boundary:

$$\mathbb{D}_b = \begin{bmatrix} \mathbb{D}_1 & \mathbb{D}_2 & \dots & \mathbb{D}_M \end{bmatrix} \tag{4.64}$$

Even though (4.62) and (4.63) are equivalent, the latter is computationally more efficient.

4.4.6 Tangent Modulus

The macroscopic boundary value problem (4.1) or its incremental version (4.5) is typically solved with an iterative scheme. The Newton-Raphson method is commonly employed, which relies on exact linearization of a global discrete residual vector within a finite element framework, which is dependent on the homogenized stress. This dependency requires linearization of the homogenized stress for each iteration. This can be achieved by either linearizing (4.33), and then discretizing the result, or by linearizing the discretized homogenized stress (4.62) or (4.63). We proceed with linearizing the latter discrete expression:

$$\begin{aligned}\frac{\partial \bar{\boldsymbol{\sigma}}^h}{\partial \bar{\boldsymbol{\varepsilon}}} &= \frac{1}{V}\mathbb{D}_b \frac{\partial \mathbb{F}_b}{\partial \bar{\boldsymbol{\varepsilon}}} \\ &= \frac{1}{V}\mathbb{D}_b \left(\frac{\partial \mathbb{F}_b}{\partial \boldsymbol{u}_i}\frac{\partial \boldsymbol{u}_i}{\partial \bar{\boldsymbol{\varepsilon}}} + \frac{\partial \mathbb{F}_b}{\partial \boldsymbol{u}_f}\frac{\partial \boldsymbol{u}_f}{\partial \bar{\boldsymbol{\varepsilon}}} + \frac{\partial \mathbb{F}_b}{\partial \boldsymbol{u}_d}\frac{\partial \boldsymbol{u}_d}{\partial \bar{\boldsymbol{\varepsilon}}} + \frac{\partial \mathbb{F}_b}{\partial \boldsymbol{u}_p}\frac{\partial \boldsymbol{u}_p}{\partial \bar{\boldsymbol{\varepsilon}}} \right). \end{aligned} \tag{4.65}$$

It follows from (4.43) and (4.50) that :

$$\frac{\partial \boldsymbol{u}_f}{\partial \bar{\boldsymbol{\varepsilon}}} = \mathbb{D}_f^T + \partial_{\bar{\boldsymbol{\varepsilon}}}\tilde{\boldsymbol{u}}_f, \qquad \frac{\partial \boldsymbol{u}_d}{\partial \bar{\boldsymbol{\varepsilon}}} = \mathbb{D}_d^T + \boldsymbol{\alpha}\partial_{\bar{\boldsymbol{\varepsilon}}}\tilde{\boldsymbol{u}}_f, \qquad \frac{\partial \boldsymbol{u}_p}{\partial \bar{\boldsymbol{\varepsilon}}} = \mathbb{D}_p^T,$$

where $\partial_{\bar{\boldsymbol{\varepsilon}}}\tilde{\boldsymbol{u}}_f = \frac{\partial \tilde{\boldsymbol{u}}_f}{\partial \bar{\boldsymbol{\varepsilon}}}$. Denoting $\frac{\partial \mathbb{F}_b}{\partial \boldsymbol{u}_i} = \mathbf{k}_{bi}$ etc., (4.65) becomes

$$\begin{aligned}\frac{\partial \bar{\boldsymbol{\sigma}}^h}{\partial \bar{\boldsymbol{\varepsilon}}} &= \frac{1}{V}\mathbb{D}_b \Big(\mathbf{k}_{bi}\partial_{\bar{\boldsymbol{\varepsilon}}}\boldsymbol{u}_i + \mathbf{k}_{bf}(\mathbb{D}_f^T + \partial_{\bar{\boldsymbol{\varepsilon}}}\tilde{\boldsymbol{u}}_f) \\ &\quad + \mathbf{k}_{bd}(\mathbb{D}_d^T + \boldsymbol{\alpha}\partial_{\bar{\boldsymbol{\varepsilon}}}\tilde{\boldsymbol{u}}_f) + \mathbf{k}_{bp}\mathbb{D}_p^T \Big) \\ &= \frac{1}{V}\mathbb{D}_b \left(\begin{bmatrix} \mathbf{k}_{bi} \\ \mathbf{k}_{bf} + \boldsymbol{\alpha}\mathbf{k}_{bd} \end{bmatrix}^T \begin{bmatrix} \partial_{\bar{\boldsymbol{\varepsilon}}}\boldsymbol{u}_i \\ \partial_{\bar{\boldsymbol{\varepsilon}}}\tilde{\boldsymbol{u}}_f \end{bmatrix} + \mathbf{k}_{bb}\mathbb{D}_b^T \right) \end{aligned} \tag{4.66}$$

Assembly of stiffness terms $\mathbf{k}_{bi}$, $\mathbf{k}_{bf} + \boldsymbol{\alpha}\mathbf{k}_{bd}$ and $\mathbf{k}_{bb}$ is straightforward. To calculate the unknown set $[\partial_{\bar{\boldsymbol{\varepsilon}}}\boldsymbol{u}_i, \partial_{\bar{\boldsymbol{\varepsilon}}}\tilde{\boldsymbol{u}}_f]$, note that $\mathbb{F}_i = \mathbf{0}$:

$$\begin{aligned}\frac{\partial \mathbb{F}_i}{\partial \bar{\boldsymbol{\varepsilon}}} &= \frac{\partial \mathbb{F}_i}{\partial \boldsymbol{u}_i}\frac{\partial \boldsymbol{u}_i}{\partial \bar{\boldsymbol{\varepsilon}}} + \frac{\partial \mathbb{F}_i}{\partial \boldsymbol{u}_f}\frac{\partial \boldsymbol{u}_f}{\partial \bar{\boldsymbol{\varepsilon}}} + \frac{\partial \mathbb{F}_i}{\partial \boldsymbol{u}_d}\frac{\partial \boldsymbol{u}_d}{\partial \bar{\boldsymbol{\varepsilon}}} + \frac{\partial \mathbb{F}_i}{\partial \boldsymbol{u}_p}\frac{\partial \boldsymbol{u}_p}{\partial \bar{\boldsymbol{\varepsilon}}} = \mathbf{0} \\ &= \mathbf{k}_{ii}\partial_{\bar{\boldsymbol{\varepsilon}}}\boldsymbol{u}_i + \mathbf{k}_{if}(\mathbb{D}_f^T + \partial_{\bar{\boldsymbol{\varepsilon}}}\tilde{\boldsymbol{u}}_f) + \mathbf{k}_{id}(\mathbb{D}_d^T + \boldsymbol{\alpha}\partial_{\bar{\boldsymbol{\varepsilon}}}\tilde{\boldsymbol{u}}_f) + \mathbf{k}_{ip}\mathbb{D}_p^T = \mathbf{0} \\ &= \begin{bmatrix} \mathbf{k}_{ii} \\ \mathbf{k}_{if} + \boldsymbol{\alpha}\mathbf{k}_{id} \end{bmatrix}^T \begin{bmatrix} \partial_{\bar{\boldsymbol{\varepsilon}}}\boldsymbol{u}_i \\ \partial_{\bar{\boldsymbol{\varepsilon}}}\tilde{\boldsymbol{u}}_f \end{bmatrix} + \mathbf{k}_{ib}\mathbb{D}_b^T = \mathbf{0} \end{aligned} \tag{4.67}$$

The first term on the left hand side of (4.67) is readily available as the upper portion of the global stiffness matrix of the converged solution, given by (4.58). By setting each column of $-\mathbf{k}_{ib}\mathbb{D}_b^T$ as the residual and solving the existing global Newton-Raphson system returns the corresponding column of the unknown set $\{\partial_{\bar{\boldsymbol{\varepsilon}}}\boldsymbol{u}_i, \partial_{\bar{\boldsymbol{\varepsilon}}}\tilde{\boldsymbol{u}}_f\}$ in (4.66).

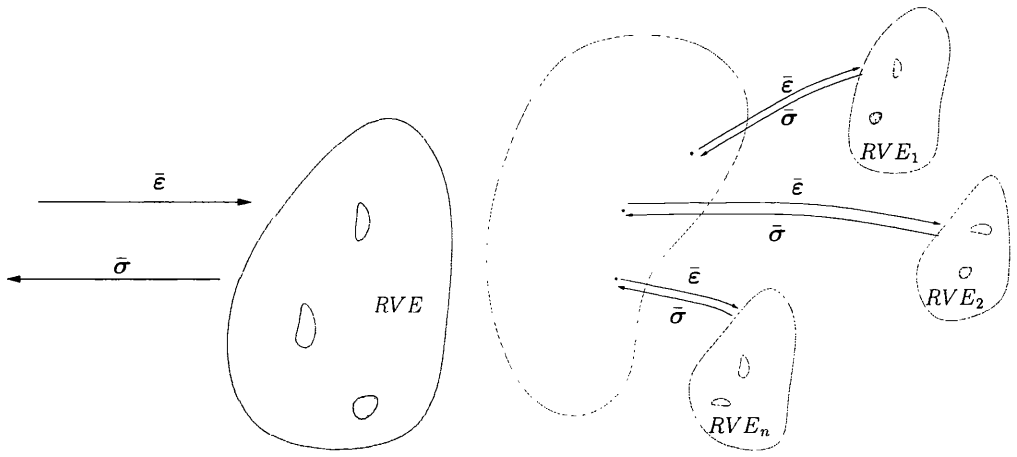

Figure 4.4: Small Strain Computer Implementation : (left) Single-Scale RVE Homogenization (right) Multi-Scale Fully Coupled Analysis

4.5 Computer Implementation

The finite element framework developed in the previous section comprises the choice of boundary condition, prescription of the macro strain, the solution algorithm, stress and consistent tangent modulus update. This model can be employed in two main contexts:

- The determination of the parameters of a canonical macroscopic constitutive model by fitting the data produced by finite element solutions of a single RVE under prescribed macroscopic strain histories, as shown in Figure 4.4 (left) (see, for instance, [37, 82, 75, 90, 34, 106]), which we refer to as *Single-Scale RVE Homogenization*,
- *Fully Coupled Two-Scale Analysis* of solids, where the macroscopic equilibrium problem is solved simultaneously with one RVE equilibrium problem for each Gauss quadrature point of the macroscopic mesh [102, 28, 78, 116]. In this case, the stress updating procedure used at each Gauss quadrature point of the macro-mesh involves the solution of an initial boundary value problem for the corresponding RVE, see Figure 4.4 (right).

4.5.1 Single-Scale RVE Homogenization

The procedure for single-scale RVE homogenization is outlined as follows:

1. Initially, depending on the choice of kinematical constraint:

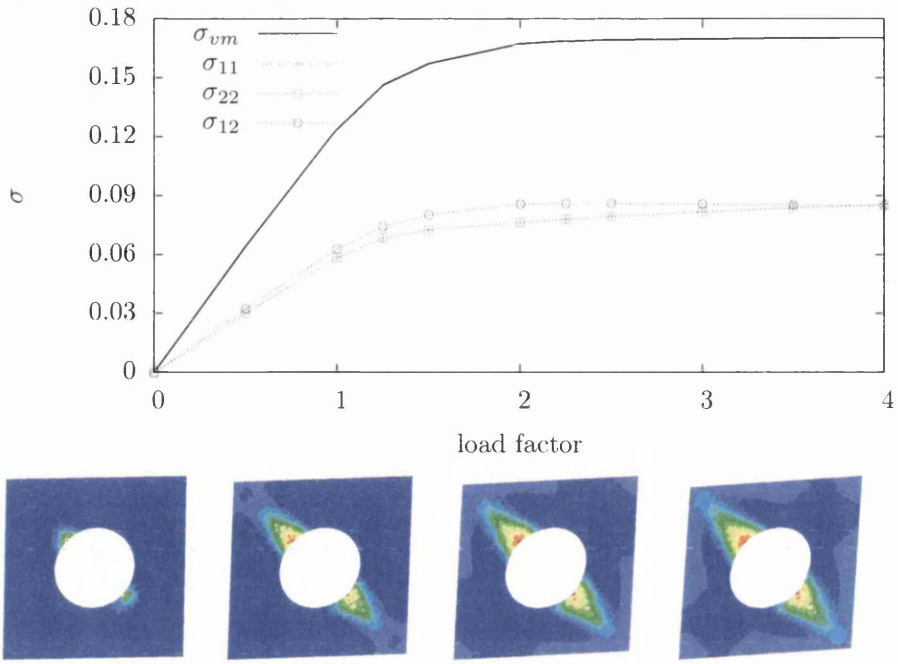

Figure 4.5: Single-Scale RVE Homogenization : Linear b.c., components of stress, development of plastic strains on deformed mesh

(a) group boundary degrees of freedom into f, p or d (see Section 4.4.1).

(b) calculate dependency coefficients $\boldsymbol{\alpha}$ (see Section 4.4.1).

2. At a typical time interval $[t^n, t^{n+1}]$, with known set $\boldsymbol{\xi}^n$ of internal variables, solve the incremental microscopic boundary value problem:

   (a) input prescribed strain multiplied by the load factor $\bar{\boldsymbol{\varepsilon}}^{n+1}$

   (b) apply prescribed displacements, using (4.50)

   (c) solve the system of equations (4.53) using a Newton-Raphson procedure

   (d) update dependent degrees of freedom,$\boldsymbol{u}_d$, by (4.43)

3. Calculate and return homogenized stress with (4.63)

To illustrate and verify the computational framework for single scale RVE homogenization, we consider an example from Partovi [89], whereby a square RVE with a circular void at its center is investigated. The size of the void corresponds to 15% of the RVE area.

Plane stress condition is assumed and the RVE matrix material is modelled by a von Mises type elastoplastic law with Young's modulus $E = 70$ GPa, Poisson's ratio

$\nu = 0.2$, initial yield stress $\sigma_0 = 243$ MPa and linear hardening modulus $H = 0.2$ GPa.

The RVE is loaded by a prescribed strain $\{\bar{\varepsilon}_{11}, \bar{\varepsilon}_{22}, 2\bar{\varepsilon}_{12}\} = \{0.001, 0.001, 0.0034\}$, multiplied by a loading factor that is increased up to 4. The RVE boundary value problem is solved, and homogenized stress $\bar{\boldsymbol{\sigma}}$ is calculated. The effective von Mises stress, given by

$$\bar{\sigma}_{vm} = \sqrt{\frac{3}{2}\bar{\boldsymbol{\sigma}}_{dev} : \bar{\boldsymbol{\sigma}}_{dev}} \tag{4.68}$$

is plotted, along with components of the homogenized stress in Figures 4.5 and 4.6 for linear, periodic and uniform traction b.c.'s respectively. Development of equivalent plastic strain during the loading path is plotted on deformed mesh (exaggerated for visualization).

For all three cases, we observe perfect agreement with the reference work [89].

4.5.2 Two-Scale Fully Coupled Analysis

The two-scale fully coupled analysis procedure follows as:

1. Initially, depending on the choice of kinematical constraint:
   (a) group boundary degrees of freedom into f, p or d (see Section 4.4.1).
   (b) calculate dependency coefficients $\boldsymbol{\alpha}$ (see Section 4.4.1).
2. At a typical time interval $[t^n, t^{n+1}]$, solve the incremental macroscopic boundary value problem. At a typical iteration step of the macro Newton-Raphson procedure, at every Gauss point, with known set $\boldsymbol{\xi}^n$ of internal variables of the RVE associated with that Gauss point,
   (a) solve the incremental microscopic boundary value problem:
      i. calculate prescribed strain (multiplied by the load factor) $\bar{\boldsymbol{\varepsilon}}^{n+1}$
      ii. apply prescribed displacements using (4.50)
      iii. solve the system of equations (4.53) using a Newton-Raphson procedure
      iv. update dependent degrees of freedom,$\boldsymbol{u}_d$, by (4.43)
   (b) Calculate homogenized stress with (4.63)
   (c) Calculate consistent tangent with (4.66)

We will use the plane strain localization example given in Kouznetsova's PhD thesis [57], to compare and verify the methodology developed for fully coupled analysis. A regularly perforated (with a strip of homogeneous material at edges) rectangular

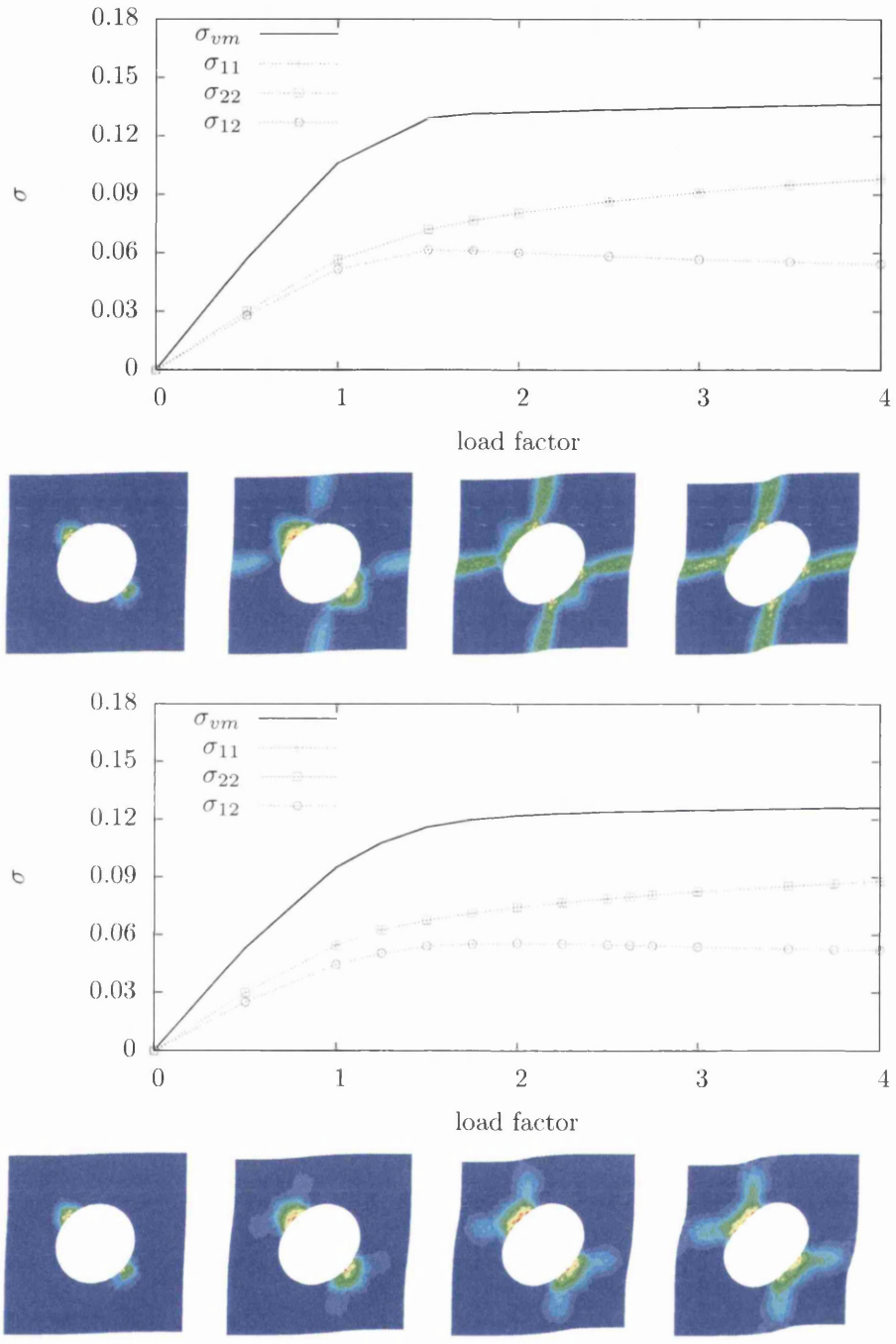

Figure 4.6: Single-Scale RVE Homogenization : components of stress, development of plastic strains on deformed mesh (top) Periodic b.c (bottom) Uniform Traction b.c .

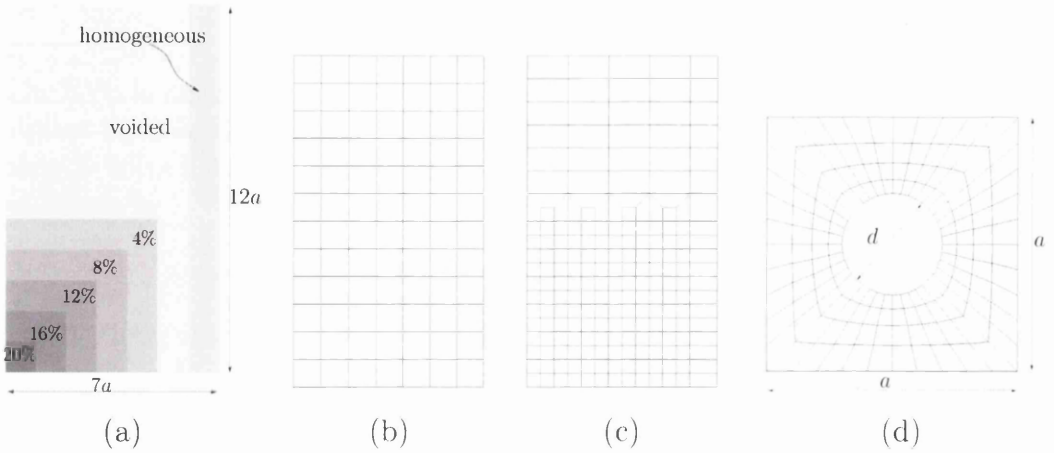

Figure 4.7: Multi-Scale Fully Coupled Analysis: (a) Initial geometry, percentages represent reduction in yield stress (b) coarse macroscopic mesh (c) fine macroscopic mesh (d) typical RVE, mesh and geometry

macroscopic structure is considered. Due to symmetry of geometry and loading, only a quarter, sized $7a$ by $12a$ (the stacking distance of the void pattern, $a = 10\,\mu$m) is modelled using a coarse mesh with 84 elements and a fine mesh with 203 elements as shown in Figure 4.7 (b) and (c) respectively, both models are integrated using standard Gauss quadrature.

All RVEs corresponding to each of those integration points have a pore of diameter $d = 0.4a$, corresponding to approximately 12.5% volume ratio, modelled initially with the same $a \times a$ square geometry as defined in Figure 4.7(d), where 160 4-noded quadrilateral elements with 4 integration points are employed and plane strain condition is assumed. Note that, unlike second order approaches such as that of the reference work [57], the absolute size of the RVE is irrelevant for the homogenization procedure in hand. Because of the well known poor performance of standard elements, F-Bar type elements [15] are used to avoid volumetric locking.

RVE material is modelled by a von Mises type perfectly plastic elastoplastic law with Young's modulus $E = 210$ GPa, Poisson's ratio $\nu = 0.3$, initial yield stress $\sigma_0 = 507$ MPa. To avoid numerical problems a very small linear hardening modulus $H = 0.0001$ is used. To trigger localization, yield stress is reduced gradually from 507 MPa down to 406 MPa in 5 stages, as shown in Figure 4.7(a). As Kouznetsova points, the smooth transition is meant to avoid the dependence of the width of localization band on the imperfection area size.

The top edge of the plate is loaded with a prescribed displacement of 3.5 μm that corresponds to 3% elongation, which justifies assumption of small strains, so, unlike the original paper, no softening at material or geometrical level is expected.

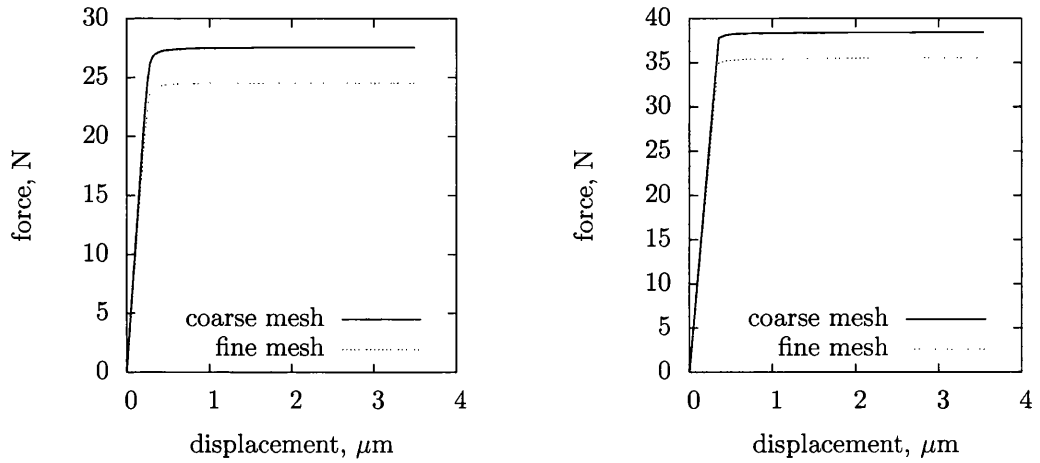

coarse	7.71E+00	3.86E-01	2.21E-03	7.85E-06	5.51E-10
fine	1.28E+01	4.37E-01	3.81E-01	6.15E-03	2.05E-03
	3.85E-04	2.28E-05	5.17E-08	2.19E-11	

Figure 4.8: Multi-Scale Fully Coupled Analysis: Macroscopic stress strain curves (left) voided solution (right) homogeneous solution, (bottom) convergence of the macroscopic Newton-Raphson procedure, at 1.4 μm .

The problem is solved in 200 time steps, by means of the consistent linearization of the homogenized stress for each of the load steps, as the convergence of residuals of the macroscopic Newton-Raphson procedure reveal in Figure 4.8.

Figure 4.8 (left) shows the load-displacement behaviour of the coarse and fine mesh. The course result is in very good agreement with the reference work, whereas the fine mesh provides a softer response. In order to check this, a single scale analysis with all the macro-structure modelled as homogeneous material has also been performed. The coarse vs fine relationship of the single scale homogeneous analysis, given in Figure 4.8 (right) is in very good agreement with the two-scale fully coupled analysis.

However, this consistency also suggests a shared strong mesh dependency, which is also apparent in the macroscopic equivalent plastic strain plots of Figure 4.9. Note that the macroscopic model does not have internal variables, instead, the equivalent plastic strain is homogenized for visualization purpose. Plastic strain accumulates within the smallest discretized volume, and this is also reflected in the width of the shear band.

Equivalent plastic strain plots of Figure 4.9 (middle) and (bottom) belong to RVEs that correspond to points A,B,C,D,E for coarse and fine meshes respectively. The maximum equivalent plastic strain occurring at those RVEs is also indicated.

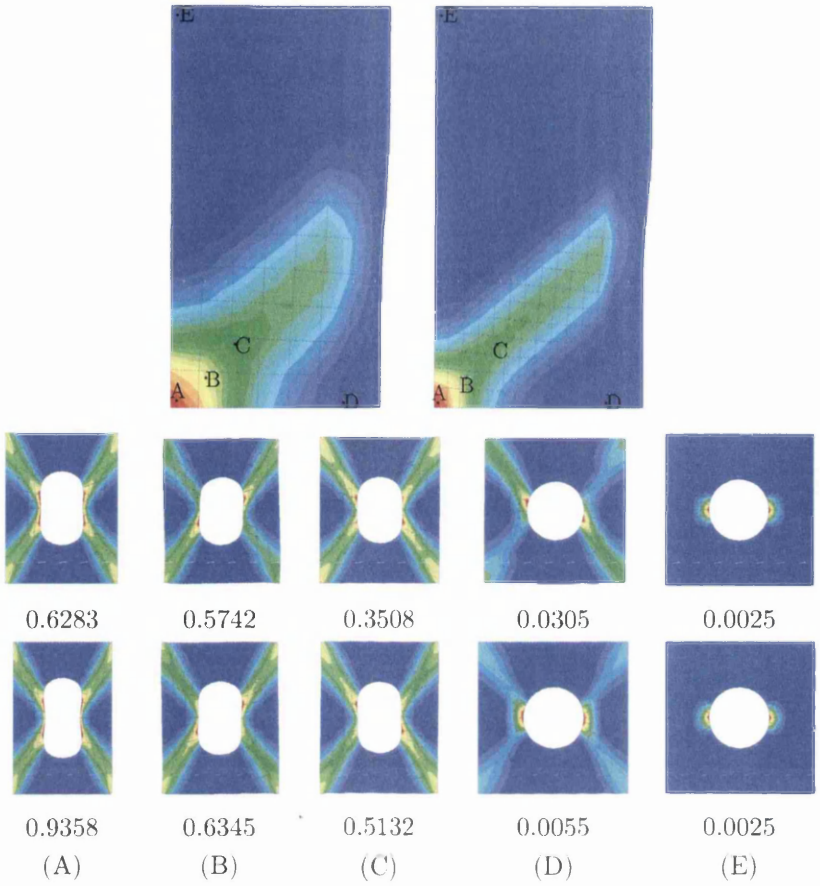

Figure 4.9: Multi-Scale Fully Coupled Analysis: equivalent plastic strain on deformed configuration, (top) coarse and fine macroscopic meshes, (middle) sample RVEs from the coarse model, (bottom) sample RVEs from the fine model, maximum equivalent plastic strain values indicated

In agreement with the last remark, as the element size gets smaller, the deformation is concentrated more, resulting in larger deformations and plastic straining. This is the well known mesh dependent localization pattern of local single scale material models, which has been inherited by the present model..

Chapter 5

Large Strain Computational Homogenization

In this Chapter, the framework for the multi-scale analysis of solids developed in the previous chapter will be extended to cover large strain problems. The homogenized stress-strain counterpart is one of possible work conjugate candidates outlined in Chapter 3. de Souza Neto and Feijóo [16], as well as Miehe *et al.*[76, 79] and Terada *et al.*[115] identify the First Piola-Kirchoff stress tensor $\boldsymbol{P}$ and the deformation gradient tensor $\boldsymbol{F}$ as the stress-strain counterparts to be homogenized in the large strain context.

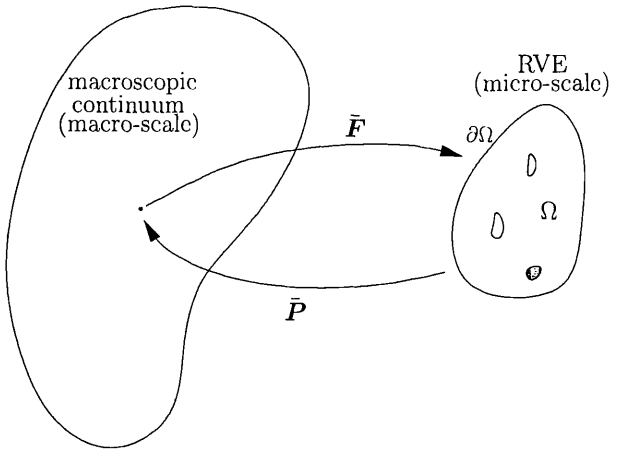

Figure 5.1: Macro-micro transition for large strains

The outline of this chapter follows closely the previous one, where we start by defining the boundary value problem at the macro scale. Then, we will formulate the large strain homogenization theory based on averaging of the First Piola-Kirchoff stress tensor $\boldsymbol{P}$ and the deformation gradient tensor $\boldsymbol{F}$ at micro scale. We will show that homogenization of $\boldsymbol{F}$ and $\boldsymbol{P}$, complemented by the Hill-Mandel principle poses a natural constraint on the possible deformation fields of the RVE, and derive the large strain counterparts for the classes of constraints.

Discrete versions the microscopic boundary value problem are developed for the large strain regime, as well as kinematical constraints, homogenized stress and accompanying consistent tangent modulus; which all fit into the computational framework developed in the previous chapter. Small differences appear in the treatment of uniform tractions and prescription of boundary displacements. The computational model is then tested for single RVE homogenization and fully coupled two-scale analysis.

5.1 Macroscopic Boundary Value Problem

The macroscopic equilibrium problem is formulated in the reference configuration in terms of the macroscopic First Piola-Kirchoff stress tensor $\bar{\boldsymbol{P}}$, prescribed body force per unit reference volume $\bar{\boldsymbol{B}}$ and boundary tractions per unit reference area $\bar{\boldsymbol{T}}$, and consists in finding a kinematically admissible displacement field $\bar{\boldsymbol{u}} \in \bar{\mathscr{K}}$ such that

$$\int_{\bar{\Omega}} \bar{\boldsymbol{P}} : \nabla \boldsymbol{\eta} \, d\bar{V} - \int_{\bar{\Omega}} \bar{\boldsymbol{B}} \cdot \boldsymbol{\eta} \, d\bar{V} - \int_{\partial\bar{\Omega}} \bar{\boldsymbol{T}} \cdot \boldsymbol{\eta} \, d\bar{A} = 0 \qquad \forall \boldsymbol{\eta} \in \bar{\mathscr{V}}, \tag{5.1}$$

A constitutive functional $\bar{\mathscr{G}}$ of the history $\bar{\boldsymbol{F}}^t(\bar{\boldsymbol{x}})$ of the deformation gradient at point $\bar{\boldsymbol{x}}$ up to time t delivers the stress:

$$\bar{\boldsymbol{P}}(\bar{\boldsymbol{x}}, t) = \bar{\mathscr{G}}(\bar{\boldsymbol{F}}^t(\bar{\boldsymbol{x}})) = \bar{\mathscr{G}}([\boldsymbol{I} + \nabla \bar{\boldsymbol{u}}(\bar{\boldsymbol{x}})]^t), \tag{5.2}$$

so that the first term in (5.1) is a functional of the solution $\bar{\boldsymbol{u}}$:

$$\int_{\bar{\Omega}} \bar{\mathscr{G}}([\boldsymbol{I} + \nabla \bar{\boldsymbol{u}}(\bar{\boldsymbol{x}})]^t) : \nabla \boldsymbol{\eta} \; dV. \tag{5.3}$$

Numerical approximations in time to problem (5.1) are obtained by using Euler-type difference schemes to integrate the constitutive equations of the model. Hence, an *incremental constitutive relation* is defined such that, for a typical time interval $[t^n, t^{n+1}]$, with known set $\bar{\boldsymbol{\xi}}^n$ of internal variables at t^n, the stress $\bar{\boldsymbol{P}}^{n+1}$ at t^{n+1} is a function of the deformation gradient $\bar{\boldsymbol{F}}^{n+1}$:

$$\bar{\boldsymbol{P}}^{n+1} = \hat{\boldsymbol{P}}(\bar{\boldsymbol{F}}^{n+1}, \bar{\boldsymbol{\xi}}^n). \tag{5.4}$$

The introduction of the incremental constitutive function (5.4) in (5.1) results in the incremental version of (5.1) which consists in finding an admissible displacement field $\bar{\boldsymbol{u}}^{n+1}$ such that

$$\int_{\bar{\Omega}} \hat{\boldsymbol{P}}(\bar{\boldsymbol{F}}^{n+1}, \boldsymbol{\xi}^n) : \nabla \boldsymbol{\eta} \, d\bar{V} - \int_{\bar{\Omega}} \bar{\boldsymbol{B}}^{n+1} \cdot \boldsymbol{\eta} \, d\bar{V} - \int_{\partial\bar{\Omega}} \bar{\boldsymbol{T}}^{n+1} \cdot \boldsymbol{\eta} \, d\bar{A} = 0 \qquad \forall \, \boldsymbol{\eta} \in \bar{\mathscr{V}}^{n+1}. \tag{5.5}$$

5.2 Coupling of Scales: Homogenization

Analogous to the small strain counterpart, the coupling of microscopic and macroscopic scales is assumed to be based on the homogenization of appropriate stress and strain tensors. Homogenization is performed at the reference configuration by averaging the first Piola-Kirchoff stress tensor $\boldsymbol{P}$, and its work conjugate, deformation gradient tensor $\boldsymbol{F}$ over the RVE volume.

5.2.1 Homogenized Deformation Gradient

The finite strain version of the homogenization assumption states that the macroscopic deformation gradient tensor $\bar{\boldsymbol{F}}$ at a point $\bar{\boldsymbol{X}}$ of the macro continuum is the volume average of all micro deformation gradients $\boldsymbol{F}$ within the RVE associated with $\bar{\boldsymbol{X}}$,

$$\bar{\boldsymbol{F}} = \frac{1}{V} \int_{\Omega} \boldsymbol{F} \, dV = \boldsymbol{I} + \frac{1}{V} \int_{\Omega} \nabla \boldsymbol{u} \, dV, \tag{5.6}$$

where Ω denotes the *reference* configuration, and V is the RVE volume in the reference configuration. The volume averaging limits the possible deformation fields of the RVE, such that $\boldsymbol{u} \in {}_{lrg}\mathscr{K}^*$, where:

$${}_{lrg}\mathscr{K}^* \equiv \left\{ \boldsymbol{v}, \text{ sufficiently regular } \Big| \int_{\Omega} \nabla \boldsymbol{v} \, dV = (\bar{\boldsymbol{F}} - \boldsymbol{I}) \, V \right\}. \tag{5.7}$$

The additive split of the micro displacement field $\boldsymbol{u}$ for finite strains comprises a component that is prescribed by the homogenized deformation gradient $\bar{\boldsymbol{F}}$, and varies linearly with $\boldsymbol{x}$, and a displacement fluctuation as:

$$\boldsymbol{u} = \boldsymbol{u}^* + \tilde{\boldsymbol{u}} = (\bar{\boldsymbol{F}} - \boldsymbol{I})\boldsymbol{X} + \tilde{\boldsymbol{u}}, \tag{5.8}$$

so that

$$\int_{\Omega} \nabla \boldsymbol{u}^* \, dV = (\bar{\boldsymbol{F}} - \boldsymbol{I}) \, V. \tag{5.9}$$

Analogous to the small strain formulation, the minimum kinematical constraint for large strains takes the form $\tilde{\boldsymbol{u}} \in {}_{lrg}\tilde{\mathscr{K}}^*$, where:

$$ {}_{lrg}\tilde{\mathscr{K}}^* \equiv \left\{ \boldsymbol{v}, \text{ sufficiently regular } \mid \int_{\partial\Omega} \boldsymbol{v} \otimes \boldsymbol{N}\, dA = \boldsymbol{0} \right\} \tag{5.10} $$

where $\boldsymbol{N}$ is the unit outward boundary normal defined in the reference configuration. Note that the large strain set only differs from the small strain set in the non-symmetry of the tensor product within the integral. Analogous to the small strain version outlined in Section 4.2.1, the actual set of kinematically admissible RVE displacement fields, ${}_{lrg}\mathscr{K} \subset {}_{lrg}\mathscr{K}^*$ is equivalent to the space of virtual kinematically admissible displacements ${}_{lrg}\mathscr{V}$ of the RVE, and the common choices for ${}_{lrg}\mathscr{V}$ analogous to (4.13), (4.14), (4.15) are given respectively as:

$$ {}_{lrg}\mathscr{V}^{min} \equiv {}_{lrg}\tilde{\mathscr{K}}^* \tag{5.11} $$

$$ {}_{lrg}\mathscr{V}^{per} \equiv \left\{ \tilde{\boldsymbol{u}} \in {}_{lrg}\tilde{\mathscr{K}}^* \;\middle|\; \tilde{\boldsymbol{u}}(\boldsymbol{X}^+) = \tilde{\boldsymbol{u}}(\boldsymbol{X}^-) \quad \forall \text{ pairs } \{\boldsymbol{X}^+, \boldsymbol{X}^-\} \in \partial\Omega \right\} \tag{5.12} $$

$$ {}_{lrg}\mathscr{V}^{lin} \equiv \left\{ \tilde{\boldsymbol{u}} \in {}_{lrg}\tilde{\mathscr{K}}^* \;\middle|\; \tilde{\boldsymbol{u}} = \boldsymbol{0} \quad \forall \boldsymbol{X} \in \partial\Omega \right\} \tag{5.13} $$

5.2.2 Homogenized First Piola-Kirchoff Stress

The macroscopic first Piola-Kirchoff tensor $\bar{\boldsymbol{P}}$ at a point $\bar{\boldsymbol{X}}$ of the macro continuum is defined as the homogenization of the micro stress field $\boldsymbol{P}$ of the RVE associated with $\bar{\boldsymbol{X}}$:

$$ \bar{\boldsymbol{P}} = \frac{1}{V} \int_{\Omega} \boldsymbol{P}\, dV. \tag{5.14} $$

The homogenized first Piola-Kirchoff tensor can be expressed in terms of the boundary traction $\boldsymbol{T}$ and body force $\boldsymbol{B}$ of the micro continuum in the reference configuration, employing the tensor relation analogous to (4.19) together with the strong form of equilibrium:

$$ \bar{\boldsymbol{P}} = \frac{1}{V} \left(\int_{\partial\Omega} \boldsymbol{T} \otimes \boldsymbol{X}\, dA - \int_{\Omega} \boldsymbol{B} \otimes \boldsymbol{X}\, dV \right). \tag{5.15} $$

5.2.3 Hill-Mandel Principle

Large strain counterpart of the Hill-Mandel principle of macro-homogeneity is expressed as:

$$ \bar{\boldsymbol{P}} : \dot{\bar{\boldsymbol{F}}} = \frac{1}{V} \int_{\Omega} \boldsymbol{P} : \dot{\boldsymbol{F}}\, dV. \tag{5.16} $$

Noting that, from (5.8),

$$\begin{aligned} \dot{\boldsymbol{F}} &= \nabla \dot{\boldsymbol{u}} \\ &= \dot{\bar{\boldsymbol{F}}} + \nabla \dot{\tilde{\boldsymbol{u}}} \ , \ \dot{\tilde{\boldsymbol{u}}} \in \mathscr{V} \end{aligned} \tag{5.17}$$

and following a similar procedure given in 4.2.3, it can be shown that the boundary traction $\boldsymbol{T}$ and the body force $\boldsymbol{B}$ belong to the functional space orthogonal to the space of kinematically admissible displacements $\mathscr{V}$:

$$\int_{\Omega} \boldsymbol{B} \cdot \boldsymbol{\eta} \ dV = 0 \ , \ \forall \boldsymbol{\eta} \in \mathscr{V}, \tag{5.18}$$

$$\int_{\partial\Omega} \boldsymbol{T} \cdot \boldsymbol{\eta} \ dA = 0 \ , \ \forall \boldsymbol{\eta} \in \mathscr{V}. \tag{5.19}$$

Note that the choices of space of virtual kinematically admissible displacements ${}_{lrg}\mathscr{V}^{min}$, ${}_{lrg}\mathscr{V}^{per}$ and ${}_{lrg}\mathscr{V}^{lin}$ given by (5.11), (5.12) and (5.13) respectively, are all defined on the boundary of the RVE. The body forces thus have to be zero over the domain:

$$\boldsymbol{B}(\boldsymbol{X}) = \boldsymbol{0} \ , \ \forall \boldsymbol{X} \in \Omega. \tag{5.20}$$

Analogous to the small strain case, the *Uniform Traction b.c.* follows from (5.19) as:

$$\boldsymbol{T}(\boldsymbol{X}) = \boldsymbol{P}(\boldsymbol{X})\boldsymbol{N}(\boldsymbol{X}) = \bar{\boldsymbol{P}}\boldsymbol{N}(\boldsymbol{X}) \ , \ \forall \boldsymbol{X} \in \partial\Omega \tag{5.21}$$

Remark 5.1 The body force orthogonal to the space defined by all three constraints considered is zero, so the homogenized First Piola-Kirchoff Stress given by (5.15) now reduces to:

$$\bar{\boldsymbol{P}} = \frac{1}{V} \int_{\partial\Omega} \boldsymbol{t} \otimes \boldsymbol{X} \ dA. \tag{5.22}$$

5.3 Microscopic Boundary Value Problem

The boundary value problem for the RVE for large strain consists of finding a kinematically admissible deformation $\boldsymbol{u} \in \mathscr{K}$, such that

$$\int_{\Omega} \boldsymbol{P} : \nabla \boldsymbol{\eta} \ dV - \int_{\Omega} \boldsymbol{B} \cdot \boldsymbol{\eta} \ dV - \int_{\partial\Omega} \boldsymbol{T} \cdot \boldsymbol{\eta} \ dA = 0 \qquad \forall \boldsymbol{\eta} \in \mathscr{V}, \tag{5.23}$$

where $\mathscr{K}$ and $\mathscr{V}$ denote, respectively, the functional set of kinematically admissible displacements and the corresponding space of virtual displacements of the RVE. As (5.18) and (5.19) indicate, both the boundary traction $\boldsymbol{T}$ and the body force $\boldsymbol{B}$ are purely reactive to the constraint, so that the virtual work equation for the RVE is given by

$$\int_{\Omega} \boldsymbol{P} : \nabla \boldsymbol{\eta} \, dV = 0 \ \ \forall \boldsymbol{\eta} \in \mathscr{V}. \tag{5.24}$$

Following the small strain case, the assumption of a generic constitutive functional $\mathscr{G}_{lrg}$, along with the equilibrium equation (5.24) defines the RVE equilibrium problem in large strains which consists in finding, for a given macroscopic deformation gradient $\bar{\boldsymbol{F}}$, a displacement fluctuation function $\tilde{\boldsymbol{u}} \in \mathscr{V}$ such that

$$\int_{\Omega} \mathscr{G}_{lrg}(\bar{\boldsymbol{F}} + \nabla\tilde{\boldsymbol{u}})\big|_t : \nabla\boldsymbol{\eta}\, dV = 0\ ,\ \forall \boldsymbol{\eta} \in \mathscr{V}. \tag{5.25}$$

As for the small strain case, we will assume that the constitutive behaviour at the micro level can be described by conventional internal variable based dissipative constitutive theories, whereby the stress tensor is obtained by integrating a set of ordinary differential equations in time for the given history of the strain tensor, typically employing Euler-type difference schemes. For a typical time interval $[t^n, t^{n+1}]$, with known set $\boldsymbol{\xi}^n$ of internal variables, the stress $\boldsymbol{P}^{n+1}$ is a function of the deformation gradient $\bar{\boldsymbol{F}}^{n+1}$. The incremental version of RVE equilibrium problem consists in finding, for a given macroscopic deformation gradient $\bar{\boldsymbol{F}}^{n+1}$ and known field $\boldsymbol{\xi}^n$ of microscopic internal variables, a kinematically admissible RVE displacement fluctuation field $\tilde{\boldsymbol{u}}^{n+1} \in \mathscr{V}$ such that

$$\int_{\Omega} \boldsymbol{P}^{n+1}(\bar{\boldsymbol{F}}^{n+1} + \nabla\tilde{\boldsymbol{u}}^{n+1}, \boldsymbol{\xi}^n) : \nabla\boldsymbol{\eta}\ dV = 0 \qquad \forall\, \boldsymbol{\eta} \in \mathscr{V}. \tag{5.26}$$

With the solution $\tilde{\boldsymbol{u}}^{n+1}$ at hand, the macroscopic stress can be computed according to (5.14) as

$$\bar{\boldsymbol{P}}^{n+1} = \frac{1}{V}\int_{\Omega} \boldsymbol{P}^{n+1}(\bar{\boldsymbol{F}}^{n+1} + \nabla\tilde{\boldsymbol{u}}^{n+1}, \boldsymbol{\xi}^n)\, dV. \tag{5.27}$$

5.4 Finite Element Approximation

In this section, we will develop the large strain non-linear finite element approximation to the microscopic boundary value problem discussed earlier. The treatment of the macroscopic boundary value problem does not differ from a standard solid mechanics problem, so it is omitted here.

The fully (time- and space-) discrete multi-scale constitutive model is obtained by introducing a conventional finite element approximation to (5.26,5.27), where, the infinite-dimensional functional space $\mathscr{V}$ and the domain Ω are replaced with finite-dimensional counterparts defined over a mesh h as ${}^h\mathscr{V}$ and ${}^h\Omega$ respectively. The corresponding fully discrete version of (5.26) consists in finding a vector $\tilde{\mathbf{u}}^{n+1} \in {}^h\mathscr{V}$ of global nodal displacements fluctuations such that

$$\int_{{}^h\Omega} \boldsymbol{\eta}^T \left[\mathbf{G}^T \mathbf{P}^{n+1}(\bar{\mathbf{F}}^{n+1} + \mathbf{G}\,\tilde{\mathbf{u}}^{n+1}, \boldsymbol{\xi}^n)\right] dV = 0\ ,\ \forall\, \boldsymbol{\eta} \in {}^h\mathscr{V}, \tag{5.28}$$

where $\mathbf{G}$ denotes the global discrete gradient matrix containg the appropriate shape function derivatives, $\mathbf{P}^{n+1}$ is the incremental constitutive functional at the RVE level that delivers the array of First Piola-Kirchhoff stress components, $\bar{\mathbf{F}}^{n+1}$ is the array of macroscopic deformation gradient components and $\boldsymbol{\eta}$ is the vector of global nodal virtual displacements.

Problem (5.28) together with the finite element-discrete version of (5.27) define the fully discretized large strain multi-scale constitutive model.

5.4.1 Boundary Condition

Problem (5.28) differs from finite element versions of conventional solid mechanics problems of the type (5.5) only in the construction of the relevant finite-dimensional space ${}^h\mathscr{V}$.

For the linear boundary displacements constraint, the solution of the finite element RVE problem follows the same route as conventional solid mechanics problems, as the construction of space ${}^h\mathscr{V}$ is trivial. For the minimally constrained and periodic boundary displacements kinematical assumptions, however, the spaces ${}^h\mathscr{V}$ are discrete versions of (5.11) and (5.12), respectively. The kinematical constraints in such cases are non-conventional but can nevertheless be imposed in a straight forward manner, as summarized in the following.

First, note that the constraints embedded in space definitions (5.11) and (5.12) – and also (5.13) – involve only the boundary of the RVE. The constraints themselves are *linear dependencies* among the RVE boundary degrees of freedom. Hence, an arbitrary vector $\tilde{\mathbf{v}} \in {}^h\mathscr{V}$ can be conveniently arranged as

$$\tilde{\mathbf{v}} = \begin{Bmatrix} \tilde{\boldsymbol{u}}_f \\ \tilde{\boldsymbol{u}}_d \end{Bmatrix} \tag{5.29}$$

The linear dependence constraint requires that

$$\tilde{\boldsymbol{u}}_d = \boldsymbol{\alpha}\, \tilde{\boldsymbol{u}}_f, \tag{5.30}$$

where $\tilde{\boldsymbol{u}}_f$ and $\tilde{\boldsymbol{u}}_d$ contain the displacement fluctuations of *free* and *dependent* degrees of freedom of the boundary respectively, and $\boldsymbol{\alpha}$ is a matrix of constraint coefficients expressing the linear dependencies that characterize the model in question. The dependencies are implemented in the same way with the small strain counterpart:

$$\boldsymbol{u}_d \;=\; (\boldsymbol{u}_d^* + \boldsymbol{\alpha}\boldsymbol{u}_f^*) + \boldsymbol{\alpha}\boldsymbol{u}_f \tag{5.31}$$

Uniform Traction b.c. For the minimally constrained case, $\boldsymbol{\alpha}$ is obtained from:

$$\mathbb{C} \begin{Bmatrix} \tilde{\boldsymbol{u}}_f \\ \tilde{\boldsymbol{u}}_d \end{Bmatrix} = \mathbf{0}, \tag{5.32}$$

where $\mathbb{C}$ is the global matrix obtained from the discrete version of the integral constraint of definition (5.11). Note that this choice of constraint means there will be a maximum number of *free* degrees of freedom of the boundary corresponding to a minimum number of *dependent* ones. The 2D implementation of the minimal constraint will be developed next.

To eliminate rigid body motion, 3 degrees of freedom are prescribed by the macro strain. The minimum number of dependent boundary degrees of freedom is 4, equal to the number of components of the stress tensor. All remaining degrees of freedom on the boundary are treated as free, and are masters of these 4 dependent degrees of freedom, as shown in Figure 5.2. Note that there is no shape limitation for the RVE for the Uniform Traction b.c.

Furthermore, that the unsymmetric (5.11) can be expressed in the discretized sense as the sum of integrals evaluated at the boundary of each boundary element e^b:

$$\sum^{b} \int_{e^b} \tilde{\boldsymbol{u}} \otimes \boldsymbol{N} \, dS = \mathbf{0}, \tag{5.33}$$

with element contributions:

$$\int_{e^b} \tilde{\boldsymbol{u}} \otimes \boldsymbol{N} \, dS = \begin{bmatrix} \int_{e^b} \sum \tilde{u}_1^q N^q \boldsymbol{N}_1 \, dS & 0 \\ 0 & \int_{e^b} \sum \tilde{u}_2^q N^q \boldsymbol{N}_2 \, dS \\ \int_{e^b} \sum \tilde{u}_1^q N^q \boldsymbol{N}_2 \, dS & 0 \\ 0 & \int_{e^b} \sum \tilde{u}_2^q N^q \boldsymbol{N}_1 \, dS \end{bmatrix},$$

where N^q is the shape function associated with node q. $\mathbb{C}^q$, the coefficient matrix for node q which multiplies the nodal displacement fluctuation vector $\tilde{\boldsymbol{u}}^q$ takes the form:

$$\mathbb{C}^q = \begin{bmatrix} a^q & 0 \\ 0 & b^q \\ b^q & 0 \\ 0 & a^q \end{bmatrix}. \tag{5.34}$$

As for small strains,

$$a^q = \int_{e^b} N^q \boldsymbol{N}_1 \, dS \quad , \quad b^q = \int_{e^b} N^q \boldsymbol{N}_2 \, dS.$$

Integration and assembly of coefficient matrices, as well as the extraction of dependency coefficients $\boldsymbol{\alpha}$ follow the same procedure as in the small strains case. After adding the contributions from all elements that share node q to $\mathbb{C}^q$, the sum given in (5.33) is expressed as the product of the global coefficient matrix $\mathbb{C}^b$ and the vector

of fluctuating displacements as:

$$\begin{aligned} \mathbb{C}^b_{(4\times bdof)}.\tilde{u}^b_{(bdof)} &= \mathbf{0}_{(4)} \\ \mathbb{C}^f_{(4\times mdof)}.\tilde{u}^f_{(mdof)} + \mathbb{C}^d_{(4\times 4)}.\tilde{u}^d_{(4)} &= \mathbf{0}_{(4)} \\ \tilde{u}^d_{(4)} = \mathbb{R}_{(4\times mdof)}\tilde{u}^f_{(mdof)}, \qquad \mathbb{R} &= -(\mathbb{C}^d)^{-1}\mathbb{C}^f \end{aligned} \tag{5.35}$$

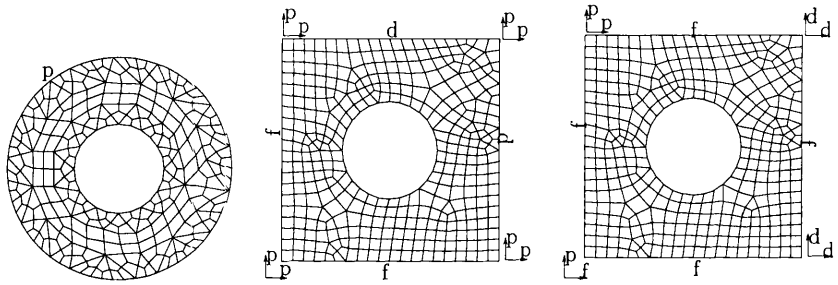

Figure 5.2: The choice of boundary condition specifies whether a boundary degree of freedom is free (f), prescribed (p) or dependent (d) on other degree(s) of freedom. Arrangement of nodes for 2-D RVE for large strains: (a) Linear b.c., (b) Periodic b.c., and (c) Uniform Traction b.c.

Periodic b.c. As for small strains, $\boldsymbol{\alpha}$ is an identity matrix for a periodic fluctuations model with pairing boundary nodes located at pairing points $\boldsymbol{X}^+$ and $\boldsymbol{X}^-$ lying on opposite sides of $\partial^h\Omega$. Displacements of corner nodes are prescribed by the macro strain, as shown on the 2-D square RVE of Figure 5.2 (b).

Linear b.c. fixes all nodal degrees of freedom associated with displacement fluctuations of the RVE boundary as zero. All RVE boundary degrees of freedom are solely prescribed by the macroscopic strain:

$$\boldsymbol{u}_b = \boldsymbol{u}_p \tag{5.36}$$

As depicted in Figure 5.2(a), there is no shape limitation for the RVE for the linear boundary displacements constraint.

5.4.2 Prescribed Displacements

The prescription of the macro deformation gradient $\bar{\boldsymbol{F}}$ is performed as follows: At each node q,

$$\begin{aligned} \boldsymbol{u}_q^* &= (\bar{\boldsymbol{F}} - \boldsymbol{I})\boldsymbol{X}_q \\ &\equiv^h \mathbb{Q}_q^T(\bar{\boldsymbol{F}} - \boldsymbol{I}), \end{aligned} \tag{5.37}$$

where, for 2D,

$$\bar{\boldsymbol{F}} - \boldsymbol{I} = \begin{Bmatrix} \bar{F}_{11} - 1 \\ \bar{F}_{21} \\ \bar{F}_{12} \\ \bar{F}_{22} - 1 \end{Bmatrix}, \quad \boldsymbol{u}_q = \begin{Bmatrix} u_1 \\ u_2 \end{Bmatrix}, \quad \mathbb{Q}_q = \begin{bmatrix} X_1 & 0 \\ 0 & X_1 \\ X_2 & 0 \\ 0 & X_2 \end{bmatrix} \tag{5.38}$$

and for 3D,

$$\bar{\boldsymbol{F}} - \boldsymbol{I} = \begin{Bmatrix} \bar{F}_{11} - 1 \\ \bar{F}_{21} \\ \bar{F}_{31} \\ \bar{F}_{12} \\ \bar{F}_{22} - 1 \\ \bar{F}_{32} \\ \bar{F}_{13} \\ \bar{F}_{23} \\ \bar{F}_{33} - 1 \end{Bmatrix}, \quad \boldsymbol{u}_q = \begin{Bmatrix} u_1 \\ u_2 \\ u_3 \end{Bmatrix}, \quad \mathbb{Q}_q = \begin{bmatrix} X_1 & 0 & 0 \\ 0 & X_1 & 0 \\ 0 & 0 & X_1 \\ X_2 & 0 & 0 \\ 0 & X_2 & 0 \\ 0 & 0 & X_2 \\ X_3 & 0 & 0 \\ 0 & X_3 & 0 \\ 0 & 0 & X_3 \end{bmatrix},$$

where $\mathbb{Q}_q$ is defined as the nodal coordinate matrix.

5.4.3 Problem Statement

We aim to find the unknown set of inner ($\boldsymbol{u}_i$) and free boundary displacements ($\boldsymbol{u}_f$), as a response to the set of prescribed displacements ($\boldsymbol{u}^*$), that satisfy the equilibrium and the kinematical constraint. The final reduced set of non-linear algebraic finite element equations to be solved is obtained by introducing representation (5.29,5.30) for $\boldsymbol{\eta}$ and $\tilde{\mathbf{u}}^{n+1}$ in (5.28). After straightforward matrix manipulations, this gives

$$\begin{Bmatrix} \mathbf{g}_i \\ \mathbf{g}_f + \boldsymbol{\alpha}^T \mathbf{g}_d \end{Bmatrix} = \begin{Bmatrix} \mathbf{0} \\ \mathbf{0} \end{Bmatrix}, \tag{5.39}$$

where $\mathbf{g}_i$, $\mathbf{g}_f$ and $\mathbf{g}_d$ are the components of the global vector

$$\mathbf{g} \equiv \int_{h\bar{\Omega}} \mathbf{G}^T \bar{\mathbf{P}}^{n+1}(\bar{\mathbf{F}}^{n+1} + \mathbf{G}\,\tilde{\mathbf{u}}^{n+1}, \bar{\boldsymbol{\xi}}^n)\, dV, \tag{5.40}$$

associated, respectively, with the internal, master and dependent degrees of freedom of the RVE.

5.4.4 Solution Procedure

The Newton-Raphson procedure which is used to solve the system $\mathbf{g} = \mathbf{0}$ is as outlined in Section 4.4.4.

5.4.5 Homogenized Stress

The homogenized stress (5.22) is expressed in the discrete setting as an assembly of integrals performed at element level:

$$\bar{\boldsymbol{P}}^h = \frac{1}{V} \sum \int_e \boldsymbol{P} dV, \tag{5.41}$$

where the integration is performed numerically in a standard manner.

Alternatively, as pointed by Miehe [79], by considering the limit $\boldsymbol{T}\, dA (= \boldsymbol{t}\, da) \rightarrow \mathbb{F}_b$, where $\mathbb{F}_b$ are the nodal forces on the RVE boundary, (5.22) can be expressed in the discrete setting as:

$$\bar{\boldsymbol{P}}^h = \frac{1}{V} \mathbb{Q}_b \mathbb{F}_b. \tag{5.42}$$

The boundary coordinate matrix, $\mathbb{Q}_b$, as the collection of all nodal coordinate matrices $\mathbb{Q}_q$ such that, for M nodes on the boundary:

$$\mathbb{Q}_b = \begin{bmatrix} \mathbb{Q}_1 & \mathbb{Q}_2 & \dots & \mathbb{Q}_M \end{bmatrix}. \tag{5.43}$$

Note that, if the out-of-plane homogenized stress is required in the plane strain case, then (5.42) can not be used alone.

5.4.6 Tangent Modulus

The Newton-Raphson method relies on exact linearization of a global discrete residual vector within a finite element framework. This vector is in fact an assembly of element residual vectors, which in turn are calculated from integration of the homogenized stress tensor. Thus, this chain of dependencies require exact linearization of the homogenized stress tensor for each iteration of the Newton-Raphson procedure. This can be achieved by either linearizing (5.22), and then discretizing the result, or by directly linearizing the discretized homogenized stress (5.41) or (5.42). We proceed with the latter as follows:

$$\begin{aligned} \frac{\partial \bar{\boldsymbol{P}}^h}{\partial \bar{\boldsymbol{F}}} &= \frac{1}{V} \mathbb{Q}_b \frac{\partial \mathbb{F}_b}{\partial \bar{\boldsymbol{F}}} \\ &= \frac{1}{V} \mathbb{Q}_b \left(\frac{\partial \mathbb{F}_b}{\partial \boldsymbol{u}_i} \frac{\partial \boldsymbol{u}_i}{\partial \bar{\boldsymbol{F}}} + \frac{\partial \mathbb{F}_b}{\partial \boldsymbol{u}_f} \frac{\partial \boldsymbol{u}_f}{\partial \bar{\boldsymbol{F}}} + \frac{\partial \mathbb{F}_b}{\partial \boldsymbol{u}_d} \frac{\partial \boldsymbol{u}_d}{\partial \bar{\boldsymbol{F}}} + \frac{\partial \mathbb{F}_b}{\partial \boldsymbol{u}_p} \frac{\partial \boldsymbol{u}_p}{\partial \bar{\boldsymbol{F}}} \right). \end{aligned} \tag{5.44}$$

It follows analogously to the small strain version that :

$$\frac{\partial \bar{\boldsymbol{P}}^h}{\partial \bar{\boldsymbol{F}}} = \frac{1}{V}\mathbb{Q}_b\left(\begin{bmatrix}\mathbf{k}_{bi}\\ \mathbf{k}_{bf}+\boldsymbol{\alpha}\mathbf{k}_{bd}\end{bmatrix}^T\begin{bmatrix}\partial_{\bar{\boldsymbol{F}}}\boldsymbol{u}_i\\ \partial_{\bar{\boldsymbol{F}}}\tilde{\boldsymbol{u}}_f\end{bmatrix}+\mathbf{k}_{bb}\mathbb{Q}_b^T\right), \tag{5.45}$$

where $\partial_{\bar{\boldsymbol{F}}}\tilde{\boldsymbol{u}}_f = \frac{\partial \tilde{\boldsymbol{u}}_f}{\partial \bar{\boldsymbol{F}}}$ etc. Also, as $\mathbb{F}_i = \mathbf{0}$,

$$\begin{bmatrix}\mathbf{k}_{ii}\\ \mathbf{k}_{if}+\boldsymbol{\alpha}\mathbf{k}_{id}\end{bmatrix}^T\begin{bmatrix}\partial_{\bar{\boldsymbol{F}}}\boldsymbol{u}_i\\ \partial_{\bar{\boldsymbol{F}}}\tilde{\boldsymbol{u}}_f\end{bmatrix}+\mathbf{k}_{ib}\mathbb{Q}_b^T = \mathbf{0}. \tag{5.46}$$

The consistent tangent is given by (5.45), where the unknowns $\partial_{\bar{\boldsymbol{F}}}\boldsymbol{u}_i$ and $\partial_{\bar{\boldsymbol{F}}}\tilde{\boldsymbol{u}}_f$ are found from (5.46) by setting each column of $-\mathbf{k}_{ib}\mathbb{Q}_b^T$ as the residual and solving the existing global Newton-Raphson system, which returns the corresponding column of the unknown set $\{\partial_{\bar{\boldsymbol{F}}}\boldsymbol{u}_i, \partial_{\bar{\boldsymbol{F}}}\tilde{\boldsymbol{u}}_f\}$ in (5.45).

Note that, the format of the calculation of the tangent modulus is indifferent to the choice of boundary condition, which is implicit in the dependencies of degrees of freedom. Temizer and Wriggers [118] argue that macroscopic tangent computations by condensation inflict increasingly higher memory allocation requirements for increasingly larger micro-structural samples that may not be easily met by standard workstations. This has not been our experience, probably for two reasons. The largest contribution to the cost of the computation comes from the first term on the left hand side of (5.46), which, in our implementation, is readily available as the upper portion of the global stiffness matrix of the converged solution, given by (4.58), so we do not need further computation or memory allocation. Furthermore, instead of merging (5.46) into (5.45), which necessitates a potentially costly inverse operation, we simply solve (5.46) for the unknown set of displacements, which are then inserted into (5.45).

5.5 Computer Implementation

The finite element framework developed in the previous section comprises the choice of boundary condition, prescription of the macro strain, the solution algorithm, stress and consistent tangent modulus update. This model can be employed in two main contexts:

- The *Single-Scale RVE Homogenization*, whereby the macroscopic constitutive response is produced by finite element solutions of a single RVE under prescribed macroscopic strain histories, as schematically illustrated in Figure 5.3 (left).
- *Fully Coupled Two-Scale Analysis* of solids, where the macroscopic equilibrium problem is solved simultaneously with one RVE equilibrium problem for each

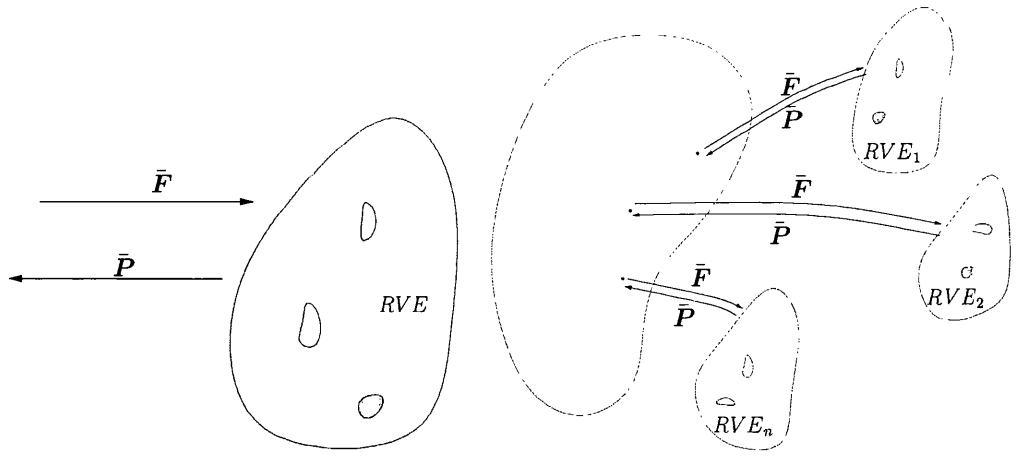

Figure 5.3: Large Strain Computer Implementation: (left) Single-Scale RVE Homogenization (right) Multi-Scale Fully Coupled Analysis

Gauss quadrature point of the macroscopic mesh [118, 115, 103]. In this case, the stress updating procedure used at each Gauss quadrature point of the macro-mesh involves the solution of an initial boundary value problem for the corresponding RVE, see Figure 5.3 (right).

5.5.1 Single-Scale RVE Homogenization

Single-scale RVE homogenization procedure comprises of:

1. Initially, depending on the choice of kinematical constraint:
   (a) group boundary degrees of freedom into f, p or d (see Section 5.4.1).
   (b) calculate dependency coefficients $\boldsymbol{\alpha}$ (see Section 5.4.1).
2. At a typical time interval $[t^n, t^{n+1}]$, with known set $\boldsymbol{\xi}^n$ of internal variables, solve the incremental microscopic boundary value problem:
   (a) input prescribed strain multiplied by the load factor $\bar{\boldsymbol{\varepsilon}}^{n+1}$
   (b) apply prescribed displacements using (5.37)
   (c) solve the system of equations (5.39) using a Newton-Raphson procedure
   (d) update dependent degrees of freedom,$\boldsymbol{u}_d$, by (5.31)
3. Calculate homogenized stress with (5.42)

An example is borrowed from Miehe [79] to verify and demonstrate the computational framework for single scale RVE homogenization in the finite strain regime: We consider a unit square RVE with a circular void and two circular stiff inclu-

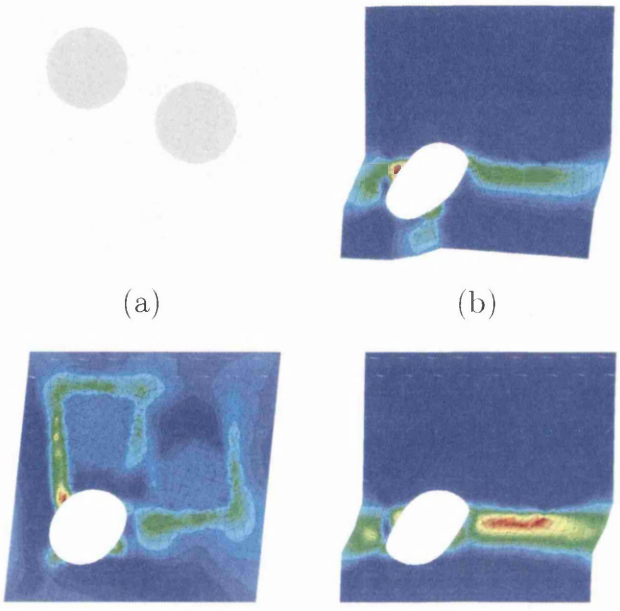

(b)	6.17E-00	7.66E-03	4.84E-03	3.74E-04	8.96E-06	4.27E-10	
(c)	4.99E-01	9.99E-03	3.73E-03	4.26E-04	1.89E-05	6.75E-06	3.00E-09
(d)	3.29E-01	6.64E-03	1.54E-03	9.06E-05	2.53E-06	3.45E-10	

Figure 5.4: Single-Scale RVE Homogenization: (a) Initial mesh of the RVE, development of equivalent plastic strain and deformed mesh for (b) Uniform Traction b.c., (c) Linear b.c. and (d) Periodic b.c. (bottom) convergence of residuals of the Newton-Raphson Scheme corresponding to different boundary conditions

sions. The void, as well as the inclusions have a radius of 0.15, and are located at $\{-0.2, -0.2\}$, $\{0.2, 0\}$ and $\{-0.2, 0.2\}$ respectively, with respect to a coordinate system with origin at the RVE center.

Plane stress condition is assumed under finite strains and the RVE matrix material is modelled by a von Mises type elastoplastic law with shear and bulk moduli $\mu_m = 8$, $K_m = 17.5$, initial yield stress $\sigma_0 = 0.45$ and linear hardening modulus $H = 0.1$. Inclusions are assumed to be Neo Hookean type hyperelastic with material properties $\mu = 100\,\mu_m$ and $K = 100\,K_m$ respectively.

The RVE is modelled by 810 standard 4 noded quadrilateral elements, and is loaded by a macroscopic deformation gradient given by:

$$\bar{\boldsymbol{F}} = \begin{bmatrix} 1 & 0.1 \\ 0 & 1 \end{bmatrix}. \tag{5.47}$$

The simple shear load represented by (5.47) is applied in 20 load steps. Figure 5.4 shows the deformed configuration of the RVE, as well as the equivalent plastic strain for uniform traction, linear and periodic boundary conditions. In very good agreement with the reference paper, a horizontal shear develops for the periodic b.c. For the uniform traction b.c., for which the softest response is obtained, an additional vertical band is observed, which also agrees with Miehe [79]. Quadratic convergence of residuals for the RVE Newton-Raphson solution procedure for all three boundary conditions during the 9^{th} load step is also presented.

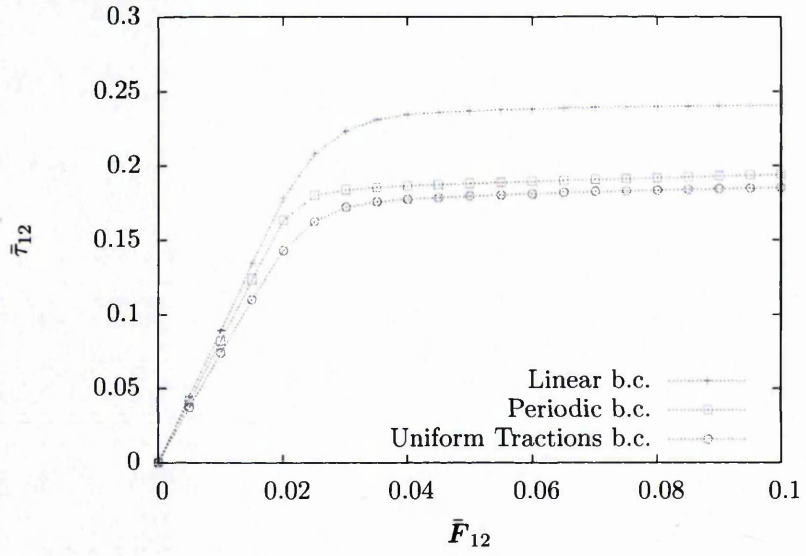

Figure 5.5: Single-Scale RVE Homogenization: (top) Macroscopic stress strain curves obtained by Uniform Traction b.c., Periodic b.c. and Linear b.c.

Figure 5.5 shows the shear component of homogenized Kirchoff stress $\bar{\tau}_{12}$ versus the shear component of applied macroscopic deformation gradient $\bar{\boldsymbol{F}}_{12}$. As expected, the uniform traction b.c. and linear b.c. mark the lower and upper bounds respectively, whereas periodic b.c. lies between them. The plot is in close agreement with the original paper, and the slight offset observed could be linked to element technology (original paper employs MINI-type mixed triangles).

5.5.2 Two-Scale Fully Coupled Analysis

Large strain procedure for two-scale fully coupled analysis is outlined as follows:

1. Initially, depending on the choice of kinematical constraint:
   (a) group boundary degrees of freedom into f, p or d (see Section 5.4.1).
   (b) calculate dependency coefficients $\boldsymbol{\alpha}$ (see Section 5.4.1).
2. At a typical time interval $[t^n, t^{n+1}]$, solve the incremental macroscopic boundary value problem. At a typical iteration step of the macro Newton-Raphson procedure, at every Gauss point, with known set $\boldsymbol{\xi}^n$ of internal variables of the RVE associated with that Gauss point,
   (a) solve the incremental microscopic boundary value problem:
      i. calculate prescribed strain (multiplied by the load factor) $\bar{\boldsymbol{\varepsilon}}^{n+1}$
      ii. apply prescribed displacements using (5.37)
      iii. solve the system of equations (5.39) using a Newton-Raphson procedure
      iv. update dependent degrees of freedom,$\boldsymbol{u}_d$, by (5.31)
   (b) Calculate homogenized stress with (5.42)
   (c) Calculate consistent tangent with (5.45)

We will use the multi-scale example given by Terada *et al.*[115], to compare and verify the methodology developed for fully coupled analysis. The authors consider an L shaped macro structure with geometry given in Figure 5.6 (left), which is loaded by a distributed load on its left face. The macro structure is discretized by 55 standard 4 noded quadrilateral elements with 4 integration points.

All 220 RVEs corresponding to each of those integration points have a pore of volume fraction 50.33%, modelled initially with the same geometry as defined in Figure 5.6 (right), where 560 standard 4 noded quadrilateral elements with 4 integration points are employed and plane stress condition is assumed.

The constitutive model for the hyperelastic solid is assumed to be of neo-Hookean type with material constants λ= 7.14 MPa and μ=3.57, which coincide with the tangential response in the reference configuration of the principal stretch based Hencky type model originally employed by Terada *et al.*[115].

The loading of the macroscopic structure is performed in two time steps. Figure 5.7 shows the deformation history of the structure at each of those steps, which are in perfect agreement with the reference paper. The von Mises homogenized stress is also plotted, which agrees with the reference paper as well. Convergence of residuals

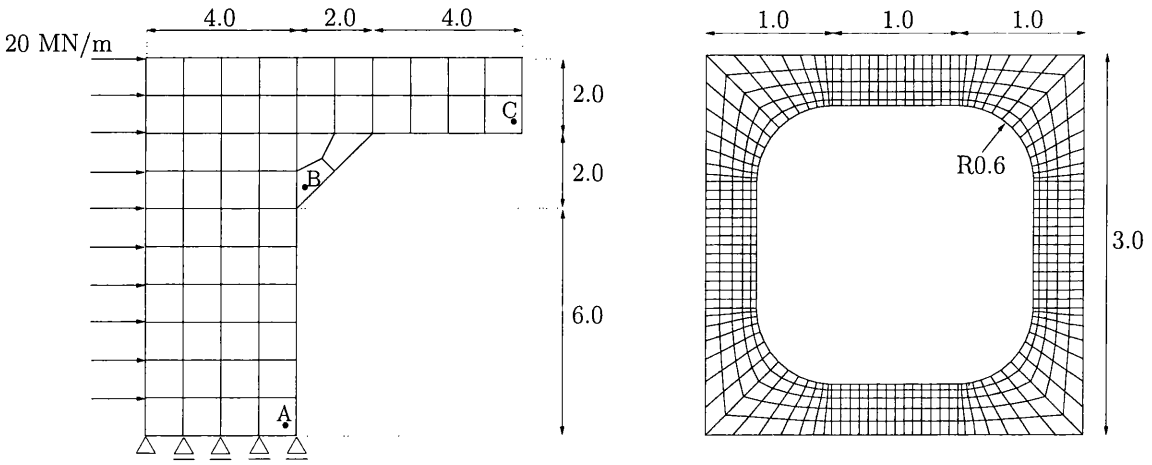

Figure 5.6: Multi-Scale Fully Coupled Analysis: Initial geometry, load and mesh: (left) macro structure (right) typical RVE

of the macroscopic Newton-Raphson procedure reveals the consistent linearization of the homogenized stress for each of the load steps.

Figure 5.8 shows the deformation history, as well as the projected von Mises stress on three distinct RVEs that correspond to points A, B and C of Figure 5.6 (left) at both time steps, which are also in perfect agreement with the original paper. Each of the RVEs reflect the deformation state of the point that they represent, i.e. the displacement gradient at point A is dominated by the shear component, which is clearly revealed in the deformation pattern of the RVE. The deformation pattern of point C is mainly rotation, which is depicted by the deformation of the RVE. Negligible stresses exist at point C but omitted from the plot for convenience.

As pointed by Terada *et al.*[115], volume averaging of RVEs that are in a state of self-equilibrium solely characterizes the macroscopic behaviour at each point, without any assumed constitutive relationship at the macroscopic level.

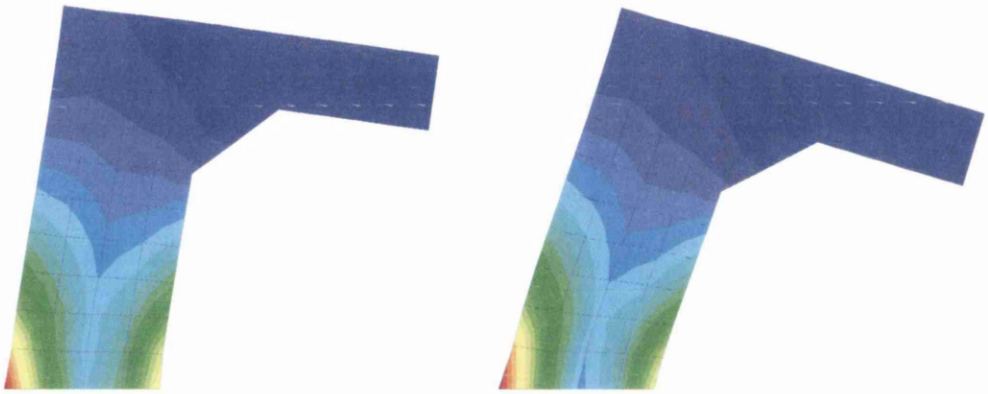

50%	3.24E-02	1.71E-01	2.49E-03	1.30E-04	6.67E-08	3.56E-13
100%	3.24E-02	2.03E-01	5.79E-03	1.07E-03	1.20E-05	1.27E-09

Figure 5.7: Multi-Scale Fully Coupled Analysis: Development of von Mises stress on deformed macroscopic mesh for (left) 50% and (right) 100% load, and (bottom) convergence of the macroscopic Newton-Raphson procedure.

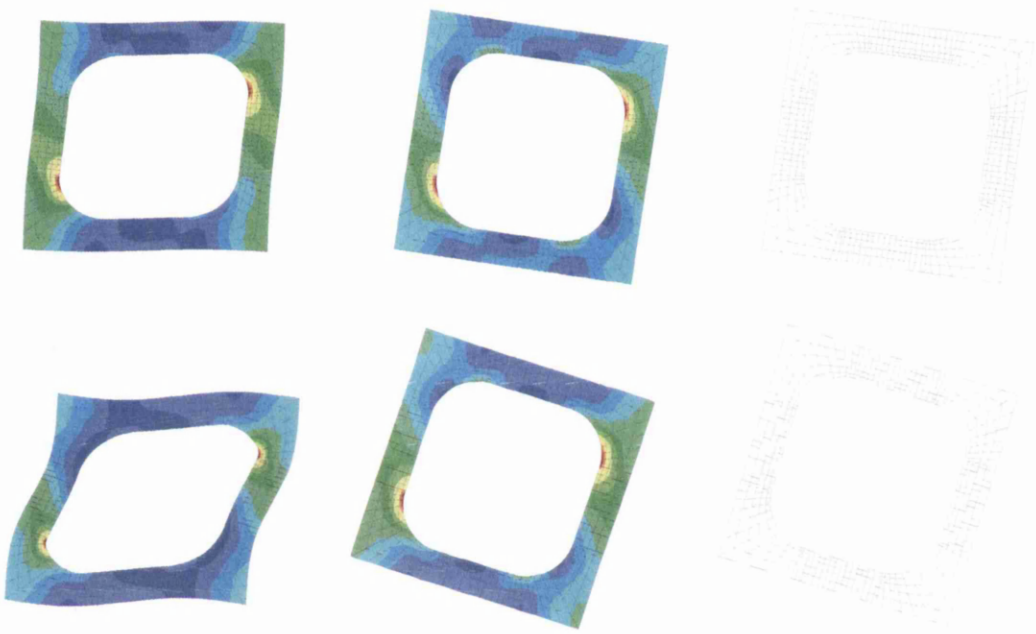

Figure 5.8: Multi-Scale Fully Coupled Analysis: Development of von Mises stress and deformed mesh on RVEs that correspond to points (left) A, (middle) B and (right) C for (top) 50% and (bottom) 100% load. See Figure 5.6 for point locations.

Chapter 6

Techniques for Efficient Implementation

Due to their suitability for implementation within non-linear finite element environments, multi-scale methods are particularly attractive for the description of complex 'macroscopic' behaviour by means of relatively simple RVEs that take into account the geometry of the micro-structure and whose response is modelled by conventional continuum non-linear constitutive laws. For the fully coupled two-scale analyses of solids, where the macroscopic equilibrium problem is solved simultaneously with one RVE equilibrium problem for each Gauss quadrature point of the macroscopic mesh [75, 76, 115], the stress updating procedure used at each Gauss quadrature point of the macro-mesh involves the solution of an initial boundary value problem for the corresponding RVE.

Memory storage (stemming, for instance, from the collection of internal variable sets of all integration points of each RVE) as well as floating-point calculation requirements make multi-scale strategies very computationally demanding in general. Their practical use in the simulation of industrially relevant problems is largely limited by the computing power available at present. Whenever feasible, such simulations often require computing times orders of magnitude greater than those normally associated with conventional single-scale analysis. To address the problem, the use of parallel computing in this context is reported [28, 71].

In this chapter, we consider two approaches to remedy different aspects of the problem: Interface discretization is a concept borrowed from fluid-structure interaction, and works by decreasing the dependency overhead of periodic and uniform traction boundary conditions. We also develop a sub-stepping procedure that obtains better initial guesses for failed iteration steps of the microscopic equilibrium Newton-Raphson scheme, which allows larger time/load steps to be prescribed at the macroscopic scale, leading to substantial savings in computing time.

6.1 Interface Discretization

The 'raw' implementation of the kinematical constraint, as described in Chapters 4 and 5 has some disadvantages. For the periodic b.c., the finite element mesh has to be symmetric on the boundary to allow one to one correspondence of nodes. The mesh cannot be locally refined. Furthermore, the fluctuating part of the displacement $\tilde{\boldsymbol{u}}$ is carried by half of the boundary degrees of freedom, which increases the relative time cost of the problem compared to linear b.c., where the boundary degrees of freedom are all prescribed and do not appear as unknowns.

The uniform traction b.c. suffers from the boundary dependency overhead substantially, as most boundary degrees of freedom are treated as free, with displacement fluctuations appearing as unknowns. Furthermore, the sparsity of the global stiffness is adversely affected by the dependency of 3 or 4 degrees of freedom on all but 3 prescribed degrees of freedom on the boundary, which makes the solution of this boundary condition considerably slower.

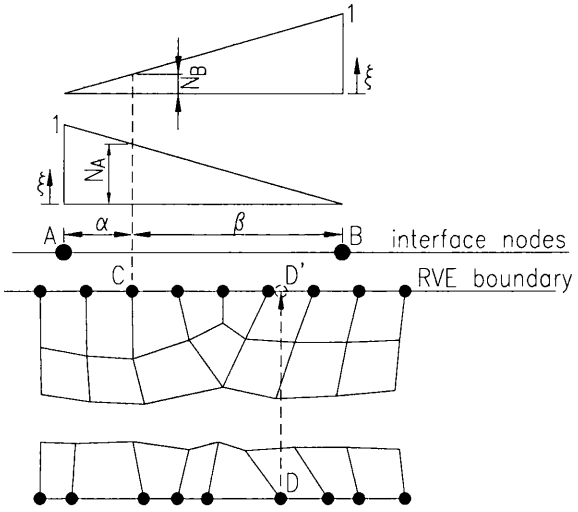

Figure 6.1: Finite Element interpolation at RVE boundary

It is tempting to apply the periodic and uniform traction boundary conditions on an independently discretized interface, similar to the one proposed by Dettmer *et al.*[25], instead of the actual boundary nodes. The interface is linked to the boundary nodes in the same master-dependent sense as set out earlier in chapters 4 and 5, but the dependency is conveyed through finite element type linear interpolation functions, so that the displacement of node C can be expressed in terms of displacements of interface nodes A and B as:

$$\boldsymbol{u}_C = \boldsymbol{u}_A N_{A(@C)} + \boldsymbol{u}_B N_{B(@C)} \tag{6.1}$$

as shown in Figure 6.1. Shape function values are obtained by the geometric relationships:

$$N_{A(@C)} = \frac{\beta}{\alpha+\beta}, \quad N_{B(@C)} = \frac{\alpha}{\alpha+\beta} \tag{6.2}$$

Periodic b.c.: Interface nodes for a typical RVE with Periodic b.c. are shown in Fig 6.2(a). Nodes on Ω^+ are geometrically dependent on interface masters, as described above for node C. Note that (6.1) and (6.2) also imply the relationship:

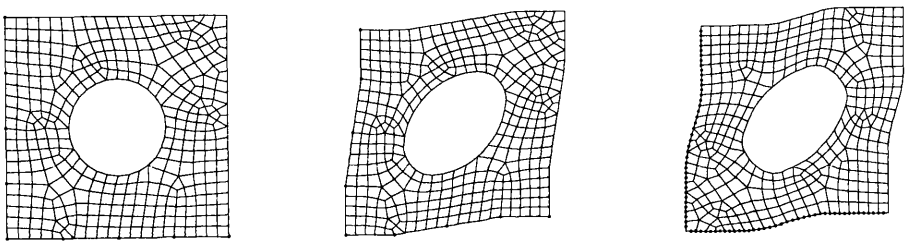

(a) (b) (c)

Figure 6.2: Periodic b.c. (a) initial mesh; and deformed mesh: (b) with and (c) without the interface

$$\tilde{\boldsymbol{u}}_C = \tilde{\boldsymbol{u}}_A N_{A(@C)} + \tilde{\boldsymbol{u}}_B N_{B(@C)} \tag{6.3}$$

so that the displacement of node C is expressed as:

$$\boldsymbol{u}_C = \boldsymbol{u}^*_C + \tilde{\boldsymbol{u}}_A N_{A(@C)} + \tilde{\boldsymbol{u}}_B N_{B(@C)} \tag{6.4}$$

For every node D on Ω^-, we assume a fictitious node D' on Ω^+, as shown in Figure 6.1, so that the periodic dependency given by $\tilde{\boldsymbol{u}}_D = \tilde{\boldsymbol{u}}_{D'}$ applies. Node D' relates to masters A and B in the same way as node C, so that the displacement of node D is expressed as:

$$\boldsymbol{u}_D = \boldsymbol{u}^*_D + \tilde{\boldsymbol{u}}_A N_{A(@D')} + \tilde{\boldsymbol{u}}_B N_{B(@D')} \tag{6.5}$$

Note that the format of (6.4) and (6.5) is the same as (4.43), where the dependency coefficients $\boldsymbol{\alpha}$ are the shape function values. Displacements of corner nodes are prescribed by the macro strain.

Introduction of interface nodes can be interpreted as pointwise enforcement of the kinematic constraint. Linear b.c. applies between these points (interface nodes),

which is clearly seen in Figure 6.2, where deformed RVE meshes with and without interface nodes are compared.

Uniform Traction b.c.: Interface nodes for a typical RVE with uniform traction b.c. are shown in Fig 6.3(a). The 3 dependent and 3 prescribed boundary degrees of freedom can be assigned to 3 corners. Kinematical constraint is enforced pointwise at interface nodes, and Linear b.c. applies for all nodes between interface nodes.

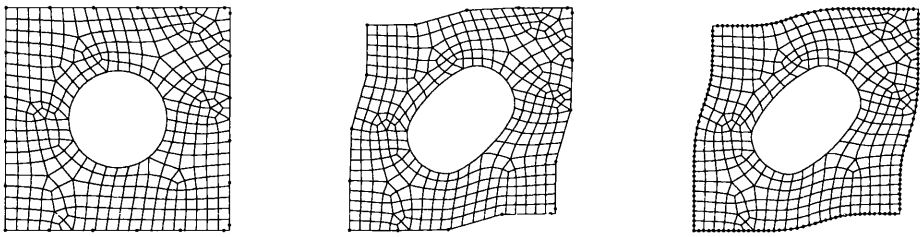

(a) (b) (c)

Figure 6.3: Uniform traction b.c., (a) initial mesh; and deformed mesh: (b) with and (c) without the interface

6.1.1 Numerical Example

A numerical example is presented to demonstrate the use of interface discretization as a means to achieve a faster solution.

A 20×36 cm plate with a 5 cm radius hole in the middle is stretched longitudinally by 0.5 per cent. Plane stress condition is assumed and because of symmetry, only a quarter of the plate is discretized into 24 quadratic elements as shown in Figure 6.4 (a) and (b).

All 96 RVEs are initially characterized by the typical RVE with a 15% void described by a single hole at its centre, and is discretized with 320 quadratic elements, as shown in 6.4 (c), with the following material properties : von Mises type elasto-plastic with Young's modulus $E = 70$ GPa, Poisson's ratio $\nu = 0.2$ and initial yield stress $\sigma_0 = 243$ MPa. Linear hardening is assumed with hardening modulus $H = 0.2$ GPa.

The target number of time steps is set to 50, and 6 different RVE boundary condition variations are tested for small and finite strain regimes: namely, periodic and

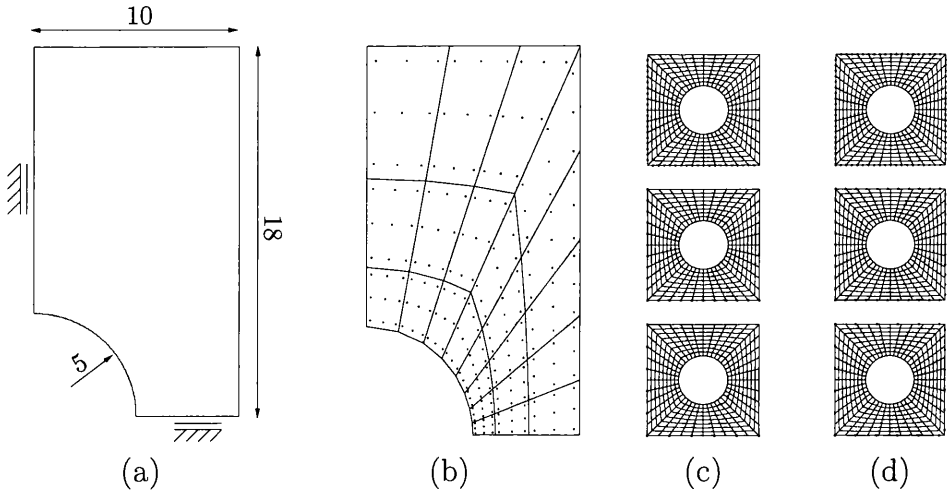

Figure 6.4: Interface discretization: (a) macro geometry and boundary conditions; (b) macro FE mesh with Gauss points; RVE FE mesh and interface nodes (c) Periodic b.c. and (d) Uniform Traction b.c. : (top) without the interface, (middle) with 10 divisions on edges, (bottom) with 5 divisions on edges

uniform traction b.c. with 5 and 10 interface nodes at edges, as well as without the interface, where all boundary nodes act as the interface, as shown in Figure 6.4 (c) and (d) respectively.

Figure 6.5 shows the reactions at the center of the plate with respect to the top edge displacement for small strains, obtained using 3 interface levels for uniform traction b.c. and periodic b.c. . While the RVE boundary discretized with 5 interface divisions differs only slightly, the RVE boundary discretized with 10 interface divisions is in good agreement with the solution acquired without the use of interface discretization. Interface discretization solution takes about 60 per cent of the time required without the interface at very small compromise of accuracy.

Figure 6.6 is the large strain version of Figure 6.5, and shows similar trends to its small strain counterpart. While the RVE boundary discretized with 5 interface divisions differs only slightly, the RVE boundary discretized with 10 interface divisions is in good agreement with the solution acquired without the use of interface discretization. Interface discretization solution takes about 50-60 per cent of the time required without the interface at negligible compromise of accuracy.

Convergence of residuals for small and finite strain regimes is given in Table 6.1 for periodic b.c. for three boundary interface variations, where it is shown that the quadratic asymptotic convergence is preserved in all three cases.

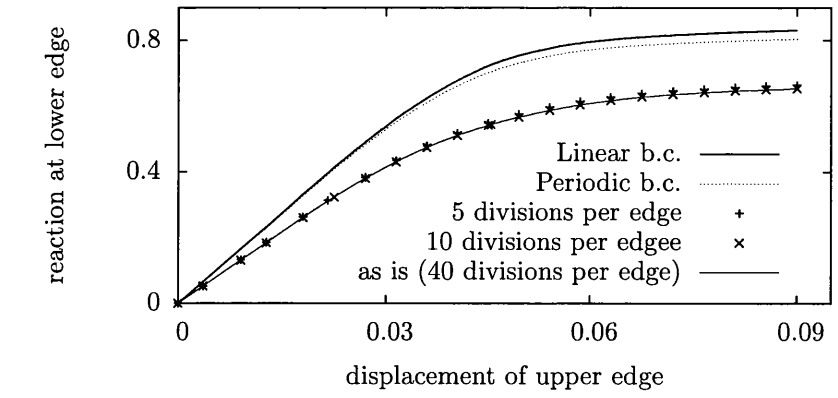

(a)

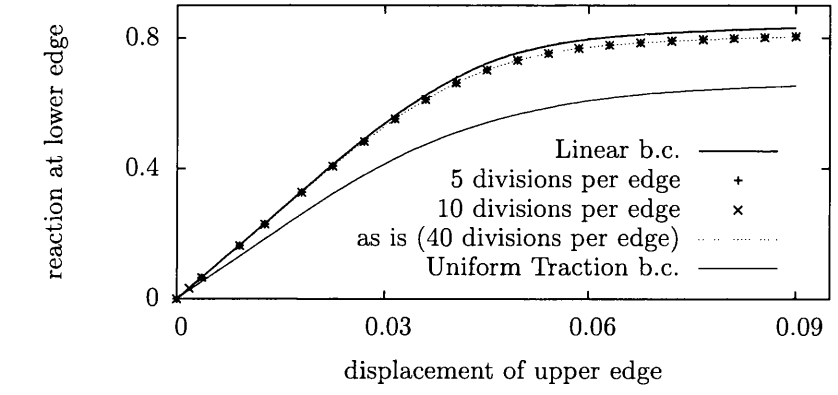

(b)

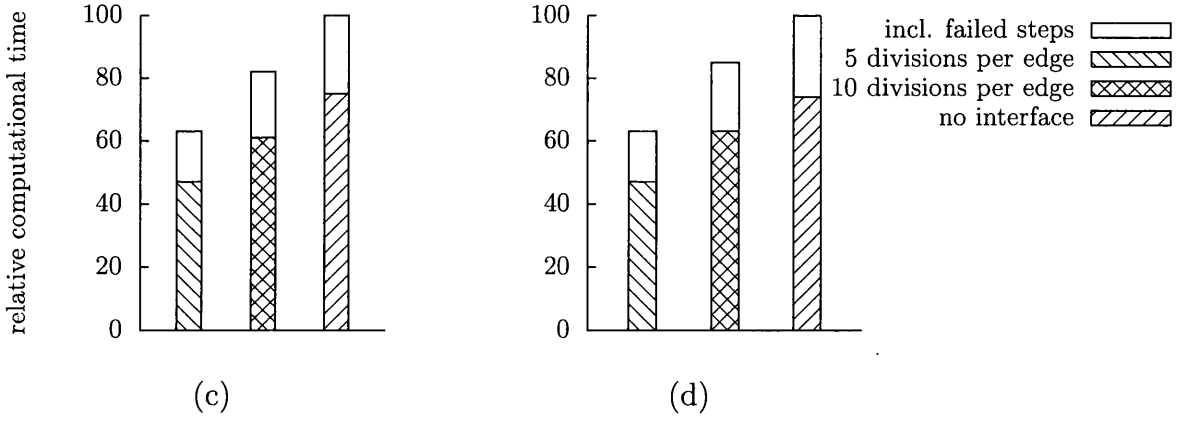

(c) (d)

Figure 6.5: Comparison of 3 interface levels at small strain regime: reaction/displacement diagram (a) uniform traction b.c. (b) periodic b.c. ; relative computational time required for (c) uniform traction b.c. (d) periodic b.c.

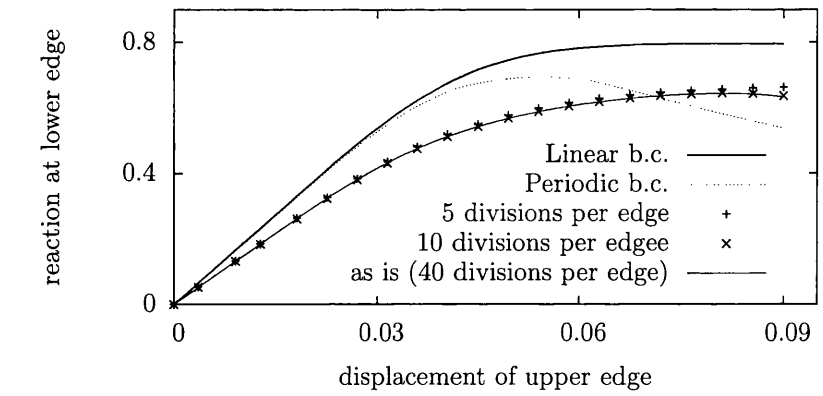

(a)

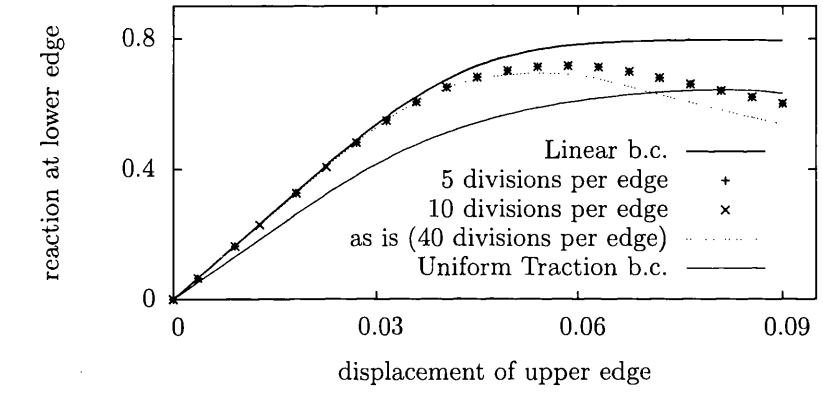

(b)

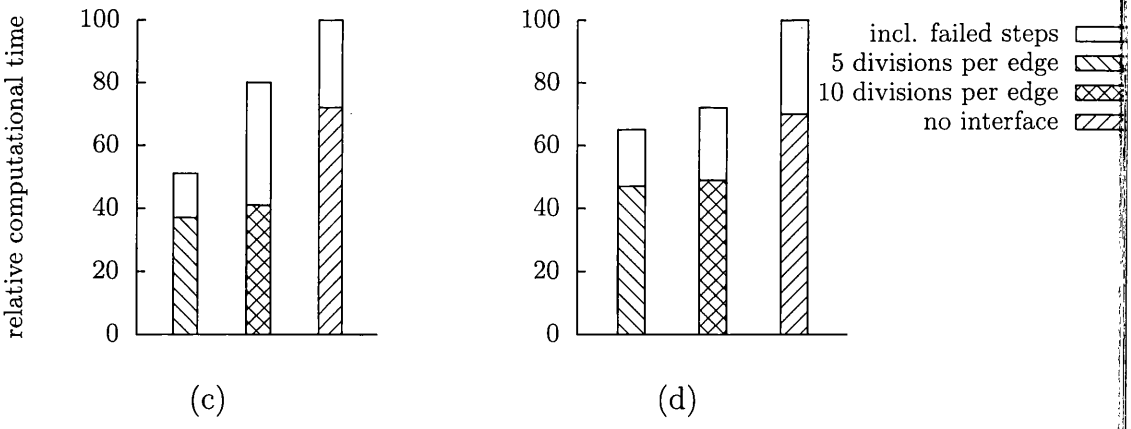

(c) (d)

Figure 6.6: Comparison of 3 interface levels at large strain regime: reaction/displacement diagram (a) uniform traction b.c. (b) periodic b.c. ; relative computational time required for (c) uniform traction b.c. (d) periodic b.c.

I	II	III
2.43E-01	2.43E-01	2.44E-01
5.91E-04	5.90E-04	5.82E-04
1.06E-05	8.77E-06	3.06E-06
2.07E-11	2.08E-11	2.25E-12

I	II	III
2.43E-01	2.43E-01	2.44E-01
5.96E-04	5.95E-04	5.87E-04
5.53E-06	1.18E-05	3.59E-06
3.79E-09	1.39E-08	4.77E-09
	1.75E-11	

Table 6.1: Convergence of residuals for periodic b.c. at time=0.2 for (left) small strain and (right) large strain regimes: (I) without the interface, (II) with 10 divisions on edges, (III) with 5 divisions on edges

6.2 Improved Initial Guess: Sub-Stepping

In this section, we will develop a sub-stepping procedure to increase the robustness and efficiency of the numerical solution scheme for the RVE equilibrium problem. The procedure has the potential to dramatically reduce computing times in coupled two-scale analyses under small strains. For finite strains, especially when dissipative constitutive models are used at the RVE level, the method almost becomes a necessity.

A number of schemes have been proposed in the literature to improve the robustness of stress-updating algorithms associated with conventional dissipative phenomenological constitutive models such as plasticity and visco-plasticity [93, 14, 26, 101]. Such schemes are generally based on the idea of ensuring convergence, for larger time steps, of the algorithm used in the solution of the non-linear system of algebraic equations resulting from the time-discretisation of the constitutive equations of the model. This has been achieved, for example, by means of improved initial guesses for the Newton-Raphson scheme adopted in the non-linear algebraic system solution [93, 14], by resorting to line-searches [26] or by sub-stepping [91, 125]. In the present context of multi-scale analysis, where the failure of the stress updating procedure has a far more serious impact on computing times, we borrow these ideas to develop a sub-stepping procedure capable of generating improved initial guesses for the Newton-Raphson scheme used in the iterative solution of the RVE equilibrium problem defined at each Gauss quadrature point of the discretised macro-continuum. We remark that the quadratic rates of asymptotic convergence that characterize the Newton-Raphson scheme are preserved by the methodology.

6.2.1 Cost of Failure

The success of the Newton-Raphson procedure in finding an acceptable solution can only be achieved if

1. The initial guess for $\mathbf{u}^{n+1}$ lies within the bowl of convergence of the Newton-Raphson scheme for the particular incremental problem in question. As the initial solution guess is typically taken as $\mathbf{u}^n$ (i.e., the initial guess for the updated configuration at t^{n+1} is the equilibrium configuration at t^n), this can be ensured by having a sufficiently small increment of applied loads $\boldsymbol{b}$ and $\boldsymbol{t}$ between t^n and t^{n+1}. Complementary procedures to enlarge the bowl of convergence of the Newton-type iterative scheme, such as line search algorithms [21], can be used to allow for larger load/time steps.

2. The updated stress (4.4) and (5.4) can be successfully obtained by the relevant computational procedure for all Gauss quadrature points of the mesh in question. Highly non-linear constitutive models are particularly prone to limit the maximum strain increment sizes for which the stress updating can be successfully accomplished. Situations where this issue becomes critical are discussed in references [13, 26, 14, 93].

Within the multi-scale constitutive modelling strategy, the stress updating procedure symbolically represented by (4.4) and (5.4) involves itself the solution of a (possibly highly non-linear) incremental equilibrium boundary value problem for the associated RVE. If a solution for the RVE equilibrium problem cannot be found for the given incremental macroscopic strain, then the updated stress cannot be computed and the macroscopic iterative solution algorithm has to be stopped. The usual course of action in such cases is to cut the macroscopic load increment and try to solve a new incremental problem with reduced load increment. In the course of the present research it has been found that this type of failure is not uncommon, even when the RVE has a relatively simple geometry and its material is modelled by, for example, standard von Mises-type elasto-plastic constitutive equations. This usually incurs a dramatic increase in overall computational costs. Note that for a macroscopic finite element discretization with n_{el} elements having n_{gauss} Gauss quadrature points each, there are $n_{el} \times n_{gauss}$ micro-scale boundary value problems to be solved at each macroscopic Newton-Raphson iteration of each macroscopic time/load step. If n_{iter} iterations are needed for the macroscopic Newton-Raphson scheme to converge, then each time/load step involves the solution of $n_{el} \times n_{gauss} \times n_{iter}$ micro-scale incremental boundary value problems. Hence, it is crucial that the solution procedure for the RVE equilibrium problem be made sufficiently robust in order to allow the macroscopic stress to be successfully updated for large macroscopic time/load increments, so that a solution for the whole macroscopic loading programme can be attained in as few increments as possible.

If the RVE equilibrium Newton-Raphson scheme fails to converge for a single step solution to $\bar{\boldsymbol{F}}^{n+1}$, set $\bar{\boldsymbol{F}}^{\text{fail}} \equiv \bar{\boldsymbol{F}}^{n+1}$ and proceed as follows:

1. Store RVE equilibrium state at t^n: $\{\tilde{\mathbf{u}}_{\text{stored}}, \bar{\boldsymbol{F}}^n_{\text{stored}}\} \leftarrow \{\tilde{\mathbf{u}}^n, \bar{\boldsymbol{F}}^n\}$
2. Sub-stepping. Compute improved guess for $\tilde{\mathbf{u}}^{n+1}$
   (a) Decompose $\bar{\boldsymbol{F}}^{\text{fail}}$, with reference to Figure 6.7:
      i. Set $\Delta\bar{\boldsymbol{F}}^{\text{fail}} \equiv \bar{\boldsymbol{F}}^{\text{fail}}(\bar{\boldsymbol{F}}^n)^{-1}$
      ii. Compute $\Delta\bar{\boldsymbol{F}}^{\text{int}} \equiv \sqrt{\Delta\bar{\boldsymbol{F}}^{\text{fail}}}$
      iii. Set mid-step macro deformation gradient, $\bar{\boldsymbol{F}}^{\text{int}} \equiv \Delta\bar{\boldsymbol{F}}^{\text{int}}\bar{\boldsymbol{F}}^n$
   (b) Set initial guess for $\tilde{\mathbf{u}}^{\text{int}}$, $\tilde{\mathbf{u}}^{(0)} \leftarrow \tilde{\mathbf{u}}^n$
   (c) Use Newton-Raphson algorithm to find $\tilde{\mathbf{u}}^{\text{int}}$ corresponding to $\bar{\boldsymbol{F}}^{\text{int}}$.
   IF attempt fails, THEN re-set $\bar{\boldsymbol{F}}^{\text{fail}} \equiv \bar{\boldsymbol{F}}^{\text{int}}$ AND GO TO 2. Repeat sub-stepping recursively until success is achieved.
   ELSE
      i. Set $\tilde{\mathbf{u}}^n \equiv \tilde{\mathbf{u}}^{\text{int}}$
      ii. Set $\bar{\boldsymbol{F}}^{\text{int}} \equiv \bar{\boldsymbol{F}}^{\text{fail}}$
      iii. GO TO (2c), exit when the outermost $\bar{\boldsymbol{F}}^{\text{int}}(\equiv \bar{\boldsymbol{F}}^{n+1})$ succeeds
3. Retrieve equilibrium state at t^n
   $\{\tilde{\mathbf{u}}^n, \bar{\boldsymbol{F}}^n\} \leftarrow \{\tilde{\mathbf{u}}_{\text{stored}}, \bar{\boldsymbol{F}}^n_{\text{stored}}\}$
4. Try $\bar{\boldsymbol{F}}^{n+1}$, using $\boldsymbol{\xi}^{n+1} \leftarrow \boldsymbol{\xi}^n$ and $\tilde{\mathbf{u}}^{\text{int}}$, available from the last step of (2).

Box 6.1: Recursive Sub-stepping Procedure

6.2.2 Robustness of the Newton-Raphson Scheme

Consider an RVE (associated with *one* Gauss integration point of the macroscopic mesh) for which an equilibrium state has been found at time station t^n. The equilibrium state of the RVE is characterized by the vector $\tilde{\mathbf{u}}^n$ of nodal displacement fluctuations, a field $\bar{\boldsymbol{\xi}}^n$ of internal variable sets and a (given) macro deformation gradient $\bar{\boldsymbol{F}}^n$. The common practice in the solution of conventional solid mechanics problems is to choose

$$\tilde{\mathbf{u}}^{(0)} := \tilde{\mathbf{u}}^n \tag{6.6}$$

as the initial guess for $\tilde{\mathbf{u}}^{n+1}$ when an iterative process of the type (4.58,4.59) is started for time/load step $[t^n, t^{n+1}]$. In the present context, however, numerical experience has demonstrated that this standard choice of initial guess too often falls outside the

bowl of convergence of the Newton-Raphson scheme, leading to convergence failure, even for relatively small incremental macroscopic deformations. This issue becomes particularly critical for elasto-plastic RVEs and has been frequently observed for RVEs with a standard J_2 finite elasto-plasticity constitutive law. Whenever the iterative process fails to converge, the updated macroscopic stress cannot be computed. The usual alternative then is to stop the macroscopic analysis and re-start it from the last equilibrium solution (at t^n) with a reduced load/time increment. As briefly explained earlier, the computational costs incurred by such failures in the present context are massive.

6.2.3 Sub-Stepping Procedure

The improved initial guess for the Newton-Raphson scheme (4.58) for solution of (4.53) will be obtained by means of a rather simple *sub-stepping* procedure. If, for a given macroscopic deformation gradient $\bar{\boldsymbol{F}}^{n+1} = \bar{\boldsymbol{F}}^{\text{fail}}$, the Newton-Raphson scheme diverges or fails to converge within a reasonable number of iterations, we proceed as follows (refer to Figure 6.7):

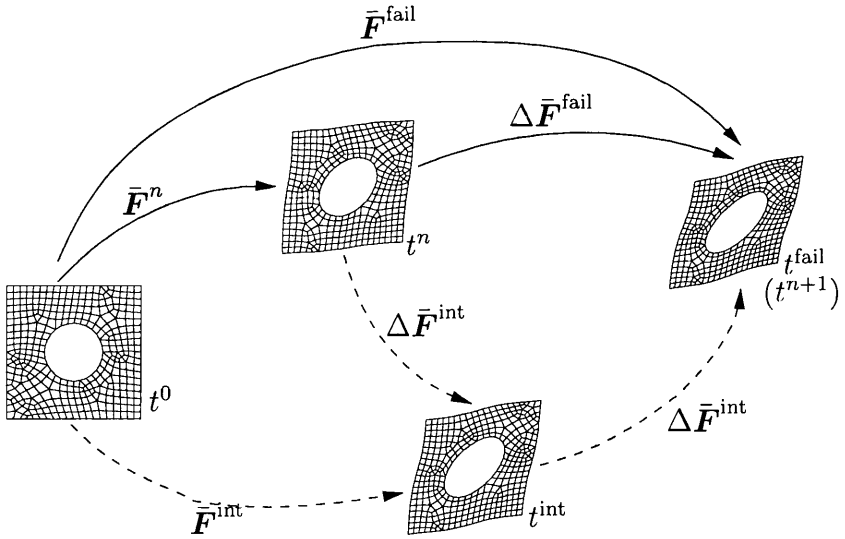

Figure 6.7: Decomposition of the deformation gradient for a failed time step $t^n \rightarrow t^{n+1}$ into two sub-steps $t^n \rightarrow t^{\text{int}} \rightarrow t^{n+1}$.

1. Split the original deformation step $\Delta\bar{\boldsymbol{F}}^{\text{fail}} \equiv \bar{\boldsymbol{F}}^{\text{fail}}(\bar{\boldsymbol{F}}^{n})^{-1}$ into two substeps and define an *intermediate configuration* so that we now have

$$\bar{\boldsymbol{F}}^{\text{int}} \equiv \Delta\bar{\boldsymbol{F}}^{\text{int}}\bar{\boldsymbol{F}}^{n}; \qquad \bar{\boldsymbol{F}}^{n+1} = \Delta\bar{\boldsymbol{F}}^{\text{int}}\bar{\boldsymbol{F}}^{\text{int}}, \tag{6.7}$$

where[1]

$$\Delta\bar{\boldsymbol{F}}^{\text{int}} \equiv \sqrt{\Delta\bar{\boldsymbol{F}}^{\text{fail}}} \tag{6.8}$$

2. Use $\tilde{\mathbf{u}}^n$ as an initial guess for the Newton-Raphson scheme to find $\tilde{\mathbf{u}}^{\text{int}}$ – the solution of the RVE equilibrium problem at the intermediate configuration corresponding to $\bar{\boldsymbol{F}}^{\text{int}}$.

3. Use the intermediate solution $\tilde{\mathbf{u}}^{\text{int}}$ as an initial guess to find $\tilde{\mathbf{u}}_{\text{est}}$ – the solution of the RVE equilibrium problem at $\bar{\boldsymbol{F}}^{n+1}$ following the two-step path $\bar{\boldsymbol{F}}^n \rightarrow \bar{\boldsymbol{F}}^{\text{int}} \rightarrow \bar{\boldsymbol{F}}^{n+1}$.

4. Finally, use $\tilde{\mathbf{u}}_{\text{est}}$ as an initial guess to find $\tilde{\mathbf{u}}^{n+1}$ – the RVE equilibrium solution for the required one-step path $\bar{\boldsymbol{F}}^n \rightarrow \bar{\boldsymbol{F}}^{n+1}$.

Note that procedures 2 and 3 above are also susceptible to convergence failure. If the RVE equilibrium Newton-Raphson scheme fails to converge for steps 2 or 3 (or both), then the sub-stepping procedure 1–4 is applied recursively, i.e., two sub-steps are performed for every failed step, until an estimate $\tilde{\mathbf{u}}_{\text{est}}$ for $\tilde{\mathbf{u}}^{n+1}$ is successfully obtained. The recursive procedure is given in Box 6.1 in pseudo-code format.

Remark: It could be argued that the incremental macro stress could be taken as the volume average of the microscopic stress field associated with estimate $\tilde{\mathbf{u}}_{\text{est}}$ itself. It is important to note, however, that if one chooses to do so, consistency between the macroscopic constitutive tangent operator and the stress updating procedure is lost, and so is the highly desirable quadratic rate of asymptotic convergence that characterizes the Newton-Raphson scheme used to solve the macroscopic equilibrium problem. Step 4 above is crucial to preserve this consistency. Experience has shown that the extra computation time spent in step 4 is usually more than compensated by the gain in convergence rate and its consequent reduction in the number of (potentially massively expensive) iterations required in the solution of the macroscopic incremental equilibrium problem.

6.2.4 Numerical Examples

Two numerical examples are presented to demonstrate the effectiveness of proposed sub-stepping scheme. First, a single RVE is subjected to a range of incremental macroscopic deformations to determine the convergence retrieving characteristics of the scheme. Then, a multi-scale example consisting of a macroscopic initial boundary value problem with a multi-scale based constitutive model is presented

[1] We use a Newton-Raphson procedure to solve for $\Delta\bar{\boldsymbol{F}}^{\text{int}}$ in (6.8), where we define the residual as $\boldsymbol{R} = \Delta\bar{\boldsymbol{F}}^{\text{int}}\Delta\bar{\boldsymbol{F}}^{\text{int}} - \Delta\bar{\boldsymbol{F}}^{\text{fail}}$, which is then linearized in a standard fashion.

to illustrate the savings on overall computational cost resulting from the use of the sub-stepping procedure.

Single-scale test

A square RVE under plane strain with a 15% void described by a single hole at its centre, is discretized by a structured mesh of 320 quadratic (8-noded) isoparametric elements with reduced (2×2) Gauss integration quadrature. The material of the RVE is modelled by means of a standard multiplicative hyperelastic-based von Mises elasto-plastic model with Young's modulus $E = 210$ GPa, Poisson's ratio $\nu = 0.29$ and initial yield stress $\sigma_0 = 450$ MPa. Linear hardening is assumed with hardening modulus $H = 0.2$ GPa. The mesh of the RVE in its initial configuration is shown in Figure 6.4 (c).

To test the proposed procedure under the large strains assumption, macro deformation gradients of the form

$$\bar{\boldsymbol{F}} = \begin{bmatrix} 1 + \alpha \times 0.05 & \beta \times 0.05 \\ 0 & 1 + \alpha \times 0.05 \end{bmatrix}$$

are imposed upon the RVE, starting from its initial configuration, for various combination of parameters α, $\beta \in [0, 1]$. Note that by varying the multipliers α and β between 0 and 1, the above tensor covers a range of the space of deformation gradients having combinations of strains with up to 5% straining in the volumetric and pure shear strain directions.

For each combination (α, β), we record the number of sub-steppings required to obtain an initial guess for $\tilde{\mathbf{u}}^{n+1}$ leading to single step convergence of the RVE equilibrium problem. A 30×30 grid of (α, β) pairs is used here to assess the algorithm over the above range of incremental deformations. The contour plot of the resulting surface in the α–β space is shown Figure 6.8(a). Numbers refer to the maximum recursion depth of sub-stepping required to achieve a convergent estimate. It illustrates clearly the effectiveness of the sub-stepping algorithm in allowing single step convergence for relatively large deformation gradient increments of the RVE. Note that convergence with the conventional initial guess (6.6), i.e., without the proposed sub-stepping algorithm, can only be achieved for a very small range of incremental deformation gradients - the black region at the left-bottom corner of Figure 6.8(a) and (b). White regions correspond to incremental deformation gradients for which the Newton-Raphson scheme fails even after the use of the sub-stepping procedure.

This result indicates that without the proposed procedure the macroscopic increments of load/time will, potentially, have to be severely limited due to the lack of robustness of the multi-scale stress updating constitutive algorithm. Such limitations usually incur substantial computational costs. This will be confirmed in

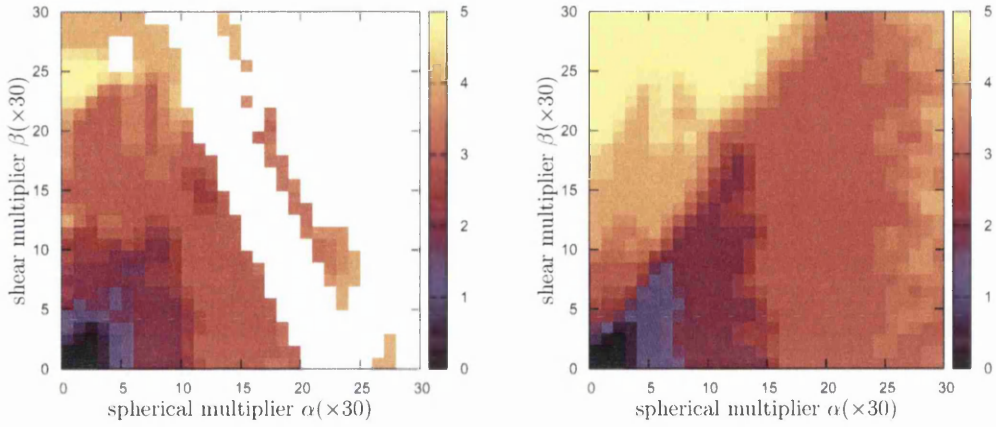

Figure 6.8: Single-scale test: maximum recursion depth of sub-stepping required to achieve a convergent estimate for (a) finite strains and, (b) small strain regime

the numerical example discussed in Section 6.2.4. Under the assumption of small deformations, the macro infinitesimal strain

$$\bar{\boldsymbol{\varepsilon}} = \begin{bmatrix} \alpha \times 0.05 & \beta \times 0.05 \\ \text{sym.} & \alpha \times 0.05 \end{bmatrix}$$

is imposed instead. The resulting contour plot is shown in Figure 6.8(b). The improvements obtained in this case are also substantial. Note that the proposed initial estimates leads to convergence for the whole range of incremental infinitesimal strain combinations covered by the present analysis. In summary, the use of the sub-stepping procedure has greatly enhanced the robustness of the Newton-Raphson scheme at the RVE level.

Multi-scale test

The purpose of this example is to demonstrate the overall computing time savings achieved with the application of the proposed sub-stepping procedure in the solution of macroscopic initial boundary value problems characterized by a multi-scale constitutive description of the underlying material. A plate measuring 20×36 cm containing a 5 cm radius hole in its centre is stretched longitudinally by 0.5 per cent. Both infinitesimal and large strain theories are considered. Because of symmetry, only a quarter of the plate is considered, which is discretized into 24 8-noded quadratic elements with (3×3) Gauss integration quadrature. See Figure 6.4 for the geometry, macro and RVE mesh.

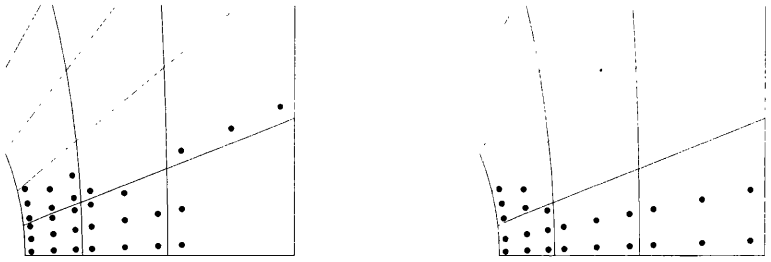

(a) (b)

Figure 6.9: Multi-scale test. RVEs for which the sub-stepping procedure was invoked: (a) small strains, (b) large strains

The plate is assumed to be made of a porous elasto-plastic material with computational multi-scale constitutive law described by RVEs of initial geometry and discretization identical to the one used in the previous examples . Plane stress condition is assumed and the RVE matrix material is modelled by a von Mises type elastoplastic law with Young's modulus $E = 70$ GPa, Poisson's ratio $\nu = 0.2$, initial yield stress $\sigma_0 = 243$ MPa and linear hardening modulus $H = 0.2$ GPa. Under the large strain assumption, a Hencky hyperelasticity-based multiplicative extension of the infinitesimal constitutive law [13] is adopted. Two types of RVE kinematical constraints are considered: periodic boundary fluctuations and minimum kinematical constraint (uniform boundary traction).

The loading programme consists in applying incrementally a uniform vertical (stretching) displacement to the nodes of the top edge of the mesh until a total axial straining of 0.5% is achieved. The target number of time steps is set as 50, and the problem is first solved without sub-stepping. Note that for the method to be effective, the maximum number of RVEs allowed to substep has to be limited, as well as the maximum depth of recurrent sub-stepping. In this example, we have set these limits to 10 and 5 respectively. We assume the method has failed to recover convergence if either of these limits is exceeded.

Results of small strain analysis for periodic and uniform traction boundary conditions are shown in Figure 6.10. For the periodic boundary condition, use of substepping reduces the required number of time steps from 133 to 60, which corresponds to 44% reduction for the computational time. For the uniform traction boundary condition, the required number of time steps is reduced from 118 to 56, here the computational time with substepping is 47% of the time without it.

Convergence of residuals for the micro Newton-Raphson procedure during substepping of a typical failed step (taking place at the last macro Newton-Raphson step of time 0.3 at the RVE at left bottom corner) is depicted in Table 6.2 (top).

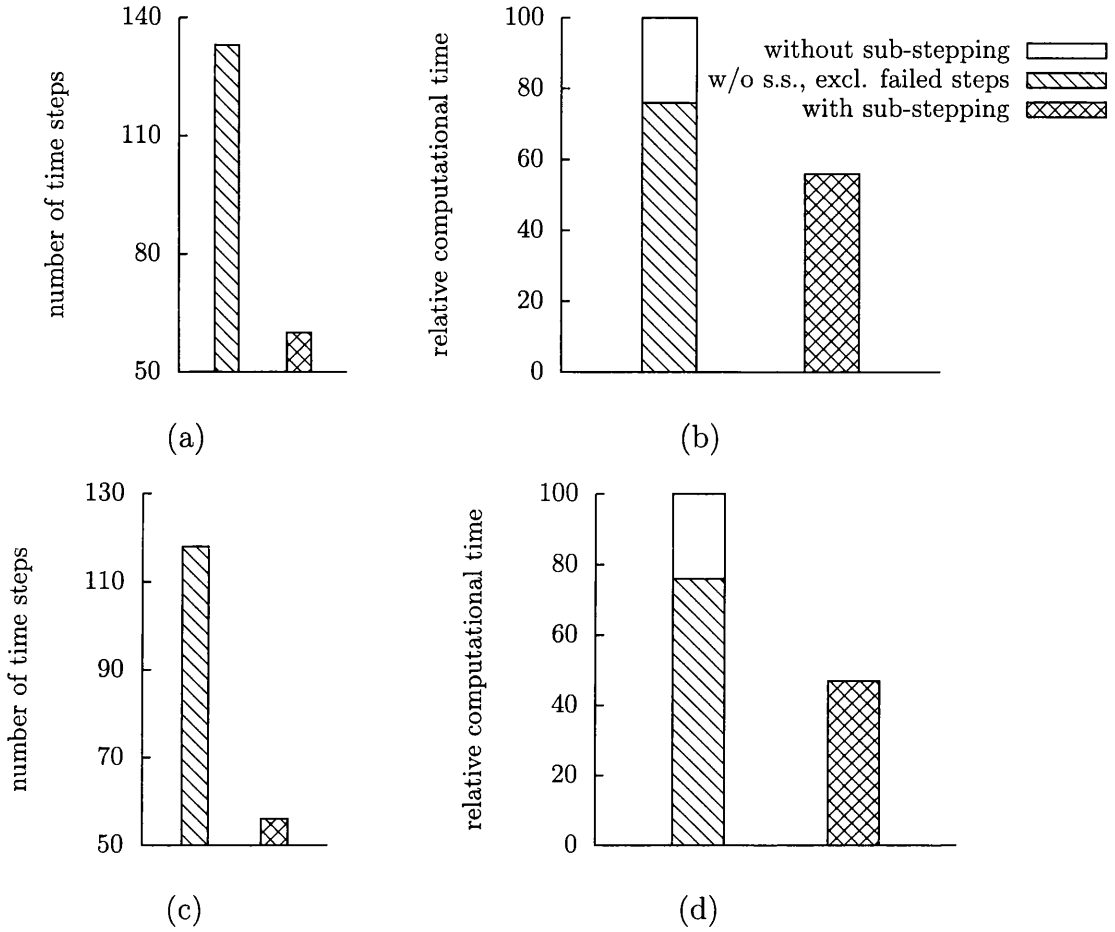

Figure 6.10: Multi-Scale Small Strain Test: (left) time steps and (right) relative computational time required for (top) periodic b.c. and (bottom) uniform traction b.c.

Sub-stepping is activated following failure of the original procedure (I). Second half of this first sub-step layer (III) fails as well, which is recovered by sub-steps IV and V respectively. Note that the estimate for step VI is set by the solution at step V, and is very close to the solution, as clearly seen in the first residual of this step.

Under the assumption of finite strains, the savings achieved by the proposed methodology are considerably more pronounced than under the small strains assumption. Figure 6.11 reveals overall speed-up factors of 3 to 4. For the periodic boundary condition, the required number of time steps is reduced from 415 to 82, where for the uniform traction boundary condition, the reduction is from 281 to 80.

The large strain version of the table of convergence of residuals for the micro Newton-Raphson procedure during sub-stepping of a typical failed step (taking place

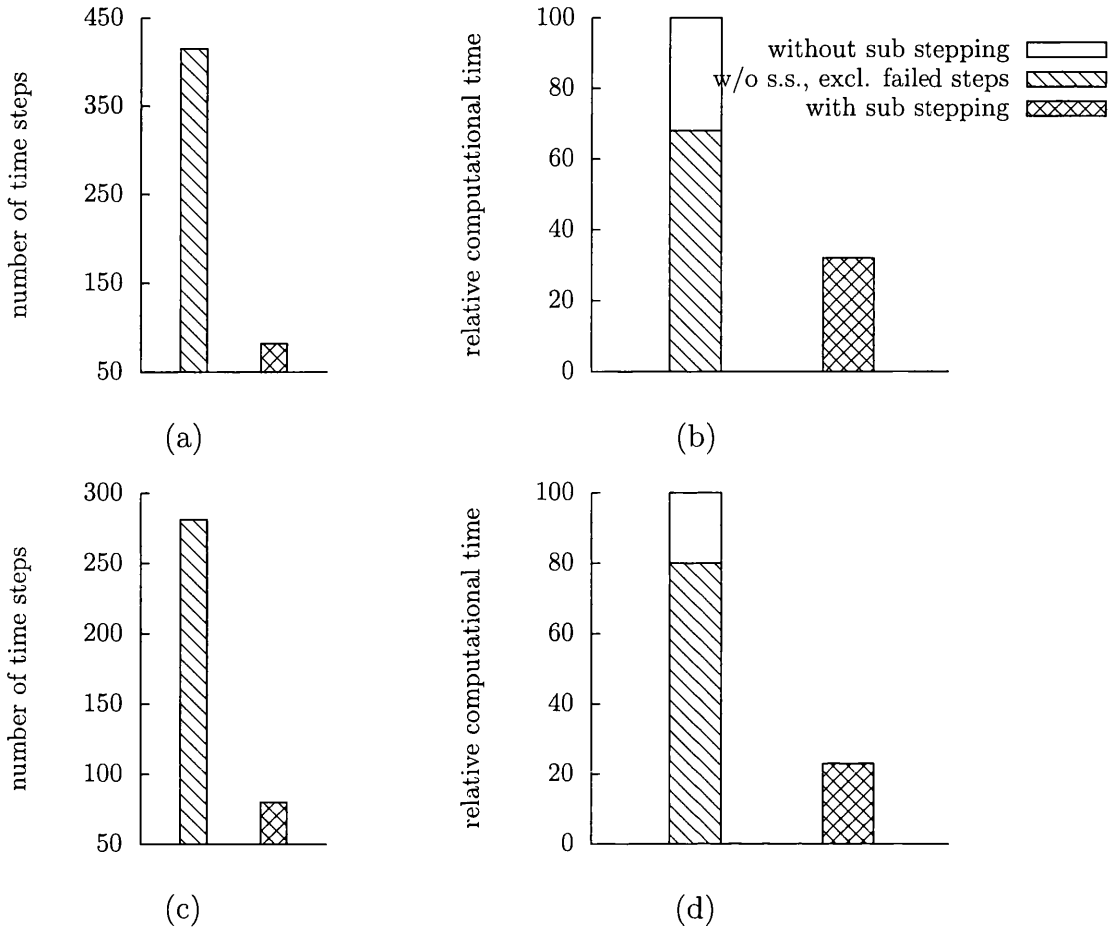

Figure 6.11: Multi-Scale Finite Strain Test: (left) time steps and (right) relative computational time required for (top) periodic b.c. and (bottom) uniform traction b.c.

at the last macro Newton-Raphson step of pseudo time 0.3 at the RVE at left bottom corner) is depicted in Table 6.2 (bottom). 3 depths of recurrent sub-stepping is necessary to recover convergence. Note that, as the method is only employed as an estimate for the Newton-Raphson scheme, the reaction/displacement diagrams with and without sub-stepping coincide exactly (down to the stipulated RVE equilibrium convergence tolerance). As expected, the RVEs for which the sub-stepping was invoked correspond to concentrations of plastic flow, as shown in Figure 6.9.

Both examples demonstrate a dramatic improvement in the robustness of the microscopic scale Newton-Raphson scheme, leading to substantial savings in overall computing time, while the quadratic rate of asymptotic convergence of the macroscopic scale Newton-Raphson scheme is preserved.

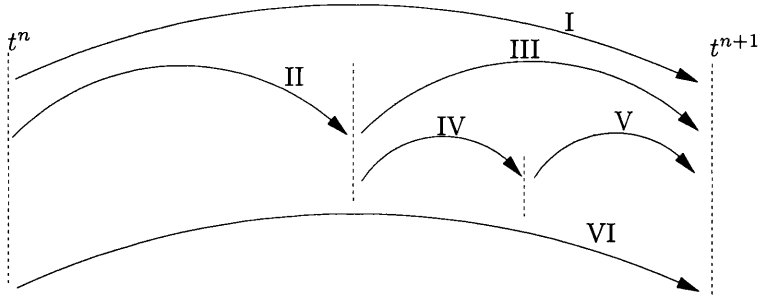

I	no	conv.						
II	3.90E-02	1.13E-04	7.92E-04	2.45E-04	8.83E-06	2.90E-06	1.63E-07	5.88E-13
III	no	conv.						
IV	7.05E-01	3.52E-03	3.43E-02	7.38E-04	1.27E-04	1.67E-05	5.55E-06	9.68E-10
V	7.05E-01	3.54E-03	2.83E-02	7.36E-04	1.77E-04	3.40E-05	2.98E-08	2.71E-14
VI	4.70E-05	1.60E-06	4.59E-11					

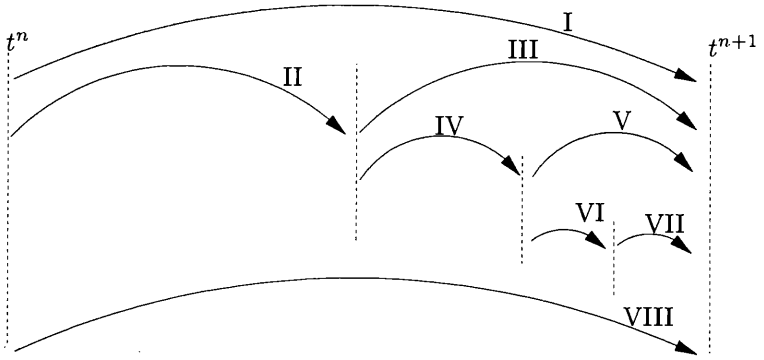

I	no	conv.						
II	9.28E-01	3.39E-06	7.17E-13					
III	no	conv.						
IV	9.94E-01	5.29E-04	2.44E-03	1.48E-04	3.9E-05	7.33E-06	1.04E-06	8.99E-08
	3.78E-13							
V	no	conv.						
VI	4.97E-01	2.58E-03	2.51E-02	3.73E-04	1.6E-04	1.94E-05	1.53E-06	3.29E-10
VII	4.97E-01	2.62E-03	1.3E-02	4.87E-04	9.4E-05	3.5E-05	1.45E-06	1.11E-10
VIII	6.06E-05	3.53E-07	1.16E-11					

Table 6.2: Convergence of residuals for micro Newton-Raphson procedure during sub-stepping of a typical failed step, pseudo time=0.3, last macro iteration, RVE at left bottom corner, (top) small strain test, (bottom) finite strain test

Chapter 7

Applications I: Fibre Reinforced Composites

Composites are natural or engineered materials that consist of two or more distinct phases or constituents with significantly different physical or chemical properties. The constituents are separated by a distinct interface which remains separate and distinct on a macroscopic level within the finished structure. The continuously distributed base constituent or phase is termed *matrix*. It surrounds the *reinforcement* phase, which usually serves to improve desired properties of the matrix. Obvious examples of natural composites are wood, bone and teeth. Wood consists of cellulose fibres embedded in a matrix of lignin, whereas bone or teeth are composed of hard inorganic crystals in a matrix dominated by collagen. Design and manufacture of synthetic composites fall into a number of areas of interest, so they are classified according to the viewpoint of that specific area in question. For a detailed read, please refer to introductory texts such as [51] or [72].

The shape, size and distribution of the reinforcement plays a significant role in the overall response of the composite. *Particle* and *short fibre* reinforced composites generally have a random distribution of the reinforcement phase, although they can be also be aligned in a preferred direction. *Long fibre* composites exhibit directional anisotropy, either unidirectional or woven into 2 directions. Long fibre composites with high fibre volume ratios tend to be packed in hexagons, whereas as the fibre volume ratio gets smaller, the packing becomes random. *Laminates* consist of layers of long fibres with altered orientations.

7.1 Introduction and Background

Accurate micro-mechanical predictions of elastic constants of a composite, which take the shape, size and distribution of the reinforcement into account, as well as

the material properties of both the matrix and the reinforcement are very desirable in engineering design, as they offer the possibility of tailoring the composite for specific needs. In the first part of this chapter we will obtain micro-mechanical predictions of elastic constants for long fibre reinforced (boron/aluminium and glass/epoxy) composites from solution of the boundary value problem of an RVE. Similar studies have appeared in the literature since 1980's: Adams and Crane [1] used separate boundary conditions for normal and shear loading, while Zhang and Evans [130] and Shi *et al.* [100] used axisymmetric unit cells. Brockenbrough *et al.* [10] investigated fibre packing and shape on the overall properties using linear boundary conditions. Sun and Vaidya [109] imposed separate boundary conditions for each property sought, Xia *et al.* [124] extracted the material properties of a square packed periodic RVE from the compliance matrix. Michel *et al.* [75] decomposed boundary displacements and solved for fluctuations of displacement in response to the prescribed strain, using Fast Fourier Transform instead of Finite Element Method.

First, mechanical properties for a boron/aluminium composite will be extracted from homogenization of square and hexagonal packed RVEs, and compared to earlier works. Next, predictions obtained from homogenized RVEs for varying fibre volume ratios of a glass/epoxy composite are compared to mechanics of materials and analytical (Hashin-Rosen and Halpin-Tsai) approaches.

Fully coupled two-scale analyses will be performed in small and large strain regimes, where no material model is assumed at the macroscopic level, and the results will be compared to those obtained using single scale anisotropic continuum material models.

A strong interface is assumed with perfect bonding of the matrix and reinforcement phases in all applications of this chapter. The methodology used for single scale examples will be outlined first:

Mechanics of materials approach employs the slab model shown in Figure 7.1(a) and is based on Voigt and Reuss assumptions of uniform strain or uniform stress, depending on the property sought. Voigt [123] assumed all the ingredients of a polycrystal experienced the same state of deformation. This crude assumption of uniform strain coincides with a simple volume weighing of phase stiffnesses, called *the rule of mixtures*:

$$K = (1-f)\,K_m + f\,K_f \tag{7.1}$$

$$G = (1-f)\,G_m + f\,G_f \tag{7.2}$$

where subscripts $(.)_f$ and $(.)_m$ denote the fibre and matrix, while f denotes the fibre volume ratio. As pointed in Chapter 4, rule of mixtures corresponds to a particular

case of the present approach, given by (4.16). Dual to Voigt assumption is uniformity of the stress over the composite, due to Reuss [95]:

$$\frac{1}{K} = \frac{1-f}{K_m} + \frac{f}{K_f} \tag{7.3}$$

$$\frac{1}{G} = \frac{1-f}{G_m} + \frac{f}{G_f} \tag{7.4}$$

which coincides with volume weighing of compliances. As Hill [46] notes, in the Voigt model the forces between grains could not usually be in equilibrium, while in Reuss model the distorted grains could not fit together. However, as shown by Hill [46], Voigt and Reuss models are the *upper* and *lower bounds* for the elastic moduli:

$$K_R \leq K \leq K_V \ , \ G_R \leq G \leq G_V \tag{7.5}$$

The mechanics of materials prediction of each property will be discussed under the relevant heading.

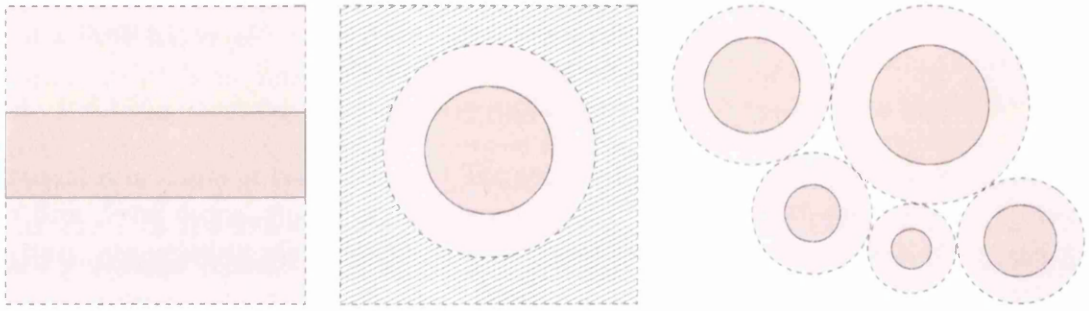

(a) (b) (c)

Figure 7.1: Models used by analytical approaches

Halpin and Tsai simplified Hermans' generalized self-consistent model [45] for a composite with aligned continuous fibres [39], and obtained a general closed form expression applicable to an extended range of reinforcement geometries:

$$\frac{\bar{P}}{P_m} = \frac{(1+\xi\eta f)}{1-\eta f} \ ; \ \eta = \frac{(\frac{P_f}{P_m}-1)}{(\frac{P_f}{P_m}+\xi)} \tag{7.6}$$

where, $\bar{P}$ is the composite property, which could be K, G or G_A. ξ has different values for the property sought. We note here the criticism by Christensen and Lo [18] and Hashin [43] about Hermans' work [45], which has implications on the Halpin and Tsai equations which are derived from it.

Hashin and Rosen used the *composite spheres/cylinders model*, where the volume is assumed to be filled by varying sizes of composite spheres having the same outside radius to inside radius ratios, as in Figure 7.1 (c), to calculate only the effective longitudinal Young's modulus, longitudinal shear modulus, longitudinal Poisson's ratio and the transverse bulk modulus of a composite [42]. They have not supplied closed form expressions for transverse properties but gave bounds for them. Christensen and Lo [18] derived G_{23} later, assuming a cylindrical particle encased in a matrix shell which is embedded within an infinite homogeneous medium whose unknown properties are the same as the composite, Figure 7.1 (b). The Hashin-Rosen-Christensen prediction of each property will be discussed under the relevant heading.

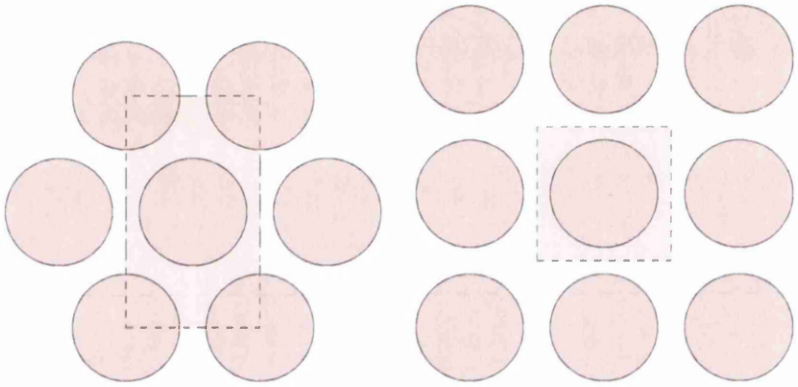

Figure 7.2: Fibre packing models : (a) Hexagonal (b) Square

Three dimensional RVEs , either square array packed cubic or hexagonal packed rectangular prisms, were used to represent various fibre volume ratios f between 10% and 60%; see, eg. Figure 7.3 for hexagonal and square packed RVE's with $f = 47\%$. To extract the homogenized response, the 3D RVE, which is aligned so that fibre direction coincides with axis 1, is subjected to a test strain. The homogenized tangent stiffness is equivalent to the transversely isotropic elasticity tensor (see Chapter 3):

$$\begin{bmatrix} C_{11} & C_{12} & C_{12} \\ & C_{22} & C_{23} \\ sym. & & C_{22} \end{bmatrix} \equiv \begin{bmatrix} \frac{E_A^2(\nu-1)}{k} & -\frac{E_A E \nu_A}{k} & -\frac{E_A E \nu_A}{k} \\ & \frac{E(E\nu_A^2 - E_A)}{k(1+\nu)} & -\frac{E(E\nu_A^2 + E_A\nu)}{k(1+\nu)} \\ sym & & \frac{E(E\nu_A^2 - E_A)}{k(1+\nu)} \end{bmatrix} \tag{7.7}$$

(a) (b) (c)

Figure 7.3: RVE initial meshes with (a) 3D hexagonal and (b) 3D square packings, fibre volume ratio f= 47 %, (c) 2D slab model

which is repeated here for convenience. Four independent equations emerge as:

$$\begin{aligned} C_{11} - \frac{E_A^2(\nu - 1)}{k} &= 0 \\ C_{22} - \frac{E(E\nu_A^2 - E_A)}{k(1+\nu)} &= 0 \\ C_{12} + \frac{E_A E \nu_A}{k} &= 0 \\ C_{23} + \frac{E(E\nu_A^2 + E_A\nu)}{k(1+\nu)} &= 0 \end{aligned} \tag{7.8}$$

where $k = E_A(\nu - 1) + 2E\nu_A^2$. Because of the apparent non-linearity in (7.8), a Newton-Raphson procedure is used to solve for the unknowns E_A, E, ν, ν_A. The procedure is repeated for the RVE constrained by linear displacements and periodic displacements boundary conditions.

Moduli G_A and G follow directly from C_{44} and C_{55} respectively.

2D RVEs were used to computationally represent the slab model, for various fibre volume ratios f between 10% and 90%; see, eg. Figure 7.3. Each RVE is a unit square which is composed of 110 quadratic finite elements. The 2D RVE is subjected to a test strain. The tangent stifness is recorded, which is then equated to the plane stress version of the transversely isotropic elasticity tensor (see Chapter 3) , found

by equating the out-of-plane components of stress to zero:

$$\begin{bmatrix} C_{11} & C_{12} & 0 \\ & C_{22} & 0 \\ sym. & & C_{33} \end{bmatrix} \equiv \frac{1}{1-n\nu^2} \begin{bmatrix} E_A & E\nu & 0 \\ & E & 0 \\ sym. & & G_A(1-n\nu^2) \end{bmatrix} \tag{7.9}$$

where $n = \frac{E}{E_A}$. G_A is given by C_{33} and n, ν are found as:

$$n = \frac{C_{22}}{C_{11}} \;\; ; \;\; \nu = \frac{C_{12}}{C_{22}} \tag{7.10}$$

which are then used to find the remaining unknowns E_A, E:

$$E_A = C_{11}(1-n\nu^2) \;\; ; \;\; E = C_{22}(1-n\nu^2) \tag{7.11}$$

The procedure is repeated for the RVE constrained by linear displacements, periodic displacements and uniform traction boundary conditions.

7.2 Variation of Material Properties with Packing Order

We consider a Boron/Aluminium composite, characterized by elastic matrix and fibre with perfect bonding, and following constituent material properties:

$$\begin{aligned} E_f &= 379.3 \text{ MPa} \;\; ; \;\; E_m = 68.3 \text{ MPa} \\ \nu_f &= 0.1 \;\; ; \;\; \nu_m = 0.3 \end{aligned}$$

Sun and Vaidya [109] compared numerical approximations for mechanical properties of the Boron/Aluminium composite with experimental [53] and analytical [42] results, as well as other workers. In the following, we use hexagonal and square packed RVEs of Figure 7.3, and derive predictions using the method outlined earlier.

Comparison of our results with Sun and Vaidya [109], Kenaga *et al.* [53] and Hashin-Rosen-Christensen [42, 18] are depicted in Table 7.1. In all but one property sought, our numerical analysis recovers the experiment and analytical calculation, as well as the reference computational work. Based on computational and analytical values, we believe that ν was reported in [53] instead of ν_A.

We remark the use of interface nodes for imposing periodic boundary conditions on non-periodic meshes. Note that structured periodic discretization of complex micro geometries is not always practical, since structured meshing is only limited to simple geometries.

Elastic Constant	Hex. Pack	Squ. Pack	Hex. in [109]	Squ. in [109]	[53]	[42]+ [18]
E_A	215.3	215.3	215	215	216	214.9
G_A	54.2	54.4	54	57.2	52	54.0
ν_A	0.195	0.195	0.19	0.19	0.29	0.204
E	133.4	144.0	136.5	144	140	128.8
G	51.0	45.8	57.9	45.9	-	51.5
ν	0.309	0.255	0.34	0.29	-	0.25

Table 7.1: Variation of Material Properties with Packing Order. Comparison of results with Sun and Vaidya [109], Kenaga *et al.* [53] and Hashin-Rosen-Christensen [42, 18].

7.3 Variation of Material Properties with Fibre Volume Ratio

We consider a glass/epoxy composite, characterized by elastic matrix and fibre with perfect bonding, and following constituent material properties:

$$\begin{aligned} E_f &= 110 \text{ MPa} \ ; \ E_m = 3.4 \text{ MPa} \\ \nu_f &= 0.22 \ ; \ \nu_m = 0.35 \end{aligned}$$

and study variation of mechanical properties of the composite with fibre volume ratios by comparing predictions obtained from 2D and 3D RVEs using the method outlined earlier to mechanics of materials and analytical approaches.

7.3.1 Longitudinal Young's Modulus

The mechanics of materials approach assumes that both the matrix and fibre are subjected to an *equal strain* in the longitudinal (fibre) direction, so that:

$$\varepsilon_A = \varepsilon_{Am} = \frac{\sigma_{Am}}{E_{Am}} = \varepsilon_{Af} = \frac{\sigma_{Af}}{E_{Af}} \tag{7.12}$$

The overall longitudinal stress is given by:

$$\sigma_A = (1-f)\sigma_{Am} + f\sigma_{Af} \tag{7.13}$$

which leads to the rule of mixtures approximation of the longitudinal modulus as:

$$\begin{aligned} E_A &= \frac{\sigma_A}{\varepsilon_A} \\ &= (1-f)E_m + fE_f \end{aligned} \tag{7.14}$$

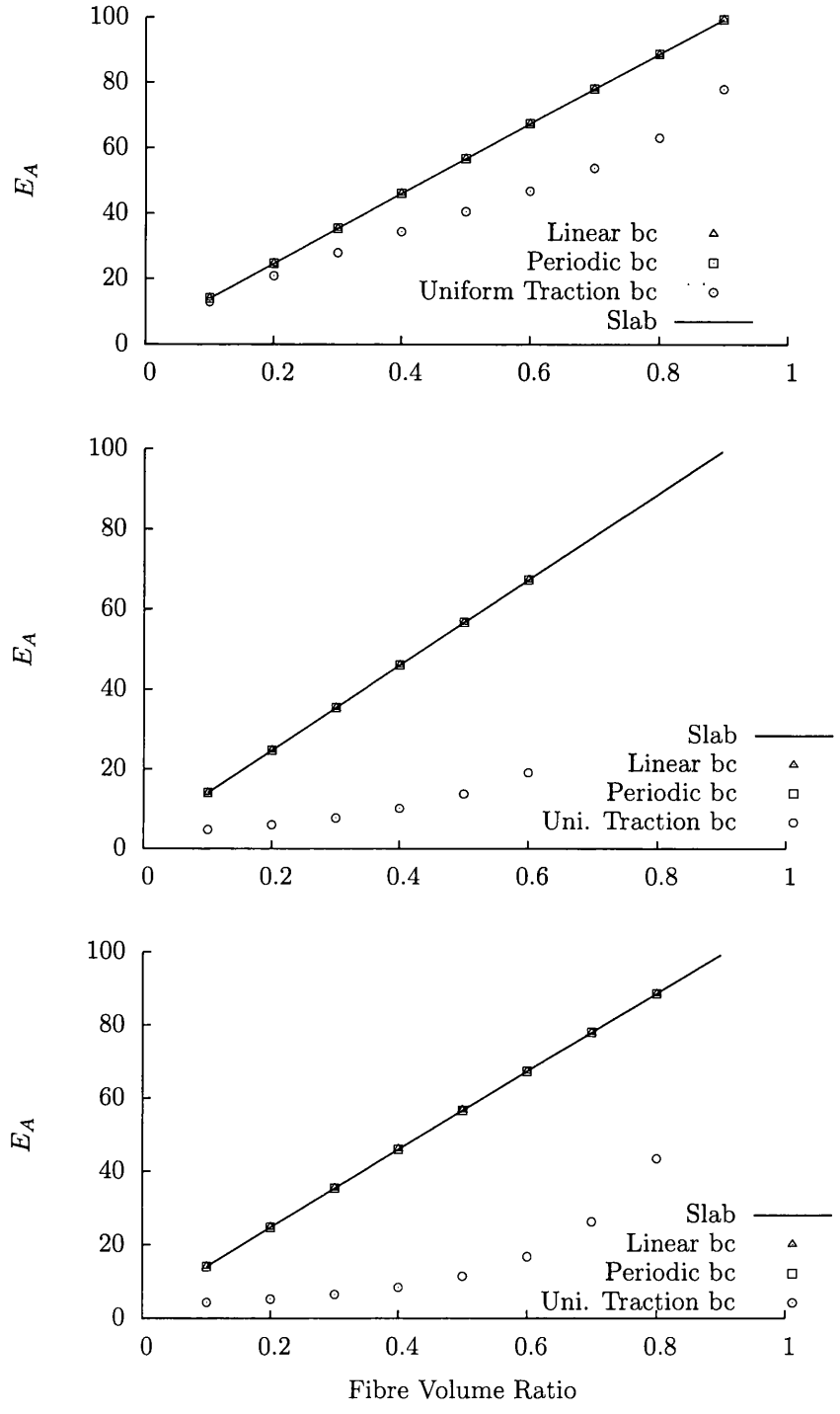

Figure 7.4: Longitudinal Modulus, E_A : Predictions with respect to fibre volume ratio: (a) 2D , (b) 3D Tetragonal Packing, (c) 3D Hexagonal Packing.

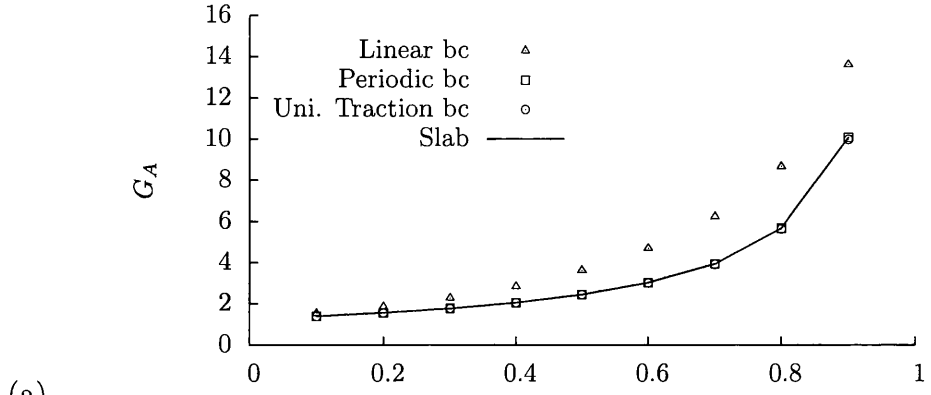

(a)

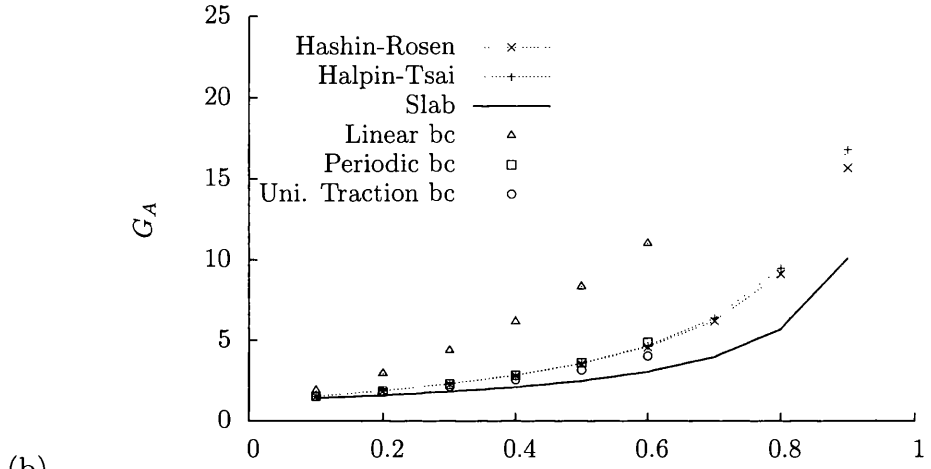

(b)

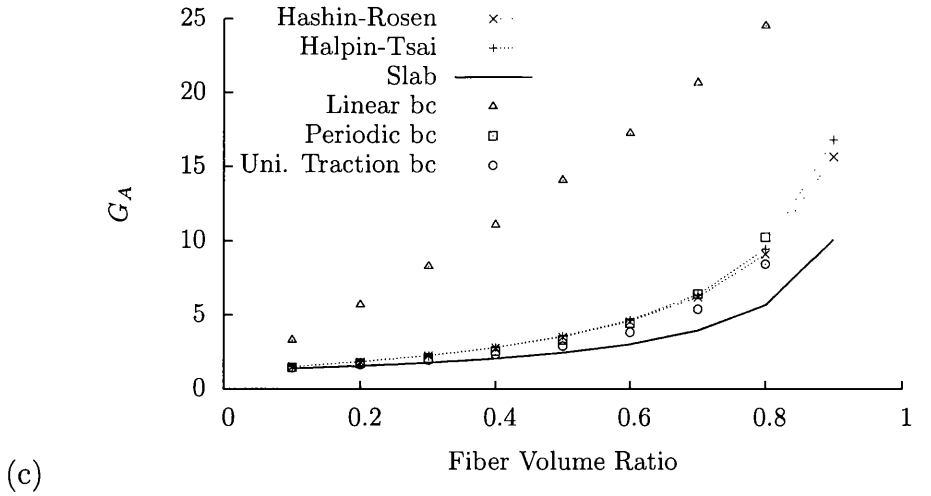

(c)

Figure 7.5: Longitudinal Shear Modulus, G_A: Predictions with respect to fibre volume ratio: (a) 2D , (b) 3D Tetragonal Packing, (c) 3D Hexagonal Packing.

Hashin-Rosen calculation differs from (7.14) by an additional term, which is negligible when the fibres are considerably stiffer than the matrix:

$$E_A = (1-f)E_m + fE_f + \frac{4(\nu_f - \nu_m)^2 \nu_m \nu_f}{\frac{f}{K_m} + \frac{1-f}{K_f} + \frac{1}{G_m}} \tag{7.15}$$

Predictions extracted from various RVE homogenizations for the longitudinal Young's modulus are compared to mechanics of materials predictions in Figure 7.4. Only minor deviations from (7.14) would have been expected, arising from the difference in Poisson's ratios of the fibre and matrix, as long as there is no inter phase sliding. Linear and periodic boundary conditions agree with the equal strain assumption for both 2D and 3D simulations, whereas uniform traction boundary condition yields a softer modulus.

7.3.2 Longitudinal Shear Modulus

Prediction of the longitudinal shear modulus ($G_A = G_{12} = G_{13}$) using the slab model is problematic as the directions 2 and 3 are not identical (with respect to a shear loading). Prediction of shear moduli G_{12} and G_{13} follows from equal stress/strain assumptions, and gives:

$$\frac{1}{G_{12}} = \frac{f}{G_f} + \frac{(1-f)}{G_m} \tag{7.16}$$

$$G_{13} = (1-f)G_m + fG_f. \tag{7.17}$$

In reality none of the above provides a reliable prediction of the shear modulus, especially (7.17). Halpin and Tsai [39] propose a modified modulus for the shear modulus:

$$G_A = \frac{G_m(1+\xi\eta f)}{1-\eta f} \quad ; \quad \eta = \frac{(\frac{G_f}{G_m} - 1)}{(\frac{G_f}{G_m} + \xi)}, \tag{7.18}$$

where ξ is taken as 1. Hashin-Rosen calculation for the longitudinal shear modulus is given as:

$$G_A = G_m + \frac{f}{\frac{1}{G_f - G_m} + \frac{1-f}{2G_m}}. \tag{7.19}$$

Predictions extracted from various RVE homogenizations for longitudinal shear modulus are compared to those by mechanics of materials, Halpin-Tsai and Hashin Rosen approaches in Figure 7.5. In 2D, uniform traction and periodic boundary conditions agree closely with the equal stress assumption, whereas linear boundary condition predicts a stiffer modulus.

In 3D, Halpin-Tsai and Hashin-Rosen predictions almost overlap, which are also

very well predicted by periodic boundary condition plots of hexagonal and square packing up to higher fibre volume ratios. For both packing arrangements uniform traction boundary condition plots provide close estimates to analytical models. The lower bound, which is formed by the equal stress/slab assumption, clearly underestimates the shear modulus, whereas both square/hexagonal packed RVEs with linear boundary condition predict stiffer modulus.

7.3.3 Longitudinal Poisson's Ratio

The longitudinal Poisson's Ratio ($\nu_A = \nu_{12} = \nu_{13}$) is obtained within the mechanics of materials approach by assuming uniform longitudinal strain:

$$\varepsilon_1 = \varepsilon_{1m} = \frac{\sigma_{1m}}{E_{1m}} = \varepsilon_{1f} = \frac{\sigma_{1f}}{E_{1f}}, \tag{7.20}$$

while the fibre and matrix are subject to equal transverse stress resulting from contraction:

$$\begin{aligned} \varepsilon_2 &= (1-f)\varepsilon_{2m} + f\varepsilon_{2f} \\ &= -(1-f)\nu_m \frac{\sigma_{1m}}{E_{1m}} - f\nu_f \frac{\sigma_{1f}}{E_{1f}} \\ &= -(1-f)\nu_m \varepsilon_1 - f\nu_f \varepsilon_1, \end{aligned} \tag{7.21}$$

so that the rule of mixtures applies to ν_A as:

$$\nu_A = -\frac{\varepsilon_2}{\varepsilon_1} = (1-f)\nu_m + f\nu_f. \tag{7.22}$$

Hashin and Rosen [42] calculation, based on composite cylinders assumption, differs from (7.22) by an additional term:

$$\nu_A = (1-f)\nu_m + f\nu_f + \frac{(\nu_f - \nu_m)(\frac{1}{K_m} - \frac{1}{K_f})\nu_m\nu_f}{\frac{f}{K_m} + \frac{1-f}{K_f} + \frac{1}{G_m}}. \tag{7.23}$$

Equal strain and Hashin-Rosen predictions for longitudinal Poisson's ratio is compared to predictions extracted from 2D and 3D RVE homogenizations in Figure 7.6. In both 2D and 3D, the periodic boundary condition very closely agrees with the equal strain assumption, as well as the Hashin-Rosen prediction. For both packing arrangements, uniform traction and linear boundary displacements imposed on the RVE form the upper and lower bounds respectively..

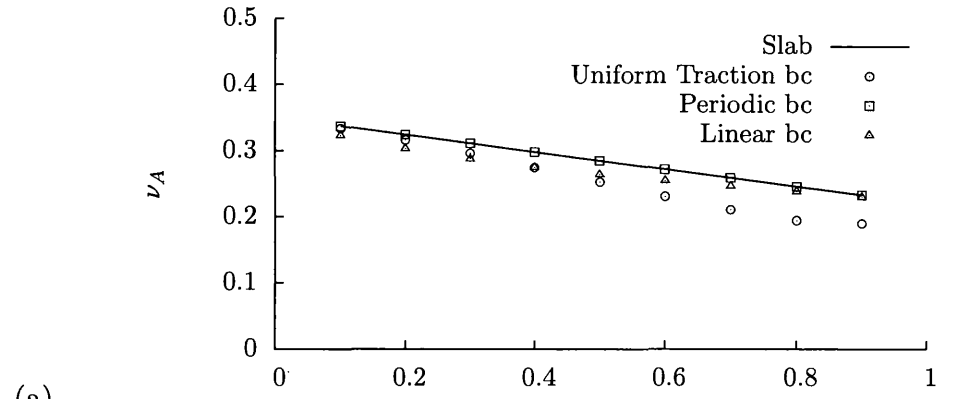

(a)

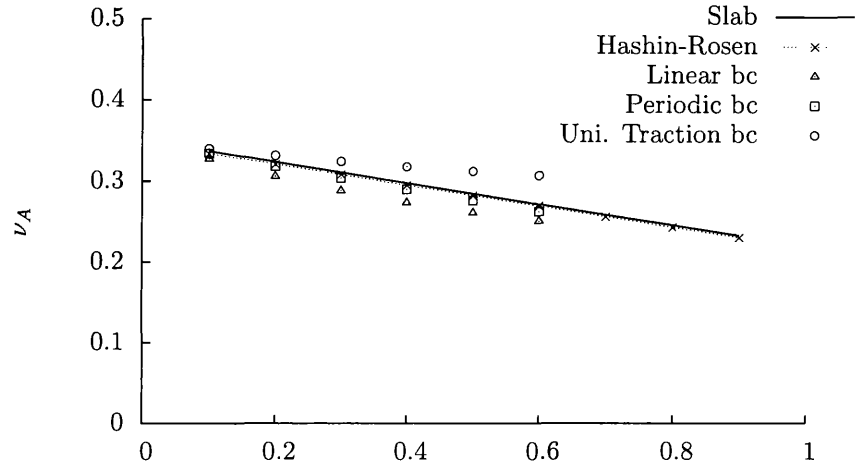

(b)

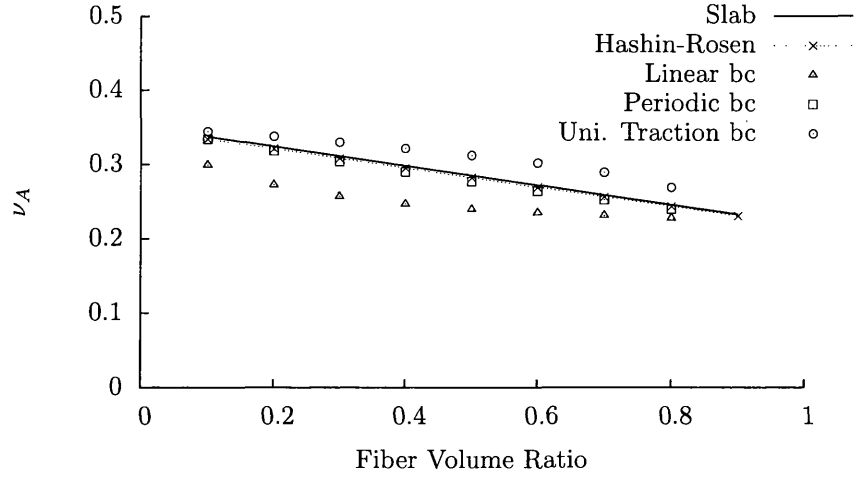

(c)

Figure 7.6: Longitudinal Poisson's Ratio, ν_A: Predictions with respect to fibre volume ratio: (a) 2D , (b) 3D Tetragonal Packing, (c) 3D Hexagonal Packing.

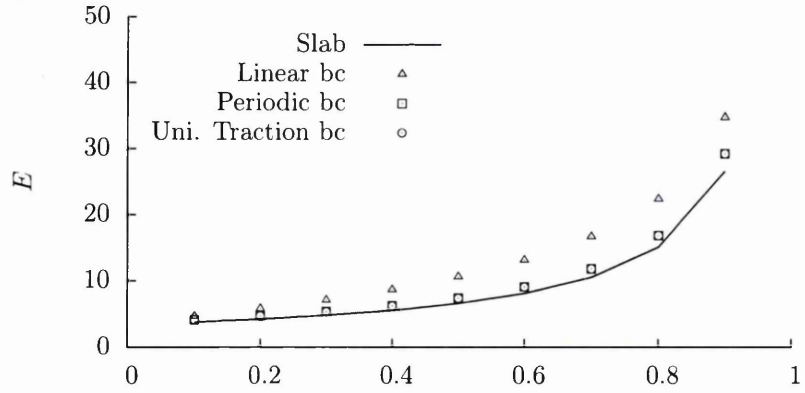

(a)

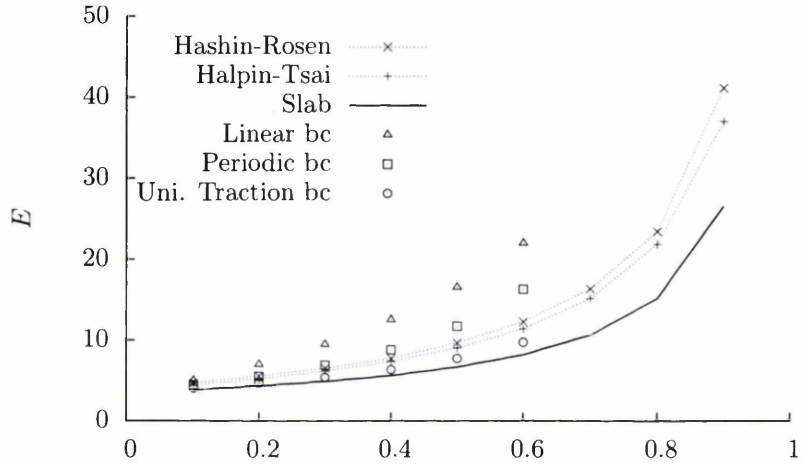

(b)

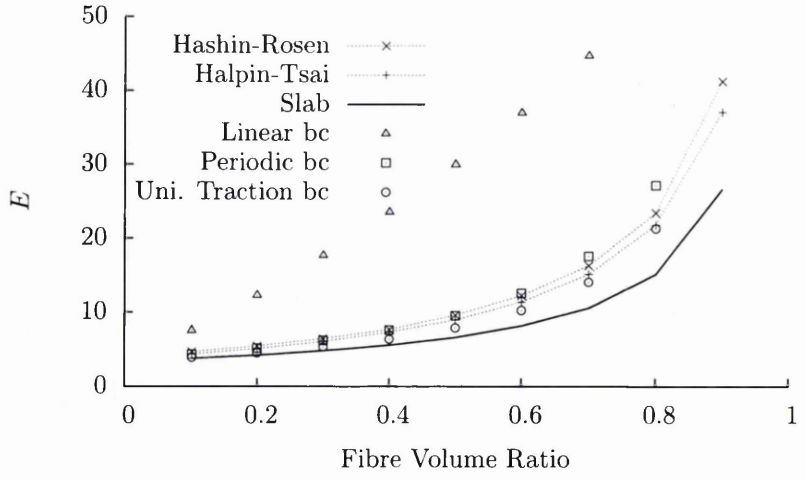

(c)

Figure 7.7: Transverse modulus, E: Predictions with respect to fibre volume ratio (a) 2D , (b) 3D Tetragonal Packing, (c) 3D Hexagonal Packing.

7.3.4 Transverse Young's Modulus

The mechanics of materials treatment for the prediction of the transverse modulus follows the *equal stress* assumption, where the fibre and matrix are assumed to be under uniform stress:

$$\sigma = \sigma_m = \varepsilon_m E_m = \sigma_f = \varepsilon_f E_f. \tag{7.24}$$

Note the obvious problem: directions 2 and 3 are not identical (with respect to a transverse load) in the slab model, in fact 3 is identical to the fibre direction. Equal stress assumption is known to underestimate the transverse modulus, however it provides a lower bound for the material behaviour. The overall transverse strain is given by:

$$\varepsilon = (1-f)\varepsilon_m + f\varepsilon_f, \tag{7.25}$$

which leads to the *Reuss* assumption for the transverse modulus:

$$\begin{aligned} \frac{1}{E} &= \frac{\varepsilon}{\sigma} \\ &= \frac{f}{E_f} + \frac{(1-f)}{E_m}. \end{aligned} \tag{7.26}$$

In reality, it is known that portions of the matrix material in between fibres in the longitudinal direction are subject to a high stress, comparable to the fibre stress, whereas portions of the matrix material laid between fibres in the transverse direction strain equally with the fibres, bearing a lower stress. (7.26), which is the lower bound, will underestimate the transverse Young's modulus.

Hashin and Rosen [42] only provide an expression for the bulk modulus:

$$K = K_m + \frac{f}{\frac{1}{K_f - K_m} + \frac{1-f}{K_m + G_m}} \tag{7.27}$$

and suggest bounds for the shear modulus. Christensen and Lo [18] calculated the effective transverse modulus from:

$$A\alpha^2 + B\alpha + D = 0, \tag{7.28}$$

where,

$$\begin{aligned} D &= 3f(1-f)^2(\beta-1)(\beta+\eta_f) \\ &+ [\beta\eta_m + (\beta-1)f + 1][\beta + \eta_f + (\beta\eta_m - \eta_f)f^3] \end{aligned} \tag{7.29}$$

$$\begin{aligned} B &= -6f(1-f)^2(\beta-1)(\beta+\eta_f) \\ &+ [\beta\eta_m + (\beta-1)f + 1][(\eta_m - 1)(\beta+\eta_f) - 2(\beta\eta_m - \eta_f)f^3] \\ &+ (\eta_m + 1)f(\beta-1)[\beta + \eta_f + (\beta\eta_m - \eta_f)f^3] \end{aligned} \tag{7.30}$$

$$\begin{aligned} A &= 3f(1-f)^2(\beta-1)(\beta+\eta_f) \\ &+ [\beta\eta_m + \eta_f\eta_m - (\beta\eta_m - \nu_f)f^3][\eta_m f(\beta-1) - (\beta\eta_m + 1)] \end{aligned} \tag{7.31}$$

and

$$\alpha = \frac{G}{G_m} \ , \ \beta = \frac{G_f}{G_m} \tag{7.32}$$

$$\eta_m = (3 - 4\nu_m) \ , \ \eta_f = (3 - 4\nu_f). \tag{7.33}$$

Once G is determined from the solution of (7.28), the transverse Young's modulus can be obtained from the complementary relation given by Hashin [43]:

$$\frac{4}{E} = \frac{1}{G} + \frac{1}{K} + 4\left(\frac{\nu_A}{E_A}\right)^2, \tag{7.34}$$

where K, ν_A and E_A follow from (7.27), (7.23) and (7.15) respectively.

For the Halpin-Tsai approach, first the transverse bulk and shear moduli are calculated:

$$K = \frac{K_m(1 + \xi_K \eta_K f)}{1 - \eta f} \ ; \ \eta_K = \frac{\left(\frac{K_f}{K_m} - 1\right)}{\left(\frac{K_f}{K_m} + \xi_K\right)} \tag{7.35}$$

and

$$G = \frac{K_m(1 + \xi_G \eta_G f)}{1 - \eta f} \ ; \ \eta_G = \frac{\left(\frac{G_f}{G_m} - 1\right)}{\left(\frac{G_f}{G_m} + \xi_G\right)}, \tag{7.36}$$

where

$$\xi_K = G_m/K_m \ ; \ \xi_G = \frac{K_m/G_m}{K_m/G_m + 2}. \tag{7.37}$$

The transverse Young's modulus can be obtained from (7.34), where E_A and ν_A are taken from the mechanics of materials approach.

Predictions for the transverse Young's modulus extracted from homogenization of 2D plane stress and 3D RVEs for varying fibre volume ratios are compared to predictions using mechanics of materials (slab), Halpin-Tsai and Hashin-Rosen-Christensen approaches in Figure 7.7.

In 2D, uniform traction and periodic boundary conditions agree closely with the equal stress assumption, whereas linear boundary condition predicts stiffer modulus.

In 3D, Halpin-Tsai and Hashin-Rosen-Christensen approaches give very close predictions, within the tight envelope defined by the periodic and uniform traction boundary condition plots of the RVE with hexagonal packing. The periodic and uniform traction boundary condition plots of the RVE with square packing also form an envelope where the Halpin-Tsai and Hashin-Rosen-Christensen plots fit in,

but is not as tight. Both envelopes tend to open up with increasing fibre volume ratios. The lower bound is formed by the equal stress/slab assumption, which clearly underestimates the transverse modulus. Both square/hexagonal packed RVEs with linear boundary condition predict stiffer modulus.

7.3.5 Transverse Poisson's Ratio

Mechanics of materials prediction of $\nu(=\nu_{23})$ is obtained by considering the volume change under an applied stress, where an expression of the transverse Poisson's ration is derived in terms of E, K, ν_A and E_A, see eg. Daniel *et al.* [22]. As noted before, the transverse modulus E is underestimated, thus mechanics of materials approach will not give a good estimate for ν.

For the Hashin-Rosen-Christensen prediction, an interdependency relation of the transverse isotropy is used:

$$G = \frac{E}{2(1+\nu)}, \tag{7.38}$$

where G and E are obtained from (7.28) and (7.34) respectively.

For the Halpin-Tsai approach, the transverse shear (7.36) and Young's (from (7.34)) moduli are inserted into (7.38) to obtain the transverse Poisson's ratio.

Predictions for the transverse Poisson's ratio extracted from homogenization of 3D RVEs for varying fibre volume ratios are compared to predictions using Halpin-Tsai and Hashin-Rosen-Christensen approaches in Figure 7.8. This is the only property where a considerable variation is observed, though Halpin-Tsai and Hashin-Rosen-Christensen predictions are close to hexagonal RVE homogenization with periodic boundary condition.

7.3.6 Verification of the Transverse Isotropy Assumption

For an ideally transversely isotropic material, C_{55} is not independent, and is related to C_{22} and C_{23}:

$$C_{55} = \frac{C_{22} - C_{23}}{2} \tag{7.39}$$

which is equivalent to the statement (7.38). Since all the properties assessed so far were extracted from the upper left quarter of the tangent stiffness matrix (7.7), and the independent modulus G_A from C_{44} or C_{66}, an assessment of how transversely isotropic the chosen packing/boundary condition combination can be made

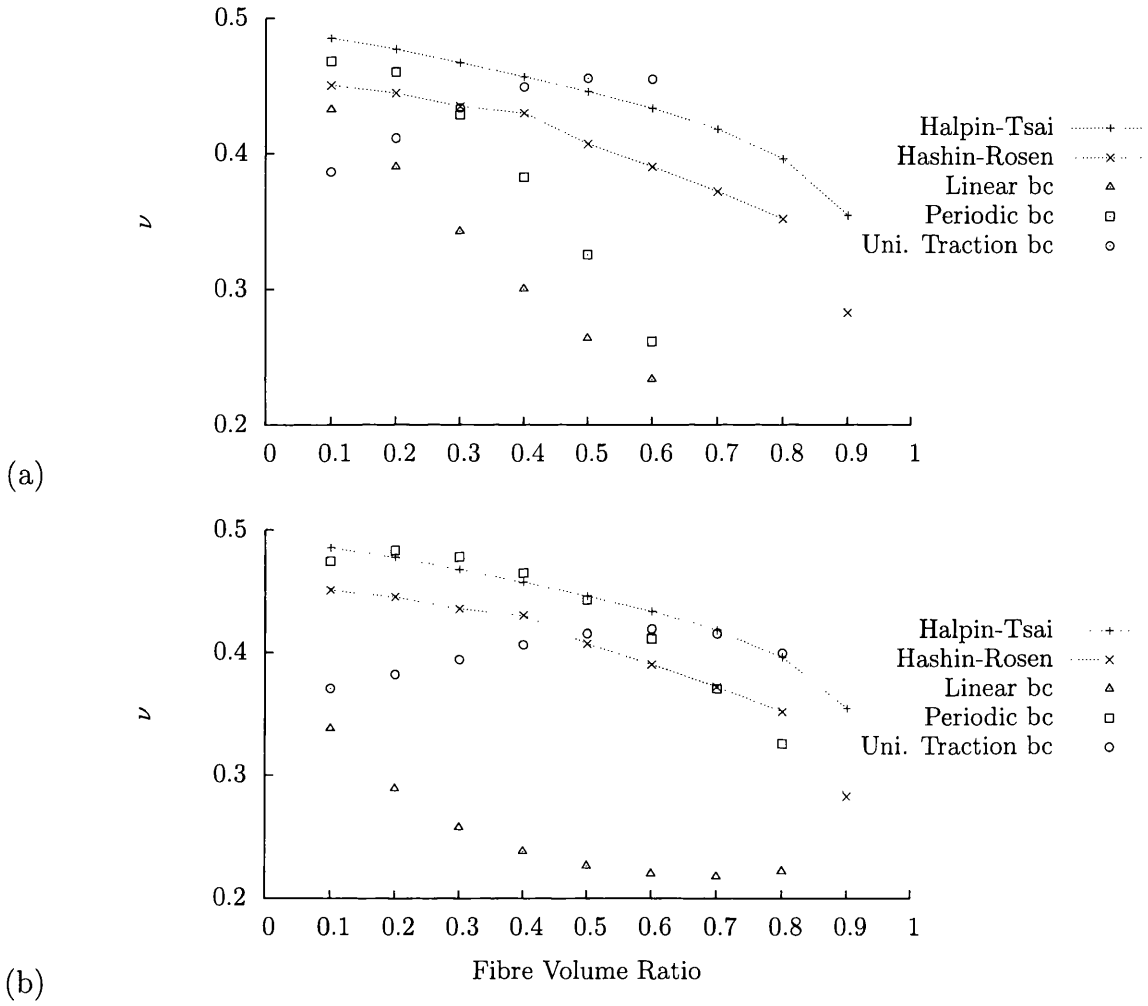

Figure 7.8: Transverse Poisson's Ratio, ν: Predictions with respect to fibre volume ratio , (a) Tetragonal Packing, (b) Hexagonal Packing.

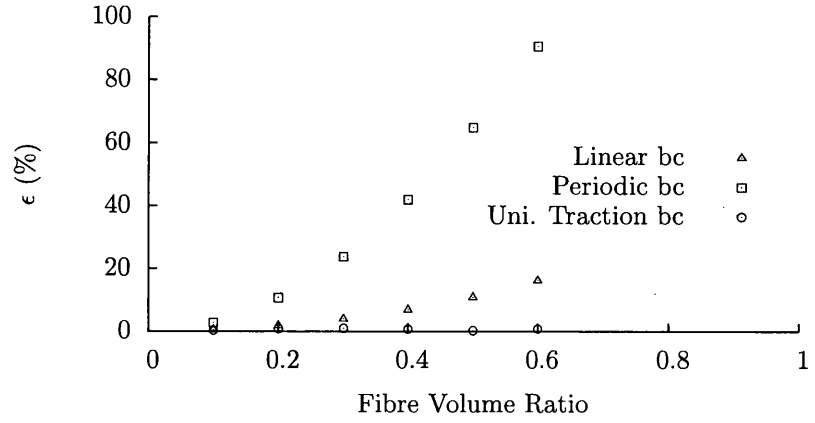

(a)

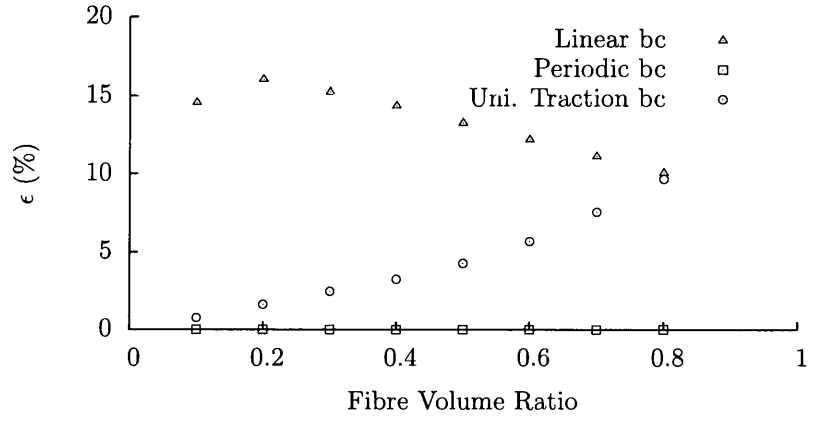

(b)

Figure 7.9: Error in transverse isotropy: Predictions with respect to fibre volume ratio , (a) Tetragonal Packing, (b) Hexagonal Packing.

by comparing both sides of (7.39). A percent error is defined as:

$$\epsilon(\%) = \frac{C_{55} - \frac{C_{22}-C_{23}}{2}}{C_{55}} \tag{7.40}$$

and is plotted on Figure 7.9. As expected, the hexagonal packing arrangement with periodic boundary condition produces transverse isotropy. The square packed RVE with uniform traction boundary condition produces excellent results as well. It can be concluded while these two combinations can be used to represent transverse isotropy, the square packed RVE with periodic boundary condition represents tetragonal isotropy.

7.4 Fibre Orientation effects on Short Beam

In this example, we perform a fully coupled two-scale small strain analysis of a long fibre composite beam, and compare the results obtained for a number of fibre volume ratios over varying fibre orientation angles. This is an extension of Partovi's work [89] in 2D and 3D.

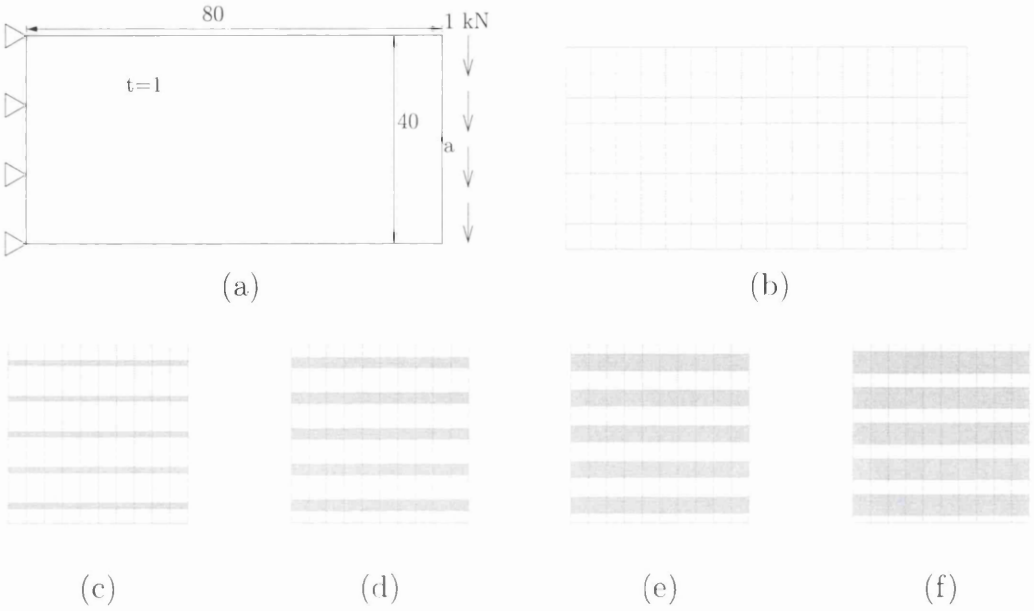

Figure 7.10: 2D Beam : (a) Geomety and boundary conditions (b) Initial mesh. RVE initial meshes with fibre volume ratios (c) 15%, (d) 30%, (e) 45%, (f) 60%

In the 2D case, a 80×40 mm rectangular cantilever beam, shown in Figure 7.10, is loaded by a 1 kN transverse force distributed along its free edge. For the fully coupled analysis under plane stress assumption, RVEs with fibre volume ratios 15%, 30%, 45% and 60%, shown in Figure 7.10 (c) to (f) are employed. Eight noded quadratic quadrilateral elements were used.

In the 3D case, a $10 \times 80 \times 120$ mm rectangular cantilever beam, shown in Figure 7.11, is loaded by a 22.4 kN transverse force distributed along its free edge. RVEs with fibre volume ratios 15%, 30%, 45% and 60%, shown in Figure 7.11 (c) to (f) are employed. Twenty noded quadratic bricks with 8 integration points were used.

In both cases, the fibre orientation is controlled by simply rotating the RVE, which could have linear, periodic or uniform traction boundary conditions, so that 0° refers to the orientation where fibres are aligned with the longitudinal axis, and 90° refers to the orientation where fibres are aligned with the transverse axis .

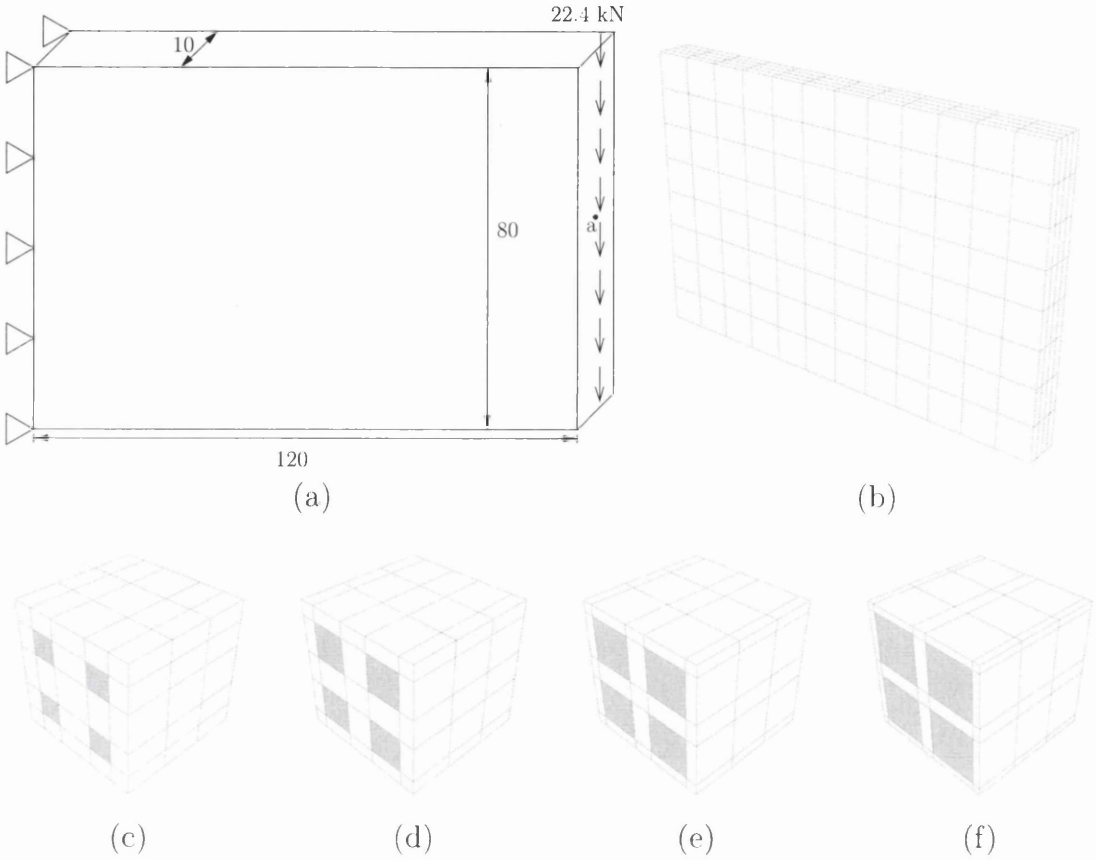

Figure 7.11: 3D Beam : (a) Geomety and boundary conditions (b) Initial mesh. RVE initial meshes with fibre volume ratios (c) 15%, (d) 30%, (e) 45%, (f) 60%

Material properties of matrix and fibre are given as:

$$\begin{aligned} E_f &= 110 \text{ MPa} \ ; \ E_m = 3.4 \text{ MPa} \\ \nu_f &= 0.22 \ ; \ \nu_m = 0.35 \end{aligned} \tag{7.41}$$

We compare vertical displacements of the free end obtained by homogeneous material models with the Halpin-Tsai and Slab models against those obtained from a fully coupled analysis, and the results are shown in Figure 7.12 for 2D and 7.13 for 3D.

For the 2D case, orientations for which the fibres are aligned with the beam axis return the smallest deformation, as expected. Also, the bending strength is governed by the longitudinal modulus of the fibre, for which, as Figure 7.4 suggests, there is good agreement between linear and periodic boundary conditions and the equal strain assumption, whereas uniform traction boundary condition yields a softer response. However, as the fibre orientation turns towards the transverse direction,

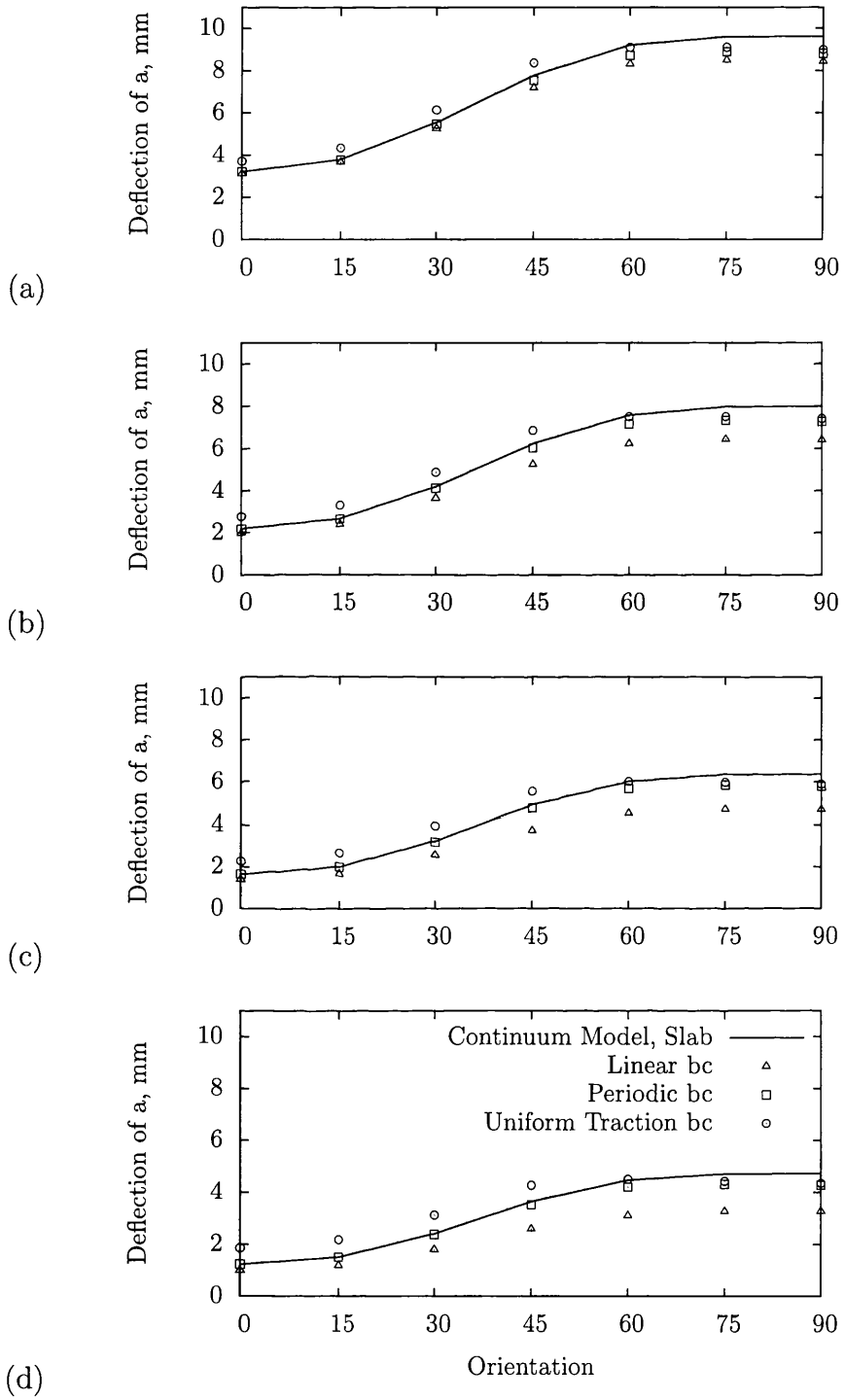

Figure 7.12: Deflection of point a for 2D Plane Stress beam for fibre volume ratios a) 15%, (b) 30%, (c) 45%, (d) 60%

the fibre transverse modulus becomes dominant, and parallel with Figure 7.7, uniform traction and periodic boundary conditions agree closely with each other while slightly offset from the equal stress assumption, whereas Linear boundary condition produces stiffer response.

For the 3D case, Periodic boundary condition is in good agreement with the Continuum Model using Halpin -Tsai prediction for all orientations of the fibres, more so for lower fibre volume ratios considered. Equal stress/slab assumption underestimates the transverse modulus, as was pointed out earlier for the single RVE homogenization and Linear boundary condition produces stiffer response.

It could be argued that material properties obtained from homogenization of a single RVE could have been employed to get the same results. While exceptionally true for small strain elasticity, this idea would not work for the next example, where finite strains and rotations exist.

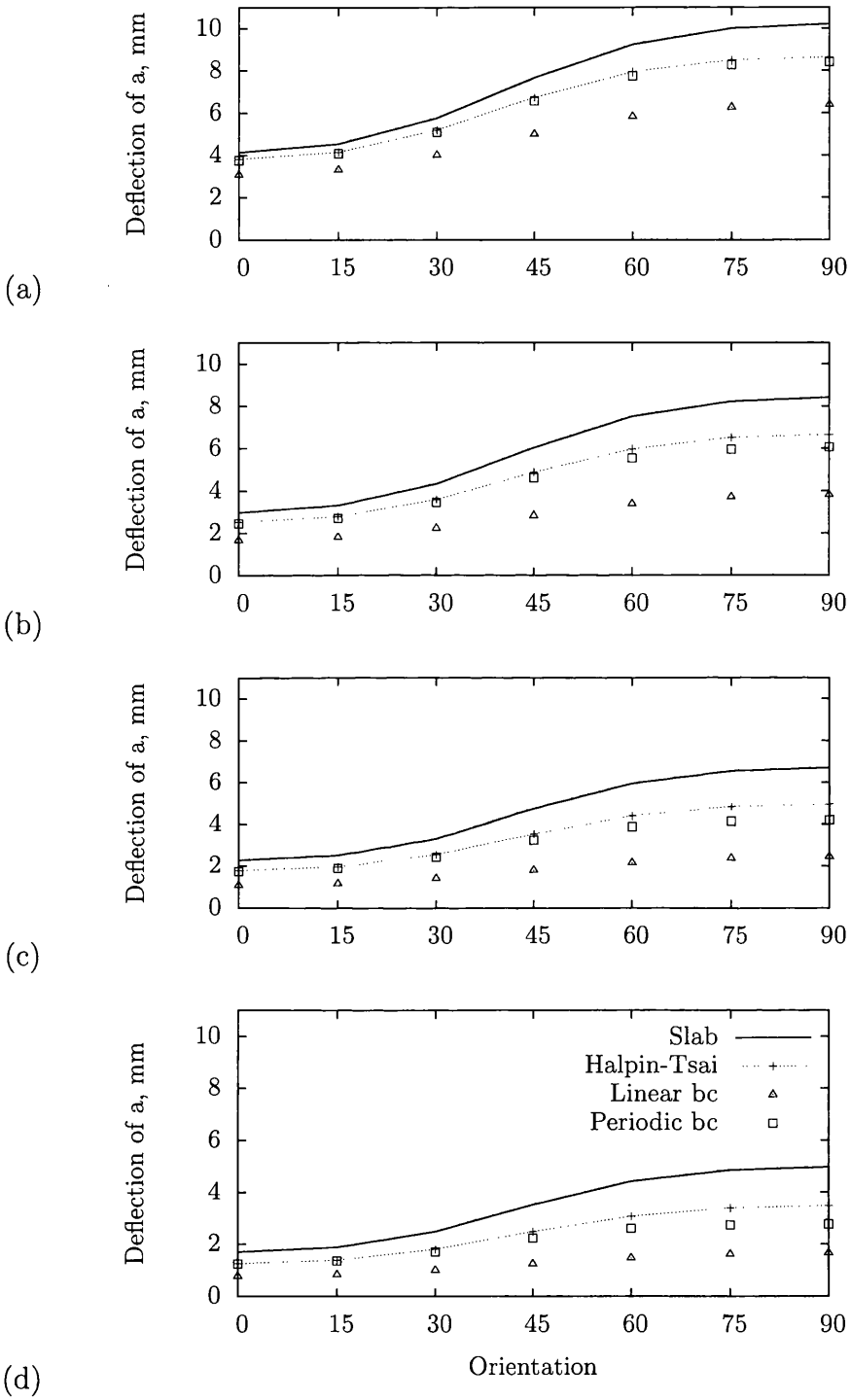

Figure 7.13: Deflection of point a for 3D beam for fibre volume ratios (a) 15%, (b) 30%, (c) 45%, (d) 60%

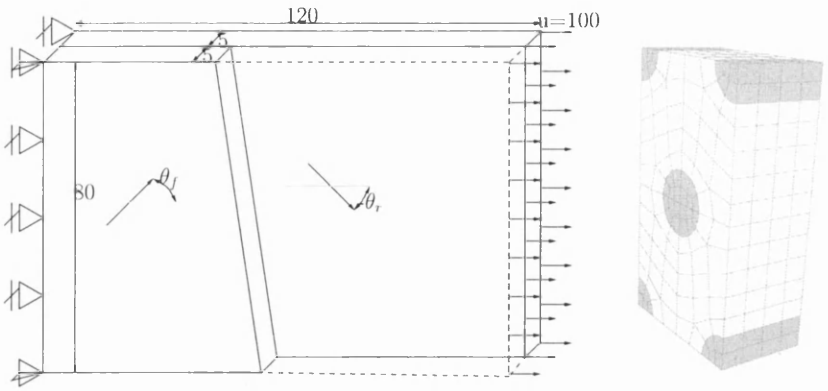

(a) (b)

Figure 7.14: Two ply laminate : (a) Geomety and boundary conditions. Initial mesh as shown in Figure 7.11 (b), (b) RVE mesh

7.5 Large Strain Stretching of a Two Ply Laminate

This example demonstrates the transverse effects of aligned fibres, and is borrowed from Apel's PhD thesis [2]. Guedes and Kikuchi [37] solved a small strain version, where they used homogenized RVE's to obtain effective mechanical properties of the laminate, with which they solved the single-scale macroscopical problem. Then they used the macroscopic stress to investigate the microscopic stress field. We will compare the multi-scale models with the large strain transversely isotropic model described in Chapter 3, the parameters of which are obtained by homogenization of a single RVE, an extension of the properties estimation procedure discussed in Section 7.1 to the range of moderately large strains.

A $10 \times 80 \times 120$ mm rectangular laminate, shown in Figure 7.14, consists of two layers of fibre reinforced material. Fibre orientations for the front and rear layers are defined by direction vectors $\boldsymbol{A}_f$ and $\boldsymbol{A}_r$ that are rotated with respect to the longitudinal axis by θ_f and θ_r respectively.

The right face of the bar is stretched by 100 mm, while the left face of the bar is fixed in the longitudinal direction. Three additional degrees of freedom in transverse and thickness directions at two corners are also constrained in order to prevent rotations around the longitudinal axis. Three material models are compared:

1. The strain energy for the large strain transversely isotropic model is expressed

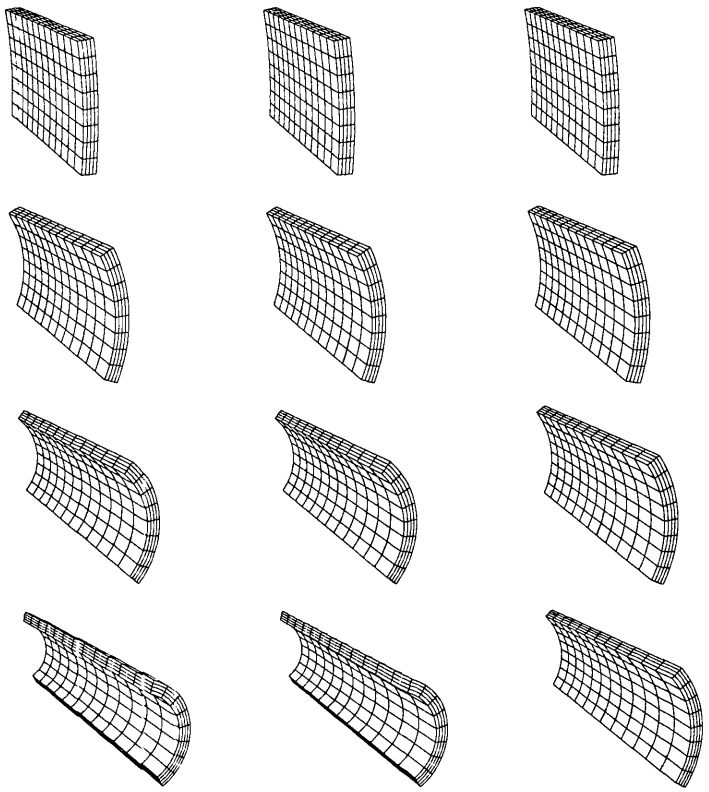

Figure 7.15: Two ply laminate, $\theta_f = 0$, $\theta_r = 90$: Deformed mesh for (a) Single-Scale model, (b) Multi-Scale model with Neo-Hookean Fibre, (c) Multi-Scale model with Ogden Fibre

as the sum of transverse and isotropic components:

$$\Psi_{iso} = \frac{\mu}{2}(I_1 - 3) - \mu \ln J + \frac{\lambda}{2}(J-1)^2, \tag{7.42}$$

$$\Psi_{trn} = [\alpha + \beta \ln J + \gamma(I_4 - 1)](I_4 - 1) - \frac{\alpha}{2}(I_5 - 1). \tag{7.43}$$

For this model, we start with the material properties of matrix and fibre of the previous example,

$$\begin{aligned} E_f &= 110 \text{ MPa} \ ; \ E_m = 3.4 \text{ MPa}; \\ \nu_f &= 0.22 \ ; \ \nu_m = 0.35. \end{aligned} \tag{7.44}$$

and use the properties estimation procedure discussed in the preceeding sections to extract the set of small strain composite properties $\{E_A, E, \nu, \nu_A, G_A\}$

for a fibre volume ratio of 15%. Then, we insert these properties into the relationships developed in Chapter 3 for parameter identification, repeated here for convenience:

$$\begin{aligned}
\mu &= \frac{E}{2(1+\nu)} \\
\lambda &= -\frac{E(E\nu_A^2 + E_A\nu)}{k(1+\nu)} \\
\beta &= \frac{E(E\nu_A^2 - E_A(\nu_A - \nu + \nu_A\nu))}{4k(1+\nu)} \\
\alpha &= \frac{E}{2(1+\nu)} - G_A \\
\gamma &= \frac{1}{8}\left(\frac{E_A^2(\nu-1)}{k} - [\lambda + 2\mu + 8\beta - 4\alpha]\right)
\end{aligned} \tag{7.45}$$

where $k = E_A(\nu - 1) + 2E\nu_A^2$. Finally, we perform a single scale FE analysis with the large strain transversely isotropic model using these parameters.

2. For large strain multi-scale simulations, we employ a Neo-Hookean type material, strain energy function of which is given by (7.42) for both fibres and matrix, with properties, equivalent to (7.44), given respectively as

$$\lambda_f = 35.421 \text{ MPa} \ , \ \mu_f = 45.082 \text{ MPa}; \tag{7.46}$$

$$\lambda_m = 2.938 \text{ MPa} \ , \ \mu_m = 1.26 \text{ MPa}. \tag{7.47}$$

The fibre orientation is controlled by simply rotating the RVE shown in Figure 7.11 (c), which has a fibre volume ratio of 15%. Only periodic bc is considered.

3. In order to match the stiffening effect caused by the transverse part of the strain energy function (7.43), an Ogden type material is also considered as the fibre material. The strain energy function for this material is given as

$$\Psi_{ogd} = \sum_{n=1}^{N} \frac{\mu_n}{\alpha_n}(\lambda_1^{\alpha_n} + \lambda_2^{\alpha_n} + \lambda_3^{\alpha_n} - 3), \quad \lambda_1\lambda_2\lambda_3 = 1, \tag{7.48}$$

where N is a positive integer, $\lambda_{i(i=1,2,3)}$ are the principal stretches and μ_n and α_n are material constants such that,

$$\mu_n\alpha_n > 0, \quad n = 1, 2, ..., N, \ \sum_{n=1}^{N} \mu_n\alpha_n = 2\mu \tag{7.49}$$

A single pair is used, given as:

$$\mu_1 = 6.714311 \ ; \ \alpha_1 = 13.42862$$

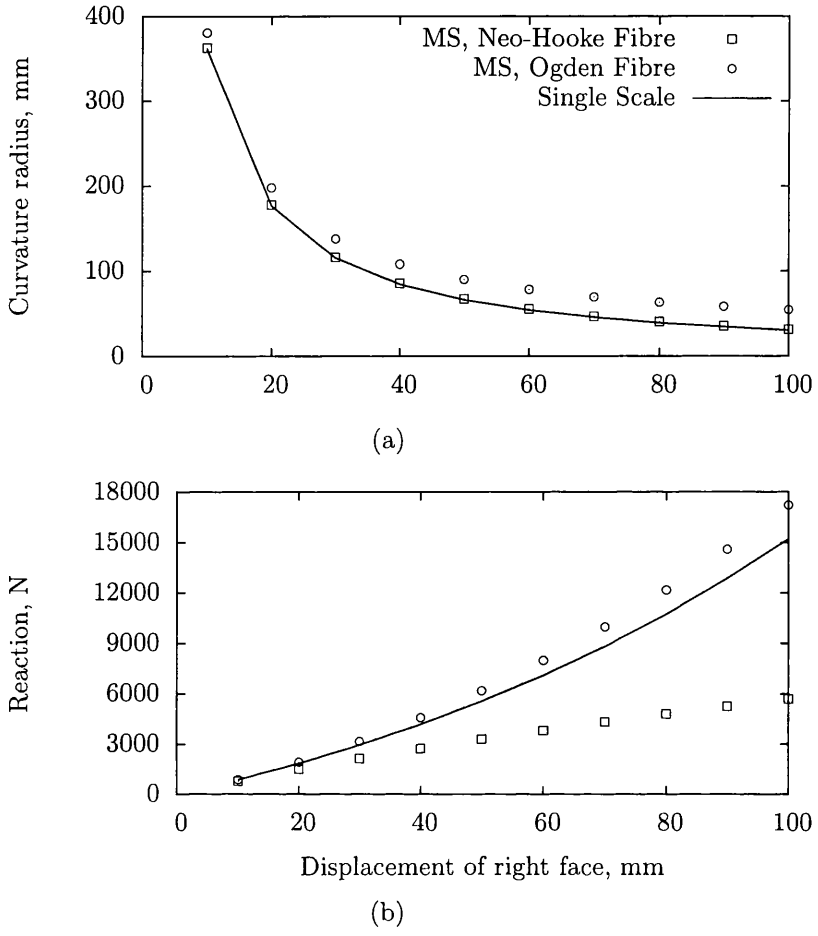

Figure 7.16: Two ply laminate, $\theta_f = 0$, $\theta_r = 90$: (a) Curvature, (b) Reaction in the longitudinal direction

The matrix material is the same with the previous model, with parameters given in (7.47).

Two layers are assigned 2 sets of fibre orientations. The first case is characterized by $\theta_f = 0°$, $\theta_r = 90°$. As the deformed meshes of Figure 7.15 reveal, fibres of the rear layer do not permit contraction, which causes the bar to deform into a groove. Curvature radius is plotted in Figure 7.16 (a), where the multi-scale model with Neo-Hookean fibre is shown to agree with the continuum model, while multi-scale model with Ogden fibre is quite close. This is an extension of the outcome of previous examples into the large strain regime. Reactions at the left face, plotted in Figure 7.16 (b) reflect the effect of fibre stiffening, where multi-scale models with Neo-Hookean/Ogden fibre are shown to substantially differ, while the latter gives

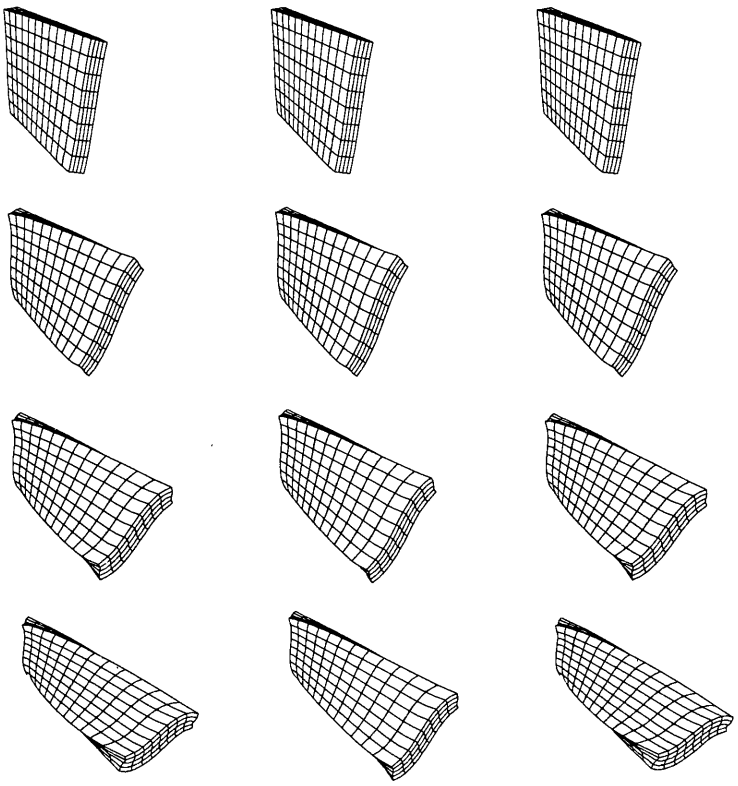

Figure 7.17: Two ply laminate, $\theta_f = 45$, $\theta_r = -45$: Deformed mesh for (a) Single-Scale model, (b) Multi-Scale model with Neo-Hookean Fibre, (c) Multi-Scale model with Ogden Fibre

results close to the continuum model.

The next case is characterized by $\theta_f = 45°$, $\theta_r = -45°$. As the stiffness is maximized in the direction of fibres, the bar is subjected to torsion to accommodate for alignment of the fibres, as shown in the deformed meshes of Figure 7.17. To quantify the rotation around the longitudinal axis, orientations of upper/lower and front/rear edges of the right face are interpolated to obtain rotations of short and long edges, which are plotted in Figure 7.18 (a) and (b) respectively, where the multi-scale model with Ogden fibre is seen to clearly agree with the continuum model. Reactions at the left face are plotted in Figure 7.18 (c), where the multi-scale model with Ogden fibre also matches with the continuum model. For this configuration the multi-scale model with Neo-Hookean fibre departs from other models visibly, for both end twist and base reactions.

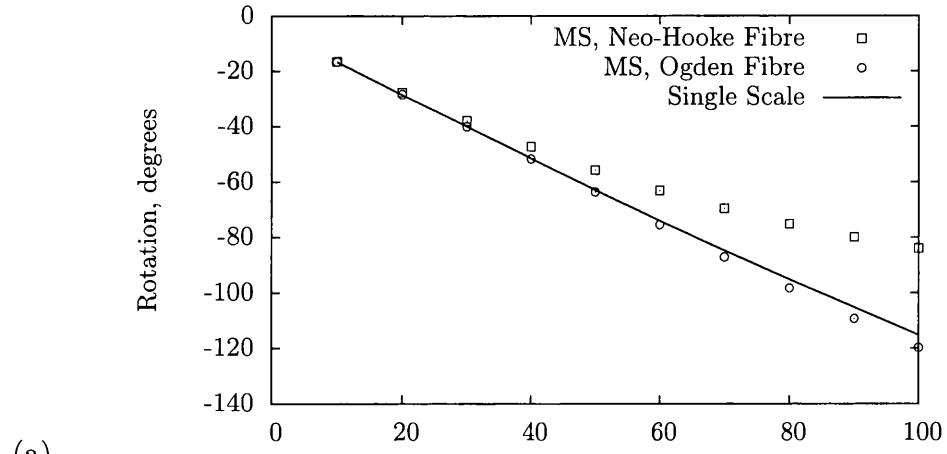

(a)

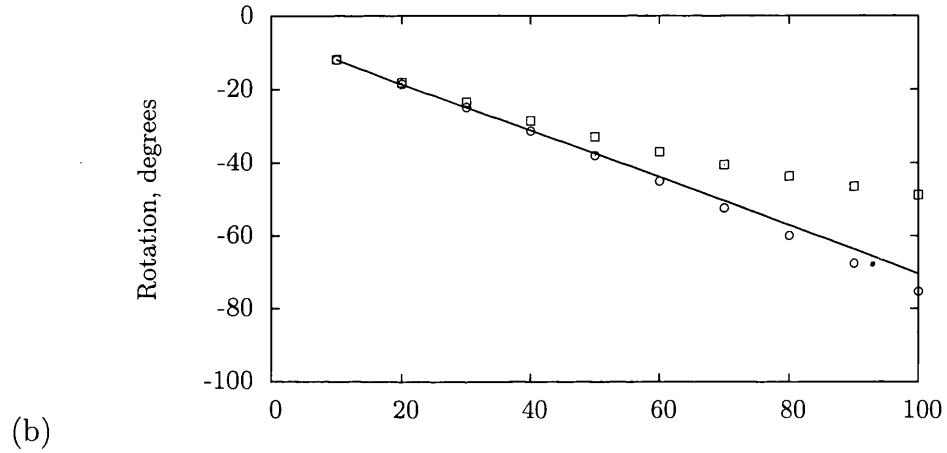

(b)

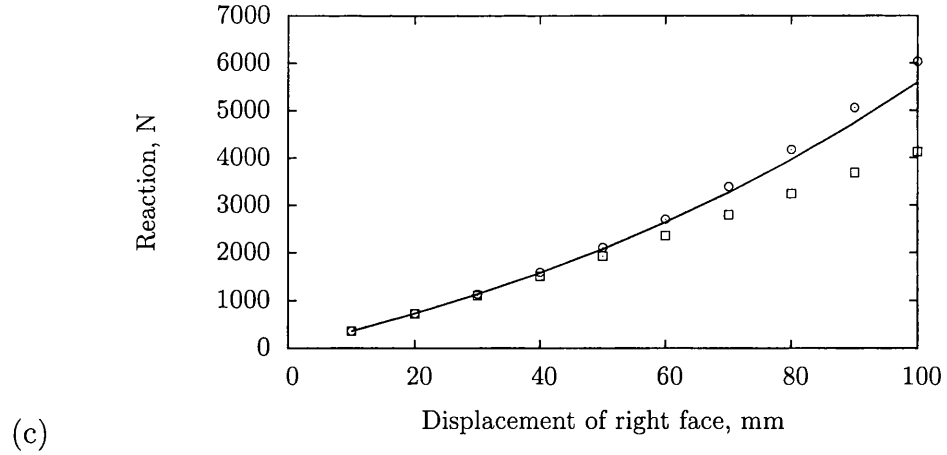

(c)

Figure 7.18: Two ply laminate, $\theta_f = 45$, $\theta_r = -45$: Rotation of (a) short and (b) long edges, (c) Reaction in the longitudinal direction

Chapter 8

Applications II: Interface Region

The previous chapter has dealt with the application of computational homogenization into modelling of long fibre composites. One major assumption was perfect bonding between the matrix and reinforcement phases, which is referred to as a strong interface, where the bond is assumed to be at least as strong as the matrix phase.

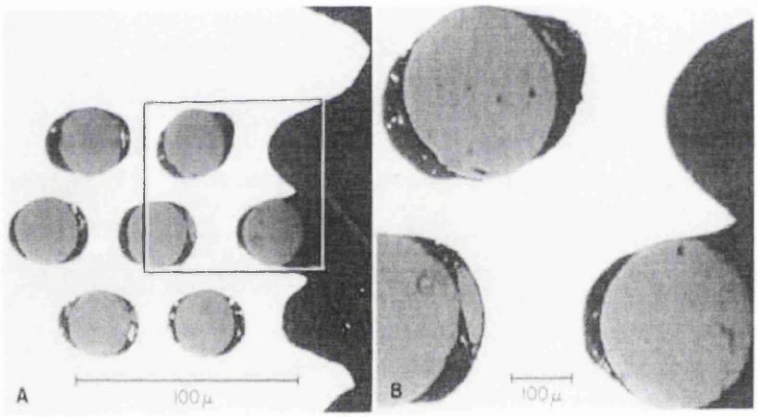

Figure 8.1: Fibre-matrix debonding in a Ni-Al_2O_3 composite under transverse loading, from Mehan and Harris [73].

Composites with a weak interface will fail at the interface as the bond is the weakest link in the system [74]. The fabrication process determines the nature of the bond, a composite could have been manufactured mechanically, by wetting, as a result of a chemical reaction, or a mix of those. As a consequence of the fabrication process, oxide films, trapped gases, high concentrations of vacancies and dislocations will be present in the interface, similar to imperfections present at grain boundaries

of metals, but to a greater extent [74].

Inter-phase cracking, debonding and sliding can cause local degradation which continuum models would fail to capture, and computational homogenization has a substantial potential for modelling in this field. This chapter deals with numerical treatment of composites with debonded inclusions, as well as the process of debonding. To this aim, first we present a geometrically non-linear frictional contact procedure, see, for instance, Wriggers [128] or Peric *et al.* [94], and demonstrate the use of this procedure for modelling interactions between debonded phases within the computational homogenization environment.

The cohesive zone model introduced by Needleman [84], and developed by e.g. Tvergaard [121, 122], or Ortiz *et al.* [85], is used to model the growth of a crack (or a debonding zone) at the interface between different constituents of the material. We implement the cohesive model into the discrete framework developed for contact, in order to study the debonding process from a damage-free configuration with opening and closing effects, as well as Coulomb frictional sliding between phases, again within the computational homogenization framework.

8.1 Frictional Contact

Assume that bodies Ω^1 and Ω^2 come into contact during their deformation histories corresponding to the deformation mappings $\boldsymbol{\varphi}^1$ and $\boldsymbol{\varphi}^2$ as shown in Figure 8.2. The constraint of impermeability is expressed as:

$$(\boldsymbol{x}^2 - \boldsymbol{x}^1) \cdot \boldsymbol{n} \geq 0 \tag{8.1}$$

By assuming a uniform contact boundary that permits existence of a point $\bar{\boldsymbol{x}}^1$ on body Ω^1 for every point $\boldsymbol{x}^2$ on Ω^2, where the distance between $\bar{\boldsymbol{x}}^1$ and $\boldsymbol{x}^2$ is minimized, a penetration function g_N can be defined as:

$$g_N = (\boldsymbol{x}^2 - \bar{\boldsymbol{x}}^1) \cdot \bar{\boldsymbol{n}} \geq 0 \tag{8.2}$$

where $\bar{\boldsymbol{n}}$ is evaluated at the minimum distance point.

Tangential contact is concerned with the relative movement betweeen two bodies has two aspects. If the point of contact does not change, the *Stick* condition sets a constraint on the tangential velocity/displacement as:

$$\dot{\boldsymbol{g}}_T = \boldsymbol{0} \;\Leftrightarrow\; \boldsymbol{g}_T = \boldsymbol{0} \tag{8.3}$$

Tangential slip is characterized by a change of the point $\boldsymbol{x}_2$ with respect to $\bar{\boldsymbol{x}}_1$. The path of sliding is calculated by integrating relative velocities.

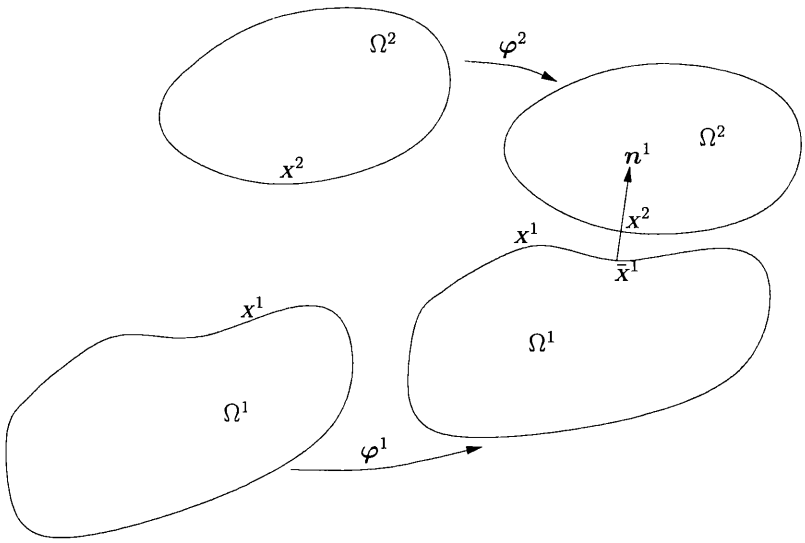

Figure 8.2: Contact between two bodies

8.1.1 Incremental Boundary Value Problem

The boundary value problem defined in Chapter 2 for a single body is now extended to involve two bodies, as well as the contact contributions C^{con}:

$$\begin{aligned} & \int_{\Omega^1} \hat{\boldsymbol{\sigma}}^1 : \nabla \boldsymbol{\eta}^1 \, dv - \int_{\Omega^1} \boldsymbol{f}^1 \cdot \boldsymbol{\eta}^1 \, dv - \int_{\partial\Omega_t^1} \boldsymbol{t}^1 \cdot \boldsymbol{\eta}^1 \, da \\ + & \int_{\Omega^2} \hat{\boldsymbol{\sigma}}^2 : \nabla \boldsymbol{\eta}^2 \, dv - \int_{\Omega^2} \boldsymbol{f}^2 \cdot \boldsymbol{\eta}^2 \, dv - \int_{\partial\Omega_t^2} \boldsymbol{t}^2 \cdot \boldsymbol{\eta}^2 \, da \\ + & \; C^{con} = 0 \quad , \forall \boldsymbol{\eta}^1, \boldsymbol{\eta}^2 \in \mathscr{V} \end{aligned} \tag{8.4}$$

subject to kinematical constraint set by (8.1). $\partial\Omega_t$ refer to parts of boundary where tractions are prescribed. Note that, as friction behaviour is path-dependent, the boundary value problem is incremental, and is stated at time station t^{n+1}.

8.1.2 Constitutive Relations

There are a number of approaches to the contact contributions C^{con} into the boundary value problem, Lagrange multipliers, penalty approach and direct elimination to name a few. In this work we adopt a constitutive equation at the interface, defined

by:

$$\begin{aligned} C^{con} &= \int_{\partial\Omega^{con}} \boldsymbol{t} \cdot \delta \boldsymbol{g}\, da \\ &= \int_{\partial\Omega^{con}} (t_N \delta g_N + \boldsymbol{t}_T \cdot \delta \boldsymbol{g}_T)\, da. \end{aligned} \tag{8.5}$$

Normal Contact

The constraint of impenetrability given by (8.2) is relaxed to postulate an elastic constitutive relationship for normal contact pressure as:

$$t_N = c_N g_N, \tag{8.6}$$

where c_N is the penalty parameter.

Elastoplastic Model for Tangential Contact

The tangential velocity could be assumed to be decomposed into a stick and a slip component as:

$$\dot{\boldsymbol{g}}_T = \dot{\boldsymbol{g}}_{Tstick} + \dot{\boldsymbol{g}}_{Tslip}. \tag{8.7}$$

By relaxing the constraint given by (8.3), we establish an elastic constitutive relationship for stick as:

$$\begin{aligned} \boldsymbol{t}_T &= c_T \boldsymbol{g}_{Tstick} \\ &= c_T (\boldsymbol{g}_T - \boldsymbol{g}_{Tslip}), \end{aligned} \tag{8.8}$$

where c_T is a constant. The constitutive model for frictional tangential slip is analogous to elastoplasticity. The flow rule is given as:

$$\dot{\boldsymbol{g}}_{Tslip} = \dot{\lambda} \frac{\partial \Phi}{\partial \boldsymbol{t}_T}, \tag{8.9}$$

where, Φ is the bounding (yield) function used as a flow potential and $\dot{\lambda}$ is the plastic parameter. A convenient choice for the bounding (yield) function is based on the Coulomb's law:

$$\Phi = ||\boldsymbol{t}_T|| - \mu\, t_N. \tag{8.10}$$

The flow rule is complete with the loading/unloading conditions given by:

$$\Phi \leq 0, \tag{8.11}$$

$$\dot{\lambda} \geq 0, \tag{8.12}$$

$$\dot{\lambda}\Phi = 0. \tag{8.13}$$

Time Integration Backward Euler scheme is used to numerically integrate the flow equation. Time discrete version of the flow equation reads:

$$\boldsymbol{g}_{Tslip} = \boldsymbol{g}^n_{Tslip} + \Delta\lambda \frac{\boldsymbol{t}_T}{||\boldsymbol{t}_T||}. \tag{8.14}$$

To keep the notation simple, all quantities without time superscript refer to t^{n+1}.

8.1.3 Return Mapping

Normal constitutive relation established by (8.6) is not path or history dependent, and is used to evaluate the normal force at each time step. For tangential contact, the elastic predictor/plastic corrector method of elastoplasticity (see Chapter 3) provides a good analogy:

Stick Predictor A trial traction is calculated assuming a purely elastic (stick) step by freezing the tangential slip at time t^n.

$$\begin{aligned} \boldsymbol{t}^{trial}_T &= c_T(\boldsymbol{g}_T - \boldsymbol{g}^{sl^n}_T) \\ &= c_T\left(\boldsymbol{g}_T - (\boldsymbol{g}^n_T - \boldsymbol{g}^{st^n}_T)\right) \\ &= \boldsymbol{t}^n_T + c_T\,\Delta\boldsymbol{g}_T. \end{aligned} \tag{8.15}$$

Check for Slip Next, the trial traction is subjected to the bound test:

$$\Phi^{\text{trial}} = ||\boldsymbol{t}^{trial}_T|| - \mu\, t_N. \tag{8.16}$$

If $\Phi^{\text{trial}} \leq 0$, then the elastic assumption is valid:

$$\boldsymbol{t}_T = \boldsymbol{t}^{trial}_T \tag{8.17}$$

Slip Corrector If $\Phi^{\text{trial}} > 0$, then $\boldsymbol{t}_T$ should be modified to account for slip. The flow rule (8.14) is inserted into the elastic constitutive relation (8.8), and by use of (8.15),

$$\boldsymbol{t}_T = \boldsymbol{t}^{trial}_T - \Delta\lambda\, c_{Tstick}\, \boldsymbol{n}^{trial}_T, \tag{8.18}$$

where,

$$\boldsymbol{n}^{trial}_T = \frac{\boldsymbol{t}^{trial}_T}{||\boldsymbol{t}^{trial}_T||}\ ;\ \Delta\lambda = \frac{\Phi^{\text{trial}}}{c_{Tstick}}. \tag{8.19}$$

The numerical model for contact with friction is summarized in Box 8.1 for the 2D case, which is exclusively used later in this thesis. Note that, some vector quantities become scalars and unit normals become sign functions.

At t^{n+1}, given μ c_N, c_T, g_N , Δg_T , t_T^n

1. Calculate Normal Force:

$$t_N = c_N\, g_N$$
$$\frac{\partial t_N}{\partial g_N} = c_N$$

2. Assume Elastic (Stick) State:

$$t_T^{trial} = t_T^n + c_T\, \Delta g_T$$

3. Check Slip Condition

$$\Phi^{\text{trial}} = t_T^{trial} - \mu\, t_N$$

(a) If $\Phi^{\text{trial}} \leq 0 \Rightarrow$ Stick:

$$t_T = t_T^{trial}$$
$$\frac{\partial t_T}{\partial g_T} = c_T \ , \ \frac{\partial t_T}{\partial g_N} = 0$$

(b) If $\Phi^{\text{trial}} > 0 \Rightarrow$ Slip:

$$sign(t_T^{trial}) = \frac{t_T^{trial}}{||t_T^{trial}||} \ ; \ \Delta\lambda = \frac{\Phi^{\text{trial}}}{c_T}$$

$$t_T = t_T^{trial} - \Delta\lambda\, c_T\, sign(t_T^{trial})$$
$$\frac{\partial t_T}{\partial g_T} = 0 \ , \ \frac{\partial t_T}{\partial g_N} = \mu\, c_N\, sign(t_T^{trial})$$

Box 8.1: Numerical Model for Contact with Friction.

8.1.4 2-D Discretization

In Figure 8.3, node Sl with nodal coordinates $\boldsymbol{x}^{Sl}$ comes into contact with the segment defined by the line joining nodes $M1$ and $M2$ with nodal coordinates $\boldsymbol{x}^{M1}$ and $\boldsymbol{x}^{M2}$ respectively. We define the unit normal and tangent vectors to the master segment as $\boldsymbol{n}$ and $\boldsymbol{a}$:

$$\boldsymbol{a} = \frac{\boldsymbol{x}^{M2} - \boldsymbol{x}^{M1}}{l} \ ; \ \boldsymbol{n} = \boldsymbol{e}_3 \times \boldsymbol{a} \tag{8.20}$$

where l is the length of the master segment given as $l = |\boldsymbol{x}^{M2} - \boldsymbol{x}^{M1}|$.

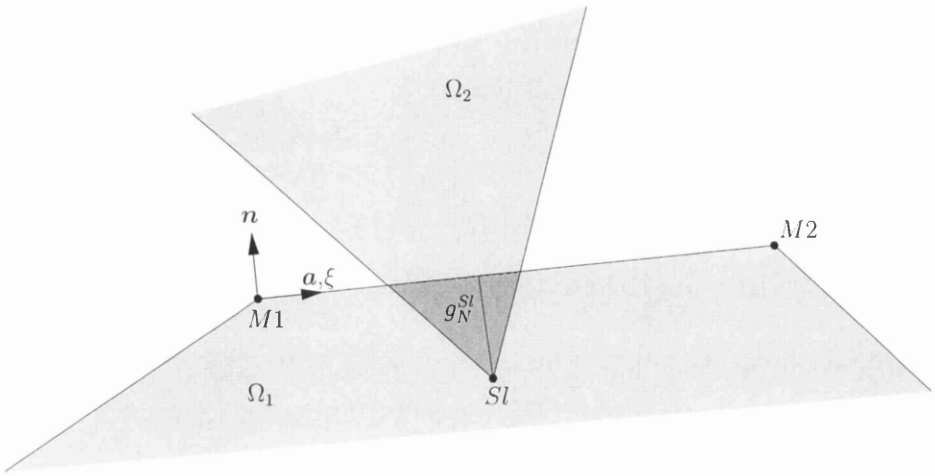

Figure 8.3: 2-D node-to-segment contact element

The relative coordinate system along the master segment is defined by ξ, so that:

$$\boldsymbol{x}(\xi) = \boldsymbol{x}^{M1} + (\boldsymbol{x}^{M2} - \boldsymbol{x}^{M1})\xi \tag{8.21}$$

ξ^{Sl} and g_N^{Sl} define the projection of the slave node on the master segment in tangential and normal directions respectively:

$$\xi^{Sl} = \frac{\boldsymbol{x}^{Sl} - \boldsymbol{x}^{M1}}{l} \cdot \boldsymbol{a} \;\; ; \;\; g_N^{Sl} = [\boldsymbol{x}^{Sl} - (1 - \xi^{Sl})\boldsymbol{x}^{M1} - \xi^{Sl}\boldsymbol{x}^{M2}] \cdot \boldsymbol{n} \tag{8.22}$$

The variation of the normal gap takes the form:

$$\delta g_N^{Sl} = [\boldsymbol{\eta}^{Sl} - (1 - \xi^{Sl})\boldsymbol{\eta}^{M1} - \xi^{Sl}\boldsymbol{\eta}^{M2}] \cdot \boldsymbol{n} \tag{8.23}$$

The relative tangential movement for stick is given as:

$$g_{Tstick}^{Sl} = \int_{\xi_0^{Sl}}^{\xi^{Sl}} l \, d\xi = (\xi^{Sl} - \xi_0^{Sl})l \tag{8.24}$$

where, ξ_0^{Sl} is the stick point on the master segment. We refer to [128] for the development of variational forms for tangential stick and slip as follows:

$$\delta g_{Tslip}^{Sl} = [\boldsymbol{\eta}^{Sl} - (1 - \xi^{Sl})\boldsymbol{\eta}^{M1} - \xi^{Sl}\boldsymbol{\eta}^{M2}] \cdot \boldsymbol{a} + \frac{g_N^{Sl}}{l}[\boldsymbol{\eta}^{M2} - \boldsymbol{\eta}^{M1}] \cdot \boldsymbol{n} \tag{8.25}$$

$$\begin{aligned} \delta g_{Tstick}^{Sl} &= [\boldsymbol{\eta}^{Sl} - (1 - \xi^{Sl})\boldsymbol{\eta}^{M1} - \xi^{Sl}\boldsymbol{\eta}^{M2}] \cdot \boldsymbol{a} + \frac{g_N^{Sl}}{l}[\boldsymbol{\eta}^{M2} - \boldsymbol{\eta}^{M1}] \cdot \boldsymbol{n} \\ &+ \frac{g_T^{Sl}}{l}[\boldsymbol{\eta}^{M2} - \boldsymbol{\eta}^{M1}] \cdot \boldsymbol{a} \end{aligned} \tag{8.26}$$

By substituting for g^{Sl}_{Tstick} using (8.24), (8.26) could alternatively be written as:

$$\delta g^{Sl}_{Tstick} = [\boldsymbol{\eta}^{Sl} - (1-\xi_0)\boldsymbol{\eta}^{M1} - \xi_0\boldsymbol{\eta}^{M2}] \cdot \boldsymbol{a} + \frac{g^{Sl}_N}{l}[\boldsymbol{\eta}^{M2} - \boldsymbol{\eta}^{M1}] \cdot \boldsymbol{n} \tag{8.27}$$

8.1.5 Contact Residual

The discrete expression of the contact contribution (8.5) for one node-to-segment pair takes the form :

$${}^{h}C^{con} = T_N \delta g^{Sl}_N + T_T \delta g^{Sl}_T \tag{8.28}$$

where $T_N = t_N A$ and $T_T = t_T A$ are extracted from the constitutive relation summarized in Box 8.1. The contact residual $\boldsymbol{\eta}^T \boldsymbol{G}$ is expressed in matrix formulation as:

$$\boldsymbol{\eta}^T \boldsymbol{G} = T_N \boldsymbol{N}^{Sl} + T_T \boldsymbol{T}^{Sl}, \tag{8.29}$$

where $\boldsymbol{\eta} = (\boldsymbol{\eta}^{M1}, \boldsymbol{\eta}^{M2}, \boldsymbol{\eta}^{Sl})^T$ and

$$\boldsymbol{N}^{Sl} = \boldsymbol{\eta}_\xi \boldsymbol{n} \tag{8.30}$$

$$\boldsymbol{T}^{Sl} = \begin{cases} \boldsymbol{\eta}_\xi \boldsymbol{a} + \frac{g^{Sl}_N}{l}\boldsymbol{\eta}_0 \boldsymbol{n} & \text{for slip} \\ \boldsymbol{\eta}_\xi \boldsymbol{a} + \frac{g^{Sl}_N}{l}\boldsymbol{\eta}_0 \boldsymbol{n} + \frac{g^{Sl}_T}{l}\boldsymbol{\eta}_0 \boldsymbol{a} & \text{for stick.} \end{cases} \tag{8.31}$$

In the above,

$$\boldsymbol{\eta}_\xi = \boldsymbol{\eta}^T \begin{Bmatrix} -(1-\xi) \\ -\xi \\ 1 \end{Bmatrix}, \quad \boldsymbol{\eta}_0 = \boldsymbol{\eta}^T \begin{Bmatrix} -1 \\ 1 \\ 0 \end{Bmatrix}. \tag{8.32}$$

8.1.6 Contact Stiffness

The contact formulation is incorporated into an implicit finite element algorithm that uses the Newton-Raphson method for solving non-linear equations, which requires that the residual be linearized, so that quadratic convergence is achieved. The linearized contact residual is given as

$$\Delta(\boldsymbol{\eta}^T \boldsymbol{G}) = \boldsymbol{N}^{Sl} \otimes \Delta T_N + \boldsymbol{T}^{Sl} \otimes \Delta T_T + T_N \Delta \boldsymbol{N}^{Sl} + T_T \Delta \boldsymbol{T}^{Sl}. \tag{8.33}$$

See Appendix A.4 for derivation of the contact stiffness.

8.1.7 Numerical Examples

A number of advanced contact benchmarks were produced by A.W.A. Konter within the FENET report FENET-UNOTT-DLE-09 [56]. Following two examples seek to verify the developed contact framework against the reference report.

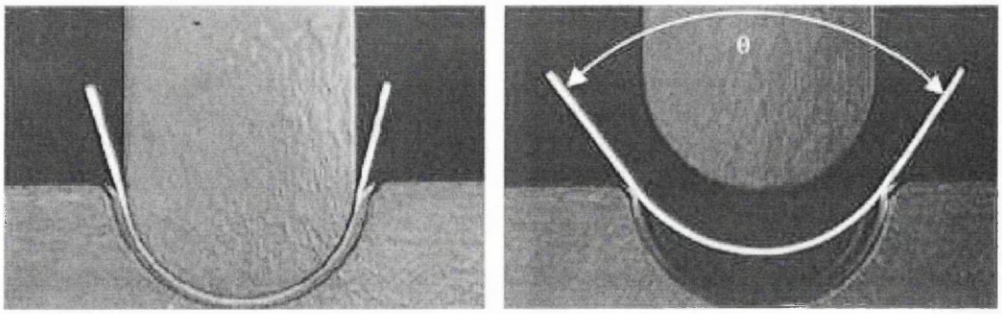

Figure 8.4: Metal forming: unconstrained cylindrical bending test. Source: Sousaa *et al.*[105]

Metal Forming

The first example is an approximation to the unconstrained cylindrical bending test, which was proposed in Numisheet 2002 [86] as spring back benchmark, where numerical simulations of the test shown in Figure 8.4 are performed to determine the forming angle, as well as the angle after release of the tool.

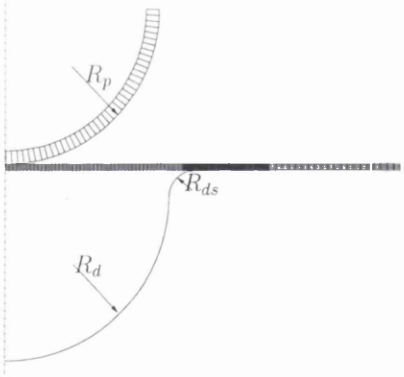

Figure 8.5: Metal forming: initial geometry

A 1 mm thick 120 × 30 sheet is formed by a 28.5 mm downward stroke of a punch of radius R_p=23.5 mm into a die of radius R_d=25 mm, with shoulder radius R_{ds}=4 mm, as shown in Figure 8.5.

The sheet is assumed to be elastoplastic with Young's modulus $E = 70.5$ GPa, Poisson's ratio $\nu = 0.342$. Plasticity is driven by Hollomon hardening [50] with $\sigma = \sigma_0 + K\varepsilon^n$, which is modelled by piecewise linear hardening. The parameters are

Friction Coefficient	Forming Angle		Angle after release	
	numerical	experiment	numerical	experiment
0.	20.51	19.6-21.0	53.26	53.4-55.8
0.1348	20.45		56.35	

Table 8.1: Metal Forming: Forming angle and angle after release for variations of friction coefficient.

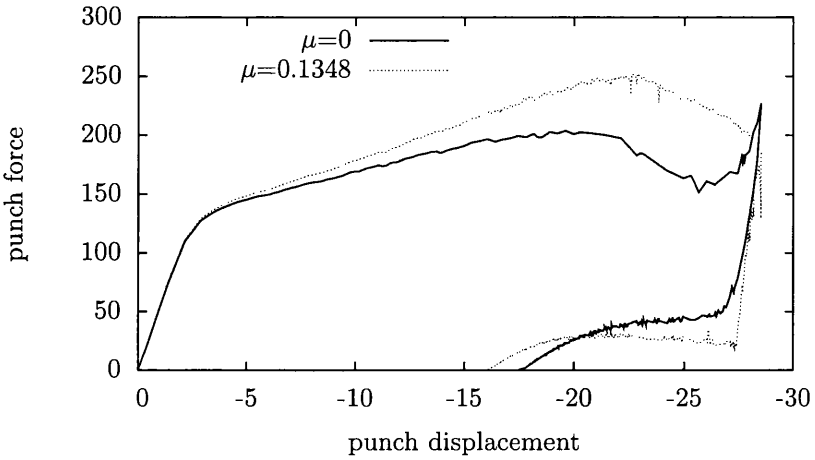

Figure 8.6: Metal forming: load displacement diagrams for μ=0. and μ=0.1348, for punch and die 50 mm wide.

given as $K = 550.4$ MPa, initial yield stress $\sigma_0 = 194$ MPa, $n = 0.223$. Because of symmetry, only half of the sheet is modelled by 800 quadrilateral F-Bar elements, 5 in thickness direction and 50 between 0 and 27 mm, 100 between 27 and 40.2 mm and 20 between 40.2 and 60 mm.

The nearly rigid punch is defined as an elastic body with Young's modulus $E = 1000$ GPa, Poisson's ratio $\nu = 0.3$, and is modelled by 39 quadrilaterals, with a contact interface on the outside surface. The die is modelled exclusively as a contact interface whose master surface is not allowed to move.

Loading and unloading consists of a 28.5 mm punch stroke down and back gradually. A 2D plane finite strain quasi static analysis is performed for friction coefficient values of 0 and 0.1348. The forming angle at the end of the stroke, as well as the angle after release of punch is shown for for variations of friction coefficient in Table 8.1, where a very good agreement with the experimental data can be observed. This

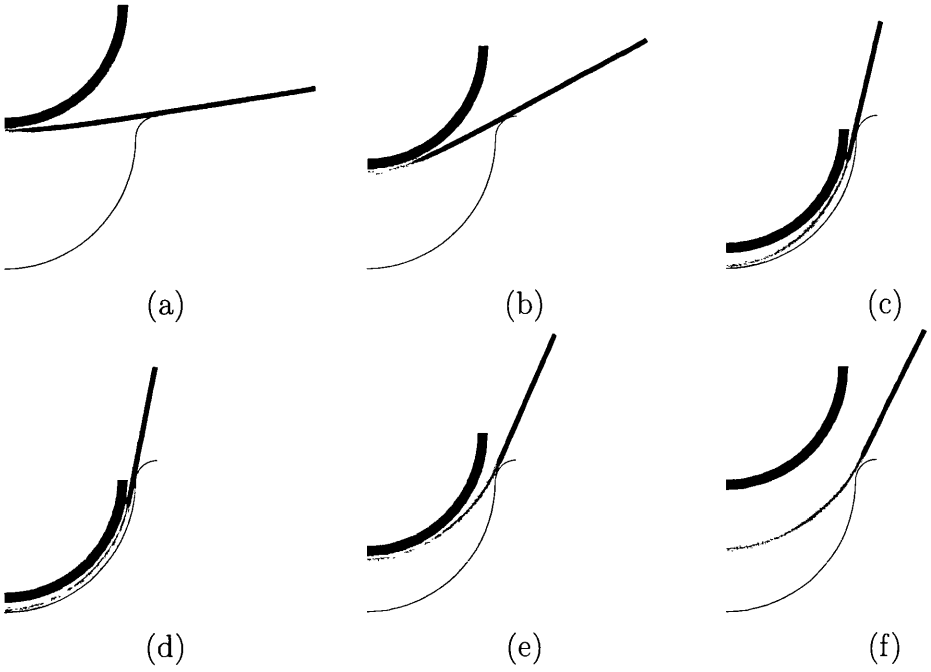

Figure 8.7: Metal forming: deformed mesh and development of plastic strains (a)-(d) loading, punch displacement:-3, -11, -27, -28.5 mm, (e)-(f) unloading, punch displacement:-19, -7 mm

is also true for the load displacement diagrams shown in Figure 8.6, where the trends obtained by commercial finite element codes in the reference paper are recovered .

Figure 8.7 shows the deformed mesh and development of plastic strains during the loading history for no friction. Towards the end of the stroke, the sheet separates from the punch, which corresponds to the softening response observed in Figure 8.6. When the sheet contacts the die surface forming continues, and the force increases to its maximum.

Steel Roller on Rubber

This benchmark refers to the observation that, when a cylindrical steel roller rotates on a rubber base, for a complete revolution of the cylinder, it will have moved a horizontal distance less than the circumference of the cylinder. The goal of the simulation is to test the ability to model two surfaces in contact whilst moving.

A steel roller with radius 30 mm is resting on a 20 mm thick 300 mm long rubber mat, as shown in Figure 8.8 (left). The necessary compression for friction is

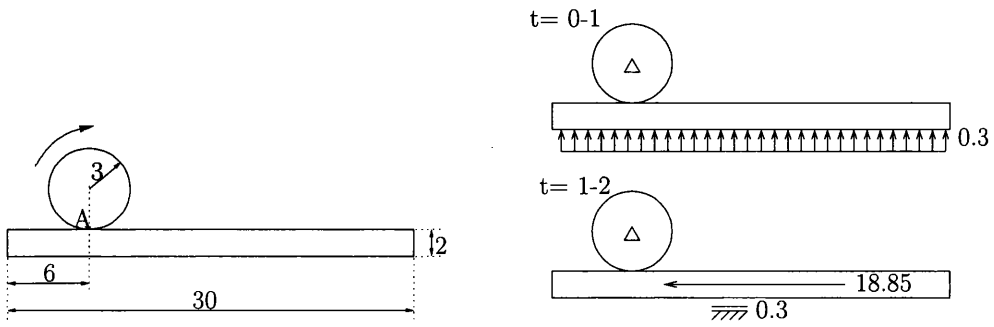

Figure 8.8: Still roller on rubber mat: (left) geometry (right) loading and boundary conditions, units in cm.

maintained by 3 mm vertical displacement of the rubber mat base. Then, a single rotation of the roller is prescribed by pulling the rubber laterally by 188.5 mm, while fixing the vertical displacement at 3 mm, as shown in Figure 8.8 (right).

Both steel roller and the rubber mat are assumed to be Neo-Hookean hyperelastic materials with material parameters given as:

- Steel Roller: μ=80, K=175

- Rubber Mat: μ=0.015, K=0.15

Contact between the roller and the mat is characterized by a coefficient of friction μ_f=0.3. A 2D plane finite strain quasi static analysis is performed where the roller/mat are modelled using 236/600 F-Bar elements respectively.

Deformed meshes over the loading history are given in Figure 8.9 for times 0, 1, 1.25, 1.5, 1.75 and 2 respectively. The roller has moved 180.9 mm, less than the circumference 188.5 as predicted, and in agreement with the FENET report [56]. Figure 8.10 shows the vertical reaction force on the roller, which is also in good agreement with the report.

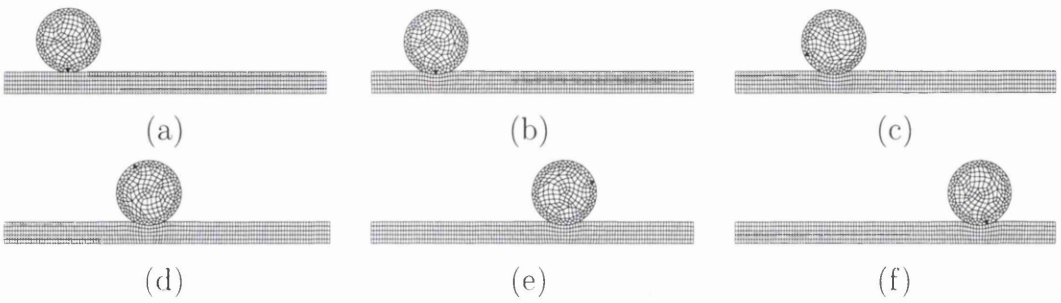

Figure 8.9: Steel roller on rubber mat: (a) initial mesh, (a)-(b) t= 0-1 : compression (c)-(f) t= 1.25, 1.5, 1.75, 2 : 360° roll

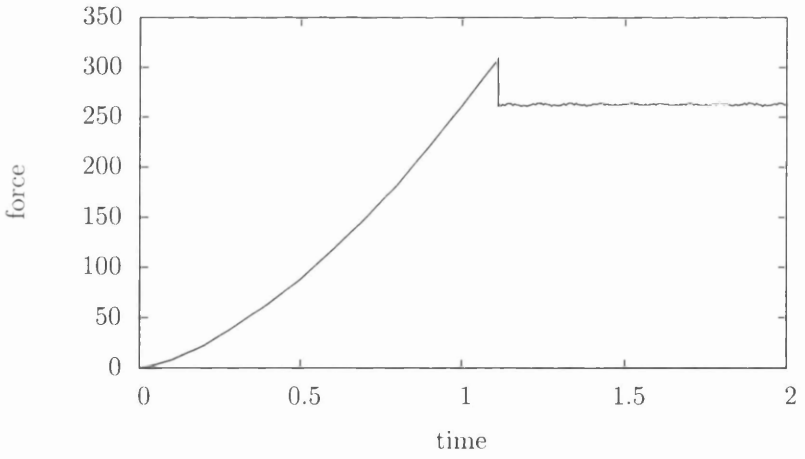

Figure 8.10: Steel roller on rubber mat: Force/Displacement diagram

8.2 Interface Contact within RVE

The goal of this example is to investigate the plastic collapse of an RVE containing a debonded nearly rigid elastic inclusion, motivated by Giusti *et al.*[34], who used RVEs to predict macroscopic yield surfaces as functions of the void ratio of the porous metal, and compared the results with the Gurson yield surface [38].

A square RVE with a rigid inclusion at its centre, 10% by volume, is considered under conditions where the matrix and the inclusion are either bonded or fully debonded. For the debonded configuration, contact with (μ=0.3) and without (μ=0) friction is considered. To stabilize the problem, the inclusion is prescribed a preliminary radial expansion by 1%. To verify the results, an RVE with a 10% void described by a single hole at its centre is also investigated, as well as the homogeneous continuum solution where the whole RVE consists of the matrix material.

The ideally plastic matrix material of the RVE is modelled by means of a standard von Mises elasto-plastic model, where the material properties are specified as: Young's modulus $E = 200$ GPa, Poisson's ratio $\nu = 0.3$ and initial yield stress $\sigma_0 = 240$ MPa. The nearly rigid elastic inclusion is modelled by Young's modulus $E = 1100$ GPa, Poisson's ratio $\nu = 0.25$.

The plane strain RVE is discretized by a mesh of (400+100) F-Bar elements. The loading programme consists in prescribing a macroscopic strain path,

$$\boldsymbol{\varepsilon}(\gamma) = \gamma \bar{\boldsymbol{\varepsilon}} \tag{8.34}$$

imposed upon the RVE, parametrized by a time factor γ, and a unit strain tensor satisfying $\|\bar{\boldsymbol{\varepsilon}}\|=1$ by:

$$\bar{\boldsymbol{\varepsilon}} = \alpha \begin{bmatrix} \frac{1}{\sqrt{2}} & 0 \\ 0 & \frac{1}{\sqrt{2}} \end{bmatrix} + \sqrt{1-\alpha^2} \begin{bmatrix} 0 & \frac{1}{\sqrt{2}} \\ \frac{1}{\sqrt{2}} & 0 \end{bmatrix}. \tag{8.35}$$

Note that by varying the load factor α between -1 and 1, the above tensor fully covers the loading spectrum in spherical and pure shear strain directions. Finite element simulations are performed for 21 α values -1.0, -0.9, ...,0,...,1.0 for all configurations. The macroscopic von Mises stress and hydrostatic pressure are extracted from the homogenized stress.

Figure 8.12 shows the variation of the macroscopic von Mises stress and the pressure for bonded/debonded/no inclusion configurations for expansive load factor α values 0.0, 0.3, 0.5, 0.7, 1.0. As expected, the debonded inclusion is not loaded at all, thus all graphs coincide with an RVE that has a hole. Figure 8.14 depicts variation of the macroscopic von Mises stress and the pressure for compressive load factor

α values 0.0, -0.3, -0.5, -0.7, -1.0, where it can be observed that the RVE with a fully debonded inclusion tends to approach an RVE with a fully bonded inclusion with increasing pressure. Observed pressure offset is due to the initial prescribed expansion.

The equivalent plastic strain is plotted on deformed RVEs, $+\alpha$ values in Figure 8.13

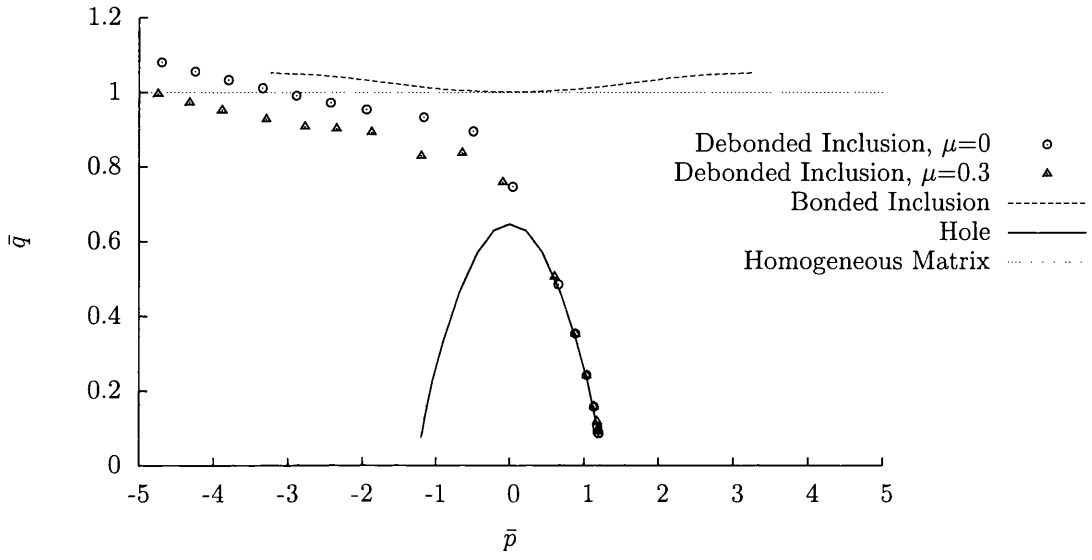

Figure 8.11: Estimated yield surfaces for inclusion that is (i)-fully bonded (ii)-fully debonded without friction (μ=0) (iii)-fully debonded with friction (μ=0.3) and (iv)-no inclusion

and $-\alpha$ values in Figure 8.15 respectively. The debonded RVE behaves like there was no inclusion for loadings that expand it, while approaching the RVE with fully bonded inclusion for compressive loadings.

Plastic collapse is assumed to occur when the macroscopic stress stops changing with increasing load. For expansive loadings it is manifested by the flattening of von Mises stress curve. For compressive loads for which the RVE stiffens, plastic collapse does not happen for the volume fraction considered. For visualization, we have picked and interpolated points that intersect a 2% offset from the elastic part of the von Mises stress curve. The pressure and von Mises components of the plastic collapse stress are normalized as:

$$\bar{p} = \frac{p}{\sigma_Y} \ , \ \bar{q} = \frac{q}{\sigma_Y} \tag{8.36}$$

Each $\bar{q}$-$\bar{p}$ couple constitutes a yield surface point, which is plotted in Figure 8.11. Note that for an RVE with a hole, the yield surface obtained in the reference paper [34] is recovered. Again, for expanding loads, the RVE with a fully debonded inclusion behaves perfectly like an RVE with a hole, whereas for shrinking loads, the RVE with a fully debonded inclusion tends to approach an RVE with a fully bonded inclusion.

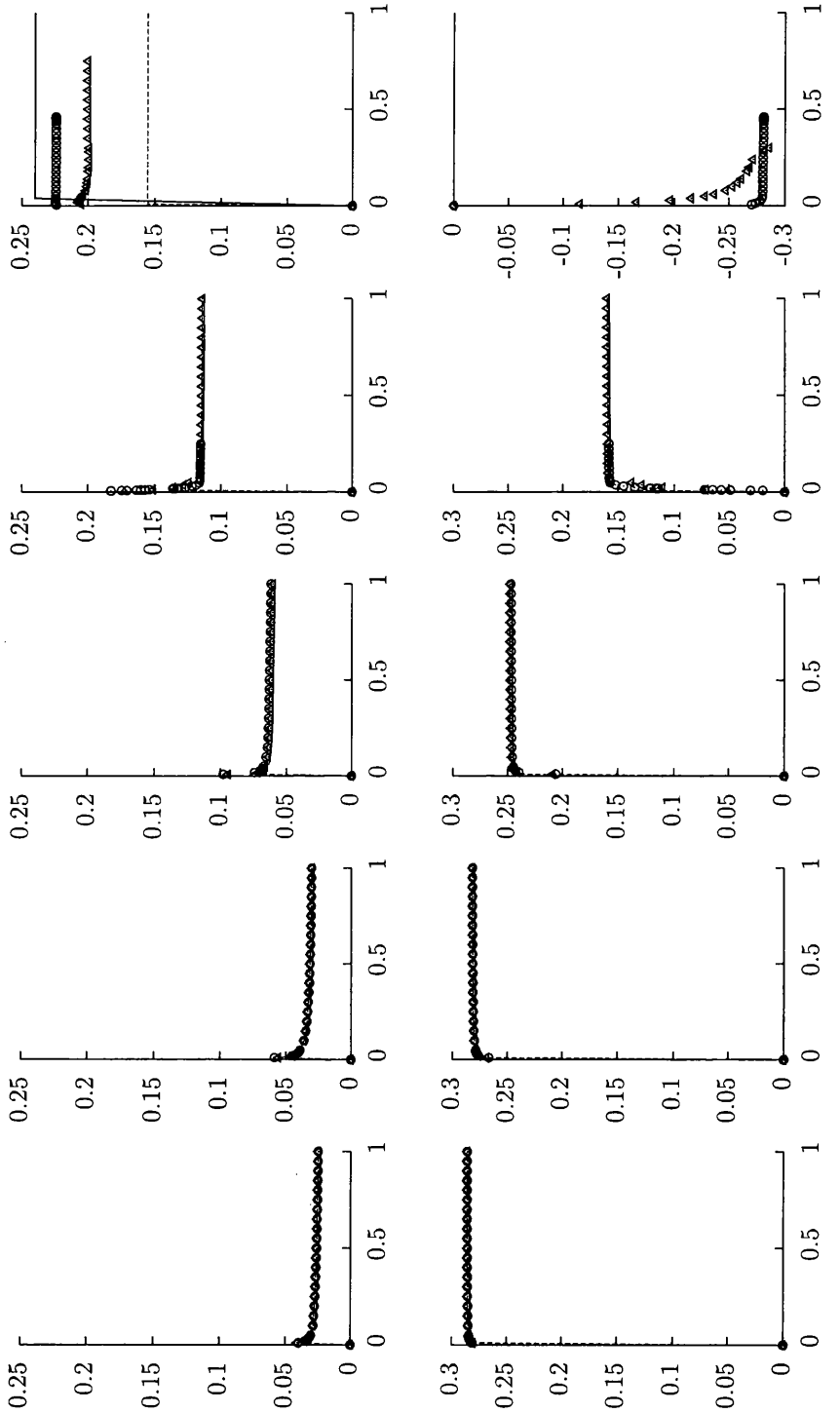

Figure 8.12: Contact within RVE: comparison of (top) von Mises Stress and (bottom) Pressure vs pseudo time, bonded/debonded/no inclusion, for expanding load factors. Refer to Fig. 8.11 for key.

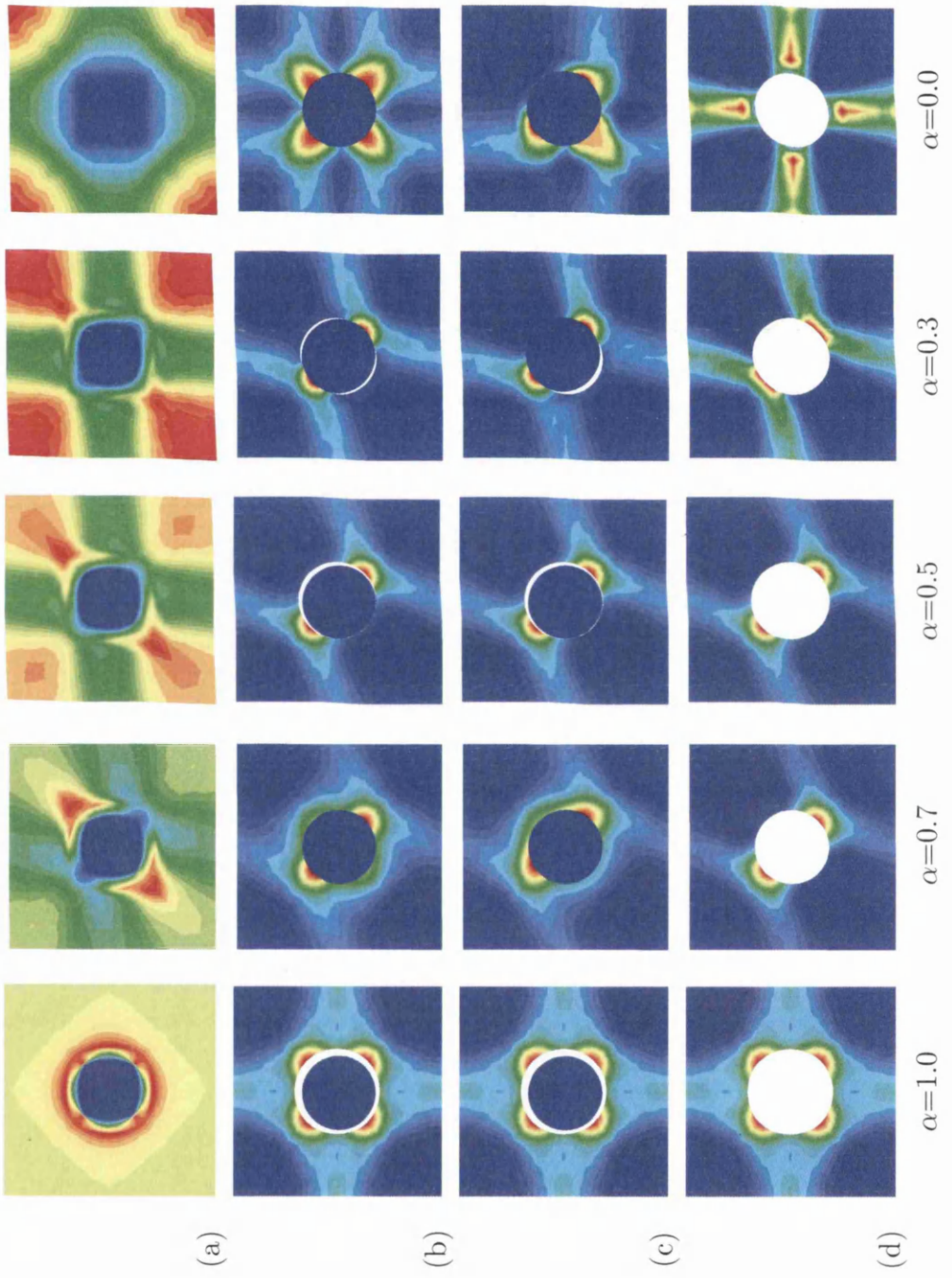

Figure 8.13: Contact within RVE: equivalent plastic strain plots for (a) fully bonded inclusion, (b) fully debonded inclusion without friction (μ=0) (c) fully debonded inclusion with friction (μ=0.3) and (d) no inclusion, for expansive load factors

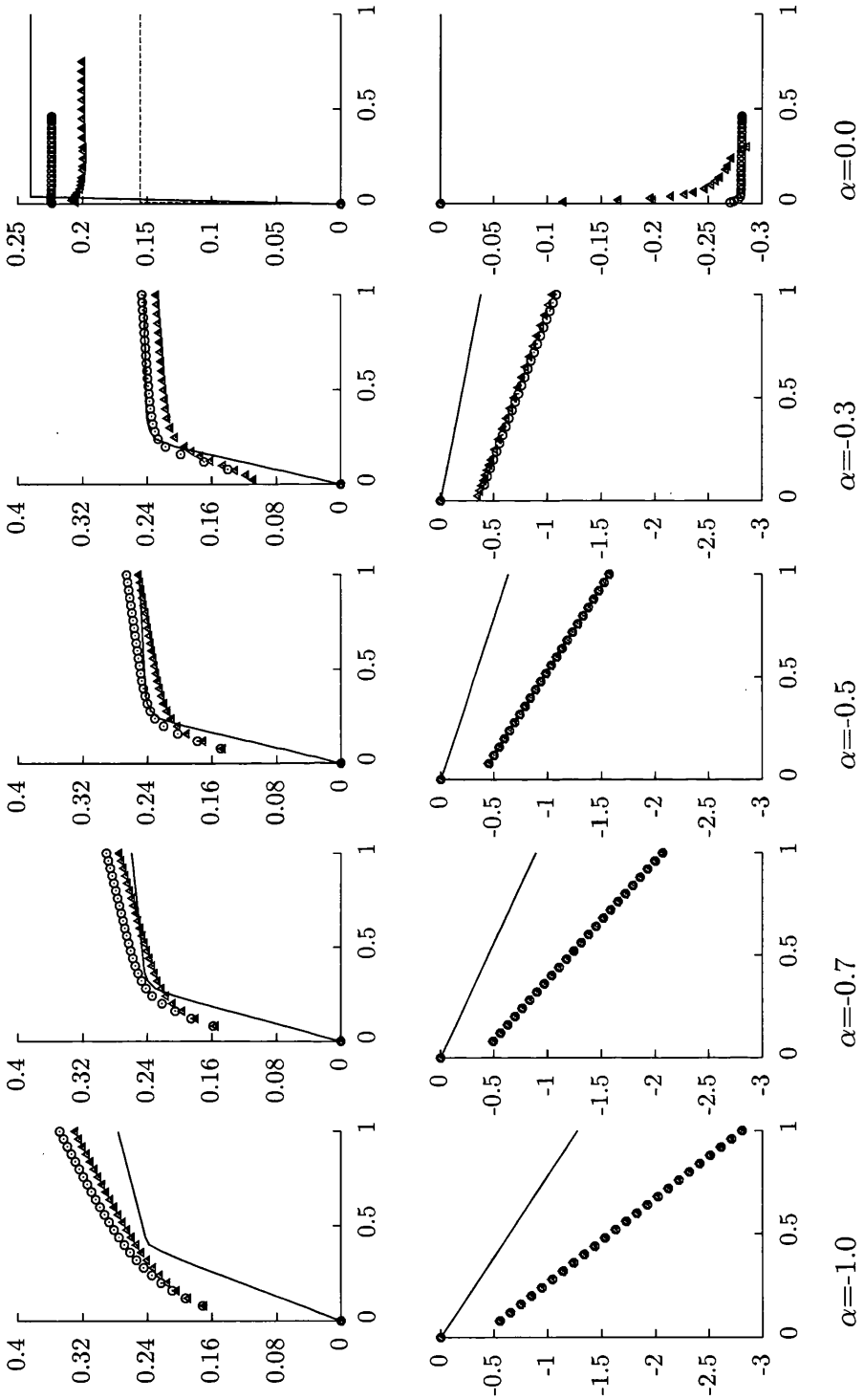

Figure 8.14: Contact within RVE: comparison of (top) von Mises Stress and (bottom) Pressure vs pseudo time, bonded/debonded/no inclusion, for compressive load factors. Refer to Fig. 8.11 for key.

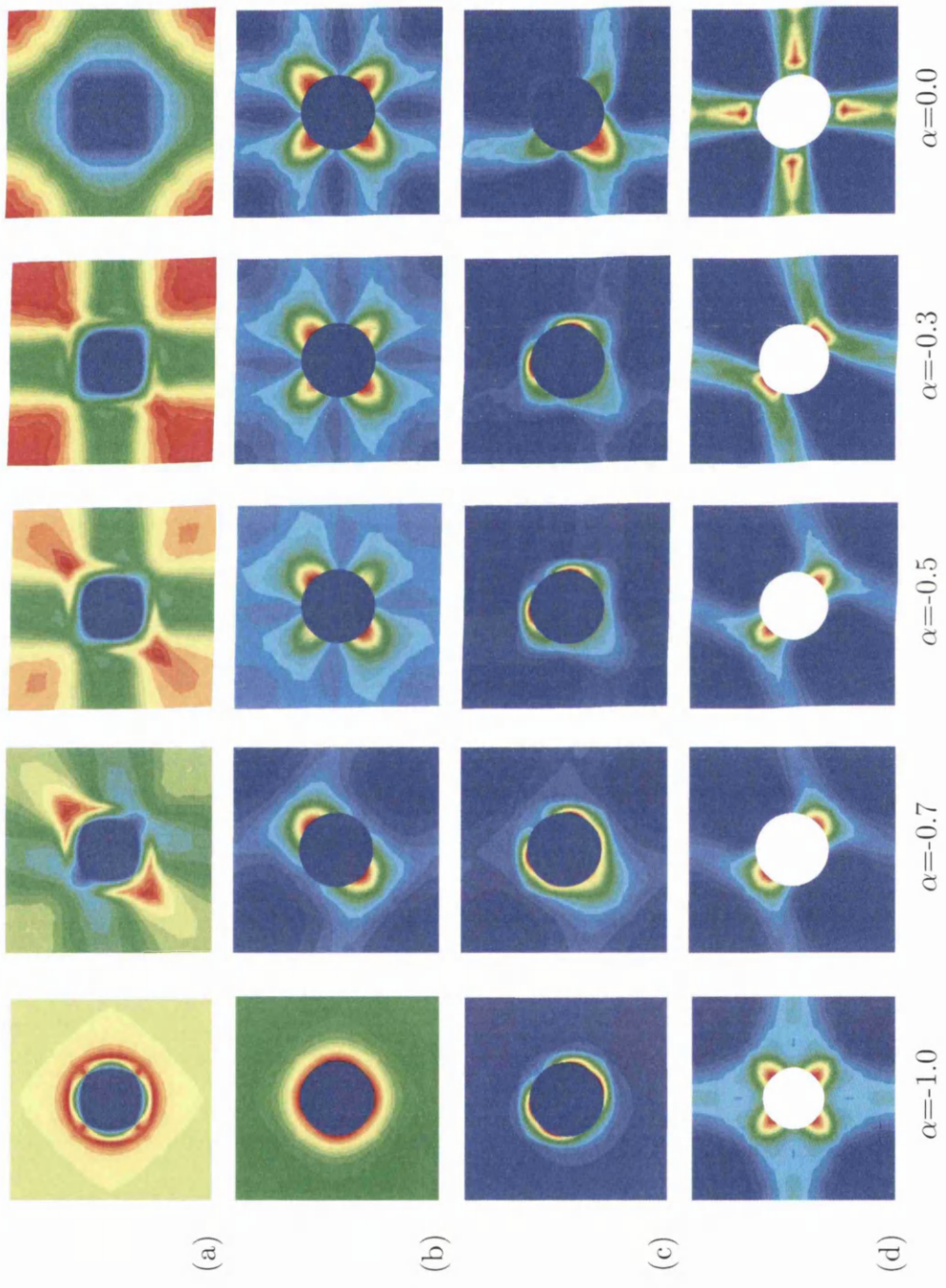

Figure 8.15: Contact within RVE: equivalent plastic strain plots for (a) fully bonded inclusion, (b) fully debonded inclusion without friction (μ=0) (c) fully debonded inclusion with friction (μ=0.3) and (d) no inclusion, for compressive load factors

8.3 Cohesive Zone Model

Consider body Ω in Figure 8.16 separated by a discontinuity $\partial\Omega^{coh}$ into two subdomains Ω^+ and Ω^-. The boundary value problem defined in Chapter 2 is extended to involve two bodies, as well as the cohesive contributions C^{coh}:

$$\begin{aligned} &\int_{\Omega^+} \hat{\boldsymbol{\sigma}}^+ : \nabla \boldsymbol{\eta}^+ dv - \int_{\Omega^+} \boldsymbol{f}^+ \cdot \boldsymbol{\eta}^+ dv - \int_{\partial\Omega^+} \boldsymbol{t}^+ \cdot \boldsymbol{\eta}^+ da \\ + &\int_{\Omega^-} \hat{\boldsymbol{\sigma}}^- : \nabla \boldsymbol{\eta}^- dv - \int_{\Omega^-} \boldsymbol{f}^- \cdot \boldsymbol{\eta}^- dv - \int_{\partial\Omega^-} \boldsymbol{t}^- \cdot \boldsymbol{\eta}^- da \\ + &\int_{\partial\Omega^{coh}} (t_N \delta g_N + \boldsymbol{t}_T \cdot \delta \boldsymbol{g}_T) da = 0 \;\; \forall \boldsymbol{\eta}^+, \boldsymbol{\eta}^- \in \mathcal{V} \end{aligned} \tag{8.37}$$

where t_N, $\boldsymbol{t}_T$ are the components of tractions on discontinuity $\partial\Omega^{coh}$ along unit normal and tangential vectors $\boldsymbol{n}$ and $\boldsymbol{t}$, that do work on displacement jumps $\boldsymbol{g}$.

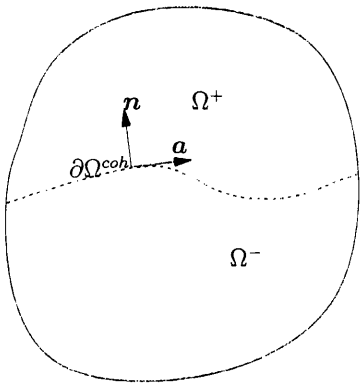

Figure 8.16: Body separated by a discontinuity

8.3.1 Constitutive Relations

The cohesive constitutive response is determined by an *ad hoc* definition of a traction separation law, as pointed by Gasser *et al.* [31]. The debonding behaviour is governed by an assumed potential ψ which relates the cohesive tractions $\boldsymbol{t}$ to the displacement jump $\boldsymbol{g}$ as:

$$\boldsymbol{t} = \frac{\partial \psi(\boldsymbol{g}, \boldsymbol{q})}{\partial \boldsymbol{g}} \tag{8.38}$$

where $\boldsymbol{q}$ denote a set of internal variables that characterize inelastic processes associated with cohesion. A number of alternative descriptions for a displacement

measure has been suggested (see e.g. [84], [121] or [85]). We will follow Ortiz *et al.* [85] and employ an effective opening displacement defined as

$$\delta = \sqrt{\beta^2 \boldsymbol{g}_T \cdot \boldsymbol{g}_T + g_N^2}. \tag{8.39}$$

where β is a weighing factor that controls the contribution of the tangential component of the displacement jump. $\boldsymbol{t}$ is decomposed into normal and tangential components:

$$\begin{aligned} \boldsymbol{t} &= \frac{\partial \psi}{\partial g_N}\boldsymbol{n} + \frac{\partial \psi}{\partial \boldsymbol{g}_T}\boldsymbol{a} \\ &= \frac{\partial \psi}{\partial \delta}\left(\frac{\partial \delta}{\partial g_N}\boldsymbol{n} + \frac{\partial \delta}{\partial \boldsymbol{g}_T}\boldsymbol{a}\right) \\ &= t_N \boldsymbol{n} + \boldsymbol{t}_T \boldsymbol{a}, \end{aligned} \tag{8.40}$$

where, by use of (8.39):

$$t_N = \frac{t}{\delta} g_N \quad , \quad \boldsymbol{t}_T = \frac{t}{\delta}\beta^2 \boldsymbol{g}_T \quad , \quad t = \frac{\partial \psi}{\partial \delta}. \tag{8.41}$$

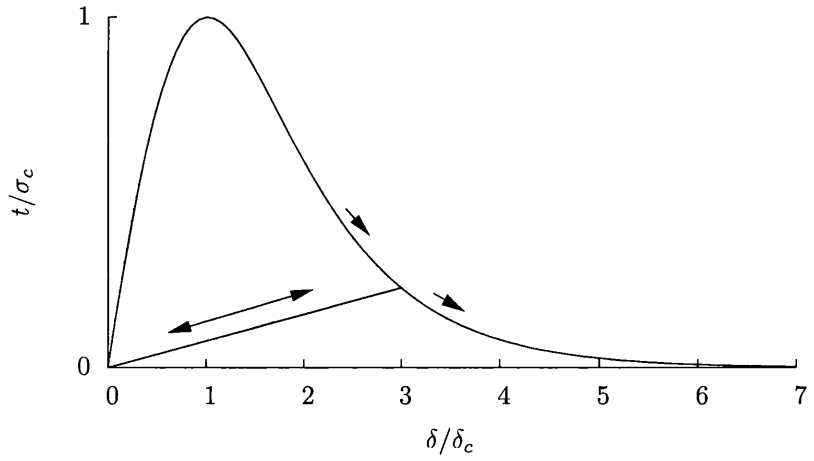

Figure 8.17: Cohesive constitutive law, loading/unloading

For loading, the Smith/Ferrante universal binding law is assumed, which is obtained from differentiation of the potential:

$$\psi = e\sigma_c \delta_c \left[1 - \left(1 + \frac{\delta}{\delta_c} e^{-\frac{\delta}{\delta_c}}\right)\right] \tag{8.42}$$

where σ_c and δ_c are the critical stress and effective opening displacement respectively. Unloading is assumed to be linear and to the origin, as depicted in the normalized loading/unloading diagram of Figure 8.17. The constitutive model is thus complete with

$$t = \begin{cases} \sigma_c \frac{\delta}{\delta_c} e^{1-\frac{\delta}{\delta_c}} & \text{for } \delta = \delta_{max} \text{ and } \dot{\delta} \geq 0 \\ \frac{t_{max}}{\delta_{max}} \delta & \text{for } \delta < \delta_{max} \text{ and } \dot{\delta} < 0 \end{cases} \tag{8.43}$$

and the stiffness term required by the Newton-Raphson procedure:

$$\frac{\partial t}{\partial \delta} = \begin{cases} \frac{\sigma_c}{\delta_c}(1 - \frac{\delta}{\delta_c}) e^{1-\frac{\delta}{\delta_c}} & \text{for } \delta = \delta_{max} \text{ and } \dot{\delta} \geq 0 \\ \frac{t_{max}}{\delta_{max}} & \text{for } \delta < \delta_{max} \text{ and } \dot{\delta} < 0. \end{cases} \tag{8.44}$$

8.3.2 Cohesive Residual

The discrete expression of the cohesive contribution from the boundary value problem (8.37) for one node-to-segment pair takes the form :

$$^h C^{coh} = T_N \delta g_N^{Sl} + T_T \delta g_T^{Sl}, \tag{8.45}$$

where $T_N = t_N A$ and $T_T = t_T A$ are extracted from the cohesive constitutive relation. The cohesive residual $\boldsymbol{\eta}^T \boldsymbol{G}^{Sl}$ is expressed in matrix formulation as:

$$\boldsymbol{\eta}^T \boldsymbol{G}^{Sl} = T_N \boldsymbol{N}^{Sl} + T_T \boldsymbol{T}^{Sl} \tag{8.46}$$

where $\boldsymbol{\eta} = (\boldsymbol{\eta}^{M1}, \boldsymbol{\eta}^{M2}, \boldsymbol{\eta}_\xi)^T$ and,

$$\boldsymbol{N}^{Sl} = \boldsymbol{\eta}_\xi \boldsymbol{n} \tag{8.47}$$

$$\boldsymbol{T}^{Sl} = \boldsymbol{\eta}_\xi \boldsymbol{a} + \frac{g_N^{Sl}}{l} \boldsymbol{\eta}_0 \boldsymbol{n} \tag{8.48}$$

where,

$$\boldsymbol{\eta}_\xi = \begin{Bmatrix} -(1-\xi)\boldsymbol{\eta}^{M1} \\ -\xi \boldsymbol{\eta}^{M2} \\ \boldsymbol{\eta}_\xi \end{Bmatrix}, \quad \boldsymbol{\eta}_0 = \begin{Bmatrix} -\boldsymbol{\eta}^{M1} \\ \boldsymbol{\eta}^{M2} \\ 0 \end{Bmatrix} \tag{8.49}$$

8.3.3 Cohesive Stiffness

The expression for the linearized cohesive residual is similar to the one developed for contact:

$$\Delta(\boldsymbol{\eta}^T \boldsymbol{G}^{Sl}) = \boldsymbol{N}^{Sl} \otimes \Delta T_N + \boldsymbol{T}^{Sl} \otimes \Delta T_T + T_N \Delta \boldsymbol{N}^{Sl} + T_T \Delta \boldsymbol{T}^{Sl} \tag{8.50}$$

see Appendix A.5 for derivation of the cohesive stiffness.

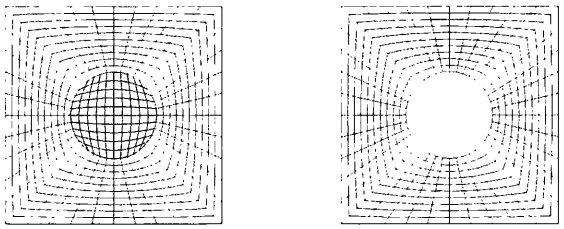

Figure 8.18: Interphase Contact within RVE: initial mesh, with and without inclusion

8.3.4 Numerical Example

This example is concerned with a debonding inclusion within a square RVE. Similar simulations have appeared in the literature: Lissenden and Herakovich [65] used the cohesive zone model within a unit cell, followed by others [52, 64]. Ghosh and coworkers [62] used Voronoi cells, and recently added bilinear and linear cohesive zone models for representing interfacial debonding and matrix crack propagation [63]. Matous and Geubelle [70] used 3D RVEs to capture debonding of reinforced elastomers, while enforcing the contact constraint by means of an exponential constitutive law, inspired by the cohesive model. Sfantos and Aliabadi [98] used the cohesive zone model within a parallel processing multi-scale boundary element method.

The nearly rigid elastic inclusion is 12.5% by volume and is located at the centre of the RVE, as shown in Figure 8.18. Debonding behaviour is governed by the cohesive model for opening and frictionless contact model for closing configurations respectively, whereas both models contribute to sliding configurations. To verify the results, the RVE is also considered under configurations where the matrix and the inclusion are either fully bonded or fully debonded. For the debonded configuration only frictionless contact (μ=0) is considered.

Plane stress condition is assumed and the RVE matrix material is modelled by a von Mises type elastoplastic law with Young's modulus $E = 170$ GPa, Poisson's ratio $\nu = 0.3$, initial yield stress $\sigma_0 = 500$ MPa with perfect plasticity. To overcome numerical difficulties a linear hardening modulus $H = 0.01$ GPa is adopted. The nearly rigid elastic inclusion has mechanical properties given as $E = 1100$ GPa and $\nu = 0.22$. The cohesive parameters are given as $\sigma_c = 0.01$ and $\beta = 0.8$. Three critical effective displacements are considered: $\delta_c = \{0.3, 0.5, 1\}\,\mu m$.

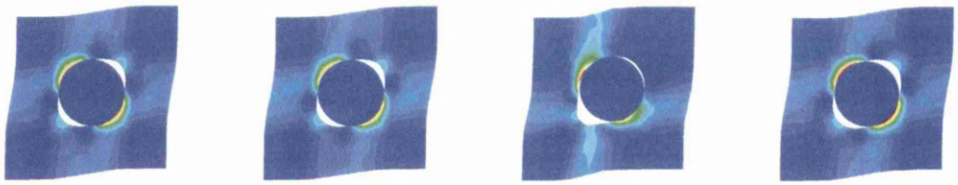

(a) (b) (c) (d)

Figure 8.19: Debonding of an inclusion: development of equivalent plastic strain on deformed mesh for cohesive critical effective displacements (a) $\delta_c = 0.3\,\mu m$, (b) $\delta_c = 0.5\,\mu m$, (c) $\delta_c = 1\,\mu m$ and (d) fully debonded inclusion without friction μ=0. Deformations were exaggerated for visualization.

The periodic RVE is loaded by a prescribed shear strain

$$\{\bar{\varepsilon}_{11}, \bar{\varepsilon}_{22}, 2\bar{\varepsilon}_{12}\} = \{0, 0, \sqrt{2}\} \tag{8.51}$$

multiplied by a loading factor that is increased up to 0.02. The RVE boundary value problem is solved, and homogenized stress $\bar{\boldsymbol{\sigma}}$ is calculated. The effective von Mises stress, given by:

$$\bar{\sigma}_{vm} = \sqrt{\frac{3}{2}\bar{\boldsymbol{\sigma}}_{dev} : \bar{\boldsymbol{\sigma}}_{dev}} \tag{8.52}$$

is plotted in Figure 8.20. As expected, debonding configurations lie between fully bonded and fully debonded configurations. Before debonding takes place, all three configurations overlap with the fully bonded configuration. Initiation of debonding follows the order of critical effective displacements $\{0.3, 0.5, 1\}\,\mu m$, and once damaged, all configurations approach the fully debonded configuration. Equivalent plastic strain is plotted on (exaggerated) deformed mesh in Figure 8.19.

Even though the simulation was performed assuming small deformations, the solution was very numerically challenging due to non-linearity associated with cohesive and contact models, as well as plasticity. This necessitates a very careful selection of parameters, and especially for large deformation simulations, use of the arc-length method might be the only way to obtain a solution..

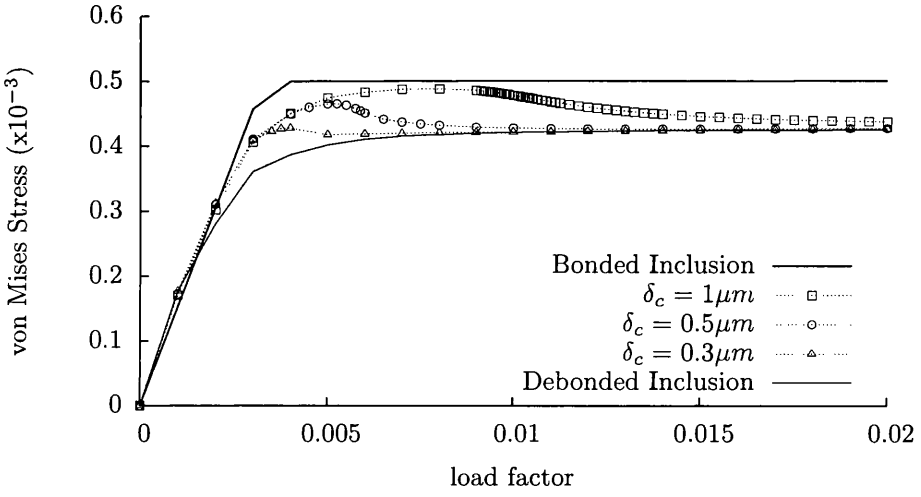

Figure 8.20: Debonding of an inclusion: von Mises Stress for cohesive critical effective displacements $\delta_c = \{0.3, 0.5, 1\}\,\mu m$ compared to fully bonded/fully debonded inclusion without friction μ=0

Chapter 9

Conclusions

The aim set at the beginning of the thesis was accomplished as far as time permitted. In other words, a compact and efficient computational framework for the multi-scale analysis of solids for small and large strain problems was developed and its capability to solve fully coupled problems efficiently was demonstrated. In what follows, a more detailed account of achievements and conclusions is presented, as well as suggestions for future research.

A multi-scale framework that linked the micro and macro scales was formulated in small and large strain regimes, based on the variational treatment of the homogenization problem. Some commonly used classes of boundary conditions of the RVE, namely uniform displacements, uniform tractions and periodic displacements with anti-periodic tractions were defined by the choice of the functional space of virtual displacements, which allowed representation of the kinematical constraint using unified master-slave type dependencies within a direct approach. The homogenized stress was consistently linearized to achieve the asymptotic convergence associated with the Newton-Raphson method. The framework was verified for single scale homogenization, as well as fully coupled multi-scale simulations using benchmark problems in small and large strain regimes.

Computer Implementation of a multi-scale framework that is capable of solving real problems requires a computer code that can handle an arbitrary number of domains very efficiently. Dettmer's Multi Physics Analysis Program [23] was extended to handle multi-scale problems which are essentially multi-domain. The new object oriented code, MPAP2, was written in C++ and Fortran from scratch, which makes it modular, expandable and efficient.

A discrete interface that is linked to the discrete RVE boundary by a finite element type interpolation was proposed. Cost savings up to 50-60 % were demon-

strated for small and large strains at the cost of negligible accuracy loss, while the asymptotic convergence of the Newton-Raphson scheme was preserved. The mesh of a realistic 3D microstructure is not, in general, periodic and interface discretization allows a periodic RVE to have a non-periodic mesh. The use of interface discretization for such scenario was demonstrated by the use of unstructured meshed 3D hexagonal packed RVEs to predict material properties of long fibre composites.

A sub-stepping procedure was proposed to obtain better estimates for the RVE equilibrium state in the finite element solution of solid mechanics problems involving the use of homogenization-based multi-scale constitutive models. Numerical examples under the assumptions of both small and finite strains have demonstrated that the proposed procedure produces a dramatic improvement in the robustness of the Newton-Raphson scheme adopted in the iterative solution of the incremental RVE equilibrium problem. As a result, larger time/load increments can be prescribed at the macroscopic scale, leading to substantial savings in overall computing time. Such savings were found to be particularly noticeable, with an overall speed-up factor of up to four, under finite strains. It should be remarked that the sub-stepping procedure preserves the quadratic rate of asymptotic convergence of the macroscopic scale Newton-Raphson scheme, without compromising the accuracy of the solution. Note that, even though the combined use of interface discretization and sub-stepping was not elaborated within the present work, it can be safely claimed that the efficiency gain would surpass that of any of these treatments alone.

Predictions for mechanical properties of long fibre composites obtained from homogenization of 2D and 3D RVEs were compared to properties obtained using analytical methods, namely the Slab, Hashin-Rosen and Halpin-Tsai models. Hexagonal and tetragonal packing arrangements were also considered, and the hexagonally packed RVE, where interface discretization was used to enforce the periodic boundary condition, was found to be consistent with both Hashin-Rosen and Halpin-Tsai approaches for all properties sought. Strong and weak points of reference analytical approaches were highlighted: while the Slab assumption can be employed safely for longitudinal Young's modulus and Poisson's ratio, only Hashin-Rosen and Halpin-Tsai models provide acceptable predictions for longitudinal shear modulus or the transverse Young's modulus. None of the three models considered provided good predictions for the transverse Poisson's ratio.

Fully coupled small strain analysis of 2D and 3D beams was conducted to investigate the effect of fibre orientation, as well as the fibre volume ratio on beam displacement. Continuum models using material properties obtained from Slab and Halpin-Tsai models were compared to the present model. Periodic RVEs were found

to be in good agreement with the analytical models, for 2D and 3D, where, as expected, orientations for which the fibres are aligned with the beam axis returned the smallest deformation. It should also be noted that minor misalignment from the beam axis has negligible effect on the deflection.

Finite strain twisting and grooving of a two ply laminate was demonstrated using the fully coupled simultaneous approach, and the response of continuum models whose parameters were obtained by linearization of the constitutive relation of a finite strain transversely isotropic model were retrieved. Note that this example was only a benchmark for the multi-scale formulation, which is able to represent more complex micro-structural phenomena like interwoven arrangement of fibres or inter phase effects, where a macro-mechanical continuum model falls short. It was performed with rather simple RVEs to save computational time. For realistic 3D simulations, **parallelization** is essential. The multi-scale problem lends itself naturally to coarse parallelization, as each RVE equilibrium problem needs to be solved seperately, independent from other RVEs. With a straightforward manipulation of the existing code, using 8 processors within a shared memory architecture, our preliminary study indicates speed up factors of 5 to 6.

Modelling of weak interfaces is an important front of micro-mechanics, as many macroscopic phenomena are linked to interfaces at different scales. A successful attempt was made to model an RVE with a fully debonded inclusion, where the interface between the inclusion and matrix was modelled using Coulomb friction law. It was demonstrated that, for expanding loads, the RVE behaved perfectly like an RVE with a hole, whereas for compressive loads, it approached an RVE with a fully bonded inclusion. The discrete contact model relied on discrete normals, which can be numerically challenging when, e.g. a slave node slides from one master segment to the next. This can be improved by introducing smooth contact models.

Debonding of an inclusion was demonstrated by embedding the cohesive zone model within the interface. It was shown that the response of an RVE with a debonding inclusion with various critical efficient opening displacements lies between fully bonded/debonded responses. The cohesive zone model employed was too simplistic and was not path-dependent; there is a need for better defined models, however, due to problems with experimentation and data acquisition in microscopic scales, this is not an easy task.

One **pitfall** of the present method is the indifference of macroscopic behaviour to the size of the RVE employed. The physical impact of the length scale, e.g. variation of mechanical properties with grain size, can not be represented by simply changing the size of the RVE. However, the exact mechanisms leading to this variation are not well established, and may not be available under a pure continuum assumption. One possible research idea would be to use the continuum assumption along with contact-cohesive framework to express macroscopic size effects taking into account continuum contributions from each grain, as well as contributions from interaction of grains with their surroundings. To facilite this, contact and cohesive discrete models need to be extended into 3D.

Another area that is in need of improvement is the proneness of the present method to localization. It was demonstrated in Chapter 4 that the present model inherits the mesh dependent localization pattern of continuum models. This needs to be addressed in the future, perhaps by extending the method into a non-local or enhanced gradient context.

A clear direction for future research appears to be the marriage of **multi-scale** and **multi-physics** approaches. Biomechanics, where a separation of scales exist naturally, could be the stage of such union.

Bibliography

[1] Adams DF., Crane DA., Finite element micromechanical analysis of a unidirectional composite including longitudinal shear loading, *Computers and Structures*, **18** (1984) 6:1153-1165.

[2] Apel N., *Approaches to the Description of Anisotropic Material Behaviour at Finite Elastic and Plastic Deformations, Theory and Numerics.* Dissertationsschrift, Bericht Nr.: I-12 Instituts fr Mechanik (Bauwesen) Lehrstuhl I, Universitt Stuttgart, Stuttgart: 2004

[3] Bao G., Hutchinson JW., McMeeking RM., Particle reinforcement of ductile matrices against plastic flow and creep, *Acta Metall. Mater.*, **39** (1991) 8:1871-1882.

[4] Benveniste Y., A new approach to the application of Mori-Tanaka's theory in composite materials, *Mechanics of Materials*, **6** (1987) 2:147-157.

[5] Benveniste Y., Revisiting the generalized self-consistent scheme in composites: Clarification of some aspects and a new formulation, *Journal of the Mechanics and Physics of Solids*, **56** (2008) 10:2984-300.

[6] Bensoussan A., Lions JL.,Papanicolaou G., Asymptotic analysis for periodic structures, North-Holland Publishing Company, Amsterdam : 1978.

[7] Beran MJ., McCoy JJ., Mean field variations in a statistical sample of heterogeneous linearly elastic solids, *Int. J. Solids Structures*, **6** (1970) 10351053.

[8] Bonet J., Wood R., *Nonlinear Continuum Mechanics for Finite Element Analysis,* Cambridge University Press, Cambridge: 1997.

[9] Bonet J., Burton AJ., A simple orthotropic, transversely isotropic hyperelastic constitutive equation for large strain computations, *Comput. Methods Appl. Mech. Engrg.*, **162** (1998) 151-164.

[10] Brockenbrough JR., Suresh S., Wienecke HA., Deformation of metal-matrix composites with continuous fibers: geometrical effects of fiber distribution and shape, *Acta Metall. Mater.*, **39** (1991) 5:735-752.

[11] Castaneda P., The effective mechanical properties of nonlinear isotropic composites. *J. Mech. Phys. Solids*, **39** (1991) 4571.

[12] Castaneda P., Exact second-order estimates for the effective mechanical properties of nonlinear composite materials. *J. Mech. Phys. Solids*, **44** (1996) 827862.

[13] de Souza Neto EA., Perić D., Owen DRJ. *Computational Methods for Plasticity: Theory and Applications,* Wiley, Chichester: 2008.

[14] de Souza Neto EA., Perić D., Owen DRJ. A model for elastoplastic damage at finite strains: Computational issues and applications. *Engng. Comput.* 1994; **11**(3):257-281.

[15] de Souza Neto EA., Perić D., Owen DRJ., Design of Simple Low Order Finite Elements for Large Strain Analysis of Nearly Incompressible Solids, *International journal of solids and structures* , **32** (1996) 20-22:3277-3296.

[16] de Souza Neto EA., Feijóo RA., Variational Foundations of Multi-Scale Constitutive Models of Solid: Small and Large Strain Kinematical Formulation, National Laboratory for Scientific Computing (LNCC), Brazil, *Internal Research and Development Report*, no.**16/2006**, 2006.

[17] Einstein A., Eine neue Bestimmung der Molekldimensionen, *Annalen der Physik*, **19** (1906) 36-62.

[18] Christensen RM., Lo KH., Solutions for effective shear properties in three phase sphere and cylinder models. *J. Mech. Phys. Solids*, **27** (1979) 315-330.

[19] Christman T., Needleman A., Suresh S. An experimental and numerical study of deformation in metal-ceramic composites, *Acta Metall. Mater.*, **37** (1989) 3029-3050.

[20] Cochrane RF., DoITPoMS Micrograph Library, *Micrograph no 212,* http://www.doitpoms.ac.uk/miclib, 01/04/2009

[21] Crisfield MA., *Non-linear Finite Element Analysis of Solids and Structures.* Volume 1: Essentials, Johen Wiley & Sons, Chichester: 1991.

[22] Daniel IM., Ishai O. *Engineering Mechanics of Composite Materials* Oxford University Press, New York Oxford: 1994.

[23] Dettmer WG., *Finite element modelling of fluid flow with moving free surfaces and interfaces including fluid-solid interaction,* Ph. D Thesis, University of Wales, Swansea: 2004.

[24] Dettmer WG., Reese S., On the theoretical and numerical modelling of Armstrong-Frederick kinematic hardening in the finite strain regime, *Comput. Methods Appl. Mech. Engrg.*, **193** (2004) 87-116.

[25] Dettmer W., Perić D., A computational framework for fluid-structure interaction: Finite element formulation and applications, *Comput. Methods Appl. Mech. Engrg.*, **195** (2006) 5754-5779.

[26] Dutko M., Perić D., Owen DRJ. Universal anisotropic yield criterion based on superquadratic functional representation: Part 1. Algorithmic issues and accuracy analysis. *Comput. Meth. Appl. Mech. Engrg.*, **109** (1993) 73-93.

[27] Eshelby DJ., Determination of the elastic field of an ellipsoidal inclusion, and related problems, *Proceedings of the Royal Society of London, A*, **241** (1957) 376396.

[28] Feyel F, Chaboche JL. FE2 multiscale approach for modelling the elastoviscoplastic behaviour of long fibre SiC/Ti composite materials *Comput. Meth. Appl. Mech. Engrg.*, **183** (2000) 309-330

[29] Fish J., Belsky V., Multi-grid method for periodic heterogeneous media Part I: Convergence studies for one dimensional case, *Computer Methods in Applied Mechanics and Engineering*, **126** (1995) 1-2:1-16

[30] Fish J., Belsky V., Multi-grid method for periodic heterogeneous media Part II: Multiscale modeling and quality control in multidimensional case, *Computer Methods in Applied Mechanics and Engineering*, **126** (1995) 1-2:17-38

[31] Gasser TC., Holzapfel GA., Modeling 3D crack propagation in unreinforced concrete using PUFEM, *Comput. Meth. Appl. Mech. Engrg.*, **194** (2005) 4:2859-2896.

[32] Geers MGD, Kouznetsova V, Brekelmans WAM., Gradient-enhanced computational homogenization for the micro-macro scale transition, *Journal de Physique IV*, **11** (2001) 145-152.

[33] Gibiansky LV, Torquato S., New method to generate three-point bounds on effective properties of composites: Application to viscoelasticity , *Journal of the Mechanics and Physics of Solids.*, **46** (1998) 4:749-783.

[34] Giusti SM., Blanco PJ., de Souza Neto EA., Feijóo RA. An assessment of the Gurson yield criterion by a computational multi-scale approach. *Engineering Computations*, 2008 (accepted for publication).

[35] Ghosh S., Lee K., Moorthy S., Multiple scale analysis of heterogeneous elastic structures using homogenization theory and Voronoi cell finite element method, *International Journal of Solids and Structures*, **32** (1995) 27-62.

[36] Ghosh S., Lee K., Moorthy S., Two scale analysis of heterogeneous elasticplastic materials with asymptotic homogenization and Voronoi cell finite element model, *Computer Methods in Applied Mechanics and Engineering*, **132** (1996) 63-116.

[37] Guedes JM, Kikuchi N., Preprocessing and postprocessing for materials based on the homogenization method with adaptive finite element methods, *Computer Methods in Applied Mechanics and Engineering*, **83** (1990)143-198

[38] Gurson, AL. Continuum theory of ductile rupture by void nucleation and growth: Part I - Yield criteria and flow rules for porous ductile media, *J. Engrg. Mat. Tech.*, Transactions of the ASME.

[39] Halpin JC., Kardos JL., The Halpin-Tsai Equations: A Review, *Polymer Engineering and Science.*, **16** (1976) 5:344-352.

[40] Hashin Z., The elastic moduli of heterogeneous materials, *J. Appl. Mech.*, **29** (1962) 143-150.

[41] Hashin Z., Shtrikman S. A variational approach to the theory of the elastic behaviour of multiphase materials, *Journal of the Mechanics and Physics of Solids.*, **11** (1963) 2:127-140.

[42] Hashin Z., Rosen BW. The elastic moduli of fiber-reinforced materials, *J. Appl. Mech.*, **31** (1964) 223-232.

[43] Hashin Z., Analysis of composite materials - a survey, *J. Appl. Mech.*, **50** (1983) 481-505.

[44] Hecht RL., Dinwiddie RB., Porter WD., *Thermal Transport Properties of Aluminum Metal Matrix Composites for Brake Applications,* Materials Science Department, Ford Research Laboratory, http://www.html.ornl.gov/tpuc/brakes.html, 01/04/2009

[45] Hermans JJ., Koninkl. Nederl. Akademie Van Wetenschappen-Amsterdam, Proceedings, Series B, 1 1967

[46] Hill R., The Elastic Behaviour of a Crystalline Aggregate, *Proceedings of the Physical Society. Section A*, **65** (1952) 5:349-354.

[47] Hill R., Elastic properties of reinforced solids: Some theoretical principles, *Journal of the Mechanics and Physics of Solids.*, **11** (1963) 5:357-372.

[48] Hill R., A self-consistent mechanics of composite materials, *Journal of the Mechanics and Physics of Solids.*, **13** (1965) 4:213-222.

[49] Hollister SJ., Kikuchi N., A comparison of homogenization and standard mechanics approaches , *Computional Mechanics*, **10** (1992) 73-95.

[50] Hollomon JH., Lubahn JD. Plastic Flow of Metals , *Physical Review*, **70** (1946) 9-10:775.

[51] Hull D., Clyne TW. *An Introduction to Composite Materials,* Cambridge Solid State Science Series, 2nd Edition Cambridge University Press, Chichester: 1996.

[52] Ismar H., Schroter F., Streicher F., Effects of interfacial debonding on the transverse loading behaviour of continuous fibre-reinforced metal matrix composites, *Computers and Structures* **79** (2001) 18:1713-1722.

[53] Kenaga D., Doyle JF., Sun CT., The characterization of boron/aluminum in the nonlinear range as an orthotropic elastic plastic material, *J. Comp. Mater.*, **27** (1987)516531.

[54] Kerner EH., The electrical conductivity of composite media, *Proc. Phys. Soc. B*, **69** (1956) 802807.

[55] Kerner EH., The elastic and thermo-elastic properties of composite media, *Proc. Phys. Soc. B*, **69** (1956) 808813.

[56] Konter AWA. *Advanced finite element contact benchmarks.* Technical Report No: FENET-UNOTT-DLE-09, Netherlands Institute for Metals Research, The Netherlands: 2005.

[57] Kouznetsova V., *Computational homogenization for the multi-scale analysis of multi-phase materials,* Ph. D Thesis, Technische Universiteit, Eindhoven: 2002.

[58] Kouznetsova V., Brekelmans WAM., Baaijens FPT., An approach to micro-macro modelling of heterogeneous materials, *Computional Mechanics*, **27** (2001) 37-48.

[59] Latif, MJA; Peric, D; Dettmer, WG, Numerical modeling of transversely isotropic elastic material at small and finite strains *2nd International Conference on Solid State Science and Technology*, Kuala Terengganu MALAYSIA, **909** (2007) 142-146.

[60] Lemaitre J., Chaboche JL., *Mechanics of Solids Materials,* Cambridge University Press, Cambridge: 1990.

[61] Le Quang H., He QC., Variational principles and bounds for elastic inhomogeneous materials with coherent imperfect interfaces , *Mechanics of Materials*, **40**(2008) 10:865-884

[62] Li S, Ghosh S., Debonding in composite microstructures with morphological variations *International Journal of Computational Methods*, **1** (2004) 1:121-149.

[63] Li S, Ghosh S., Modeling interfacial debonding and matrix cracking in fiber reinforced composites by the extended Voronoi cell FEM, *Finite Elements in Analysis and Design*, **43** (2007) 5:397-410.

[64] Lissenden CJ., Fiber-matrix interfacial constitutive relations for metal matrix composites, *Composites Part B: Engineering*, **30** (1999) 3:267-278.

[65] Lissenden CJ., Herakovich CT., Numerical modelling of damage development and viscoplasticity in metal matrix composites, *Computer Methods in Applied Mechanics and Engineering*, **126** (1995) 3-4:289-303.

[66] Lorca JL., Needleman A., Suresh S. An analysis of the effects of matrix void growth on deformation and ductility in metal ceramic composites, *Acta Metall. Mater.*, **39** (1991) 23172335.

[67] Lubliner J., *Plasticity Theory,* Macmillan Publishing Company, New York: 1990.

[68] Luo HA., Weng GJ., On Eshelby's inclusion problem in a three-phase spherically concentric solid, and a modification of Mori-Tanaka's method, *Mechanics of Materials*, **6** (1987) 4:347-361.

[69] Mandel J., *Plasticité Classique et Viscoplasticité,* CISM Lecture Notes, Udine, Italy, Springer-Verlag

[70] Matous K., Geubelle P., Multiscale modelling of particle debonding in reinforced elastomers subjected to finite deformations, *International Journal for Numerical Methods in Engineering*, **65** (2006) 2:190-223.

[71] Matsui K., Terada K., Yuge K., Two-scale finite element analysis of heterogeneous solids with periodic microstructures,*Computers and Structures*, **82** (2004) 7-8:593-606.

[72] Matthews FL., Rowlings RD. *Composite Materials: Engineering and Science* Woodhead Publishing Limited, 5th Edition The Alden Press, Oxford : 2006

[73] Mehan RL., Harris TA *Air Force Materials Laboratry Report, AFML-TR-71-150,* August 1971

[74] Metcalfe AG., *Interfaces in Metal Matrix Composites, Vol. 1* Academic Press, New York :1974

[75] Michel JC., Moulinec H., Suquet P., Effective properties of composite materials with periodic microstructure: A computational approach, *Comput. Methods Appl. Mech. Engrg.* **172** (1999) 109-143.

[76] Miehe C., Shotte J., Schröder J., Computational micro-macro transitions and overall moduli in the analysis of polycrystals at large strains, *Comput. Materials Sci.*, **16** (1999) 372-382.

[77] Miehe C., Koch A., Computational micro-to-macro transitions of discretized microstructures undergoing small strains, *Archive of Applied Mechanics*, **72** (2002) 11:1285-1322.

[78] Miehe C., Strain-driven homogenization of inelastic microstructures and composites based on an incremental variational formulation, *International Journal for Numerical Methods in Engineering*, **55** (2002) 300-317.

[79] Miehe C., Computational micro-to-macro transitions for discretized microstructures of heterogeneous materials at finite strains based on the minimization of averaged incremental energy, *Comput. Methods Appl. Mech. Engrg.*, **192** (2003) 559-591.

[80] Miehe C. and Bayreuther CG., On multiscale FE analyses of heterogeneous structures: from homogenization to multigrid solvers, *Int. J. Numer. Methods Engrg.*, **71** (2007) 11351180.

[81] Mori T., Tanaka K., Average stress in the matrix and average elastic energy of materials with misfitting inclusions, *Acta Metallurgica*, **21** (1973) 571-574.

[82] Moulinec H., Suquet P., A numerical method for computing the overall response of nonlinear composites with complex microstructure, *Computer Methods in Applied Mechanics and Engineering*, **157** (1998)1-2:69-9.

[83] Mura T., *Micromechanics of defects in solids,* Martinus Nijhoff, The Hague, (1982).

[84] Needleman, A., A continuum model for void nucleation by inclusion debonding, *Journal of Applied Mechanics*, **54** (1987) 3: 525-531.

[85] Ortiz M., Pandolfi A., Finite-deformation irreversible cohesive elements for three-dimensional crack-propagation analysis, *International Journal for Numerical Methods in Engineering*, **44** (1999) 9: 1267-1282.

[86] Numisheet 2002, *Proceedings of the fifth international conference and workshop on numerical simulation of 3D sheet forming processes,* Jeju Island, Korea: 2002.

[87] Zohdi TI., Oden JT., Rodin GJ., Hierarchical modeling of heterogeneous bodies, *Comput. Meth. Appl. Mech. Engrg.*, **138** (1996) 1-4:273-298

[88] Oden JT., Zohdi TI., Analysis and adaptive modeling of highly heterogeneous elastic structures, *Comput. Meth. Appl. Mech. Engrg.*, **148** (1997) 3-4:367-391

[89] Partovi M., *Computational Strategies for Multiscale Analysis of Material Behaviour,* Ph. D Thesis, University of Wales, Swansea: 2006.

[90] Pellegrino C., Galvanetto U., Schrefler BA. Computational techniques for periodic composite materials with non-linear material components. *Int. J. Num. Meth. Engng.*, **46**:1609-1637, 1999.

[91] Pérez-Foguet A, Rodríguez-Ferran A, Huerta A. Consistent tangent matrices for substepping schemes, *Comput. Meth. Appl. Mech. Engrg.*, **190** (2001) 4627-4647.

[92] Perić D., *Computational Plasticity, Lecture Notes,* University of Wales, Swansea: 2004.

[93] Perić D., On a class of constitutive equations in viscoplasticity: Formulation and computational issues. *Int. J. Num. Meth. Engrg.*, **36** (1993) 1365-1393.

[94] Perić D., Owen RJ. Computational model for 3-D contact problems with friction based on the penalty method *Int. J. Num. Meth. Engrg.*, **35** (1992) 6:1289-1309

[95] Reuss A., Berechnung der Fliessgrense von Mischkristallen auf Grund der Plastizitätsbedingung für Einkristalle, *Zeitschrift fur Angewandte Mathematik un Mechanic*, **9** (1929) 49-58

[96] Ross MH., Kaye GI., Lippincolt WP., *Histology: A Text and Atlas (4th Edition),* Williams and Wilkins, Philadelphia, 2003, http://pathology.mc.duke.edu, 01/04/2009

[97] Sanchez-Palencia E., Zaoui A., *Homogenization techniques for composites.* In: Homogenization Techniques for Composite Media, Springer-Verlag, Berlin :1985.

[98] Sfantos GK., Aliabadi MH., Multi-scale boundary element modelling of material degradation and fracture, *Comput. Methods Appl. Mech. Engrg.* **196** (2007) 7:1310-1329.

[99] Simo JC., Hughes TJR., *Computational Inelasticity,* Springer-Verlag, New York: 1998.

[100] Shi N., Wilner B., Arsenault RJ., An FEM study of the plastic deformation process of whisker reinforced SiC/Al composites, *Acta Metall. Mater.*. **40** (1992) 11:2841-2854.

[101] Sloan SW. Substepping schemes for the numerical integration of elastoplastic stress-strain relations, *International Journal for Numerical Methods in Engineering,* **24** (1987) 893-911.

[102] Smit RJM, Brekelmans WAM, Meijer HEH., Prediction of the mechanical behavior of nonlinear heterogeneous systems by multilevel finite element modeling, *Comput. Methods Appl. Mech. Engrg.* **155** (1998) 181-192.

[103] Somer DD., de Souza Neto EA., Dettmer WG., Perić D. A sub-stepping scheme for multi-scale analysis of solids, *Comput. Methods Appl. Mech. Engrg.* **198** (2009) 9-12:1006-1016.

[104] Somer DD., *Elastoplastic Computational models for small and large strain problems,* MRes Thesis, University of Wales, Swansea: 2005.

[105] Sousa RJA., Correia JPM. , Simes FJP., Ferreira JAF., Cardoso RPR., Gracio JJ., Barlat F., Unconstrained springback behavior of AlMgSi sheets for different sitting times *International Journal of Mechanical Sciences*, **50** (2008) 9, 1381-1389.

[106] Speirs DCD., de Souza Neto EA., Perić D. An approach to the mechanical constitutive modelling of arterial wall tissue based on homogenization and optimization. *Journal of Biomechanics*, **41** (2008) 12:2673-2680.

[107] Speirs D., *Characterisation of Materials with Hyperelastic Microstructures through Computational Homogenisation and Optimisation Methods,* Ph. D Thesis, University of Wales, Swansea: 2007.

[108] Spencer AJM., Modelling of Finite Deformations of Anisotropic Materials, *in J. Gittus et al., eds. Large Deformations of Solids, Physical Basis and Mathematical Modelling* Elsevier Applied Sciences: 1986.

[109] Sun CT., Vaidya RS., Prediction of composite properties from a representative volume element, *Composites Science and Technology* **56** (1996) 2:171-179.

[110] Suquet P., Elements of homogenization for inelastic solid mechanics. In: E. Sanchez-Palencia and A. Zaoui, Editors, *Homogenization Techniques for Composite Media, Lecture Notes in Physics* **272** (1987) Springer Verlag, Berlin, 193278.

[111] Talbot DRS., Willis JR., Some simple explicit bounds for the overall behavior of nonlinear composites , *International Journal of Solids And Structures*, **29** (1992) 14-15:1981-1987.

[112] Talbot DRS., Willis JR., Bounds of third order for the overall response of nonlinear composites, *Journal of the Mechanics and Physics of Solids.*, **45** (1997) 1:87-111.

[113] Talbot DRS., Willis JR., Bounds for the effective constitutive relation of a nonlinear composite, *Proceedings of the Royal Society of London, A*, **460** (2004) 2049:2705-2723.

[114] Taya M., Arsenault RJ., A comparison between a shear lag type model and an eshelby type model in predicting the mechanical properties of a short fiber composite, *Scripta Metallurgica*, **21** (1987) 349.

[115] Terada K., Saiki I., Matsui K., Yamakawa Y., Two-scale kinematics and linearization for simultaneous two-scale analysis of periodic heterogeneous solids at finite strain, *Comput. Methods Appl. Mech. Engrg.*, **192** (2003) 3531-3563.

[116] Terada K, Kikuchi N., A class of general algorithms for multi-scale analysis of heterogeneous media, *Comput. Methods Appl. Mech. Engrg.*, **190** (2001) 5427-5464.

[117] Terada K, Kikuchi N., *Nonlinear homogenization method for practical applications, In Computational Methods in Micromechanics, vol. AMD-212/MD-62,* Ghosh S , Ostoja-Starzewski M (eds). ASME: New York: 1995; 1-16.

[118] Temizer I., Wriggers P., On the computation of the macroscopic tangent for multiscale volumetric homogenization problems *Comput. Methods Appl. Mech. Engrg.*, **198** (2008) 3-4:495-510

[119] Timothy B., *Human Trabecular Bone 2,* http://archive.nyu.edu, 01/04/2009

[120] Toledano A., Murakami H., A high-order mixture model for periodic particulate composites, *International Journal of Solids and Structures*, **23** (1987) 7:989-1002

[121] Tvergaard V., Effect of fibre debonding in a whisker-reinforced metal, *Materials Science and Engineering A*, **125** (1990) 2:203-213

[122] Tvergaard V., Fibre debonding and breakage in a whisker-reinforced metal, *Materials Science and Engineering A*, **190** (1995) 1-2:215-222

[123] Voigt W., *Lehrbuch der Kristallphysik,* Teubner, Berlin: 1910.

[124] Xia Z., Zhang Y., Ellyin F., A unified periodical boundary conditions for representative volume elements of composites and applications, *International Journal of Solids and Structures*, **40** (2003) 8:1907-1921.

[125] Wang W, Datcheva M, Schanz T, Kolditz O., A sub-stepping approach for elastoplasticity with rotational hardening, *Computional Mechanics*, **37** (2006) 266-278.

[126] Willis JR., Variational and related methods for the overall properties of composites, *Advances in Applied Mechanics*, **21** (1981)

[127] Willis JR., Randomly Inhomogeneous Media, In: E. Sanchez-Palencia and A. Zaoui, Editors, *Homogenization Techniques for Composite Media, Lecture Notes in Physics* **272** (1987) Springer Verlag, Berlin, 281-337.

[128] Wriggers P., *Computational Contact Mechanics,* Wiley, New York : 2002.

[129] Zienkiewicz OC, Taylor RL. *The Finite Element Method,* McGraw-Hill, London: 1991.

[130] Zhang WC., Evans KE., Numerical prediction of the mechanical properties of anisotropic composite materials, *Computers and Structures*, **29** (1988) 3413-422.

Appendix A

Derivation of Some Expressions Referred in the Thesis

A.1 Equivalence of norms of Mandel and Kirchoff Stress Tensors

$\boldsymbol{\tau}$ is the push forward of $\boldsymbol{S}$ so that $\boldsymbol{\tau} = \boldsymbol{F}\boldsymbol{S}\boldsymbol{F}^T$ or $\boldsymbol{S} = \boldsymbol{F}^{-1}\boldsymbol{\tau}\boldsymbol{F}^{-T}$

$$\begin{aligned} \boldsymbol{M} &= \boldsymbol{F}^p\boldsymbol{F}^{-1}\boldsymbol{\tau}\boldsymbol{F}^{-T}\boldsymbol{F}^T\boldsymbol{F}\boldsymbol{F}^{p^{-1}} \\ &= (\boldsymbol{F}\boldsymbol{F}^{p-1})^{-1}\boldsymbol{\tau}\boldsymbol{F}\boldsymbol{F}^{p^{-1}} \\ \boldsymbol{M} &= \boldsymbol{F}^{e^{-1}}\boldsymbol{\tau}\boldsymbol{F}^e \end{aligned} \tag{A.1}$$

$$\begin{aligned} \boldsymbol{M} : \boldsymbol{M} &= \boldsymbol{F}^{e^{-1}}\boldsymbol{\tau}\boldsymbol{F}^e : \boldsymbol{F}^{e^{-1}}\boldsymbol{\tau}\boldsymbol{F}^e \\ &= \boldsymbol{\tau}\boldsymbol{F}^{e^{-T}}\boldsymbol{F}^{e^{-1}}\boldsymbol{\tau}\boldsymbol{F}^e\boldsymbol{F}^{e^T} : \boldsymbol{I} \\ &= \boldsymbol{\tau}\boldsymbol{b}^{e^{-1}}\boldsymbol{\tau}\boldsymbol{b}^e : \boldsymbol{I} \\ &= \boldsymbol{\tau}\boldsymbol{b}^{e^{-1}}\boldsymbol{b}^e\boldsymbol{\tau} : \boldsymbol{I} \\ \boldsymbol{M} : \boldsymbol{M} &= \boldsymbol{\tau} : \boldsymbol{\tau} \end{aligned} \tag{A.2}$$

so that,

$$\|\boldsymbol{M}\| = \sqrt{\boldsymbol{M} : \boldsymbol{M}} = \sqrt{\boldsymbol{\tau} : \boldsymbol{\tau}} = \|\boldsymbol{\tau}\|$$

$$tr[\boldsymbol{M}] = \boldsymbol{F}^{e^{-1}}\boldsymbol{\tau}\boldsymbol{F}^e : \boldsymbol{I} = \boldsymbol{\tau}\boldsymbol{F}^e\boldsymbol{F}^{e^{-1}} : \boldsymbol{I} = tr[\boldsymbol{\tau}]$$

$$\begin{aligned}
\|\boldsymbol{M}^{\text{dev}}\| &= \sqrt{\boldsymbol{M}^{\text{dev}} : \boldsymbol{M}^{\text{dev}}} \\
&= \sqrt{\boldsymbol{M} : \boldsymbol{M} - \frac{1}{3} tr^2[\boldsymbol{M}]} \\
&= \sqrt{\boldsymbol{\tau} : \boldsymbol{\tau} - \frac{1}{3} tr^2[\boldsymbol{\tau}]} \\
\|\boldsymbol{M}^{\text{dev}}\| &= \|\boldsymbol{\tau}^{\text{dev}}\| \qquad \text{(A.3)}
\end{aligned}$$

A.2 Elastoplastic Consistent Tangent for Small Strains

As the stress update formulation is in terms of deviatoric stress and strain, first $\frac{\partial \boldsymbol{s}}{\partial \boldsymbol{e}}$ will be formulated.

$$\begin{aligned}
\frac{\partial \boldsymbol{s}}{\partial \boldsymbol{e}} &= \frac{\partial \boldsymbol{s}^{\text{trial}}}{\partial \boldsymbol{e}} - 2\mu \frac{\partial \Delta\lambda \boldsymbol{n}^{\text{trial}}}{\partial \boldsymbol{e}} \\
&= \frac{\partial \boldsymbol{s}^{\text{trial}}}{\partial \boldsymbol{e}} - 2\mu \left(\frac{\partial \Delta\lambda}{\partial \boldsymbol{e}} \otimes \boldsymbol{n}^{\text{trial}} + \Delta\lambda \frac{\partial \boldsymbol{n}^{\text{trial}}}{\partial \boldsymbol{e}} \right) \qquad \text{(A.4)}
\end{aligned}$$

where,

$$\begin{aligned}
\frac{\partial \boldsymbol{s}^{\text{trial}}}{\partial \boldsymbol{e}} &= 2\mu \boldsymbol{\mathcal{I}} \qquad \text{(A.5)} \\
\frac{\partial \Delta\lambda}{\partial \boldsymbol{e}} &= \frac{1}{2\mu(1 + \frac{H}{3\mu})} \frac{\partial \Phi^{\text{trial}}}{\partial \boldsymbol{e}} \\
&= \frac{1}{2\mu(1 + \frac{H}{3\mu})} \frac{\partial \sqrt{\boldsymbol{s}^{\text{trial}} : \boldsymbol{s}^{\text{trial}}}}{\partial \boldsymbol{s}^{\text{trial}}} : \frac{\partial \boldsymbol{s}^{\text{trial}}}{\partial \boldsymbol{e}} \\
&= \frac{1}{2\mu(1 + \frac{H}{3\mu})} \boldsymbol{n}^{\text{trial}} : 2\mu \boldsymbol{\mathcal{I}} \\
&= \frac{1}{1 + \frac{H}{3\mu}} \boldsymbol{n}^{\text{trial}}
\end{aligned}$$

$$\begin{aligned}
\frac{\partial \boldsymbol{n}^{\text{trial}}}{\partial \boldsymbol{e}} &= \frac{\partial \boldsymbol{n}^{\text{trial}}}{\partial \boldsymbol{s}^{\text{trial}}} : \frac{\partial \boldsymbol{s}^{\text{trial}}}{\partial \boldsymbol{e}} \\
&= \frac{1}{\sqrt{\boldsymbol{s}^{\text{trial}} : \boldsymbol{s}^{\text{trial}}}} (\boldsymbol{\mathcal{I}} - \boldsymbol{n}^{\text{trial}} \otimes \boldsymbol{n}^{\text{trial}}) : 2\mu \boldsymbol{\mathcal{I}} \\
&= \frac{2\mu}{\sqrt{\boldsymbol{s}^{\text{trial}} : \boldsymbol{s}^{\text{trial}}}} (\boldsymbol{\mathcal{I}} - \boldsymbol{n}^{\text{trial}} \otimes \boldsymbol{n}^{\text{trial}})
\end{aligned}$$

Now (A.4) becomes:

$$\begin{aligned}\frac{\partial \boldsymbol{s}}{\partial \boldsymbol{e}} &= 2\mu\boldsymbol{\mathcal{I}} - 2\mu\left(\frac{1}{1+\frac{H}{3\mu}}\boldsymbol{n}^{\text{trial}}\otimes\boldsymbol{n}^{\text{trial}} + \Delta\lambda\frac{2\mu}{\sqrt{\boldsymbol{s}^{\text{trial}}:\boldsymbol{s}^{\text{trial}}}}(\boldsymbol{\mathcal{I}} - \boldsymbol{n}^{\text{trial}}\otimes\boldsymbol{n}^{\text{trial}})\right) \\ &= 2\mu\left(1 - \frac{2\mu\Delta\lambda}{\sqrt{\boldsymbol{s}^{\text{trial}}:\boldsymbol{s}^{\text{trial}}}}\right)\boldsymbol{\mathcal{I}} - 2\mu\left(\frac{1}{1+\frac{H}{3\mu}} - \frac{2\mu\Delta\lambda}{\sqrt{\boldsymbol{s}^{\text{trial}}:\boldsymbol{s}^{\text{trial}}}}\right)\boldsymbol{n}^{\text{trial}}\otimes\boldsymbol{n}^{\text{trial}}\end{aligned}$$

Let,

$$\beta = 1 - \frac{2\mu\Delta\lambda}{\sqrt{\boldsymbol{s}^{\text{trial}}:\boldsymbol{s}^{\text{trial}}}} \tag{A.6}$$

and,

$$\begin{aligned}\gamma &= \frac{1}{1+\frac{H}{3\mu}} - \frac{2\mu\Delta\lambda}{\sqrt{\boldsymbol{s}^{\text{trial}}:\boldsymbol{s}^{\text{trial}}}} \\ &= \frac{1}{1+\frac{H}{3\mu}} - (1-\beta)\end{aligned}$$

so that,

$$\frac{\partial \boldsymbol{s}}{\partial \boldsymbol{e}} = 2\mu\beta\boldsymbol{\mathcal{I}} - 2\mu\gamma\boldsymbol{n}^{\text{trial}}\otimes\boldsymbol{n}^{\text{trial}}$$

Now $\boldsymbol{\mathcal{C}}_{ep} = \frac{\partial\boldsymbol{\sigma}}{\partial\boldsymbol{\varepsilon}}$ can be derived from $\frac{\partial\boldsymbol{s}}{\partial\boldsymbol{e}}$ using $\boldsymbol{\sigma} = \boldsymbol{s} + Ktr[\boldsymbol{\varepsilon}]\boldsymbol{I}$, so that,

$$\boldsymbol{\mathcal{C}}_{ep} = K\frac{\partial tr[\boldsymbol{\varepsilon}]\boldsymbol{I}}{\partial\boldsymbol{\varepsilon}} + \frac{\partial\boldsymbol{s}}{\partial\boldsymbol{e}} : \frac{\partial\boldsymbol{e}}{\partial\boldsymbol{\varepsilon}} \tag{A.7}$$

Recall the definition of deviatoric strain given as:

$$\boldsymbol{e} = \boldsymbol{\varepsilon} - \frac{1}{3}tr[\boldsymbol{\varepsilon}]\boldsymbol{I}$$

so that,

$$\begin{aligned}\frac{\partial\boldsymbol{e}}{\partial\boldsymbol{\varepsilon}} &= \frac{\partial\boldsymbol{\varepsilon}}{\partial\boldsymbol{\varepsilon}} - \frac{1}{3}\frac{\partial tr[\boldsymbol{\varepsilon}]\boldsymbol{I}}{\partial\boldsymbol{\varepsilon}} \\ &= \boldsymbol{\mathcal{I}} - \frac{1}{3}\boldsymbol{I}\otimes\boldsymbol{I}\end{aligned}$$

$$\begin{aligned}\boldsymbol{\mathcal{C}}_{ep} &= K\boldsymbol{I}\otimes\boldsymbol{I} + (2\mu\beta\boldsymbol{\mathcal{I}} - 2\mu\gamma\boldsymbol{n}^{\text{trial}}\otimes\boldsymbol{n}^{\text{trial}}) : (\boldsymbol{\mathcal{I}} - \frac{1}{3}\boldsymbol{I}\otimes\boldsymbol{I}) \\ &= K\boldsymbol{I}\otimes\boldsymbol{I} + 2\mu\beta(\boldsymbol{\mathcal{I}} - \frac{1}{3}\boldsymbol{I}\otimes\boldsymbol{I}) - 2\mu\gamma(\boldsymbol{n}^{\text{trial}}\otimes\boldsymbol{n}^{\text{trial}}) : \boldsymbol{\mathcal{I}} \\ &\quad -\frac{2\mu\gamma}{3}(\boldsymbol{n}^{\text{trial}}\otimes\boldsymbol{n}^{\text{trial}}) : (\boldsymbol{I}\otimes\boldsymbol{I})\end{aligned}$$

Note that

$$\begin{aligned}(\boldsymbol{n}^{\text{trial}} \otimes \boldsymbol{n}^{\text{trial}}) : (\boldsymbol{I} \otimes \boldsymbol{I}) &= \left(\frac{\boldsymbol{s}^{\text{trial}}}{\sqrt{\boldsymbol{s}^{\text{trial}} : \boldsymbol{s}^{\text{trial}}}} \otimes \frac{\boldsymbol{s}^{\text{trial}}}{\sqrt{\boldsymbol{s}^{\text{trial}} : \boldsymbol{s}^{\text{trial}}}}\right) : (\boldsymbol{I} \otimes \boldsymbol{I}) \\ &= \frac{1}{\boldsymbol{s}^{\text{trial}} : \boldsymbol{s}^{\text{trial}}}(\boldsymbol{s}^{\text{trial}} \otimes \boldsymbol{s}^{\text{trial}}) : (\boldsymbol{I} \otimes \boldsymbol{I}) \\ &= \frac{1}{\boldsymbol{s}^{\text{trial}} : \boldsymbol{s}^{\text{trial}}}(\boldsymbol{s}^{\text{trial}} : \boldsymbol{I})(\boldsymbol{s}^{\text{trial}} \otimes \boldsymbol{I}) \\ &= \frac{1}{\boldsymbol{s}^{\text{trial}} : \boldsymbol{s}^{\text{trial}}} tr[\boldsymbol{s}^{\text{trial}}](\boldsymbol{s}^{\text{trial}} \otimes \boldsymbol{I}) \\ &= 0\end{aligned}$$

as $tr[\boldsymbol{s}^{\text{trial}}]$ is zero. Now the consistent tangent modulus becomes:

$$\begin{aligned}\boldsymbol{\mathcal{C}}_{ep} &= K\boldsymbol{I} \otimes \boldsymbol{I} + 2\mu\beta(\boldsymbol{\mathcal{I}} - \frac{1}{3}\boldsymbol{I} \otimes \boldsymbol{I}) - 2\mu\gamma(\boldsymbol{n}^{\text{trial}} \otimes \boldsymbol{n}^{\text{trial}}) \qquad \text{(A.8)} \\ \beta &= 1 - \frac{2\mu\Delta\lambda}{\sqrt{\boldsymbol{s}^{\text{trial}} : \boldsymbol{s}^{\text{trial}}}} \\ \gamma &= \frac{1}{1 + \frac{H}{3\mu}} - (1 - \beta)\end{aligned}$$

A.3 Elastoplastic Consistent Tangent for Large Strains

An increment of the stress can be expressed as:

$$\delta\boldsymbol{S} = \frac{\partial \boldsymbol{S}}{\partial \boldsymbol{C}} : \delta\boldsymbol{C} + \frac{\partial \boldsymbol{S}}{\partial \boldsymbol{C}^p} : \delta\boldsymbol{C}^p + \frac{\partial \boldsymbol{S}}{\partial \Delta\lambda} : \delta\Delta\lambda \qquad \text{(A.9)}$$

in matrix notation:

$$\begin{Bmatrix}\delta\boldsymbol{S}_{11} \\ \delta\boldsymbol{S}_{22} \\ \delta\boldsymbol{S}_{33} \\ \delta\boldsymbol{S}_{12} \\ \delta\boldsymbol{S}_{23} \\ \delta\boldsymbol{S}_{31}\end{Bmatrix} = \left[\begin{array}{c} \\ \frac{\partial \boldsymbol{S}}{\partial \boldsymbol{C}} \\ \\ \\ \\ \\ \\ \end{array}\right] \cdot \begin{Bmatrix}\delta\boldsymbol{C}_{11} \\ \delta\boldsymbol{C}_{22} \\ \delta\boldsymbol{C}_{33} \\ 2\delta\boldsymbol{C}_{12} \\ 2\delta\boldsymbol{C}_{23} \\ 2\delta\boldsymbol{C}_{31}\end{Bmatrix} + \left[\begin{array}{c|c} & \\ \frac{\partial \boldsymbol{S}}{\partial \boldsymbol{C}^p} & \frac{\partial \boldsymbol{S}}{\partial \Delta\lambda} \\ & \\ & \\ & \\ & \\ & \end{array}\right] \cdot \left\{\begin{array}{c}\delta\boldsymbol{C}_{p11} \\ \delta\boldsymbol{C}_{p22} \\ \delta\boldsymbol{C}_{p33} \\ 2\delta\boldsymbol{C}_{p12} \\ 2\delta\boldsymbol{C}_{p23} \\ 2\delta\boldsymbol{C}_{p31} \\ \hline \delta\Delta\lambda\end{array}\right\} \qquad \text{(A.10)}$$

similarly for $\boldsymbol{R}^p$ and Φ it can be written:

$$0 = \frac{\partial \boldsymbol{R}^p}{\partial \boldsymbol{C}} : \delta\boldsymbol{C} + \frac{\partial \boldsymbol{R}^p}{\partial \boldsymbol{C}^p} : \delta\boldsymbol{C}^p + \frac{\partial \boldsymbol{R}^p}{\partial \Delta\lambda} : \delta\Delta\lambda \qquad \text{(A.11)}$$

$$0 = \frac{\partial \Phi}{\partial \boldsymbol{C}} : \delta\boldsymbol{C} + \frac{\partial \Phi}{\partial \boldsymbol{C}^p} : \delta\boldsymbol{C}^p + \frac{\partial \Phi}{\partial \Delta\lambda} : \delta\Delta\lambda \qquad \text{(A.12)}$$

or, in matrix notation:

$$\left\{\begin{array}{c}0\\0\\0\\0\\0\\0\\\hline 0\end{array}\right\} = \left[\begin{array}{c}\frac{\partial \boldsymbol{R}^p}{\partial \boldsymbol{C}}\\\hline \frac{\partial \Phi}{\partial \boldsymbol{C}}\end{array}\right] \cdot \left\{\begin{array}{c}\delta \boldsymbol{C}_{11}\\\delta \boldsymbol{C}_{22}\\\delta \boldsymbol{C}_{33}\\2\delta \boldsymbol{C}_{12}\\2\delta \boldsymbol{C}_{23}\\2\delta \boldsymbol{C}_{31}\end{array}\right\} + \left[\begin{array}{c|c}\frac{\partial \boldsymbol{R}^p}{\partial \boldsymbol{C}^p} & \frac{\partial \boldsymbol{R}^p}{\partial \Delta\lambda}\\\hline \frac{\partial \Phi}{\partial \boldsymbol{C}^p} & \frac{\partial \Phi}{\partial \Delta\lambda}\end{array}\right] \cdot \left\{\begin{array}{c}\delta \boldsymbol{C}_{p11}\\\delta \boldsymbol{C}_{p22}\\\delta \boldsymbol{C}_{p33}\\2\delta \boldsymbol{C}_{p12}\\2\delta \boldsymbol{C}_{p23}\\2\delta \boldsymbol{C}_{p31}\\\hline \delta\Delta\lambda\end{array}\right\} \tag{A.13}$$

or,

$$\begin{aligned}\left\{\begin{array}{c}\delta \boldsymbol{C}_{p11}\\\delta \boldsymbol{C}_{p22}\\\delta \boldsymbol{C}_{p33}\\2\delta \boldsymbol{C}_{p12}\\2\delta \boldsymbol{C}_{p23}\\2\delta \boldsymbol{C}_{p31}\\\hline \delta\Delta\lambda\end{array}\right\} &= -\left[\begin{array}{c|c}\frac{\partial \boldsymbol{R}^p}{\partial \boldsymbol{C}^p} & \frac{\partial \boldsymbol{R}^p}{\partial \Delta\lambda}\\\hline \frac{\partial \Phi}{\partial \boldsymbol{C}^p} & \frac{\partial \Phi}{\partial \Delta\lambda}\end{array}\right]^{-1} \left[\begin{array}{c}\frac{\partial \boldsymbol{R}^p}{\partial \boldsymbol{C}}\\\hline \frac{\partial \Phi}{\partial \boldsymbol{C}}\end{array}\right] \cdot \left\{\begin{array}{c}\delta \boldsymbol{C}_{11}\\\delta \boldsymbol{C}_{22}\\\delta \boldsymbol{C}_{33}\\2\delta \boldsymbol{C}_{12}\\2\delta \boldsymbol{C}_{23}\\2\delta \boldsymbol{C}_{31}\end{array}\right\} \\ &= -\left[dR^{-1}\right]_{7\times 7} \left[L\right]_{7\times 6} \left\{\delta \boldsymbol{C}\right\}_{6\times 1}\end{aligned}$$

by substituting (A.14) into (A.10), the consistent tangent modulus is found as:

$$\begin{aligned}\boldsymbol{\mathcal{C}}_{ep} &= \left[\begin{array}{c}\frac{\partial \boldsymbol{S}}{\partial \boldsymbol{C}}\end{array}\right] - \left[\begin{array}{c|c}\frac{\partial \boldsymbol{S}}{\partial \boldsymbol{C}^p} & \frac{\partial \boldsymbol{S}}{\partial \Delta\lambda}\end{array}\right] \left[\begin{array}{c}dR^{-1}\end{array}\right] \left[\begin{array}{c}L\end{array}\right] \\ &= \left[M\right]_{6\times 6} - \left[N\right]_{6\times 7} \left[dR^{-1}\right]_{7\times 7} \left[L\right]_{7\times 6}\end{aligned} \tag{A.14}$$

Note that the last column of $\left[N\right]$ is zero, so that the last row of $\left[dR^{-1}\right]$ can be omitted to give the tangent modulus as:

$$\boldsymbol{\mathcal{C}}_{ep} = \left[M\right]_{6\times 6} - \left[N\right]_{6\times 6} \left[dR^{-1}\right]_{6\times 7} \left[L\right]_{7\times 6} \tag{A.15}$$

In the above expression, $\left[M\right]$ is given by (3.106), which is also the tangent for purely elastic deformations ($\Phi < 0$).
Note that $\left[dR\right]$ has already been established in (3.100), $\left[N\right]$ is given by (3.105), and was used to construct $\left[dR\right]$.
Two components of $\left[L\right]$ are given as:

$$\frac{\partial \Phi}{\partial \boldsymbol{C}} = \frac{\partial \|[\boldsymbol{C}\boldsymbol{S}]^{\mathrm{dev}}\|}{\partial \boldsymbol{C}} \tag{A.16}$$

$$\frac{\partial \boldsymbol{R}^p}{\partial \boldsymbol{C}} = \left(\Delta\lambda \boldsymbol{\mathcal{I}} - \frac{\Delta\lambda^2}{2!}\frac{\partial \boldsymbol{f}\boldsymbol{C}^{p^{-1}}\boldsymbol{f}}{\partial \boldsymbol{f}} + \frac{\Delta\lambda^3}{3!}\frac{\partial \boldsymbol{f}\boldsymbol{C}^{p^{-1}}\boldsymbol{f}\boldsymbol{C}^{p^{-1}}\boldsymbol{f}}{\partial \boldsymbol{f}} + \ldots\right) : \frac{\partial \boldsymbol{f}}{\partial \boldsymbol{C}} \tag{A.17}$$

A.4 Contact Consistent Tangent

$\Delta \boldsymbol{N}^{Sl}$ and $\Delta \boldsymbol{T}^{Sl}$ follow from (8.30) and (8.31) as:

$$\begin{aligned}
\Delta \boldsymbol{N}^{Sl} &= \boldsymbol{n} \otimes \Delta \boldsymbol{\eta}_\xi + \boldsymbol{\eta}_\xi \Delta \boldsymbol{n} \\
&= -\boldsymbol{\eta}_0 \,.\, \boldsymbol{n} \otimes \Delta \xi + \boldsymbol{\eta}_\xi \Delta \boldsymbol{n} && \text{(A.18)} \\
\Delta \boldsymbol{T}^{Sl}_{slip} &= \boldsymbol{a} \otimes \Delta \boldsymbol{\eta}_\xi + \boldsymbol{\eta}_\xi \Delta \boldsymbol{a} + \boldsymbol{\eta}_0 \,.\, [\boldsymbol{n} \otimes (\frac{1}{l} \Delta g_N^{Sl} - \frac{g_N^{Sl}}{l^2} \Delta l) + \frac{g_N^{Sl}}{l} \Delta \boldsymbol{n}] \\
&= -\boldsymbol{\eta}_0 \,.\, \boldsymbol{a} \otimes \Delta \xi + \boldsymbol{\eta}_\xi \Delta \boldsymbol{a} \\
&\quad + \boldsymbol{\eta}_0 \,.\, [\boldsymbol{n} \otimes (\frac{1}{l} \Delta g_N^{Sl} - \frac{g_N^{Sl}}{l^2} \Delta l) + \frac{g_N^{Sl}}{l} \Delta \boldsymbol{n}] && \text{(A.19)} \\
\Delta \boldsymbol{T}^{Sl}_{stick} &= \Delta \boldsymbol{T}_{slip} + \boldsymbol{\eta}_0 \,.\, [\boldsymbol{a} \otimes (\frac{1}{l} \Delta g_T^{Sl} - \frac{g_T^{Sl}}{l^2} \Delta l) + \frac{g_T^{Sl}}{l} \Delta \boldsymbol{a}] && \text{(A.20)}
\end{aligned}$$

$\Delta \xi^{Sl}$, Δg_N^{Sl} and Δg_T^{Sl} have the same form with (8.23) and (8.26)

$$\begin{aligned}
\Delta \xi^{Sl} &= \frac{1}{l} \Delta \boldsymbol{u}_\xi \,.\, \boldsymbol{a} + \frac{g_N^{Sl}}{l^2} \Delta \boldsymbol{u}_0 \,.\, \boldsymbol{n} && \text{(A.21)} \\
\Delta g_N^{Sl} &= \Delta \boldsymbol{u}_\xi \,.\, \boldsymbol{n} && \text{(A.22)} \\
\Delta g_{Tstick}^{Sl} &= \Delta \boldsymbol{u}_\xi \,.\, \boldsymbol{a} + \frac{g_N^{Sl}}{l} \Delta \boldsymbol{u}_0 \,.\, \boldsymbol{n} + \frac{g_T^{Sl}}{l} \Delta \boldsymbol{u}_0 \,.\, \boldsymbol{a} && \text{(A.23)}
\end{aligned}$$

while Δl, $\Delta \boldsymbol{a}$ and $\Delta \boldsymbol{n}$ are

$$\begin{aligned}
\Delta l &= \frac{1}{2l} (2(\boldsymbol{x}_2 - \boldsymbol{x}_1) \Delta \boldsymbol{u}_2 - 2(\boldsymbol{x}_2 - \boldsymbol{x}_1) \Delta \boldsymbol{u}_1) \\
&= \boldsymbol{a} \,.\, \Delta \boldsymbol{u}_0 && \text{(A.24)} \\
\Delta \boldsymbol{a} &= \frac{1}{l} \Delta \boldsymbol{u}_0 - \frac{1}{l^2} (\boldsymbol{x}_2 - \boldsymbol{x}_1) \otimes \Delta l \\
&= \frac{1}{l} \Delta \boldsymbol{u}_0 - \frac{1}{l} \boldsymbol{a} \otimes \boldsymbol{a} \,.\, \Delta \boldsymbol{u}_0 \\
&= \frac{1}{l} (\boldsymbol{I} - \boldsymbol{a} \otimes \boldsymbol{a}) \,.\, \Delta \boldsymbol{u}_0 \\
&= \frac{1}{l} \boldsymbol{n} \otimes \boldsymbol{n} \,.\, \Delta \boldsymbol{u}_0 && \text{(A.25)} \\
\Delta \boldsymbol{n} &= \boldsymbol{e}_3 \times \Delta \boldsymbol{a} \\
&= -\frac{1}{l} \boldsymbol{a} \otimes \boldsymbol{n} \,.\, \Delta \boldsymbol{u}_0 && \text{(A.26)}
\end{aligned}$$

so that,

$$
\begin{aligned}
T_N \Delta \boldsymbol{N}^{Sl} &= T_N \big(\boldsymbol{\eta}_0 \,.\, -\frac{1}{l} \boldsymbol{n} \otimes \boldsymbol{a} \,.\, \Delta \boldsymbol{u}_\xi \\
&+ \boldsymbol{\eta}_0 \,.\, -\frac{g_N^{Sl}}{l^2} \boldsymbol{n} \otimes \boldsymbol{n} \,.\, \Delta \boldsymbol{u}_0 + \boldsymbol{\eta}_\xi \,.\, -\frac{1}{l} \boldsymbol{a} \otimes \boldsymbol{n} \,.\, \Delta \boldsymbol{u}_0 \big) \qquad \text{(A.27)} \\
T_T \Delta \boldsymbol{T}_{slip}^{Sl} &= T_T \big(\boldsymbol{\eta}_0 \,.\, \frac{1}{l} (\boldsymbol{n} \otimes \boldsymbol{n} - \boldsymbol{a} \otimes \boldsymbol{a}) \,.\, \Delta \boldsymbol{u}_\xi + \boldsymbol{\eta}_\xi \,.\, \frac{1}{l} \boldsymbol{n} \otimes \boldsymbol{n} \,.\, \Delta \boldsymbol{u}_0 \\
&+ \boldsymbol{\eta}_0 \,.\, -\frac{g_N^{Sl}}{l^2} (2\boldsymbol{a} \otimes \boldsymbol{n} + \boldsymbol{n} \otimes \boldsymbol{a}) \,.\, \Delta \boldsymbol{u}_0 \big) \qquad \text{(A.28)} \\
T_T \Delta \boldsymbol{T}_{stick}^{Sl} &= T_T \Delta \boldsymbol{T}_{slip} + T_T \big(\boldsymbol{\eta}_0 \,.\, \frac{1}{l} \boldsymbol{a} \otimes \boldsymbol{a} \,.\, \Delta \boldsymbol{u}_\xi \\
&+ \boldsymbol{\eta}_0 \,.\, \frac{g_N^{Sl}}{l^2} \boldsymbol{a} \otimes \boldsymbol{n} \,.\, \Delta \boldsymbol{u}_0 + \boldsymbol{\eta}_0 \,.\, \frac{g_T^{Sl}}{l^2} \boldsymbol{n} \otimes \boldsymbol{n} \,.\, \Delta \boldsymbol{u}_0 \big) \qquad \text{(A.29)}
\end{aligned}
$$

where $\Delta \boldsymbol{u}_\xi$ and $\Delta \boldsymbol{u}_0$ are defined in the same way $\boldsymbol{\eta}_\xi$ and $\boldsymbol{\eta}_0$ in (8.32). The first two terms are linearized as:

$$
\begin{aligned}
\boldsymbol{N}^{Sl} \otimes \Delta T_N &= \boldsymbol{N}^{Sl} \otimes \Delta t_N A \\
&= \boldsymbol{N}^{Sl} \otimes A \big(\frac{\partial t_N}{\partial g_N} \Delta g_N \big) \\
&= \boldsymbol{\eta}_\xi . (A c_N \, \boldsymbol{n} \otimes \boldsymbol{n}) . \Delta \boldsymbol{u}_\xi \qquad \text{(A.30)}
\end{aligned}
$$

and,

$$
\begin{aligned}
\boldsymbol{T}^{Sl} \otimes \Delta T_T &= \boldsymbol{T}^{Sl} \otimes \Delta t_T A \qquad \text{(A.31)} \\
&= \boldsymbol{T}^{Sl} \otimes A \big(\frac{\partial t_T}{\partial g_T} \Delta g_T + \frac{\partial t_T}{\partial g_N} \Delta g_N \big) \qquad \text{(A.32)}
\end{aligned}
$$

After insertion of $\frac{\partial t_T}{\partial g_T}$ and $\frac{\partial t_T}{\partial g_N}$, which are extracted from the constitutive model summarized in Box 8.1, $\boldsymbol{T}^{Sl} \otimes \Delta T_T$ is calculated as one of:

$$
\begin{aligned}
(\boldsymbol{T}^{Sl} \otimes \Delta \boldsymbol{T}^{Sl})_{stick} &= \frac{A \, c_T}{l} \big(\boldsymbol{\eta}_0 . \boldsymbol{a} \otimes \boldsymbol{a} . \Delta \boldsymbol{u}_0 + \boldsymbol{\eta}_0 . g_N^{Sl} \boldsymbol{a} \otimes \boldsymbol{n} . \Delta \boldsymbol{u}_0 \\
&+ \boldsymbol{\eta}_0 . g_N^{Sl} \boldsymbol{n} \otimes \boldsymbol{a} . \Delta \boldsymbol{u}_0 + \boldsymbol{\eta}_0 . \frac{g_N^{Sl} g_N^{Sl}}{l} \boldsymbol{n} \otimes \boldsymbol{n} . \Delta \boldsymbol{u}_0 \big) \qquad \text{(A.33)} \\
(\boldsymbol{T}^{Sl} \otimes \Delta \boldsymbol{T}^{Sl})_{slip} &= A \, \mu \, c_N \, sign(t_T^{trial}) \big(\boldsymbol{\eta}_\xi . \boldsymbol{a} \otimes \boldsymbol{n} . \Delta \boldsymbol{u}_\xi \\
&+ \boldsymbol{\eta}_0 . \frac{g_N^{Sl}}{l} \boldsymbol{n} \otimes \boldsymbol{n} . \Delta \boldsymbol{u}_\xi \big) \qquad \text{(A.34)}
\end{aligned}
$$

where (8.27) was used in formulating (A.34) and $\boldsymbol{\eta}_{\xi 0}$ is defined as:

$$
\boldsymbol{\eta}_{\xi 0} = \boldsymbol{\eta}^T \begin{Bmatrix} -(1 - \xi_0^{Sl}) \\ \xi_0^{Sl} \\ 1 \end{Bmatrix} \qquad \text{(A.35)}
$$

Note that for the geometrically linear case, (A.24), (A.25) and (A.26) vanish.

$$\Delta \boldsymbol{N}^{Sl} = -\boldsymbol{\eta}_0 \,.\, \boldsymbol{n} \otimes \Delta\xi \tag{A.36}$$

$$\Delta \boldsymbol{T}^{Sl}_{slip} = -\boldsymbol{\eta}_0 \,.\, \boldsymbol{a} \otimes \Delta\xi + \boldsymbol{\eta}_0 \cdot \frac{1}{l}\boldsymbol{n} \otimes \Delta g^{Sl}_N \tag{A.37}$$

$$\Delta \boldsymbol{T}^{Sl}_{stick} = \Delta \boldsymbol{T}^{Sl}_{slip} + \boldsymbol{\eta}_0 \cdot \frac{1}{l}\boldsymbol{a} \otimes \Delta g^{Sl}_T \tag{A.38}$$

A.5 Cohesive Consistent Tangent

$T_N \Delta \boldsymbol{N}^{Sl}$ and $T_T \Delta \boldsymbol{T}^{Sl}$ are given by (A.27) and (A.29) respectively, where, in 2D, $T_N = A t_N$ and $T_T = A t_T$. The first two terms are linearized as:

$$\begin{aligned} \boldsymbol{T}^{Sl} \otimes \Delta T_T &= \boldsymbol{T}^{Sl} \otimes A\beta^2 \left((\frac{\partial t}{\partial \delta} - \frac{t}{\delta}) \frac{g_T}{\delta} \Delta\delta + \frac{t}{\delta} \Delta g_T \right) \\ \boldsymbol{N}^{Sl} \otimes \Delta T_N &= \boldsymbol{N}^{Sl} \otimes A \left((\frac{\partial t}{\partial \delta} - \frac{t}{\delta}) \frac{g_N}{\delta} \Delta\delta + \frac{t}{\delta} \Delta g_N \right) \end{aligned} \tag{A.39}$$

t and $\frac{\partial t}{\partial \delta}$ follow from the constitutive relation (8.43) and (8.44), while $\Delta\delta$ follows from (8.39):

$$\begin{aligned} \Delta\delta &= \frac{\partial \delta}{\partial g_T} \Delta g_T + \frac{\partial \delta}{\partial g_N} \Delta g_N \\ &= \frac{1}{\delta} (\beta^2 g_T \Delta g_T + g_N \Delta g_N) \end{aligned} \tag{A.40}$$

so that,

$$\begin{aligned} \boldsymbol{T}^{Sl} \otimes \Delta T_T &= \boldsymbol{T}^{Sl} \otimes \frac{A\beta^2}{\delta} \left((\frac{\partial t}{\partial \delta} - \frac{t}{\delta}) \frac{g_T}{\delta} (\beta^2 g_T \Delta g_T + g_N \Delta g_N) + t \Delta g_T \right) \\ &= \boldsymbol{T}^{Sl} \otimes \frac{A\beta^2}{\delta} \left(\left[(\frac{\partial t}{\partial \delta} - \frac{t}{\delta}) \frac{\beta^2 g_T^2}{\delta} + t \right] \Delta g_T \right. \\ &\qquad \left. + \left[(\frac{\partial t}{\partial \delta} - \frac{t}{\delta}) \frac{g_T g_N}{\delta} \right] \Delta g_N \right) \\ \boldsymbol{N}^{Sl} \otimes \Delta T_N &= \boldsymbol{N}^{Sl} \otimes \frac{A}{\delta} \left((\frac{\partial t}{\partial \delta} - \frac{t}{\delta}) \frac{g_N}{\delta} (\beta^2 g_T \Delta g_T + g_N \Delta g_N) + t \Delta g_N \right) \\ &= \boldsymbol{N}^{Sl} \otimes \frac{A}{\delta} \left(\left[(\frac{\partial t}{\partial \delta} - \frac{t}{\delta}) \frac{\beta^2 g_T g_N}{\delta} \right] \Delta g_T \right. \\ &\qquad \left. + \left[(\frac{\partial t}{\partial \delta} - \frac{t}{\delta}) \frac{g_N^2}{\delta} + t \right] \Delta g_N \right) \end{aligned} \tag{A.41}$$

Δg_N and Δg_T are given by (A.22) and (A.23)